Multi-Wavelength Studies of Wind Driving Cataclysmic Variables

Dugan Kenneth Witherick

Thesis submitted for the Degree of Doctor of Philosophy
of the University of London

Department of Physics & Astronomy
UNIVERSITY COLLEGE LONDON

October 2004

ProQuest LLC
789 East Eisenhower Parkway
P.O. Box 1346
Ann Arbor, MI 48106-1346

ABSTRACT

This thesis presents several case studies of disc winds from high-state cataclysmic variable stars, based on multi-wavelength time-series spectroscopy. The research presented here primarily focuses on three low-inclination, nova-like systems: RW Sextansis, V592 Cassiopeiae and BZ Camelopardalis. The aim was to derive and compare key spectral line diagnostics of the outflows, spanning a wide range of ionisation and excitation using (new) FUSE, HST, IUE and optical data.

Analysis of the far-UV time-series of RW Sex reveals the wind to be highly variable but generally confined to between ~ -1000 and ~ 0 km/s for all ionisation states; no evidence of the wind at red-shifted velocities is found. This wind is modulated on the orbital period of the system and it is argued that the observed variability is due to changes in the blue-shifted absorption rather than a variable velocity emission. The Balmer profiles observed in the optical time-series of V592 Cas were found to be characterised by three components: a broad, shallow absorption trough, a narrow central emission and a blue-shifted absorption from the disc wind. The wind is also found to be modulated on the systems orbital period, although this modulation is slightly out of phase with the Balmer emission radial velocities. The wind of BZ Cam was found to behave very differently to that of RW Sex and V592 Cas. At times, it was seen (in the Balmer lines and some of the He I lines) to be extremely strong and variable but at other times is was seemingly not present; there was no evidence to suggest that it is modulated on the orbital or any other period.

This study is an immense source of data on CV disc winds and importantly tries to parameterise three nova-like CVs to understand the similarities and differences between them and their winds.

ACKNOWLEDGEMENTS

I would like to take this opportunity to thank a number of people who have provided me with help and support during my PhD. Firstly, I would like to thank my supervisor, Dr. Raman Prinja who, throughout the three years has continued to provide me with a consistently high level of support and guidance. I would also like to thank Dr. Linda Smith, Prof. Ian Howarth and Dr. Simon Clarke for advice not only on my PhD but on a future academic career in astronomy. For discussions and advice regarding stellar and accretion disc winds, I would like to thank Christian Knigge, Stan Owocki and Coel Hellier. I would additionally like to thank my friends and colleagues who have continued to support me during the last three years (in no particular order, apologies to those I have missed); Jay Abbott, Adam Burnley, Jo Fabbri, Robin Garrod, Phil Holtom, Sarah Kendrew, Ki-Won Lee, Dawn Leslie, Tamara Repolust, Fabrizio Sidoli, Sam Searle and Sam Thompson.

A special mention must go to my girlfriend, Fiona Groenhout, who has managed to brighten my life during the most difficult and stressful times of my PhD. Finally, I would like to thank my family, whose belief in me has got me to where I am today.

Whatever you do will be insignificant, but it is very important that you do it.

- Mahatma Gandhi

Contents

List of Figures

List of Tables

CHAPTER 1

Introduction

Cataclysmic variable stars or CVs, are fascinating astronomical targets involving an interacting binary, where mass is being transferred to a white dwarf from a low mass secondary star. Through a combination of their luminosity and their proximity to Earth, they are relatively bright targets (RW Sex has a V magnitude of 10.6) making them important objects for studying the processes of accretion and the evolution of binary stars. With so many sub-topics to research, the study of CVs has become impossibly large to be researched as a whole and as such they must be researched one sub-topic at a time. The particular CV sub-topic chosen for study in this thesis is winds or outflows from the accretion discs.

Given that winds from accretion discs are also observed in other astrophysical targets such as active galactic nuclei, X-Ray binaries and some types of young stellar objects, the question arises as to why study these winds from CVs when they can be studied in these many other objects. The simple answer to that question is accessibility. Other than the benefits of their relative brightness (e.g. observing them does not require large telescopes and, they can be studied with fast spectroscopy), they also have short orbital periods (typically a few hours) meaning that it is possible to observe orbital effects to the winds (if any exist) within one night of observations. Another important reason for studying disc winds from CVs is that these winds are thought to originate from the UV dominated inner regions of the accretion disc meaning that they can be easily studied in detail using the UV resonance lines. Thus CVs probably provide the best environments for studying winds from accretion discs of any astronomical target.

This thesis presents four detailed case studies of accretion disc winds from non-magnetic, nova-like cataclysmic variable stars, using time-series multi-wavelength spectroscopy. These case studies are followed by a time-independent far-UV survey of a number of cataclysmic variables of both nova-like and dwarf novae type. The purpose of this chapter is to provide an introduction to cataclysmic variable stars, and to provide background information about the structure and nature of nova-like and dwarf novae systems. Furthermore, an overview of winds and current disc winds theories for cataclysmic variables is presented.

1.1 What are cataclysmic variables?

Cataclysmic variable stars (or CVs) are semi-detached binary star systems consisting of a white dwarf (the primary star) and a late spectral type (typically G, K or M stars), low mass, main-sequence star (the secondary). With orbital periods between 80 minutes and 5 days, they are considered as being short period binaries and, with binary separations on orders of a few solar radii, they are small in comparison to many stellar astrophysical targets.

Most CVs form from a non-contact binary system through the loss of angular momentum (King 1988). Angular momentum is believed to be extracted from such a system through two processes; gravitational radiation and stellar magnetic braking. Gravitational radiation is generated by accelerating masses and in the case of the binary system, the energy used to create the gravitational radiation is extracted from the binary orbit. In the process of stellar magnetic braking, ionised particles emitted from the red dwarf as a stellar wind, flow along open magnetic field lines of this secondary star and flung away from the star. These ionised particles extract substantial angular momentum from the red dwarf and hence the binary orbit since the secondary is tidally locked into the binary system. The result of losing the angular momentum from the binary system is that the orbit shrinks, along with the Roche Lobe of the secondary star. The Roche Lobe is an equipotential surface of constant gravitational potential, which defines the boundary of where material is gravitationally bound to a star. The Roche Lobe of the secondary star continues to shrink and eventually comes into contact with the surface of the secondary star. In the case of CVs, the proximity of the two stars distorts the Roche Lobe into a double tear drop pattern, which are joined together at the inner Lagrangian point (or L_1

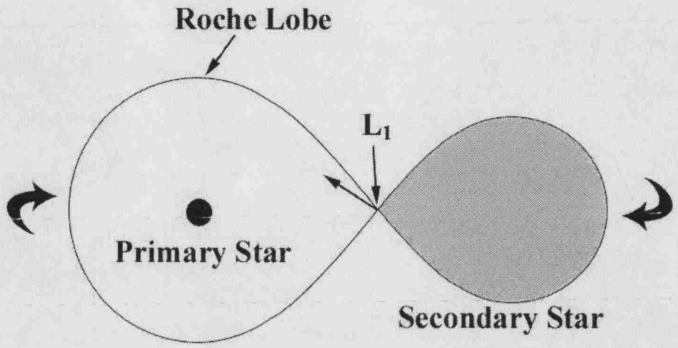

Figure 1.1: A cataclysmic variable system. The secondary star has filled the Roche Lobe (solid line) and mass is transferring to the primary star through the inner Lagrangian point (L_1). The stars orbit about the binary centre of mass.

see Fig. 1.1), where the gravity from the two stars balances. The random particle motions of the gas close to L_1, results in hydrogen-rich material overflowing the Roche Lobe, through L_1, and towards the primary star. Angular momentum must be conserved in this mass transfer and this means that material cannot fall directly onto the white dwarf. In the early stages of CV formation, the transferring gas forms a ring of material (since this is the configuration with the lowest energy) around the white dwarf. The ring of gas is heated by a combination of the supersonic impact from the accretion stream and viscous processes which are not well understood but, are believed to be mainly due to magnetic fields tied into the accretion disc; quite often these viscous processes are modelled with the α disc formulation of Shakura & Sunyaev (1973), where the viscous stress is proportional to the pressure of the gas and, α is a constant of proportionalility. The heating up of the gas results in a loss of gravitational potential energy and some of the material begins to fall closer to the disc. However, angular momentum must still be preserved so, a small amount of the material moves to greater radii to balance the material spiralling into the white dwarf and, the net result is the formation of an accretion disc.

The geometry of a CV resulting from components such as the accretion disc and the two stars, means that any observation of a system is highly dependent on the angle from which it is seen. One method of categorising a CV is through its inclination angle, which refers to the angle that the normal to the binary orbital plane makes to the line of sight; thus a very low inclination system is nearly face-on and a very high inclination system is nearly edge on. However in practice, definition of whether a system has a high or low

inclination angle is more closely related to whether it is an eclipsing system or not. In systems with a high enough inclination angle (greater than $\sim 65°$), the secondary star can eclipse the white dwarf, accretion disc and bright spot for a small portion of the orbit. The resulting eclipse light curve can reveal important information about the accretion disc, such as the relative brightness of the individual components and, their size and locations. Since the inclination angle is purely an observational effect, the observed range of values should represent a uniform distribution at all angles, with an average of around 45°. However in reality, difficulties in measuring the inclination angles at the extremes can somewhat affect this distribution.

1.2 The Structure and Properties of the CV Components

In the generic model of an non-magnetic CV, there are six main components: the secondary star, the accretion stream, the bright spot, the accretion disc, the boundary layer and, the primary star or white dwarf; in some cases there can be a seventh component in the form of an outflow from the accretion disc. Fig. 1.2 is a diagram of a non-magnetic CV with many of the important features labelled. Magnetic CVs, such as polar and intermediate polar systems, can vary significantly from this model; these differences are briefly discussed in § 1.2.1 although it should be noted that these systems are not the focus of this study. What follows is a description of the CV components.

The *secondary component* of a CV is typically a low mass, main-sequence star of spectral type, late K or M and is therefore referred to as a red dwarf. The low surface temperatures (typically less than 4000 Kelvin) and small size means that their contribution to the luminosity of the entire CV is small and is typically confined to near-infrared (or near-IR) and IR wavelengths. The donated spectrum of the red dwarf would typically consist of narrow absorption lines, a few molecular bands and, in some cases, chromospheric emission lines.

The small surface areas and low temperatures of red dwarfs means that they progress very slowly along the main sequence in comparison to the star which became the white dwarf. The star would be generating its energy from the proton-proton chain and therefore there would be a slow conversion of hydrogen to helium in the core of the star (the primary branch of the proton-proton chain is briefly shown below).

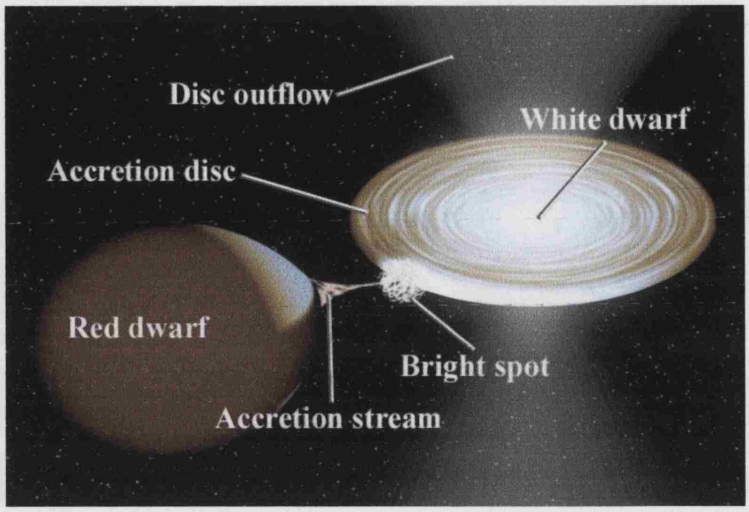

Figure 1.2: A visualisation of a non-magnetic CV with several of the major components labelled. The image was generated using the binary simulation code of R. Hynes, Southampton University.

$$^{1}\mathrm{H} + ^{1}\mathrm{H} \rightarrow ^{2}\mathrm{H} + e^{+} + \nu_e + 0.42\mathrm{MeV} \quad (1.1)$$

$$^{1}\mathrm{H} + ^{2}\mathrm{H} \rightarrow ^{3}\mathrm{He} + \gamma + 5.49\mathrm{MeV} \quad (1.2)$$

$$^{3}\mathrm{He} + ^{3}\mathrm{He} \rightarrow ^{4}\mathrm{He} + ^{1}\mathrm{H} + ^{1}\mathrm{H} + 5.49\mathrm{MeV} \quad (1.3)$$

As this process continues, the abundance of hydrogen in the core decreases and to maintain the nuclear burning rate the temperature and density increase; this increase in temperature inevitably results in the expansion of the star. If the red dwarf were in a pre-cataclysmic binary, it is feasible for the star to expand sufficiently to make contact with the Roche Lobe and thus begin mass transfer to the primary star. However, the time-scale for this stellar expansion is on the order of the age of the Galaxy and therefore this would be the originating process for a CV for only a very small number of systems; angular momentum loss is still believed to be the key process whereby mass transfer begins in the pre-cataclysmic binary (see § 1.1) system.

When the secondary star comes into contact with the Roche Lobe, material is transferred towards the white dwarf through the inner Lagrangian point or L_1. The flow of material from the secondary to the primary star is called the *accretion stream*. Initially the material forms a ring of gas around the white dwarf but later, the accretion stream

feeds the accretion disc with mass from the secondary star. The trajectory of the accretion stream is controlled in part by the Coriolis effect and can be estimated by integrations of the equations of motion for a particle in a rotating binary frame, resulting in the equation:

$$\frac{1}{2}\dot{r}^2 + \Phi_R^2 = const. \tag{1.4}$$

where $\dot{r}$ is the particle velocity and Φ_R is the total gravitational potential at a specified location. The initial velocity of the material in the stream would be sonic but, as the particles get close to the white dwarf, they would be flowing at highly supersonic velocities. However, the particles can never escape the Roche Lobes because their velocities continue to fall as they approach these equipotential surfaces. In CVs where an accretion disc has formed, the accretion stream collides with the edge of the accretion disc at supersonic speeds, resulting in what is known as the hot or bright spot.

The *bright spot* of a CV is the region of the accretion disc where the accretion stream impacts. A shock occurs at the location of impact which heats up the region of the disc around the impact, resulting in the strong emission of light, typically at optical wavelengths. For some CVs, this bright spot can give off more light than all of the other components combined but usually, it is just a strong contributor to the overall spectrum. Sometimes, the bright spot can give off a strong, but narrow Balmer emission which varies sinusoidally in the velocity-time plane on the systems orbital period; for this reason, it can used to aid in the determination of binary orbit solutions. The location of the bright spot is determined by the trajectory of the accreting material and the size of the accretion disc but this is normally some distance from the line joining the centre of the two stars.

Perhaps the most characteristic feature of a CV is the *accretion disc.* These discs are believed to exhibit a wide range of properties. They can be thick, thin, flared, tilted, warped, and in a steady or non-equilibrium state depending on a number of factors including the mass transfer rate from the donor star. For the most part, the gravitational field of the secondary star has little impact on the motion of the particles in the disc but, where a disc is particularly large, the outer regions can be affected by tidal interactions. The particles in the accretion disc are believed to undergo Keplerian orbits and so their velocities are described by

$$v = \left(\frac{Gm_1}{r}\right)^{0.5} \tag{1.5}$$

where m_1 is the mass of the white dwarf and r is the radius of the orbit around the white dwarf. The thickness of the accretion disc is generally determined by hydrostatic equilibrium and is thus normally small since the original accretion stream is in the orbital plane of the CV and, even the impact of the bright spot would not deflect much material above the orbital plane.

The contribution from the accretion disc to the spectrum of a CV is significant. The continuum output from the disc can be estimated by assuming that the disc consists of a series of concentric blackbody emitters of increasing temperature towards the white dwarf, ranging from $\sim$ 5000 K at the outer edges to $\sim 10^4$ K at the inner edge (see Fig. 1.3). The resulting continuum can contribute flux to the CV spectrum from far-UV wavelengths down to the infra-red and beyond, although the flux typically peaks around UV and optical wavelengths (e.g. Shakura & Sunyaev 1973); the blackbody continuum of a CV accretion disc is actually well approximated by the Kurucz model continuum of an early-type B star (Kurucz 1993). The luminosity of the accretion disc can be estimated with the equation

$$L = \frac{G\dot{M}M_1}{R_1} \tag{1.6}$$

where $\dot{M}$ is the mass transfer rate from the donor star, M_1 is the mass of the white dwarf and R_1 is the radius of the white dwarf; only half of this luminosity would be available to the accretion disc, the other half of the luminosity would probably be released at the boundary layer between the accretion disc and the white dwarf.

The spectral line contribution to the overall spectrum from the accretion disc would depend on the current state that the disc was in. The accretion disc typically contributes strong hydrogen (Paschen, Balmer and Lyman), helium (both He I and He II), calcium and iron lines but, whether these lines are in absorption or emission is dependent on the current state of the disc and the inclination angle of the system. If a system is in a state of quiescence then it is common for the lines to be in emission, broad and double peaked; the double peak is due to the summation of the line of sight velocities of the material in the accretion disc (see Fig. 1.4 and Horne & Marsh 1986). Direct evidence of the accretion disc was provided by high inclination, eclipsing systems and these double peaked emission lines. Observations of these systems during eclipse showed that the blue-ward peak of the emission was eclipsed before the red-ward peak, indicating that

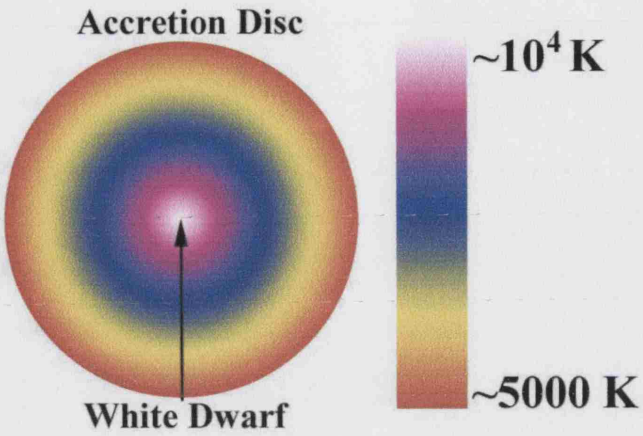

Figure 1.3: A figure demonstrating the temperature profile of an accretion disc. The quoted temperatures and relative size are representative values only.

the emission lines originated from a large, extended region i.e. the accretion disc (see Young & Schneider 1981). For CVs in a state of outburst (or constant outburst in the case of nova-like systems), the spectral lines are typically in absorption since the emission lines have been quenched by the strong continuum of the disc and, absorption cores have developed in their place.

The *boundary layer* is located between the accretion disc and the white dwarf and, it is where the fast moving gas of the accretion thermalises and radiates much of its kinetic energy to match the surface velocity of the white dwarf; Keplerian gas velocities of the inner disc are on the order of a few 1000 km/s while example white dwarf rotational velocities (or $v \sin i$) are 150 km/s for U Gem (Sion *et al.* 1994) and 600 km/s for VW Hyi (Sion *et al.* 1995). The temperature (and therefore luminosity) of the boundary layer is dependent on the differential in velocities of the accretion flow and the white dwarf surface but, it is typically $\sim 10^5$ K so the radiation is primarily at soft X-ray and EUV wavelengths.

The final component to a cataclysmic variable is the *primary star* (other than a disc outflow if one is present) or white dwarf. White dwarfs are the final evolutionary stage of some low mass (but not very low mass) stars and are supported from gravitational collapse by electron degeneracy pressure. The white dwarfs in CVs weigh between ~ 0.5 – 1 $M_\odot$ and, although they are the heavier component of the system, they only need to be 20% heavier than the secondary star for a stable CV to exist. Their temperatures tend to be higher than standard white dwarfs since they can be heated by the accretion disc

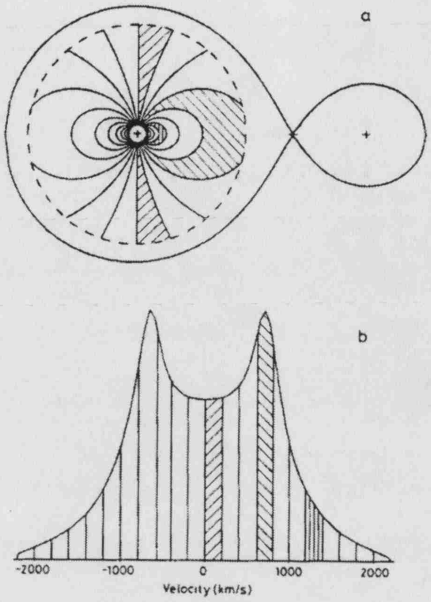

Figure 1.4: (a) The Keplerian accretion disc model in a binary of mass ratio $q = 0.15$. The different patterns represent areas with the same velocity. (b) The resulting (synthetic) emission profile of the accretion disc in (a) assuming that the system is observed edge on. The patterned emission regions correspond to the same areas in (a). Reproduced from Horne & Marsh (1986).

or the boundary layer: estimates currently put those temperatures at between 10000 and 50000 K depending on the type of CV which the white dwarf is seated in. The spectrum of the central white dwarf would peak around the UV and far-UV, and consist of Lyman α and Balmer absorption. The relative strength of the white dwarf flux in comparison to the other components is obviously dependent on a number of factors such as the white dwarf temperature but, the contribution is large and it is not unexpected for the white dwarf to be the primary source of flux at UV wavelengths.

1.2.1 Magnetic Cataclysmic Variables

The description provided above of a CV is a generic formulation for non-magnetic systems. When a CV is referred to as being magnetic or non-magnetic, it refers to the magnetic field strength of the primary star or white dwarf. The magnetic field strength of a white dwarf is already particularly high in comparison to an average star like the sun (greater than 1000 times stronger) due to the conservation of magnetic flux as the original star

collapsed; even in those CVs where the white dwarf magnetic field is considered weak, it still has an impact on the environment around the accretion disc. However, in some CVs, the magnetic field is so strong it actually disrupts the accretion disc, and material can flow along field lines instead of spiralling onto the white dwarf.

Magnetic CVs are categorised according to the strength of the magnetic field of the white dwarf and the resulting effect it has on the accretion disc. The magnetic field strength of a white dwarf in a non-magnetic CV is $\sim 10^4$ G while the field strength in the polar or AM Her CVs is much stronger, at between 10^6 and 10^7 G. In polar CVs, the magnetic field strength of the white dwarf is strong enough to completely control the transfer of the ionised material from the donor star and, an accretion disc never forms. Instead, the accreting material flows along the field lines onto the poles of the white dwarf. The magnetic field strength of the white dwarf is also so strong that it interacts with the field of the secondary star, coupling the two together so that the white dwarf rotates at the same rate as the revolution of the binary. The coupling means that the X-ray, UV and optical radiation from these systems vary on the orbital period. The interaction between the infalling gas and the magnetic field results in the radiation of naturally polarised cyclotron emission. Close to the white dwarf, the relatively high free-fall energy of the infalling gas is converted into thermal energy through a very strong shock; the plasma that remains after the shock emits at hard X-ray wavelengths.

With field strengths between 10^5 – $10^6 G$, intermediate polars have insufficient field strength to couple the rotation of the white dwarf and the secondary star together and so the white dwarf typically rotates on a much shorter period. Also, the field is strong enough to disrupt the accretion disc but only close to the white dwarf, so an accretion disc forms minus the most central parts. DQ Her stars are a sub-set of intermediate polars with extremely short rotation periods.

1.3 Non-magnetic CVs in more detail

1.3.1 Categorising Non-Magnetic CVs

Non-magnetic CVs are normally categorised by their light curves and spectrum characteristics. The four main subgroups of CVs are: the dwarf novae, the classical novae, the recurrent novae, and the nova-likes. In this section, these subgroups are described in more detail.

Dwarf novae are CVs which undergo multiple but temporary increases in luminosity of between 2-5 magnitudes. The large changes in luminosity are thought to be associated with the state of the accretion disc. For most of the time, a dwarf nova and therefore its accretion disc, is in a state of quiescence but sometimes there is a large increase in the mass transfer rate from the donor star and the accretion disc becomes large and hot from the increased release of gravitational potential energy, and subsequently there is a significant increase in luminosity. These outbursts occur pretty regularly, on time-scales ranging from approximately 10 days to as much as several decades, depending on the system in question. Dwarf novae can also be further sub-divided into three distinct groups (Z Cam stars, SU UMa stars and U Gem stars) which are dependent upon their outburst characteristics. These characteristics are:

SU UMa These dwarf novae occasionally undergo a super-outburst which is approximately 0.7 magnitudes stronger than a normal outburst and also lasts five times longer.

Z Cam These dwarf novae experience long periods (up to years) in a semi-outburst state although no full outbursts are observed during this time.

U Gem This group of dwarf novae includes all other systems.

Classical novae are CVs which have been observed to undergo one eruption but, these eruptions are much greater in luminosity than the outburts observed for the dwarf novae systems. A classical novae will typically undergo an increase of luminosity between 6 and 19 magnitudes and the larger the increase, the shorter time the outburst lasts for (in the case of systems which only increase by 6 magnitudes, the outburst has been observed to last for years). The best explanations put forward for these outbursts so far is that the hydrogen rich material which has built up on the surface white dwarf, suffers from sufficient heat and pressure that it undergoes thermonuclear runaway. Many of these systems are later reclassified as nova-like systems (described below). Recurrent novae are very similar to classical novae except that they repeat their outbursts; this could make it difficult to distinguish between a strong dwarf novae and a weak recurrent novae but, recurrent novae eject gases at high velocity during outburst, which can be detected spectroscopically.

Nova-like CVs are those systems which are not observed to undergo any outburst or

eruption. In some cases, magnetic stars and dwarf novae are classified as nova-like systems until further observations prove otherwise. As with dwarf novae, the nova-like category can be subdivided into a number of smaller groups. These sub-groups are:

RW Tri The spectra of this sub-group of nova-like systems is characterised by an emission spectrum, with particularly strong Balmer lines.

UX UMa The spectra of this sub-group of nova-like systems is characterised by the presence of broad Balmer absorption which is believed to relate to relatively high mass transfer rates from the donor star. However, these systems can and do sometimes have other lines such as He I and He II lines in emission at optical wavelengths and, in a small number of cases the Balmer absorption can have a weak emission core.

SW Sex This sub-group of nova-like CVs is characterised by a number of properties identifed by Thorstensen *et al.* (1991) such as phase 0.5 absorption, although many of the characteristics are dependent on the system having a high inclination. This sub-group is discussed in more detail in § 4.6.

VY Scl This sub-group of nova-like systems are often referred to as anti-dwarf novae. Most of the time they are in a persistant state of outburst, as with the UX UMa systems. However occasionally these systems undergo a change of state to quiescence, resulting in a drop in luminosity of between 1.5 and 2 magnitudes.

In the above list of nova-like sub-groups, SW Sex stars and VY Scl stars have been listed as two distinct sub-groups of nova-like CVs. However, it should be made clear that this is not necessarily the case since many SW Sex stars are in fact VY Scl stars and, many VY Scl stars are SW Sex stars.

1.3.2 Orbital Periods

The only system parameter which is accurately known for most CVs is the orbital period. A CV's orbital period can give some indication of its size. Newton's generalisation of Kepler's third law gives:

$$P_{\rm orb}^2 = \frac{4\pi^2 a^3}{G[M_1 + M_2]} \tag{1.7}$$

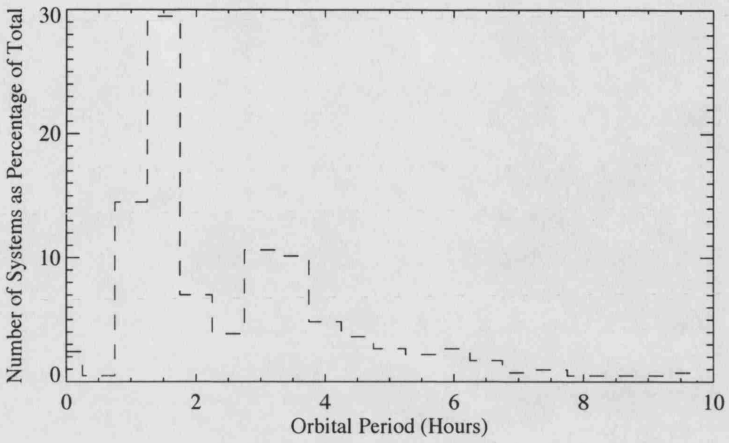

Figure 1.5: The distribution of orbital periods for nova-like and dwarf novae systems, from Ritter & Kolb (2004).

where M_1 and M_2 are the masses of the primary and secondary stars and, a is the binary separation of the two stars. Therefore if the mass of one of the stars is known and, the mass ratio of the two stars is known (often referred to as q and is determined by $\frac{M_2}{M_1}$), it is possible to calculate the binary separation of the two stars; often the masses of the two stars are not known but, by providing a suitable estimate to the values, it is possible to calculate an approximation.

The orbital period can be determined photometrically using the orbitally modulated changes to the CVs light curve. However, there are cases when the photometrically determined period is a few percent shorter or longer than the true orbital period (this phenomenom is known as superhumping and it is discussed in more detail in § 3.7) and in these situations, the orbital period can instead be determined spectroscopically using the phase dependent velocity shifts of emission lines originating from the bright spot. The range of orbital periods extends from $\sim$ 80 minutes to around 5 days, although most systems have an orbital period between 80 minutes to 10 hours; Fig. 1.5 is a histogram showing the orbital period distribution of nova-like and dwarf novae systems using data collected from Ritter & Kolb (2004). It is clear from Fig. 1.5 that the orbital period distribution of CVs is not random, there is a definite lower limit of around 80 minutes and there is a significant drop in the number of systems towards a period of 10 hours. Importantly, there is also a reduced number of systems between 2 to 3 hours which is referred to as the 2 to 3 hour period gap.

The 80 minute lower limit to the orbital periods of CVs is thought to be real and not an observational effect; the solution to why this lower limit exists is provided by Paczynski & Sienkiewicz (1981) and Rappaport *et al.* (1982). The mass of the secondary star is sufficient for it to support hydrogen burning and as such, it has the mass-radius relationship of a main-sequence star, where the smaller the mass the smaller the radius. However, the star is transferring mass onto the primary star and at some point it has lost so much mass that it can no-longer support hydrogen burning in its core. When this happens the star becomes degenerate and its mass-radius relationship changes to that of a partially degenerate brown dwarf, so that the lower the mass, the larger the radius. For mass transfer to take place, the radius of the secondary star must be greater than the radius of the Roche Lobe but, the radius of the Roche Lobe provides very narrow limits on the orbital period. Since the secondary star initially reduces in size and then increases in size, there is a physical minimum radius to that star which provides a minimum Roche Lobe radius and therefore a minimum orbital period.

When the 2-3 hour period gap was originally discovered it was named as so because there were absolutely no CVs within that period range. However, that is no longer the case and as Fig. 1.5 shows, there are a number of systems with orbital periods between 2-3 hours, although the number of systems is still quite low. The favoured explanation for the reduction in the number of observed system in this period range is the interruption (or reduced efficiency) of magnetic braking of the secondary star which is thought to be the mechanism for extracting angular momentum from the binary orbit. The masses of the secondary stars which coincide with the period gap correspond to stars who's internal structures are changing from a deep convective envelope to total convection. When this conversion occurs, the magnetic field rearranges causing the angular momentum loss to significantly decrease and in response, the secondary star contracts within the Roche Lobe, stopping the transfer of mass onto the white dwarf. Although stellar magnetic braking has ceased, a CV within the period gap can continue to lose angular momentum through the radiation of gravity waves, albeit at a much slower rate. This loss of angular momentum and subsequent drop in binary separation means that the orbital period of the CV slowly decreases and hence it slowly moves through the period gap towards the lower end. The reduction in the binary separation (and corresponding shrinkage of the Roche Lobe), means that the secondary star will eventually come into contact with the Roche Lobe again and mass transfer to the primary star will re-start. The orbital periods

at which this occurs corresponds to the bottom of the period gap.

What has been provided in this section is an introduction into the structure and nature of (mainly non-magnetic) CVs. The study of CVs can cover a large number of subjects ranging from the mechanisms behind the outbursts to the evolution of these systems. For information about these and the many other subject areas of CVs, it is recommended that the reader consults Warner (1995).

1.4 Stellar and Accretion Disc Winds

The focus of this study is of course the accretion disc winds from CVs so the purpose of this section is to provide background information about them. From the existence of P-Cygni profiles at UV wavelengths to the belief that line-driving is the dominant force, CV disc winds share some common properties with the stellar winds from massive luminous stars so, initially a brief introduction into stellar winds (with focus on the winds from massive luminous stars) is given.

1.4.1 What is a Stellar Wind?

A stellar wind is an outflow of material from the surface of a star. Strictly speaking this outflow must be continuous but, between systems there can be a significant difference in strength and behaviour. A stellar wind is important in many ways. If the stellar wind of a particular star is strong enough and the resulting mass-loss is sufficient, then the evolution of that star can be seriously affected. For example, a star could originally have enough mass to form a black hole when it eventually died but, through the action of mass-loss during its lifetime, it may no longer have sufficient mass to achieve this end and instead forms a neutron star. Stellar winds can also have a wider impact on the interstellar medium through the injection of energy and momentum and, chemically enriched material.

The two fundamental parameters used to describe a stellar wind are, its mass loss rate (or $\dot{M}$) and its terminal velocity (or v_∞). $\dot{M}$ is usually in units of solar masses per year and simply describes the mass of material that the star loses due to its outflow every year. Example values for mass loss rates are $\sim 10^{-14}$ $M_\odot$ yr^{-1} for the Sun and $\sim 10^{-6}$ $M_\odot$ yr^{-1} for a typical luminous, massive star. Taking the latter of these two examples, if the star maintained such a mass-loss rate for a million years, then during this time it would

have lost the equivalent mass of the Sun. v_∞ is the terminal velocity that the outflowing material is accelerated to and is often in units of km/s. The measured terminal velocity can often depend on the line from which the measurement was taken but, a reasonable value for an O-type star for example is 2500 km/s.

One of the most important equations of a stellar wind is that of mass continuity. Using the assumption of a spherically symmetric wind, the equation states that the mass flowing through a sphere centred on the star is the same no matter what the radius, since no mass in the wind is either created or destroyed. The equation of mass continuity is

$$\dot{M} = 4\pi r^2 \rho(r) v(r) \tag{1.8}$$

where r is the radius, $\rho(r)$ is the density of the material at r and $v(r)$ is the velocity of the material at r. The assumption of most stellar winds is that they are continually accelerated from the surface of the star until they reach v_∞ and, to describe the velocity at every radius (and therefore the overall acceleration) a velocity law is used. Different acceleration processes can result in different velocity laws but, for many stars the β formulation is used which is

$$v(r) = v_0 + (v_\infty - v_0)\left(1 - \frac{r_*}{r}\right)^\beta \tag{1.9}$$

where v_0 is the initial velocity of the material, r_* is the radius of the star and, β is the parameter used to describe the rate at which the wind is accelerated (a typical value for a hot star is 0.8).

1.4.2 Observations of Stellar Winds

The most extensively studied stellar wind is the solar wind or, the outflow of particles from the surface of the Sun. With an observing platform within the wind, the Sun provides a unique opportunity to observe a stellar outflow up close, rather than at a significant distance. The solar wind has been studied through its affects on specific objects such as the Earth's atmosphere (the aurorae) and more directly such as through NASA's Genesis mission, to collect particles from the solar wind and return them to Earth for further analysis; despite the failure of Genesis' parachute system some particles of the wind have still been retrieved. The solar wind is relatively weak and transparent and it would not

be possible to study it in much detail if it were instead at a distance of even the most local of stars. The winds from the hot, OB stars are particularly strong and show some opacity at certain wavelengths (typically UV to optical) meaning that they can be studied in great depth. As it has already been mentioned, the winds from hot, OB stars show some similar properties to CV disc winds so what follows is a discussion of how the winds from these systems can be observed and therefore studied.

Strong stellar winds in a wide range of star types are typically studied using the lines that form within them. There are five main ways in which lines can form in any type of outflow, and these are:

Pure Absorption An excited atom is further excited to a higher energy level, followed by a spontaneous emission to a lower than original state.

Masering An excited atom is hit by a photon, resulting in the emission of another photon of the same frequency (i.e. the result is that there are two photons of the same frequency, rather than just the one).

Collisional or Photo-excitation An atom is excited from the ground state through collisions or photo-excitation and this is followed by the subsequent release of a photon.

Recombination An electron recombines with an ion and, photons are released as the ion cascades down the energy levels.

Line scattering A photon is absorbed by an atom but, then re-emitted at the same frequency in a random direction, independent of the original photons direction. The emitted photon will be Doppler shifted in frequency space, depending on the motions of the absorbing particle.

Resonance scattering is a form of line scattering occurring in low density material, where the atom resonates between the ground state and an excited state through the constant absorption and subsequent re-emission of photons of the correct wavelength. Resonance scattering is believed to be the most common line formation process involved in the creation of a P-Cygni profile, which is the characteristic profile observed in the spectra of the hot OB stars.

P-Cygni profiles are mostly seen at far-UV and UV wavelengths (but not always, they are also seen in some optical lines) and they are one of the most important diagnostic tools

in the study of strong stellar winds. By comparing an observed P-Cygni profile with a simulated one, it is possible to determine v_∞, $\dot{M}$ and β for a particular star; what follows is a description of how the profile is formed, using Fig. 1.6. Firstly, this description of how a P-Cygni profile forms is based on the star (labelled S) having a spherically symmetric, accelerating wind and is seen by the observer, indicated by the label O. If no stellar wind were present then the observer would see just the continuum emitted from the star and any associated stellar lines. The first impact the stellar wind has on the continuum is to resonantly scatter some of the photons which have been emitted from the sides of the star (the regions labelled A) and therefore would not have originally been seen, into the line of sight of the observer to produce an excess of emission, as demonstrated by the plot labelled A in the bottom of Fig. 1.6. The scattering ions have a range of velocities (and therefore a range of line of sight velocities) through their acceleration from the surface of the star and so the impact on the emission is to provide a considerable spread in velocity, either side of the line centre. However, the ions which are travelling in the tube of gas between the star and the observer (labelled B) are scattering some of the photons out of the line of sight meaning that there is an additional absorption component to be added to the continuum. This absorption component is predominantly blue-shifted because the ions which have scattered the photons are moving towards the observer (see the plot labelled B in Fig. 1.6). The corresponding tube of gas on the opposite side of the star (labelled C) makes no contribution to the P-Cygni profile because it is occulted by the disc of the star. The combination of this blue-shifted absorption and broad emission results in the P-Cygni profile, approximated by the plot labelled P in Fig. 1.6.

This description of a P-Cygni profile only considers a perfect scenario and there is in fact considerable variation in the shape of a P-Cygni profile, depending on the strength and overall characteristics of the contributing absorption and emission. For example, the strength of the wind formed absorption and emission can be greatly affected if there is already photospheric absorption for a particular line and, both components can also be affected by the size of the star with respect to the windy region; this second issue it particularly important for CV winds due to the comparative size of the wind and the accretion disc which it projects against.

In the very strongest of stellar winds, with mass loss rates greater than 10^{-6} $M_\odot$ yr^{-1}, it becomes increasingly common to see emission lines of hydrogen and helium in the optical. This emission is believed to be mainly due to recombination and is thought to

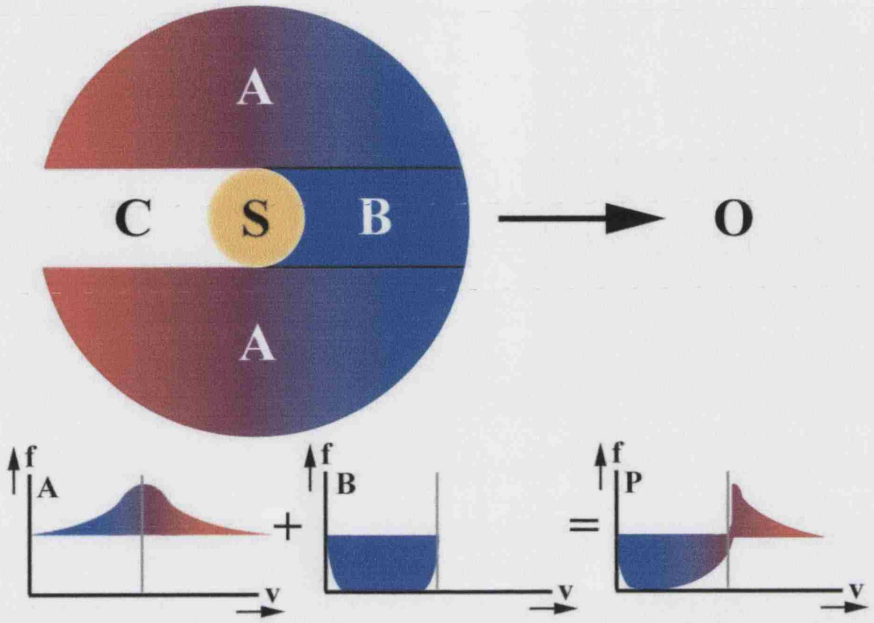

Figure 1.6: A figure demonstrating the formation of the P-Cygni profile; a complete description is given in the text. The labelled components are: S - the star, O - the observer, A - the gas responsible for the emission component, B - the gas responsible for the absorption component, C - the gas corresponding to component B, on the opposite side of the star to the observer but, also occulted from view. Adapted from Lamers & Cassinelli (1999).

form in the higher density regions of the wind, very close to the surface of the star. These emission lines are normally symmetric and their strength and profile shape relate to the velocity law of the wind (or β law where used) and the degree of mass-loss that the star exhibits.

1.4.3 What Accelerates/Drives a Stellar Wind?

Regardless of the size or temperature of a star, any mechanism that drives a wind must be strong enough and act over a long enough distance so as to accelerate the outflowing particles beyond the escape velocity of the star. For cool stars such as the Sun, the driving force behind the wind is believed to be coronal gas pressure, from a super heated corona. Theories for heating the corona to millions of degrees include micro-flares and, the transfer of energy from the sub-surface convective zone to the coronal gas through magnetic reconnection but, regardless of the heating method, the result is an extremely

hot gas with a pressure too high to be contained by the interstellar medium. The original model for the gas pressure driven wind was developed for the Sun by Parker (1960) using current knowledge of the Sun and the conservation of momentum equation

$$\left(1-\frac{a^2}{v^2}\right)v\frac{dv}{dr}=-\frac{GM}{r^2}+\frac{2a^2}{r}-\frac{da^2}{dr} \tag{1.10}$$

where v is the velocity, M is the mass of the star and a is the isothermal sound speed of the gas, given by

$$a(r)^2=\frac{RT}{\mu} \tag{1.11}$$

where R is the gas constant, T is the temperature and μ is the mean atomic weight of the particles, assuming the perfect gas conditions apply. If the wind is assumed to be isothermal then $T = constant$ throughout the wind and the equation reduces to

$$\left(1-\frac{a^2}{v^2}\right)v\frac{dv}{dr}=-\frac{GM}{r^2}+\frac{2a^2}{r} \tag{1.12}$$

In the above equation of motion, there is a point at which the right hand side changes sign. The exact point at which this occurs is called the critical point and associated with it are a critical velocity given by the equation $v_c = a$ and a critical radius, given by the equation $r_c = \frac{GM}{2a^2}$. For any given star who's wind is driven by gas pressure, there is only ever one solution which is compatible with the observations. This critical (or transonic) solution for the Sun (assuming an isothermal gas temperature of 1.5×10^6K) is $v_c = 160$km/s and $r_c = 3.9\mathrm{R}_\odot$.

Current theories of stellar structure suggest that the larger, hotter stars lack the strong convective zones necessary to produce a superheated corona and thus the winds from these systems cannot be driven by its pressure expansion. However, hot stars have enormous luminosities in comparison to cool stars; the luminosity, radius and temperature (assuming that it is a blackbody radiator) of a star are related by

$$L=4\pi R^2\sigma T_{eff}^4 \tag{1.13}$$

where L is luminosity, σ is the Stefan-Boltzmann constant, R is the star's radius and T_{eff} is its effective temperature, which shows that the luminosity of a star scales to the fourth

power of the temperature. So, rather than being driven by the coronal gas pressure which is relatively weak for a large hot star, the wind is driven by the shear pressure of the outflowing radiation.

The simplest case of radiation pressure is Thomson scattering, where the photons transfer momentum to free electrons in the outflow. The process is independent of wavelength, and the degree of interaction between the radiation and the free electrons is given by the interaction cross section or opacity. The opacity for electron scattering in an ionised gas is given by

$$\kappa_e = \frac{\sigma_e}{\mu_e} \tag{1.14}$$

where σ_e is the Thomson cross-section ($0.66 \times 10^{-24} \mathrm{cm}^2$) and μ_e is the mean atomic mass per free electron. For solar mass fractions of hydrogen, the opacity is calculated to be 0.34 $\mathrm{cm}^2\mathrm{g}^{-1}$. The momentum flux of the radiation at any distance from the star is given by

$$\frac{L}{4\pi r^2 c} \tag{1.15}$$

where L is the luminosity and c is the speed of light. The product of this radiative momentum flux and the free-electron opacity gives the force per unit mass (and therefore acceleration) from the Thomson scattering

$$g_e(r) = \frac{\kappa_e L}{4\pi r^2 c}. \tag{1.16}$$

The force on the outer layers of a star due to Thomson scattering are often compared to the retarding force due to the stars gravity (or GM/r^2), giving rise to the Eddington parameter, or

$$\Gamma_e = \frac{\kappa_e L}{4\pi G M c}. \tag{1.17}$$

As $\Gamma_e \rightarrow 1$, the force due to the Thomson scattering becomes increasingly strong in comparison to the stars gravity and, when the two forces are equal, a natural limit called the Eddington limit is reached. This is an important limit because Γ_e is independent of radius

so, if a star had sufficient conditions to reach this limit, it would become gravitationally unbound; Eta Carinae is an example of a star very close to this limit. For a star like the Sun, Γ_e would be on the order of 2×10^{-5} meaning that the effect on the outflow due to Thomson scattering is very small. However, for a large, hot star $\Gamma_e \sim 0.5$ so Thomson scattering can provide significant assistance in the driving of an outflow. However, observations of the winds from hot stars suggest a more gradual acceleration than would be provided by Thomson scattering so, it is necessary to consider the additional radiation pressure process of line scattering.

In the process of line scattering, it is necessary for the photon to be scattered to have just enough energy to shift the bound electron from one energy level to another. It might be considered that such a finely tuned process could not result in the enormous winds generated if it were not for two additional processes involved, resonance and Doppler shifting. The effect of resonance is to increase the chances that scattering will occur by increasing the interaction cross section of the bound electron; the discrete energy levels act as the resonant cavity. The amplification by the resonance to the interaction cross-section in comparison to free electron scattering (for single line at a single frequency) is given by the quality of the resonance, or

$$Q \approx \frac{\nu_0}{A} \tag{1.18}$$

where ν_0 is the frequency of the line and A is the decay rate of the excited state; for allowed atomic transitions, Q can be as high as 10^7. It can be assumed that for a typical hot star wind, the number of bound electrons compared to the number of free electrons is on the order of 10^{-4} and thus, the relative strength of the line scattering in comparison to the free-electron scattering (given by the parameter $\bar{Q}$) becomes

$$\bar{Q} \approx Q \times \text{rel. prop. of bound electrons to free electrons} = 10^7 \times 10^{-4}. = 1000 \tag{1.19}$$

Thus, using the example of a typical hot star again, where $\Gamma \sim 0.5$, the force on the wind from the star would be 500 times that of the stars gravity. $\bar{Q}$ (which was introduced by Gayley 1995) actually refers to the ratio of the maximum possible line force when all possible lines are exposed to an unattenuated stellar continuum and, the free electron scattering force. In a static atmosphere, there would of course be considerable

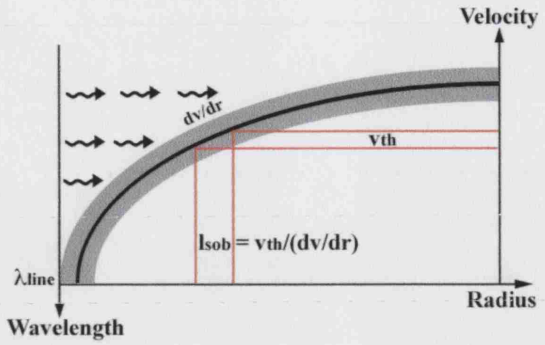

Figure 1.7: The Doppler-shifting line-resonance absorption for an accelerating outflow. The photons emitted from the star with a wavelength slightly too blue for scattering, continue through the outflow without interacting until they are red-shifted into a narrow line resonance whose width is set by the thermal broadening of the line (indicated by the shaded region). The shape of the line is not a true representation of a velocity law. Adapted from an article on stellar winds by Owocki (2001).

line saturation so many lines would not be exposed to the strong radiation and therefore the overall line force would be small. For this reason the inner atmosphere of these stars remains gravitationally bound.

The purpose of the Doppler shifting in a stellar wind is to continually shift the local line resonance of the accelerating outer atmosphere of the star, so that the ions are less affected by the problems of line saturation. In effect this means that the ions have a continual force applied to them due to line scattering throughout the wind and they are not limited to photons of just the right wavelength. Solving the process of line scattering in an accelerating outflow was simplified by the late Russian astrophysicist Sobolev (see Fig. 1.7) who developed the approximation (otherwise known as the Sobolev approximation) where line scattering at any radius can be described by local conditions in a "resonance layer" of thickness $l_{Sob} \equiv \frac{v_{th}}{(dv/dr)}$ (also known as the Sobolev length). This approximation has been often used for modelling stellar winds but, in the case of CV winds it will be shown that this approximation has been used off and on as its validity for the geometry of a CV system was continually re-evaluated.

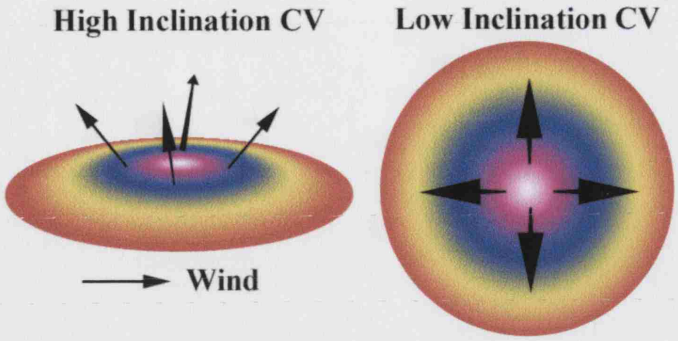

Figure 1.8: A demonstration of the inclination effects to a wind originating from an accretion disc.

1.4.4 Disc Winds from CVs

Especially with the advent of the International Ultraviolet Explorer (or IUE), P-Cygni profiles have been observed in the spectra of numerous non-magnetic CVs; see Greenstein & Oke (1982), Prinja & Rosen (1995) and Hoard & Szkody (1997) for examples. A comparison between P-Cygni profiles of different systems has shown that they are often weak or non-existent in CVs associated with low mass transfer rates such as dwarf novae in quiescence, or in high inclination systems. Cordova & Mason (1982) recognised that this dependence on inclination angle and the relative similarities with the P-Cygni profiles of OB stars means that these winds probably originate from the accretion disc and are driven by line radiation pressure. The belief is that in the inner parts of the disc, the radiation pressure is sufficient to drive material from the surface; this explains the dependence on inclination angle (see Fig. 1.8).

However similar CV disc winds are to OB stellar winds, they are also very different. Drew & Verbunt (1985) demonstrated that the shape of the P-Cygni profiles of CV winds is not well matched by theoretical profiles generated from models of OB stellar winds; the absorption minimum of CV P-Cygni profiles is much closer to the line centre than is observed for stellar winds for example. These differences can occur for two major reasons: (1) a difference in the physical conditions inside of the wind between OB stellar winds and CV disc winds and (2) the geometry of a CV is very different to that of a single star with a spherically symmetric outflow. Therefore, to accurately model the wind driven line profiles of these systems it is necessary to also model the structure of the wind, based on this geometry. An attempt at modelling this geometry to recreate a single line profile

was presented in Drew (1986) and Drew (1987) (the first paper introduced the geometry but assumed the system was face on and, the second paper introduced the effects of the CV inclination angle). The model assumed the Sobolev approximation for line transfer, a point source origin for the wind (i.e. the white dwarf) and a simple linear velocity law which is inferred from the shape of real observations. Mauche & Raymond (1987) also attempted to produce a similar model but with a less sophisticated radiation transfer process to the Drew (1986) model; it produced similar results.

The Drew (1986) and Mauche & Raymond (1987) models represented vast improvements in fitting the CV P-Cygni profiles in comparison to what was possible from the OB stellar wind models previously used but, to produce these results, ionisation structures had to be assumed for the winds. The problem with re-creating the ionisation structure of a CV wind stems from a conflict with theory and observation. Strong lines of C IV Si IV and N V are observed from CV winds but, theory predicts that the radiation from the boundary layer around the white dwarf would result in ionisation stages much greater than this. Attempts to explain this problem have been made, such as a slowly accelerating wind (Drew & Verbunt 1985) and a radiatively shocked wind (Mauche & Raymond 1987) but neither solution is completely satisfactory. There have been further investigations into the ionisation structure such as Shlosman & Vitello (1993) and Hoare & Drew (1993); the latter of these two papers investigated the possibility of wind-driving CVs having a cool or non-existent boundary layer. However, since no models have yet been able to match the strengths of the N V, Si IV and C IV lines, it is clear that the ionisation structure of CV winds is still not completely understood.

The original models of Drew (1986) and Mauche & Raymond (1987) proved suitable for comparison with IUE data but, with the launch of the Hubble Space Telescope (or HST) it was necessary to improve the models to more accurately reflect the observed profiles. The line synthesis code presented in Knigge *et al.* (1995) showed vast improvements over the previous models by using Monte Carlo techniques so that analytical assumptions such as the Sobolev technique were no longer needed. The other main features introduced in this new code were multi-line scattering, a rotational velocity component to the outflow and a biconical outflow geometry whereby the wind emanates from an inner ring of the disc and not just from the point source of the wind (see Fig. 1.9). One of the major advantages to this Monte Carlo model was that it was not necessary to model the system at each inclination angle since this information was already provided by the information

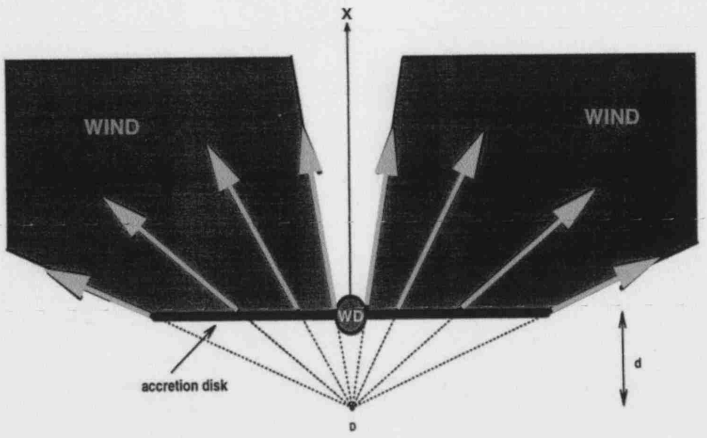

Figure 1.9: The wind geometry used for the model presented by Knigge *et al.* (1995) (reproduced from the same paper).

in the final directions of the photons. The synthetic line profiles generated by this model produced much better matches to the new UV spectra than any of the previous models and it showed that a biconical outflow was a much better representation of the disc wind than a wind emanating from a central target; similar conclusions were made about the wind geometry by Shlosman & Vitello (1993) using the model that they developed.

The computer models of CV disc winds which have so far been described have been purely kinematic in nature and no attempts were made to model the line driving forces involved. They were also somewhat limited to modelling the line profiles of single lines (C IV in particular) and therefore not capable of modelling entire spectra; Wade & Hubeny (1998) presented a grid of model far and mid-UV spectra for CV accretion discs but, this model failed to take into account the outflowing gases above the disc. Models of the line driving forces involved in a CV disc wind were first presented by Pereyra *et al.* (1997). The purpose of the analytical and numerical hydrodynamic models presented were not to generate synthetic line profiles but, to analyse the conditions under which a disc wind forms, using a one-dimensional model and, to investigate the observed terminal velocities and mass loss rates using a series of two dimensional models. The models agreed well with the observations but, they showed the necessity of shocks to form in the outflow for a P-Cygni profile to be generated. The major caveat of the Pereyra *et al.* (1997) model is that it did not sufficiently resolve the inner disc regions of the wind, which is the critical region where the outflow is still subsonic and is undergoing initial acceleration. Proga *et al.* (1998) therefore improved upon the model of Pereyra *et al.* (1997) with a numerical two-

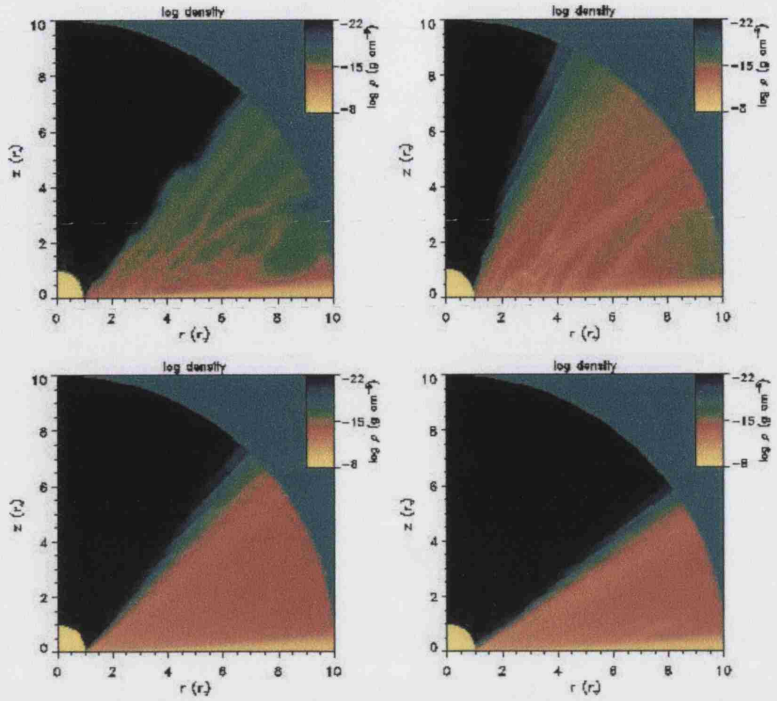

Figure 1.10: Example density maps generated by the hydrodynamic model of Proga *et al.* (1998), showing the effect of varying the mass-loss rate and the stellar component to the radiation field. r is the distance from the centre of the disc (and hence the white dwarf) in units of the white dwarf radius. z is the perpendicular distance above the plane of the accretion disc, in units of the white dwarf radius. Reproduced from Proga *et al.* (1998).

dimensional hydrodynamic model which suitably resolved the inner disc regions. Their model also produced results comparable to spectroscopic observations but, they found that for a wind to be driven it was necessary for the effective luminosity of the disc (this is the luminosity of the accretion disc multiplied by the relative strength of line scattering in comparison to free electron scattering or $\bar{Q}$) to be greater than the Eddington limit (see § 1.4.3). Using this model they also found that the outflow underwent significant variations in velocity and density because of variations in the vertical components of gravity and radiation pressure, meaning that overall such an outflow would be very unsteady (see Fig. 1.10).

There have been numerous attempts to improve the hydrodynamical models of disc winds to present a more accurate picture of what is happening in these systems. For example, although Proga *et al.* (1998) discovered the outflows to be unsteady, the scal-

ing of the resulting time-averaged mass-loss rates and terminal velocities with luminosity compared well with the mass-loss rates and terminal velocities of steady flows driven by a central object, as it is with OB stellar winds. Thus, in Proga *et al.* (1999) (and Feldmeier & Shlosman 1999), the method for calculating line acceleration for one-dimensional radial flows developed by Castor *et al.* (1975) were adapted for three-dimensional geometry and used in a two-dimensional time-dependent hydrodynamical model. The results from Proga *et al.* (1999) were later used by Proga *et al.* (2002) to generate synthetic wind driven line profiles for comparison with HST observations of the nova-like system, IX Vel; this did not prove to be successful as the synthetic model lines did not match the observations very well. This showed that although the hydrodynamic models had improved the understanding of the disc winds, they were still reasonably distant from the full solution.

All of the models presented so far have assumed that line driving is the only force involved with accelerating a disc wind but, there are some flaws with this assumption related to the disc luminosity and the maximum possible line force. It was shown in § 1.4.3 that the force generated through line scattering has to be greater than the force due to gravity for a flow to be accelerated away from the disc. This can be written in terms of the line force multipler $\bar{Q}$, the Eddington parameter Γ and gravity g,

$$\bar{Q}\Gamma g > g \tag{1.20}$$

or

$$\bar{Q}\Gamma > 1. \tag{1.21}$$

Gayley (1995) showed that for a wide range of conditions $\bar{Q} \approx 2000$ so as a minimum limit

$$\Gamma > 5 \times 10^{-4} \tag{1.22}$$

but, Γ can be approximated by

$$\Gamma =\sim 10^{-5} \frac{L}{M} \left(\frac{L_{\odot}}{M_{\odot}} \right) \tag{1.23}$$

so the limit becomes

$$\frac{L}{M} > 50\left(\frac{L_\odot}{M_\odot}\right). \tag{1.24}$$

Although this scaling is strictly speaking for the purposes of stellar winds, as Proga *et al.* (1999) discovered, the scaling for stellar winds proves to be suitable for disc winds as well. If the central star were assumed to be a white dwarf with a mass of $1M_\odot$, then this limit becomes related to luminosity only, or

$$L > 50L_\odot \tag{1.25}$$

so an accretion disc would need a luminosity on the order of 50 $L_\odot$ for line scattering to be the driving force of the wind. The luminosity of an accretion disc can be estimated using equation 1.6, so assuming a mass transfer rate of $10^{-9}M_\odot$ yr^{-1} and a white dwarf radius of 10^4 km, then the resulting disc luminosity would be only $\sim 2L_\odot$ which would make the luminosity of this system far too small to drive a stellar wind. This is of course a rough approximation and it is possible that not only could this limit for line driving be smaller, but CVs with far greater luminosities are probably to be found. However, what this approximation does show is that it is difficult to make line scattering the only driving force for the winds of many CVs.

Proga (2000) introduced the concept of magneto-centrifugal assisting force in a predominantly line driven disc wind. Blandford & Payne (1982) showed that it is possible for a wind to be driven from an accretion disc by a strong, large scale, magnetic field threading the disc, although these magnetic fields would require a thermal assistance to actually escape the disc. The two-dimensional time-dependent model presented, showed that in systems where the disc luminosities are low and the mass-loss rates are at the lower end of possible values, the extra assistance of the magnetic field improved the mass-loss rates by several orders of magnitudes above the unassisted values; no observed change in mass-loss rate was observed for the high luminosity CVs. It was also shown that for systems with a magneto-centrifugally driven wind, line driving can provide the initial assistance to lift the gas from the surface of the disc when a thermal assistance is not available. The results of this modelling suggest that a magneto-centrifugal assistance to line driving would considerably increase the number of CVs observed to have a disc wind, in comparison to a purely line driven scenario.

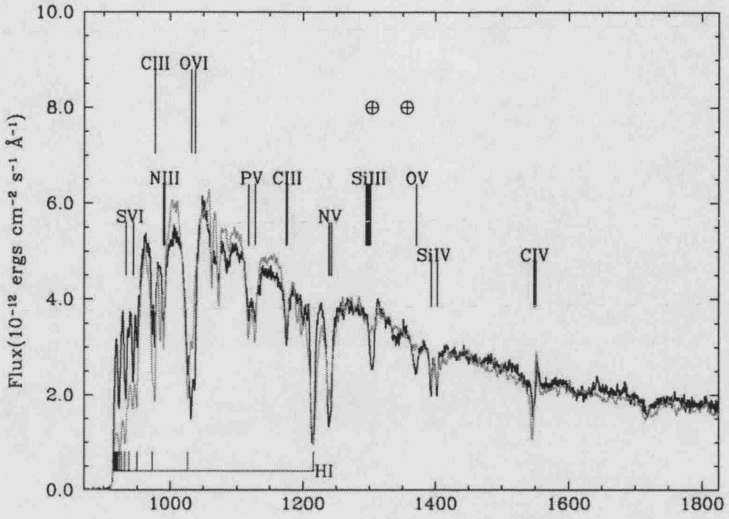

Figure 1.11: A comparison between the HUT spectrum of Z Cam (black line) and a synthetic wind driven CV spectrum generated by Long & Knigge (2002) (reproduced from the same paper).

The extensive development in the hydrodynamic models of CV disc winds has significantly improved their understanding but, they have so far failed make the synthetic line profiles more realistic. The line profile synthesis codes were also still only capable of simulating single line profiles and no code had been presented to simulate entire spectra, whether they were based on hydrodynamic codes or not. This changed when a hybrid line synthesis code utilising both the Sobolev approximation and a Monte Carlo algorithm was presented by Long & Knigge (2002). The model was a significant improvement on any of the previous line synthesis models in that it solved the thermal and ionisation balances and it could take into account the destruction and creation of line photons from within the wind. However, the most important difference this code has had over anything previous was the ability to simulate an entire UV spectrum and not just a single line profile. This was a significant step in the development of these codes and although the result is not a perfect match for real observations (see Fig. 1.11, where a synthetic spectrum generated by the model is compared with a Hopkins Ultraviolet Spectrum of Z Cam) it is nonetheless very impressive.

1.5 The Aim of this Thesis

In § 1.4.4 a description was given of the development of CV disc wind codes, both line synthesis and hydrodynamical. Although there has been a steady improvement in both of these code types over the years, it is clear that CV disc winds are still not clearly understood. It is also noteworthy that although some of the disc wind codes are time-dependent and are showing clear structure on relatively short time-scales, the line synthesis codes are still time-independent and are likely to remain so for some time. Observations of CV P-Cygni profiles also show significant variability in shape and size and any comparison of synthetic profiles with real observations has only been successful for the time-averaged spectra of a limited number systems; disc wind models still fail to predict sufficient emission for low inclination CVs for example. This lack of clear understanding of CV disc winds raises the need for detailed, time-series studies into the disc wind characteristics of individual systems. Therefore, the primary aim of this thesis is to present detailed time-series analysis of several wind driving CVs, with the purpose of providing clear descriptions of the time-dependent characteristics of those winds.

In this thesis, disc wind case studies are presented for the low inclination, high state, nova-like CVs, RW Sex, V592 Cas and BZ Cam using ultraviolet and optical time-series spectroscopic observations. Each case study begins with a full and detailed account of the time-dependent characteristics of the disc winds, and ends with a discussion about the origins and nature of those observations. As a final step of this thesis, the far-UV, time-averaged, disc wind characteristics of a number of CVs are presented and discussed.

CHAPTER 2

Data Reduction and Analysis

Throughout this thesis, certain techniques are repeatedly used to reduce raw image frames to fully calibrated spectra and, to analyse this fully calibrated spectra. This chapter presents a brief and generalised view of these techniques so that continuous focus can be given in each case study towards the analysis and the results from the analysis.

2.1 Data Reduction

The purpose of data reduction in spectroscopy is to convert the raw exposed image frames of an observation to wavelength and flux calibrated spectra. Some of the data used in this thesis were collected from space-based telescopes such as IUE, HST and the far-Ultraviolet Spectroscopic Explorer (or FUSE) and so were automatically reduced by pipeline software (e.g. CalFUSE for FUSE data). However, the two optical time-series of spectra presented in § 4 and § 6 were reduced manually using the Image Reduction and Analysis Facility (or IRAF[1]) software package. In both cases, the data consisted of long slit spectroscopy of a bright point source target so the reduction process required only two steps: processing the data frames to remove the artefacts of the observational process and, the extraction/calibration of the spectra from the cleaned frames. In this section, a generalised and simplified account is given of both steps, starting with the processing of the raw data frames.

[1] IRAF is distributed by the National Optical Astronomy Observatories, which are operated by the Association of Universities for Research in Astronomy, Inc., under cooperative agreement with the National Science Foundation.

2.1.1 The Processing of the Data Frames

Correct processing of spectroscopic frames normally requires the following data to have been collected during the observing run:

Bias frames These are zero second exposures which are used to remove any structure resulting from the readout of images from the CCD.

Flat-field frames These are exposures of a flatly illuminated surface and are used to compensate for variability in the sensitivity of the pixels across the whole CCD. Typically a quartz lamp is used as the illuminating source.

Object frames These are the exposures of the actual targets and any spectrophotometric standard stars. Normally the spectrograph will be configured so that dispersion axis runs parallel to one of the sides of the CCD if possible.

Dark frames These are data frames with the same exposure times as object frames but with the shutter closed so that the effect of temperature on the CCD (i.e. the generation of thermal electrons) can be removed from the observations. A description of these frames is provided for completeness although some CCDs take a dark frame and subtract it automatically while others are sufficient cooled or are efficient enough so that dark frame subtraction is not necessary.

Wavelength calibration or arc frames These are exposures of a calibration arc lamp with a well known spectrum and are used during the calibration process to add a wavelength scale to the object frames.

The first step in any form of data reduction is to examine the individual frames to look for faults i.e. an object frame with no spectrum or an incorrectly identified arc frame. This examination must also extend to the image headers to confirm that information such as the exposure time and airmass values are correct as these could affect the reduction procedures to follow. On most CCD frames there is an area of the image referred to as the overscan region. By fitting the overscan region of every frame with a low order function and subtracting the result, it is possible to remove any brightness offset that may exist in all of the raw data frames (including the bias and flat-field frames). The next step is to remove the effects of the CCD readout from every frame, so all the bias frames of a single night are combined using an averaging algorithm to produce a mean bias frame.

During any exposure, cosmic ray events can produce "bright spots" within the image so ideally, any averaging algorithm used should be able to spot such events and remove them. The object, arc and flat-field frames are then processed to remove the average bias and trimmed to remove the overscan regions.

At this stage of the data reduction process the effects of reading the data from a CCD and the underlying noise of the CCD have been removed. The next step is to flat-field the data frames which is normally performed to remove the variations in pixel sensitivity across the CCD but, it can also be used to compensate for any low order wavelength sensitivity that the CCD might have. Initially the flat-field frames are combined using an averaging algorithm again, so as to create an average flat-field frame. If a quartz lamp has been used for the flat-field illumination then it will be necessary to remove the effects of the quartz spectrum along the dispersion axis, by fitting a low order function and normalising by the resulting fit. The CCD response is then removed from all of the object frames by dividing them by the normalised, average flat-field frame. The next step in the data reduction process is the extraction of the spectra and subsequent calibration.

2.1.2 The Extraction and Calibration of Spectra

In § 2.1.1 an account was given of how the raw data frames from a nights observation are processed to remove the effects of the CCD readout noise and the variations to the pixel sensitivity, to leave just the object frames (which may include spectrophotometric standard stars if flux calibration is to be performed at a later stage) and the wavelength arc frames; the next step is to extract spectra from both the object and wavelength arc frames. In the case of long slit spectroscopy, the process of extracting the spectrum is relatively simple and much of the work is performed by the software but, it should still be performed carefully. For each spectrum, the following process is performed although typically for a time-series of spectra it is possible to perform the process on one spectrum and the software can automatically reconfigure for the remaining frames.

The first step in this process is to locate the spectrum on the frame by plotting cuts along the spatial axis of the image frame and marking the peak in brightness (ignoring any cosmic ray features present). A region either side of this peak is defined as the extraction window by either specifying a certain number of pixels either side or a limit of intensity, above which the data should be extracted. Similarly, background windows should be defined either side of this central peak but well separated from it. During the

extraction process, a linear function is fit across these background windows to remove any effects from sky illumination. Although it is generally hoped that the dispersion axis of the exposed spectrum will be exactly parallel with one side of the CCD, this is normally not the case so before the extraction can take place, a low order function must be defined for the software so it can trace the location of the spectrum across the data frames.

When the extraction process is set to run on an object frame, the following steps happen. Firstly, the software uses the initial guess of the spectrum location and the low order function provided to find and trace the location of the spectrum. At each point along the dispersion axis an extraction aperture is created, centred on spectrum, and the values within the extraction aperture are summed. Also at each point along the dispersion axis, a fit to the background is performed and the result is subtracted from the summed value from the extraction aperture. A plot of the pixel value against pixel number along this dispersion axis gives the 1-D, uncalibrated spectrum. Spectra are extracted from the wavelength arc frames using the trace and extraction aperture results from the closest (in time) object frame; no background subtraction is performed on these frames.

After the extraction of the 1D spectra from the 2D frames, the next step is to calibrate those frames onto a wavelength scale. The emission lines in the arc frames are identified and their wavelengths are used to determine a function that relates pixel number to wavelength (otherwise known as a dispersion solution). Much care must be given into finding this dispersion solution because a poorly fitted solution can have a significant impact on any science resulting from the spectra. The dispersion solution of the nearest (in time) arc frame is then applied to the object spectra to produce the wavelength calibrated object spectra; often these object frames are further interpolated onto a linear wavelength scale.

The wavelength calibrated object spectra may contain a mixture of target systems and spectrophotometric standard stars. In some cases it is satisfactory to have just the wavelength calibrated spectra and if necessary, to normalise these spectra by fitting a low order function to the continua and then divide through by this function. However, in many cases it is desirable to have the flux calibrated spectra. To flux calibrate a spectrum it is first necessary to confirm that the calibration information is available for the standard star. The calibration information contains a list of wavelength bandpasses and the flux level of the star in each band; the following steps assume that the correct airmass is stated in the headers of all target and standard star spectra. A response function is generated for

each standard star spectrum available using software which integrates over the bandpasses, compensates for airmass, divides by the exposure time and compares with the calibration information available. Once this process is repeated for a number of standard stars, a response function corresponding to each nights observations is generated. This response function is then applied to the individual target wavelength calibrated spectra to finally produce the wavelength and flux calibrated target spectra.

2.2 Data Analysis Techniques

In this section a description is given of some of the techniques and procedures used to analyse the reduced and calibrated spectra. Most of this analysis was performed using scripts and procedures written for the Interactive Data Language (or IDL) software package by the author, as part of this thesis.

2.2.1 Recording the Properties of a Line Profile

Throughout this thesis, much focus is given to measuring the properties of the line profiles so they can, for example, be compared at different times. The strength of a stellar line is one of its fundamental properties and it is normally defined in terms of the equivalent width. The equivalent width is best defined as the rectangular area between a normalised continuum and zero, with an identical size to the integrated area of the line profile underneath the continuum (see Fig. 2.1); mathematically, the equivalent width (or W) is given by

$$W = \sum \frac{F_c - F_\lambda}{F_c} d\lambda \tag{2.1}$$

where $F_c = 1$ is the normalised continuum intensity, F_λ is the line profile intensity and $d\lambda$ is the sampling in wavelength space. Since the height of the equivalent width rectangle already has a defined length of 1, the only side that can change size is the width which is in wavelength space so typically, the equivalent width strength of a profile is given units of Angstroms or Å; absorptions lines give positive equivalent widths and emission lines give negative equivalent widths.

The core intensity, line width and line centre are other properties that are possible to measure from a spectral line. In the case of an extremely complex line profile, it maybe

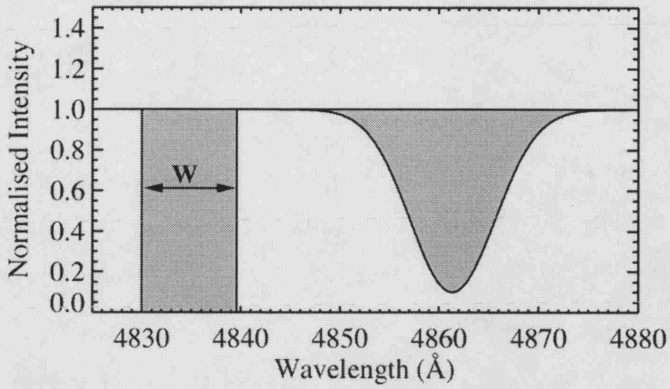

Figure 2.1: An example measurement of equivalent width from the Hβ (4861Å) profile. What is shown is a simulated profile and the equivalent width that the line profile corresponds to.

necessary to make these measurements by eye but in many cases, the shape of a stellar line is well approximated by the Gaussian profile so these values can be found by performing a fit to the line with one. Traditionally, the equation for a Gaussian distribution (as a function of x) is given by

$$f(x) = \frac{1}{\sqrt{2\pi\sigma^2}} \exp \frac{-(x-\bar{x})^2}{2\sigma^2} \tag{2.2}$$

where $\bar{x}$ is the mean and σ is the standard deviation of the data set. However, for the purposes of this thesis, this equation has been adapted to give intensity as a function of wavelength (or x) across a normalised spectral line with a Gaussian shape and is given by

$$I = c \times \exp \frac{-(x-\mu)^2 \times 4 \times \ln 2}{HWHI^2} + 1.0 \tag{2.3}$$

where c is the core intensity of the line, μ is the centre wavelength of the line and, $HWHI$ is the half-width at half intensity of the line, see Fig. 2.2 for an example Gaussian profile.

To perform a single Gaussian fit to a spectral line, it would first be necessary to make educated guesses of these three parameters, μ, c and $HWHI$. These initial guesses, along with a formula such as equation 2.3 and, the wavelength and flux data from the real spectrum, would be entered into an appropriate algorithm to find the best fit of these parameters to the data. One algorithm which is often used for this fitting process (and is

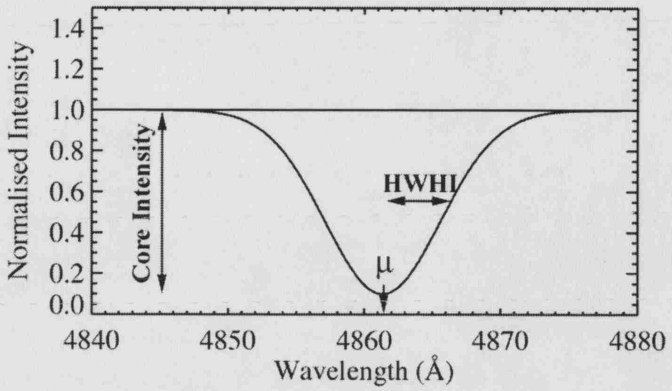

Figure 2.2: A figure showing the core intensity (c), half-width at half intensity ($HWHI$) and line centre μ of a Gaussian profile. The parameters of the profile shown are: $HWHI = -0.9$, $HWHI = 10$Å and $\mu = 4861$Å (i.e. the rest wavelength of the Hβ line).

used throughout this thesis) is the least squares algorithm, which uses the assumption that the best fit curve of a given type, is the curve which has the minimal sum of deviations squared from the data provided. The process is an iterative one and in many successful cases, the algorithm used will converge at the best fit values. As it will be shown in § 4 such a least squares fit to a spectral line does not have to be limited to just one Gaussian profile. If a spectral line consists of more than one component (such as an emission and an absorption component) and both of these components would be accurately modelled by a Gaussian profile, then it is possible to modify the initial input equation to take this into account i.e.

$$I = c_1 \times \exp \frac{-(x-\mu_1)^2 \times 4 \times \ln 2}{HWHI_1^2} + c_2 \times \exp \frac{-(x-\mu_2)^2 \times 4 \times \ln 2}{HWHI_2^2} + 1.0 \qquad (2.4)$$

where the parameters with the subscript of 1 are for one component such as the absorption, and the parameters with the subscript of 2 are for the other component to the spectral line such as the emission. For every new component added to the formula it would be necessary to provide initial guesses to the related parameters and some care would have to be taken with limiting values to those parameters but often such a two Gaussian fit can be very successful. When three or more Gaussian components are fitted to a profile, extra special care has to be taken with the initial guesses and limiting values since it is possible for a profile fit to be good even though the contributions provided by the

individual components may be unrealistic. It should be noted that in this thesis, most line centre measurements are quoted in velocity space and not wavelength space. The conversion from wavelength to velocity is performed using the equation

$$v = c \times \frac{\lambda - \lambda_0}{\lambda_0} \tag{2.5}$$

where v is velocity, c is the speed of light, λ is the wavelength to be converted and λ_0 is the rest wavelength of the spectral line.

2.2.2 Temporal Variance Spectra

There is some effort in this thesis towards analysing the temporal variability of the wind profiles of each CV. Part of the initial characterisation of the temporal behaviour is to locate the active regions along each line profile and for this purpose, a temporal variance spectrum (or TVS) is created. The TVS is a method by which to quantify the changes that occur to a line profile at each bin in velocity or wavelength space. Multiple equations have been defined in literature of how to calculate the TVS for a data set but for this thesis the equation to be used is

$$TVS_j = \frac{1}{N-1}\sum_{i=1}^{N} d_{ij}^2 \qquad \text{(Fullerton } et\ al.\text{ 1996)} \tag{2.6}$$

which refers to the jth wavelength pixel of the ith spectrum when there are N spectra in the data-set. d_{ij} is referred to as the residual spectrum and it is defined as

$$d_{ij} = S_{ij} - \overline{s}_j \tag{2.7}$$

where S_{ij} represents a specific matrix element and $\overline{s}_j$ is the column average given by

$$\overline{s}_j = \frac{1}{N}\sum_{i=1}^{N} S_{ij}. \tag{2.8}$$

The TVS spectrum is then just a plot of the TVS against wavelength (or velocity) across the line profile.

If a particular point in a spectrum was not varying then the TVS value at that point would theoretically be 0. However, every real spectrum contains noise meaning that any

inactive part of the spectrum such as the continuum (assuming that the spectrum has been correctly normalised) will still have a finite TVS value based on this noise, the stronger the noise the larger this finite TVS value is. The parts of the line profile which are in fact active, will have a TVS value which is above this background noise level of variance since those parts of the line profile would be affected by the noise as well as the activity. There would of course be some variability in the noise across a spectrum but inherently, the active regions would be indicated by significantly larger TVS value than the background.

2.2.3 Fourier Analysis

In at least three chapters of this thesis (i.e. § 3, 4 and 5), a lot of emphasis is placed on modulated variability in the line profiles and not just sporadic variability. The modulated variability is sometimes searched for in measurements taken from the line profiles such as the velocity of absorption minimum, and other times it is the actual flux levels within the spectra which are analysed for modulated variability. The technique which is consistently used throughout this thesis to search for modulation is Fourier synthesis or analysis (the Fourier procedures used in this thesis were written by A. Fullerton of The John Hopkins University). Joseph Fourier (1807) recognised that any 2π-periodic function $f(x)$ could be represented by the following summation

$$f(x) = a_0 + \sum_{k=1}^{\infty}(a_k \cos kx + b_k \sin kx) \tag{2.9}$$

which is referred to as the Fourier series; the coefficients a_0, a_k and b_k are given by

$$a_0 = \frac{1}{2\pi}\int_0^{2\pi} f(x)dx, a_k = \frac{1}{\pi}\int_0^{2\pi} f(x)\cos(kx)dx, b_k = \frac{1}{\pi}\int_0^{2\pi} f(x)\sin(kx)dx. \tag{2.10}$$

In essence, these theories of representing periodic data with simple functions of varying frequency and amplitude led to their use in frequency analysis.

In the context of this thesis, a data set which may or may not have modulated variability is passed through a Fourier transform algorithm. Any function which is dependent on time ($f(t)$) can be defined as the superposition of both positive and negative contributions at all frequencies ν or,

$$f(t) = \int_{-\infty}^{+\infty} d\nu F(\nu) e^{+2\pi i\nu t}, -\infty \leq t \leq +\infty \qquad \text{(Roberts } et\ al. \text{ 1987).} \tag{2.11}$$

The spectrum of f is given by the Fourier transform (FT) and it defines the contribution of each ν to f. The Fourier transform is therefore given by

$$F(\nu) \equiv FT[f] \equiv \int_{-\infty}^{+\infty} dt f(t) e^{-2\pi i\nu t}, -\infty \leq \nu \leq +\infty. \tag{2.12}$$

The Fourier transform plots which are used throughout this thesis are referred to as power spectra and they show the contribution of ν to the variance of f, or

$$P(\nu) = |F(\nu)|^2, -\infty \leq \nu \leq +\infty; \tag{2.13}$$

it is this power spectrum that is calculated by the Fourier transform algorithm. Strong peaks or signals in these power spectra, with respect to the other data points in the plot can reveal possible periodic modulation on the data being analysed.

Using the Fourier transform technique for frequency analysis of data collected from any time-series is flawed because the representation of a continuous function (which is what the algorithm assumes) by a finite number of data points will result in a frequency or power spectrum that is distorted by the incompleteness of the sampling and the limited frequency resolution provided by the data. In effect this initial power spectrum, otherwise referred to as the "dirty" spectrum, is a convolution of the data sampling (otherwise known as the window function) and the actual frequency function of the data. However, an attempt can be made at deconvolving these two components by passing the data through a CLEAN algorithm. The CLEAN algorithm was originally developed by Högbom (1974) for two dimensional aperture synthesis although it was later developed to handle other types of data. The aim of the CLEAN algorithm is to find the strongest peaks in the "dirty" power spectra and to subtract a fraction g (referred to as the gain) of these peaks from the data. This procedure is repeated until all that is left in the "dirty" power spectrum is the noise and the components removed from the "dirty" power spectrum represents the CLEAN power spectrum. This procedure is often successful in removing false signals from the power spectrum but it can also end up removing the real signals so it should be used with some caution.

CHAPTER 3

FUSE and HST Ultraviolet Spectroscopy of RW Sextansis

The results from an ultraviolet study of RW Sex are presented in this chapter. The study uses time-series spectroscopy, primarily from the Far Ultraviolet Spectroscopic Explorer (or FUSE) and also the Hubble Space Telescope (or HST).

3.1 Introduction

With a V magnitude of ~10.6, RW Sex is one of the brightest nova-like cataclysmic variable stars. It is a well studied system and is the ideal target with which to begin this investigation into CV disc outflows. The outflows from CVs are well viewed in the ultraviolet regime so this study utilises data collected with two well respected UV instruments, FUSE and HST. This chapter continues by providing a literature review of the target, followed by an introduction to previous observations. Afterwards, the FUSE and HST data are introduced and the results of analysing the data is presented. The meaning of the results is discussed in the final section.

3.2 Literature Review

During the earlier years of the detailed study of RW Sex, it was more commonly referred to as BD-7° 3007 and was believed to be an unusual hot star. Time-series analysis by Cowley & MacConnell (1972) and Hesser *et al.* (1972) revealed that the star flickered rapidly in

ways which were similar to CVs. Cowley & MacConnell (1972) also revealed RW Sex to have broad hydrogen lines in absorption, with weak and variable central emission. They originally placed the star with a 12000 Kelvin blackbody but the UV observations revealed this to be incorrect. Later, further photometric and spectroscopic observations revealed the system to be a cataclysmic variable of the nova-like sub-group. With the identification of RW Sex as a nova-like system, Cowley *et al.* (1977) went on further to derive an orbital period of 0.25 days and a radial velocity amplitude $K = 74$ km/s; they did not detect the presence of the secondary star. As confirmed by it's nova-like classification, they also did not detect any large outbursts from the system.

IUE observations demonstrating the disc wind from RW Sex were first presented by Greenstein & Oke (1982). They showed the spectral lines to have weak emission but strong, broad, blue-shifted absorption, with terminal velocities up to -4500 km/s for spectral lines such as N V 1240Å and C IV 1550Å. The interpretation of the outflow from these observations were of a hot and fast wind and with a high hydrogen to metal ratio it was felt that radiation pressure could not be the driving force; current computer models (e.g. Long & Knigge 2002) attempting to recreate the spectra of windy CVs such as RW Sex, use a combination of radiation pressure and magneto-hydrodynamics to simulate the outflowing material so it is felt that this conclusion was incorrect. X-ray radiation was provided by Greenstein & Oke (1982) as the alternative driving force of the disc wind and an integrated X-ray flux from the system of $F_x = 1.9 \times 10^{-12}$ erg cm^{-2} s^{-1} (provided to the authors by private communication from Cordova and Mason) acted as evidence to support this theory. In comparing the ultraviolet spectrum of RW Sex with AM CVn, the authors also concluded that the system contains a small disc and an F-type secondary star.

Bolick *et al.* (1987) performed a rather more detailed study of RW Sex with photometry and optical spectroscopy, acquired with the 1.2 and the 2.2-metre MPI/ESO telescopes based at La Silla, Chile. The analysis of the radial velocity measurements revealed a period of 0.24486±0.00062 days and a radial velocity amplitude $K = 101 \pm 10$ km/s; this result was consistent with previously determined values (e.g. Cowley *et al.* 1977). By making assumptions about the system such as the size relationship of the secondary star, they used a standard accretion disc model to determine system parameters including the systems inclination angle ($32° \leq i \leq 52$ °) and the mass ratio between the two stars ($M_1/M_2 = 1.5 \pm 0.5$). One especially important result from modelling the system was that

the secondary star cannot be an F-type dwarf as previously suggested by Greenstein & Oke (1982) because the flux distribution and spectrum were inconsistent with this theory.

Beuermann *et al.* (1992) performed a time-series analysis of RW Sex spectra obtained with the 2.2 metre ESO/MPI telescope at La Silla. Their aim was to present a study of the Balmer lines using spectra taken within the 4200 to 5000Å range, therefore encompassing the Hβ and Hγ lines. The first obvious result from this new data was a slightly revised orbital period of 0.24507 days, derived by fitting Lorentz profiles to the wings of the Balmer lines. The important result which one must take from this paper is that Beuermann *et al.* believed that the narrow Balmer emission lines from the secondary star are actually chromospheric emission from the illuminated and heated hemisphere of the secondary star which faces the disc and the white dwarf. They used this information to help them constrain the mass ratio and determine the orbital elements of the secondary star although the narrow and broad components were separated interactively. Nonetheless, the mass ratio they obtained from this method ($M_1/M_2 = 1.35 \pm 0.10$) was consistent with Cowley *et al.* (1977) and with the mass ratio and period relationship suggested by Warner (1973).

It is obviously much easier to interpret what is seen of a cataclysmic variable when there is information about both stars within the system. With low inclination CVs it is often extremely difficult to determine orbital solutions for the secondary star since there is no eclipse from which the absolute phase may be determined, although alternative methods do exist whereby with sufficient information the absolute ephemeris can be determined. Vande Putte *et al.* (2003) use one of these alternative methods, called skew mapping, to measure the real radial velocity motion of the secondary star of RW Sex. Skew mapping is a technique where a template spectrum of the secondary star is rotationally broadened to provide a close fit to the actual spectrum, and then the resulting template is cross correlated with the observations to find the radial velocity at each phase point. In Vande Putte *et al.* (2003), near-IR spectra collected at the Isaac Newton Telescope (or INT) were cross-correlated with a template spectrum; discovering that the radial velocity amplitude of the secondary star, $K_2 = 144 \pm 18$ km/s, provided an opportunity to determine a more accurate estimate of the systems inclination angle, $i = 34° \pm 2°$.

CVs are generally well observed in X-rays and RW Sex is no exception. The earliest X-ray observations of the system were taken with the High Energy Astrophysical Observatory 2 (later renamed to the Einstein Observatory) and the European Space Agency's

X-ray Observatory (or EXOSAT). Greenstein & Oke (1982) used some of the early observations to provide evidence for their theory that RW Sex has an X-ray driven wind. By modelling the Einstein observations with an optically thin Bremsstrahlung spectrum, Eracleous *et al.* (1991) discovered that the X-rays actually originated from the boundary layer of the CV. A lack of detectable modulation also acted as evidence counteracting the X-ray driven wind proposal. The last set of X-ray observations of RW Sex to be published were those taken with the German/UK/US ROentgen SATellite (or ROSAT) which were presented in Verbunt *et al.* (1997) although there were no further conclusions made.

Polidan *et al.* (1990) described a far and extreme ultraviolet survey of five CVs using data collected using the ultraviolet spectrometers on both Voyager 1 and Voyager 2. Using these results along with neutral hydrogen values derived from IUE spectra, their aim was to place upper limits on the system flux in the extreme-ultraviolet band of 600-700Å which detailed model accretion discs suggest should originate from the inner accretion disc. The net result from this study was that they did not find any EUV emission for any of the systems including RW Sex.

At the opposite end of the spectrum to X-rays and the extreme-ultraviolet there are radio waves; given the multi-wavelength nature of cataclysmic variables, it would not be unreasonable for there to have been a radio study of RW Sex, especially given that it is one of the brightest nova-like systems visible. A 6-cm radio survey of 6 cataclysmic variables (including RW Sex) was performed by Cordova *et al.* (1983) using the Very Large Array (VLA) in New Mexico. The theory was that since the system has a high mass accretion rate and shows evidence for mass-loss then one might expect to see radio free-free emission from the gas cloud surrounding the system. Unfortunately there was no detection of a radio signal from RW Sex or the local area (the flux density was measured at $\leqslant 0.15$ mJy) and a later 6-cm radio study using the Jodrell Bank Lovell-Mk II broad-band interferometer by Nelson & Spencer (1988) also failed to yield a detection (the flux density was measured at $< 2.3-2.9$ mJy). Numerous studies have failed to find detectable radio emission from nova-like CVs so it appears that these results for RW Sex are not unusual.

A brief summary of studies/publications related to RW Sex have been listed in this section; Table 3.2 is a summary of parameters from some of these publications, which have been adopted for the remainder of this chapter. In § 3.3 some of the observations listed in this section are shown in more detailed and discussed.

Parameter	Value	Reference
Type	UX Uma	1
Period	0.24507 days	2
Magnitude Range	10.4 V - 10.8 V	3
Inclination	$34 \pm 2°$	4
Distance	150 parsecs	2
E(B-V)	<0.03	5
RA	10:19:56.62	2
DEC	-08:41:56.0	2

Table 3.1: System parameters for RW Sex which will be used throughout this study. References: (1) Warner (1987) (2) Beuermann *et al.* (1992) (3) Downes *et al.* (2001) (4) Vande Putte *et al.* (2003) (5) Mauche *et al.* (1988)

3.3 Observations of RW Sex

3.3.1 Optical Observations - FEROS

Fig. 3.1 shows sample spectral lines from a normalised optical spectrum of RW Sex, taken with the Fibre-fed, Extended Range, Échelle Spectrograph (or FEROS) on the MPG/ESO-2.20 metre telescope, based at La Silla in Chile. This single exposure lasted 1200 seconds and was taken on the 17th February 2003, during an observing run of the rapid rotator, HD 64760. FEROS is a bench mounted spectrograph, capable of observing from 3500Å to 9000Å at high resolution in a single spectrum. The spectra presented here have been reduced using the pipeline reduction package written for it in ESO-MIDAS.

The Hα profile observed in Fig. 3.1 appears to be made up of three or more components. There is a strong, broad, central emission but this is seemingly superimposed on a broader but very shallow absorption which spans from the blue wing to the red wing. However, there is significantly more absorption across the red wing than across the blue wing which suggests that there is an additional source of blue-ward absorption. The source of this blue-ward only absorption is unknown from just this one profile but one possible source is an accretion disc wind. The Hβ profile is very similar to the Hα profile although the emission is now somewhat weaker in comparison to the absorption. A comparison of this profile with Fig. 2 of Beuermann *et al.* (1992) demonstrates the

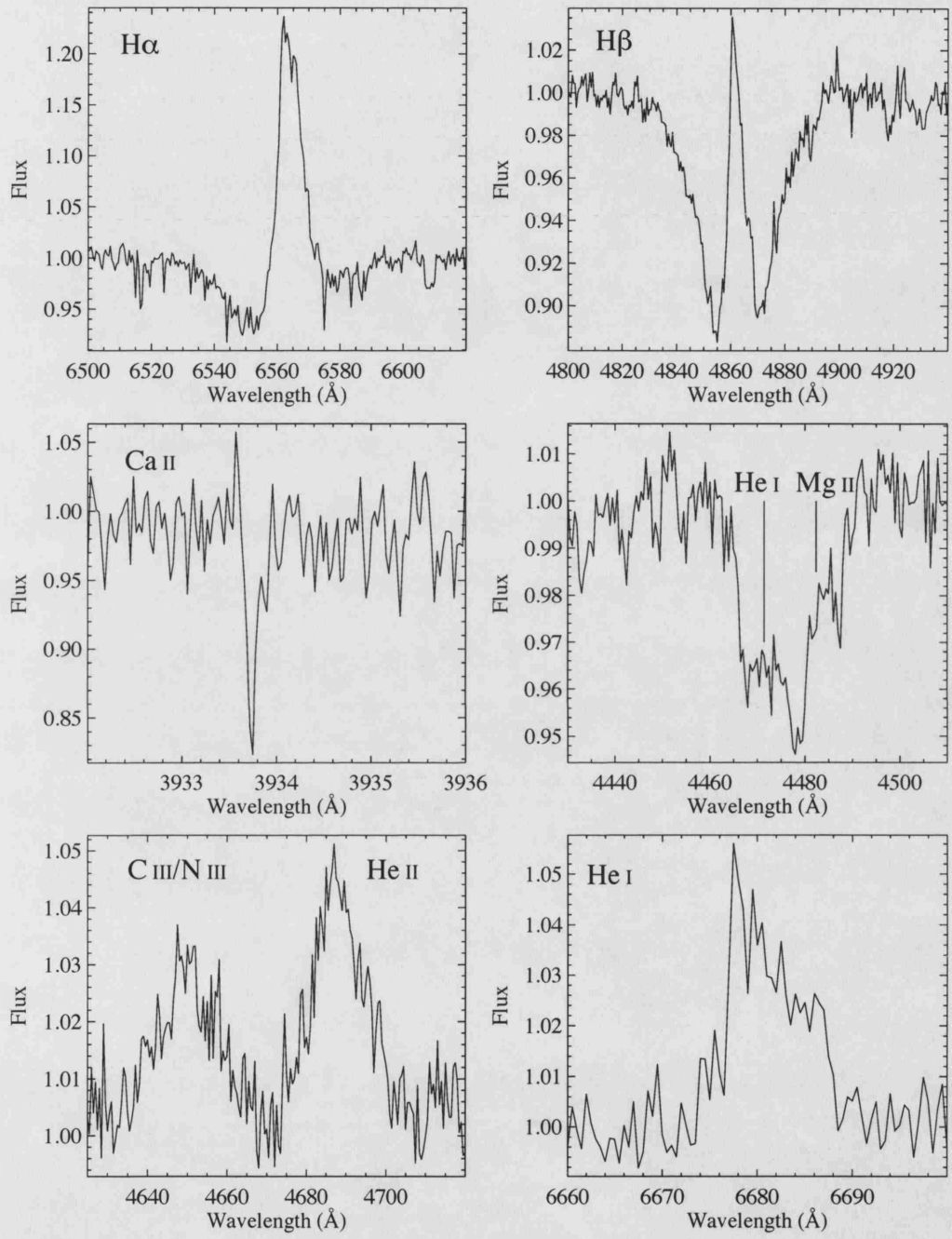

Figure 3.1: Sample spectral lines from a normalised optical spectrum of RW Sex taken with FEROS on the MPG/ESO-2.20 metre telescope based at La Silla in Chile. The exposure was taken on the 17th February 2003 and lasted 1200 seconds. The spectrum was reduced using the FEROS pipeline software.

variable nature of the Balmer lines; in the latter publication the Hβ profile is the same shape but the absorption is slightly stronger and the emission is slightly weaker.

From Fig. 3.1, one might question the stellar origins of the Ca II because it is an extremely narrow line and unfortunately no confirmation can be given in this spectrum. It is only mentioned twice in literature, by Cowley & MacConnell (1972) who mention the line as being in absorption, and Bolick *et al.* (1987) where the line is observed to be considerably stronger in emission in comparison to what is seen in Fig. 3.1. A comparison of the He I 4471 Å and Mg II lines in the adjacent plot, with that of Bolick *et al.* (1987) and Beuermann *et al.* (1992) does not reveal any significant changes in the profiles. There is also little variability between the view of the C III/N III Bowen blend and the He II 4686 Å lines in Fig. 3.1, and Bolick *et al.* (1987) and Beuermann *et al.* (1992). In the latter papers, there does appear to be more contamination between the two lines than what is observed in the FEROS observations but this is likely the result of a poorer resolution.

The final spectral feature shown in Fig. 3.1 is the He I 6678 Å line. This line is not actually mentioned in any literature about RW Sex and although the observations presented by Beuermann *et al.* (1992) do cover the necessary wavelength to view the line, they lack the resolution to resolve the profile. This He I line has an unusual shape. Although the peak in its emission is on the rest wavelength, towards the blue there is a rapid drop in flux but, towards the red, the flux drops far less rapidly and, the profile is actually relatively broad and somewhat red-centric. It is possible that the shape of the profile (and especially the "spike" at 6678 Å) is actually instrumental or has arisen during some part of the reduction process but without any comparable data, it is not possible to tell.

3.3.2 Ultraviolet Observations - IUE

The International Ultraviolet Explorer (IUE) was a joint project between NASA, ESA and PPARC and ran from 1978 to 1996. The telescope had two spectrographs; the long wavelength spectrograph operated in the 1850 to 3300 Å range and the short wavelength spectrograph operated in the 1150 to 2000 Å band. Each spectrograph had two dispersion modes; in low resolution mode the instrument produced a resolution of 6-7 Å, while in high resolution mode the spectra were imaged at a resolution of 0.1-0.3 Å. Each spectrograph had two cameras, a primary and redundant camera; LWP and LWR for the long wavelength spectrograph and, SWP and SWR for the short wavelength spectrograph.

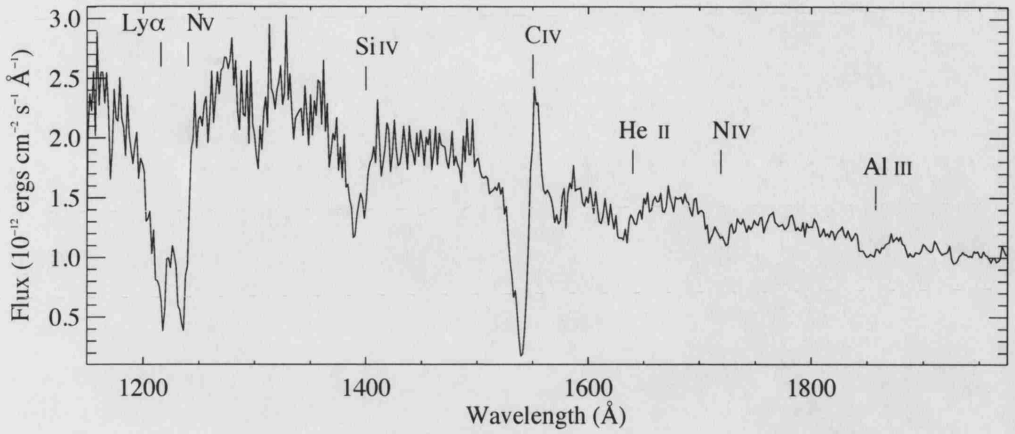

Figure 3.2: A low-resolution IUE short wavelength spectrum of RW Sex with resonance lines marked (SWP22705). The exposure was taken on the 10th April 1984 and lasted 480 seconds.

There have been numerous ultraviolet exposures of RW Sex taken with IUE for projects ranging from a study of dwarf nova and nova-like disc winds to a study combining data retrieved with the Voyager space probe to determine the nature of the inner disc and boundary regions. The high-resolution spectra of RW Sex collected with the IUE have been published in papers such as Prinja & Rosen (1995) (where they found a C IV blue edge velocity of ~ -4550 km/s and an absorption maximum at ~ -1035 km/s); here, two of the low resolution observations are shown, one from each of the spectrographs arms (Figs. 3.2 and 3.3).

Fig. 3.2 is a low-resolution IUE short wavelength spectrum of RW Sex, taken in 1984. In the spectrum there is a multitude of interesting lines. At the very blue end of the spectrum (at around 1200 Å) is the Lyα and N V lines. There is a strong blending in the Lyα absorption and the blue wing of the N V doublet. The latter also has little evidence of emission, unlike the C IV 1550 Å line which a similarly shaped blue-shifted absorption but also quite a strong emission component. Apart from the N V and C IV lines, there is a Si IV line in absorption and numerous other shallow absorption lines, all of which provide convincing evidence for a strong outflow from the system. The high blue edge velocities of these lines (as measured by Prinja & Rosen (1995) for example) suggest that this outflow or wind is relatively fast.

In contrast to the short wavelength IUE spectrum shown in Fig. 3.2, the long wavelength spectrum shown if Fig. 3.3 is rather featureless. The 2200Å interstellar dust ab-

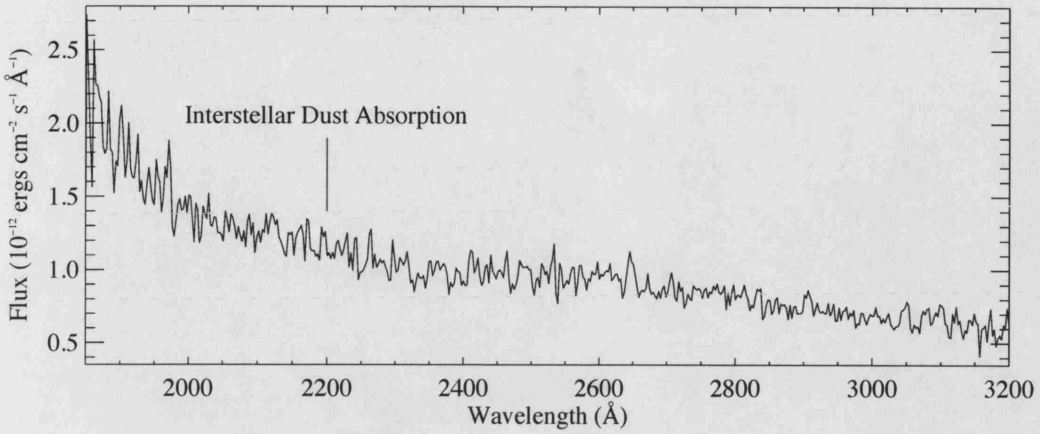

Figure 3.3: A low resolution IUE long wavelength spectrum of RW Sex with the 2200Å interstellar absorption feature marked (LWR01583). The exposure was taken on the 30th May 1978 and lasted 1230 seconds.

sorption feature is not visible, which is consistent with estimates of E(B-V) for this system at ~ 0 (e.g. Greenstein & Oke 1982; Mauche *et al.* 1988).

3.3.3 Ultraviolet Observations - TUES

The TUES or Tübingen Echelle Spectrograph was built and controlled by the University of Tübingen in Germany. It flew aboard the Orbiting and Retrievable Far and Extreme Ultraviolet Spectrograph (ORFEUS)-SPAS II mission in 1996 and was designed to secure spectra in the 900 to 1400Å range at relatively high resolution ($\Delta\lambda/\lambda \sim 10000$). The instrument's life only lasted the duration of the shuttle flight but in that short time, it managed to take nearly 240 spectra of 62 targets; fortunately for this study, one of those targets happened to be RW Sex.

Fig. 3.4 is the mean ultraviolet spectrum of RW Sex, created by averaging the four TUES spectra. Spectra from this instrument covers the entire range that FUSE does (albeit at a far lower resolution) so provides an ideal preview to what can be expected in the FUSE observations. When these observations are compared with those of FUSE, the long term variability of the lines can also be investigated. It should be noted that the continuum flux levels of this system appear to be very similar to the far-UV flux levels from Voyager data presented in Polidan *et al.* (1990), suggesting that the mass accretion rate is relatively stable. In the spectrum shown in Fig. 3.4 a mixture of broad stellar absorption lines can be seen, along with some evidence of narrower interstellar lines of H I

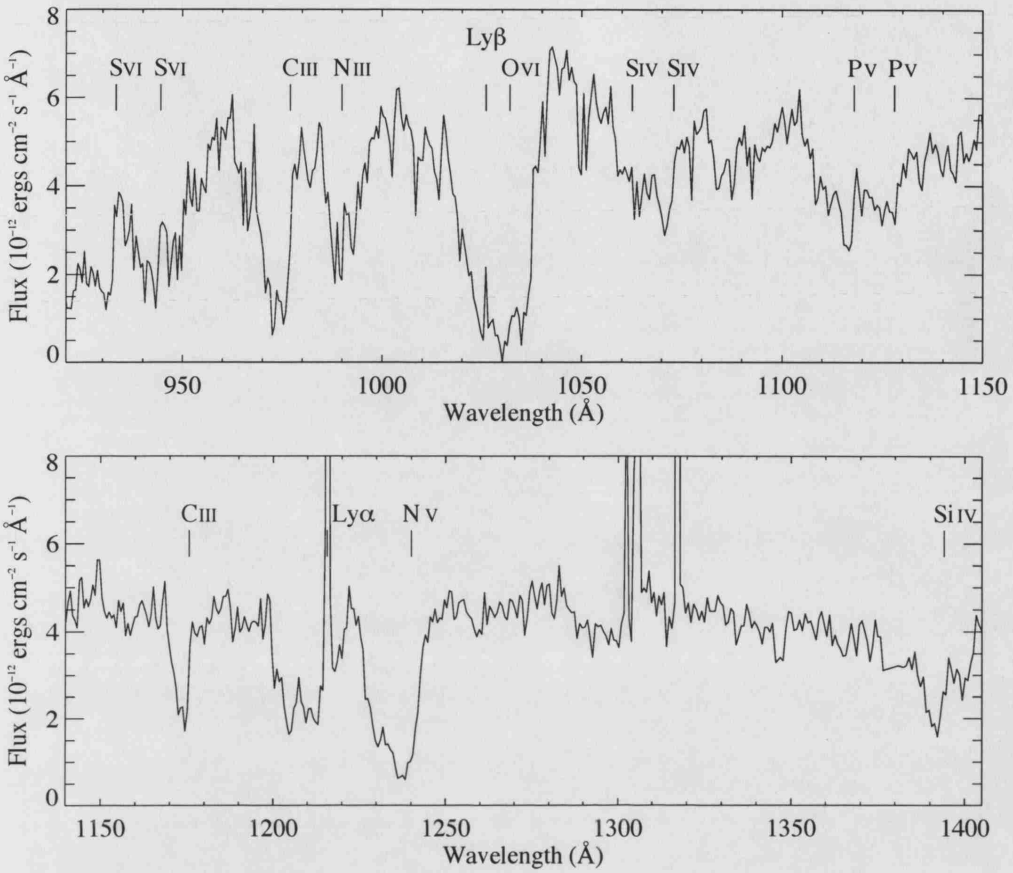

Figure 3.4: The mean TUES (ultraviolet) spectrum of RW Sex, taken in 1996. Several important lines have been indentified.

and metallic ions. It is possible that more, narrow lines may be present in the spectrum but the spectrum had to be binned to 20 pixels to improve signal-to-noise to a more suitable level. An important feature of the marked stellar absorption lines is that for all lines the absorption is heavily blue-shifted (the rest wavelengths are indicated by the marks), showing that the outflowing material is moving towards the observer at considerable velocity. The stellar absorption lines are typically seen to reach their maximum depth at relatively low velocities and towards greater velocities there is a a gradual decrease in strength. If a simple monotonic velocity law were assumed for the outflow (this is unknown but not an unreasonable assumption) then this observed behaviour in the line depth would suggest that most of the material is close to the originating source of the outflow.

Fig. 3.5 demonstrates the variability of the C III 1176 Å profile by displaying two examples from the TUES time-series; the two spectra are separated in times by approximately

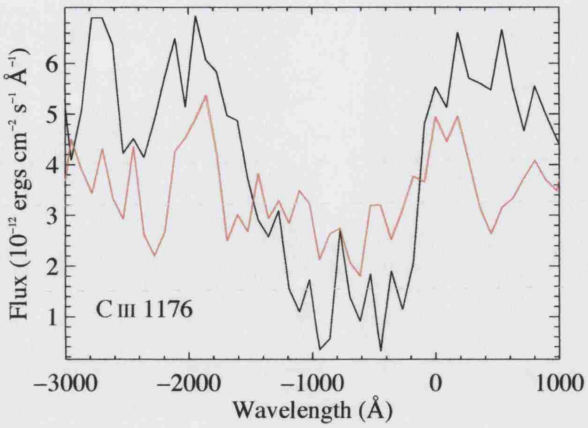

Figure 3.5: An example of the line profile variability present in the TUES spectra of RW Sex. The black line is spectrum *tues2208_1* and the red line is spectrum *tues2208_4*; the spectra are separated in time by approximately 12 days.

12 days; this plot clearly shows the variability of the wind-formed lines in the RW Sex spectrum. In the later (red solid line) spectrum, the blue-shifted absorption has reduced in strength and it now appears to be more symmetric than before (the low velocity wing has become shallower). There does appear to be some variability in the continuum either side of the spectral line but this is most likely due to errors in the flux calibration. With such a low resolution and a phase coverage, it is difficult to make too much interpretation of the line profiles so further analysis of these lines is deferred to the FUSE data.

3.4 The Observations

Two sets of time-series data were analysed for this study, one set taken with the Goddard High Resolution Spectrograph (or GHRS) on the Hubble Space Telescope (or HST) and, one set taken with the Far Ultraviolet Spectroscopic Explorer (or FUSE). In this section the two instruments are introduced and a brief summary is given for each set of observations.

3.4.1 The FUSE Observations

Most of this chapter is based around the analysis of the FUSE time-series. The Far Ultraviolet Spectroscopic Explorer is a NASA-supported space based telescope, designed to observe the far-ultraviolet band with a high spectral resolution. FUSE has four optical

Aperture	Keyword	Dimensions (arcseconds)
High Resolution	HIRS	1.25×20
High Throughput	MDRS	4×20
Large Square	LWRS	30
Pinhole	PINH	~ 0.5 (diameter)

Table 3.2: A summary of the four apertures available on FUSE.

Data ID	UT Start Time	Exposure Time (seconds)
B1040101000	14:48 13th May 2001	25680.529

Table 3.3: A summary of the FUSE time-series observations of RW Sex. The values listed here were obtained from the Multi-mission Archive at the Space Telescope Science Institute (MAST).

channels; two are coated with SiC and are therefore named SiC1 and SiC2 and, two are coated with LiF and are called LiF1 and LiF2. For FUSE, the wavelength range between ~905 and 1105Å is covered by the SiC channels and the wavelength range between ~980 and 1188Å is covered by the LiF channels. Each channel also has two segments, labelled A and B. Using the 8 segments across the 4 channels, FUSE manages to produce spectra covering the range 905 to 1188 Å with a relatively high spectral resolution of $\sim$ 20000. It should be noted that a distortion known as the 'worm' affects observations using LiF1B. The FUSE spectra are collected in one of two modes; photon address mode or spectral image mode. Photon address mode is also known as time-tag or TTAG mode and is when the X and Y location, arrival time and pulse height of each detected event is recorded. Spectral image mode (otherwise known as HIST mode) is where the photon events are accumulated in bins so that the arrival time of each photon is lost; for bright sources (where the count rate is greater than 2500 per second) the TTAG mode would create too many events and would end up using all of the available disc space on the computer. The targets are observed through one of four apertures, HIRS, MDRS, LWRS and PINH; Table 3.2 summarises the aperture properties. See Moos (2000) and Sahnow *et al.* (2000) for a more complete review of FUSE.

The data in this study were collected on the 13th May 2001 in TTAG mode through the

large aperture; Table 3.3 summarises the observation. The total exposure time amounted to 24000 seconds and was spread over a 40 hour time period; for this study the data was binned into 25 spectra with effective exposure times of around 1000 seconds, after pipeline reduction using CALFUSE v.1.8.7. For the purposes of this study (and for simplicity), the analysis was limited to data collected in the SiC2A, LiF1A and LiF2A since they provided the best views of the desired spectral features. Despite the relatively low continuum signal-to-noise ($\sim$ 10), the high spectral resolution ($\sim$ 0.1 Å) and the large spectral range has made this time-series ideal for analysing the wind formed spectral features. The analysis of the FUSE observations is presented in § 3.5.

3.4.2 The HST Observations

The Hubble Space Telescope (or HST) is an orbiting observatory with a 2.4-metre reflecting telescope. It was developed as a joint programme between the National Aeronautics and Space Administration (NASA) and the European Space Agency (ESA) and it was deployed by the space shuttle Discovery in 1990. The observations used in this study were secured using an instrument which has been replaced on HST during a service mission, the Goddard High Resolution Spectrograph or GHRS. The GHRS was an ultraviolet spectrograph which used two 521-channel Digicon detectors, one which was sensitive from 1150 to 1700Å and one which was sensitive from 1150 to 3200Å. The instrument had three resolution modes; low, medium and high, which are summarised in Table 3.4. The data presented in this study were secured on the 4th May 1996 and were part of an observing programme to study the accretion discs and winds of low inclination CVs; there were three targets, BZ Cam (an optical study of this system is presented in § 6; the HST results are presented by Prinja *et al.* 2000*b*), V603 Aql (an old nova, the results of analysing this HST data is presented in Prinja *et al.* 2000*a*) and RW Sex.

This HST data, which are summarised in Table 3.4.2 was acquired with the telescope in accumulate mode (ACCUM) where the instrument is allowed to accumulate enough photons to reach a desired signal-to-noise level. The G140L grating was used in first order which effectively gave a resolution of 2000. The observations were all made through the Large Science Aperture (or LSA) which is 1.74 arcsec square. The observations were reduced using the standard pipeline; this reduction technique is explained in detail in Prinja *et al.* (2000*b*). Although these observations are limited to the extent to which they span the orbit of RW Sex (only about 50 per cent), they have a very high temporal reso-

Resolution mode	Resolution at 1200Å	Limiting Magnitude
Low	2000	19
Medium	20,000	16
High	100,000	14

Table 3.4: A table of the three resolution modes of the Goddard High Resolution Spectrograph on the Hubble Space Telescope.

Data set	UT Start Time	Exposure Time (seconds)
Z37V0104T	4th May 1996 13:03	544.0
Z37V0103T	4th May 1996 13:03	4.8
Z37V0105T	4th May 1996 13:17	544.0
Z37V0106T	4th May 1996 13:30	544.0
Z37V0109T	4th May 1996 15:03	435.2
Z37V0108T	4th May 1996 14:50	544.0
Z37V0107T	4th May 1996 14:37	544.0

Table 3.5: A summary of the HST observations of RW Sex. The values listed here were obtained from the Multi-mission Archive at the Space Telescope Science Institute (MAST).

lution with 38 exposures covering the wavelength range 1140 to 1436 Å and 75 exposures covering the range from 1367 to 1663 Å, both with a spectral resolution of $\sim$ 0.8Å. The analysis of the HST observations is presented in § 3.6.

3.5 Analysis of the FUSE Time-Series

In this section, the analysis of the FUSE time-series is presented.

3.5.1 The Spectrum

Fig. 3.6 is the time-averaged spectrum of RW Sex from the combined channels of this FUSE time-series. An initial comparison of this spectrum with the mean TUES spectrum in Fig. 3.6 and the Voyager spectrum presented by Polidan *et al.* (1990) reveals there

Ion	λ_0(Å)	I.P. Previous of Ion (eV)	I.P of Ion (eV)
C III	977.020, 1125.65, 1175.6	24.4	47.9
N III	989.799	29.6	47.5
N IV *	923.06	47.5	77.5
P IV	950.657	30.2	51.4
S IV	1062.66, 1072.97	34.8	47.3
P V	1117.98, 1128.01	51.4	65.0
S VI	933.39, 944.52	72.7	88.0
O VI	1031.93, 1037.62	113.9	138.1

Table 3.6: This table lists the disc wind diagnostics lines present in the FUSE spectra. The table has been split into those lines which are considered to be low ionisation (upper panel) and those which are considered to be high ionisation for the conditions (lower panel). * N IV is an excited transition.

to be some variation in the flux levels over the 15 year time-span that the observations cover; the flux levels in the TUES spectrum are slightly greater than what it observed in Fig. 3.6. However, there does not appear to be a significant change in the spectral lines present and their profiles, apart from what might be expected given the differences in spectral resolution. The spectrum demonstrates strong examples of wind diagnostics lines of nitrogen, sulphur, phosphorus and oxygen lines. They are all relatively similar in shape, showing a large, broad blue-shifted absorption and an apparent absence of emission or absorption red-wards of the line centre. The Lyβ line is also present but its characteristics are less obvious in this time-averaged view of the spectrum and will be discussed in more detail later. There are also many narrow interstellar lines of molecular hydrogen present in the spectra but many of these cannot be seen in Fig. 3.6 because of the resolution of the plot.

Fig. 3.7 combines FUSE, IUE and, optical data points from Beuermann *et al.* (1992) to produce a view of a significant section of the continuum of RW Sex. The example IUE spectrum selected matches the strength of the FUSE spectrum quite well and demonstrate a long term stability in the high mass accretion rate and the accretion disc. A Kurucz model spectrum of a star with an effective temperature of 21000K and a surface gravity of $\log g = 3.0$ has been shifted to match the far-UV flux and overplotted; a star with

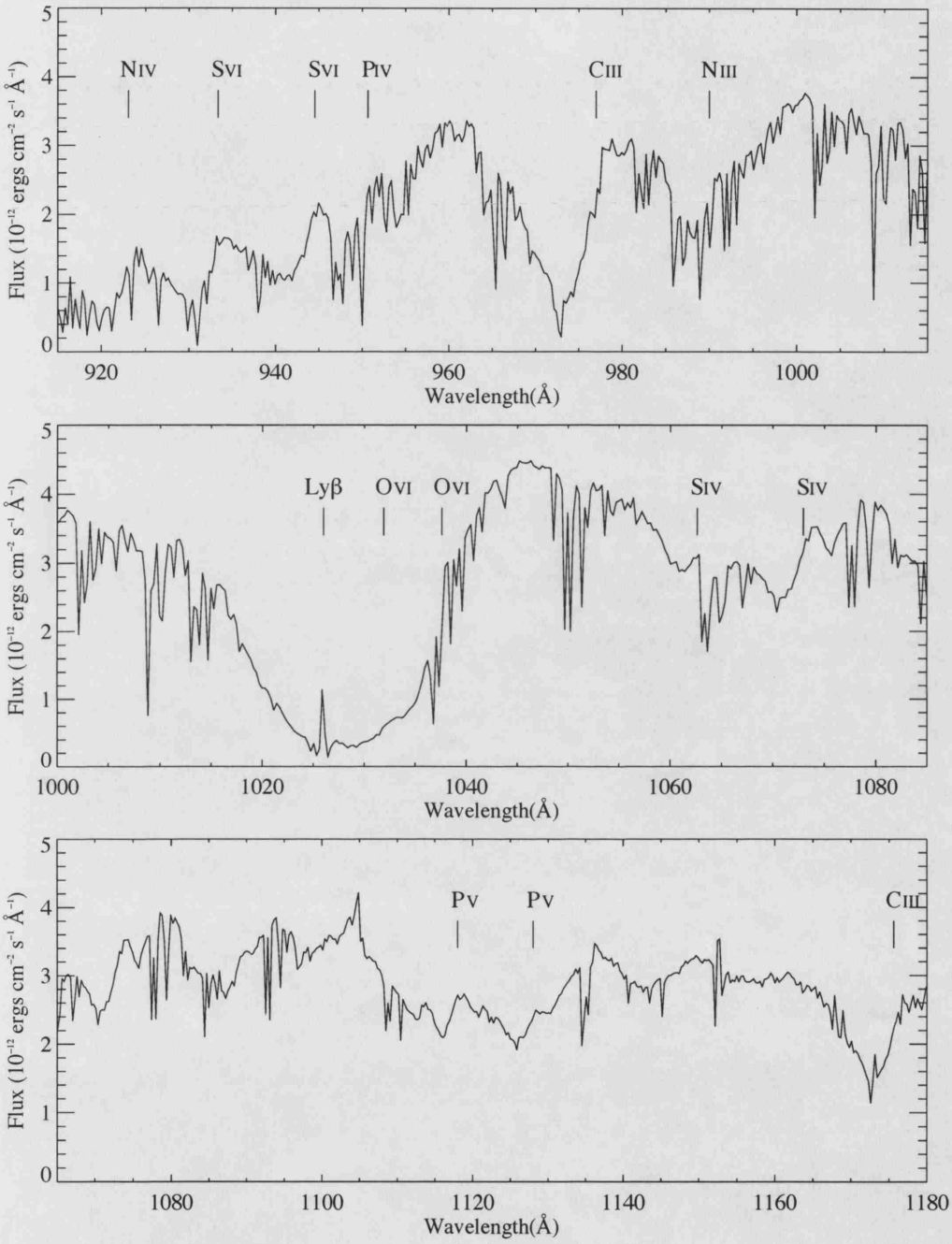

Figure 3.6: The time-averaged spectrum of RW Sex from the combined channels of the FUSE time-series. Several important lines have been marked. A limited number of the narrow interstellar lines of molecular hydrogen are visible in this plot.

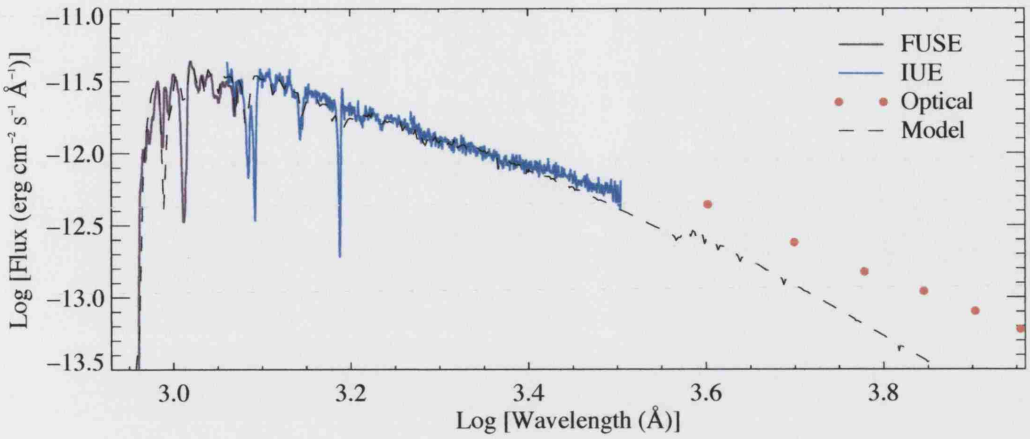

Figure 3.7: The combined FUSE (purple line), IUE (blue) line and optical (red dots) for RW Sex. The FUSE spectrum is the time-averaged profile shown in Fig. 3.6 and the two IUE lines that constitute the IUE spectrum are the exposures SWP26080 and LWR06494. The optical data points have been estimated from the low resolution optical spectrum taken in 1986 and presented in Beuermann *et al.* (1992). The dashed line is a Kurucz model atmosphere (Kurucz 1993) for a star with an effective temperature of 21000K and a surface gravity ($\log g$) of 3.0.

this temperature approximates a mid B spectral type. The model spectrum matches the continuum strength and shape of the far-UV and UV regimes, although at longer wavelengths the model breaks down because it was not designed to simulate the multiple blackbody continuum of an accretion disc, and it does not simulate the secondary star, although the latter component is unlikely to make significant contributions to the flux at optical wavelengths. Although there is a gap in the data of this plot, across the Balmer jump, the location of the IUE data in relation to the optical data points infers a relatively flat Balmer jump which is similar to what has been found in other high state CVs such as BZ Cam, UX UMa and V795 Her.

3.5.2 Line Profile Variability

In § 3.5.1 the time independent nature of the far-UV FUSE spectrum of RW Sex was outlined. However, as with any time-varying astronomical target, the time-averaged spectrum only reveals a small amount of information about what is happening in a system and can lead the astronomer into false conclusions. Initial views of the FUSE resonance

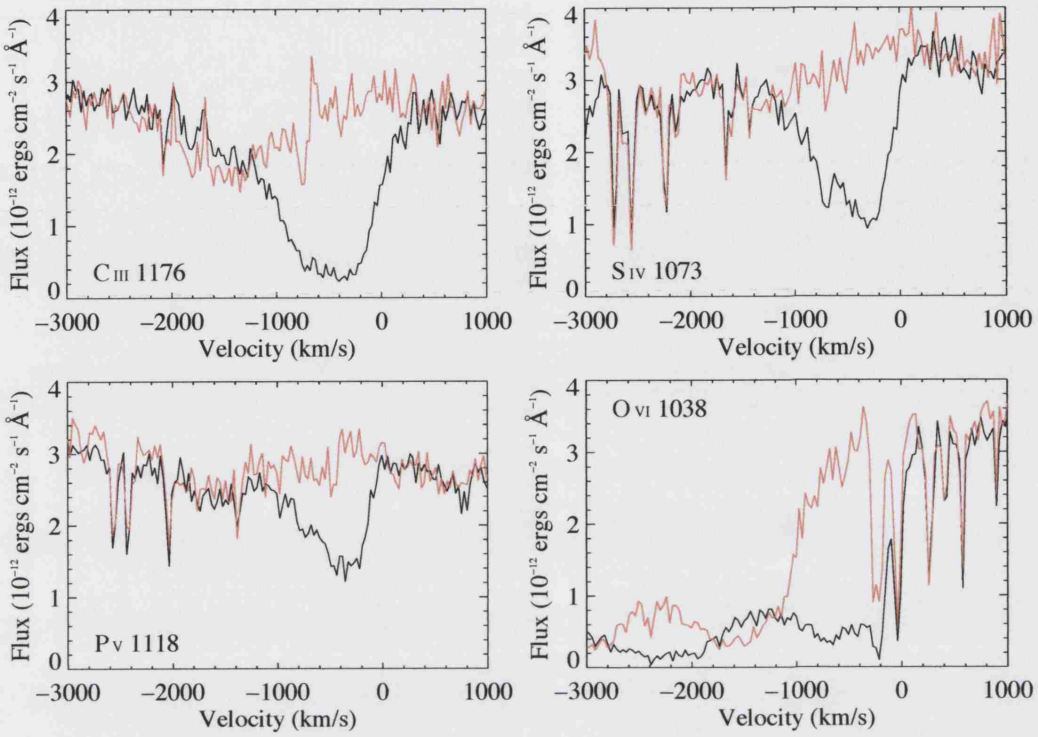

Figure 3.8: Example of the line profile variability in the FUSE time-series of RW Sex. The red lines were observed approximately 10 hours after the black lines, which corresponds to 1.7 times the orbital period.

line profiles show them to be extremely variable (see Prinja *et al.* 2003); these changes will be presented in detail in this section.

Fig 3.8 contains plots of four of the wind diagnostics lines (of varying stages of ionisation) at two different times so that the degree to which the lines vary can be seen; the same two sets of exposures (which are separated by 10 hours, or approximately 1.7 times the orbital period) are shown for all four lines. For all four spectral lines, the black solid lines show a strong, blue-shifted absorption superimposed on the underlying continuum; there appears to be significant asymmetry in the absorption as the low velocity edges (close to the rest wavelengths) are much steeper than the high velocity wings. Generally the absorption does not appear to extend much greater from the line centre than -1000 km/s although there is some absorption in the C III 1176 Å at positive velocities. In the later (red solid line) spectrum, it appears as though the absorption has almost completely filled in; it is now much shallower and the peak in absorption depth has shifted blue-wards to greater negative velocities (~ -1500 km/s). This repetition of large variability in these

four lines is repeated throughout the time-series.

The two spectra shown in Fig. 3.8 were selected because the squared summed differences over a selected velocity range (between -1000 and 0 km/s) for the four lines was calculated to be the greatest for these two spectra than any other pair of spectra in the entire FUSE time-series. That the same two spectra were found to have the greatest differences for the four selected lines suggests that all four ions are varying in phase. It can also be seen that for all four ions the red edge of the variable absorption is at $\sim +250$ km/s although the very large changes to the line profiles occur at negative velocities. At velocities greater than +250 km/s there does not appear to be any noticeable change in the profile shape or strength, for all four ions.

3.5.3 Temporal Variance Spectra

The observed changes of the wind line profiles can be quantified by determining the temporal variance spectrum (or TVS) for each ion; TVS are described in § 2.2.2. Fig. 3.9 has plots of the TVS for several key sections of the FUSE time-series of RW Sex. Within the four selected regions, there are very strong indications of line profile activity. In the multitude of lines that are displayed in this figure, a common behaviour can be observed; the variance is only observed at negative (blue) velocities. The shape of the TVS profiles for the individual lines are relatively similar and seemingly independent of the ionisation stage of the ion; moving towards the blue from the line centre, there is a sharp rise to maximum levels of variance followed by a far more gradual reduction in variance beyond where it peaks. In cases where there are doublet lines, the peak in variance is not flanked by such steep sides for the weaker of the pair which is perhaps because less variance is spread over the same velocity range. In all cases the variance does appear to peak just less than -500 km/s; there is some variability in the location of where the variance of the profile reaches the confidence level on the blue side (between ~ -1500 and ~ -900 km/s), but this does not appear to be related to the species or ionisation stage.

When a comparison is made between the TVS and the mean spectrum shown underneath, some interesting points are discovered. Firstly, although the peak in variance for each line is typically between -500 and -300 km/s, the peak in the absorption depth is actually at a slightly greater distance from the line centre (~ -700 km/s). If a monotonic velocity law was again assumed, then it could be interpreted from this information that the region of the wind close to the accretion disc (and therefore close to the emitting re-

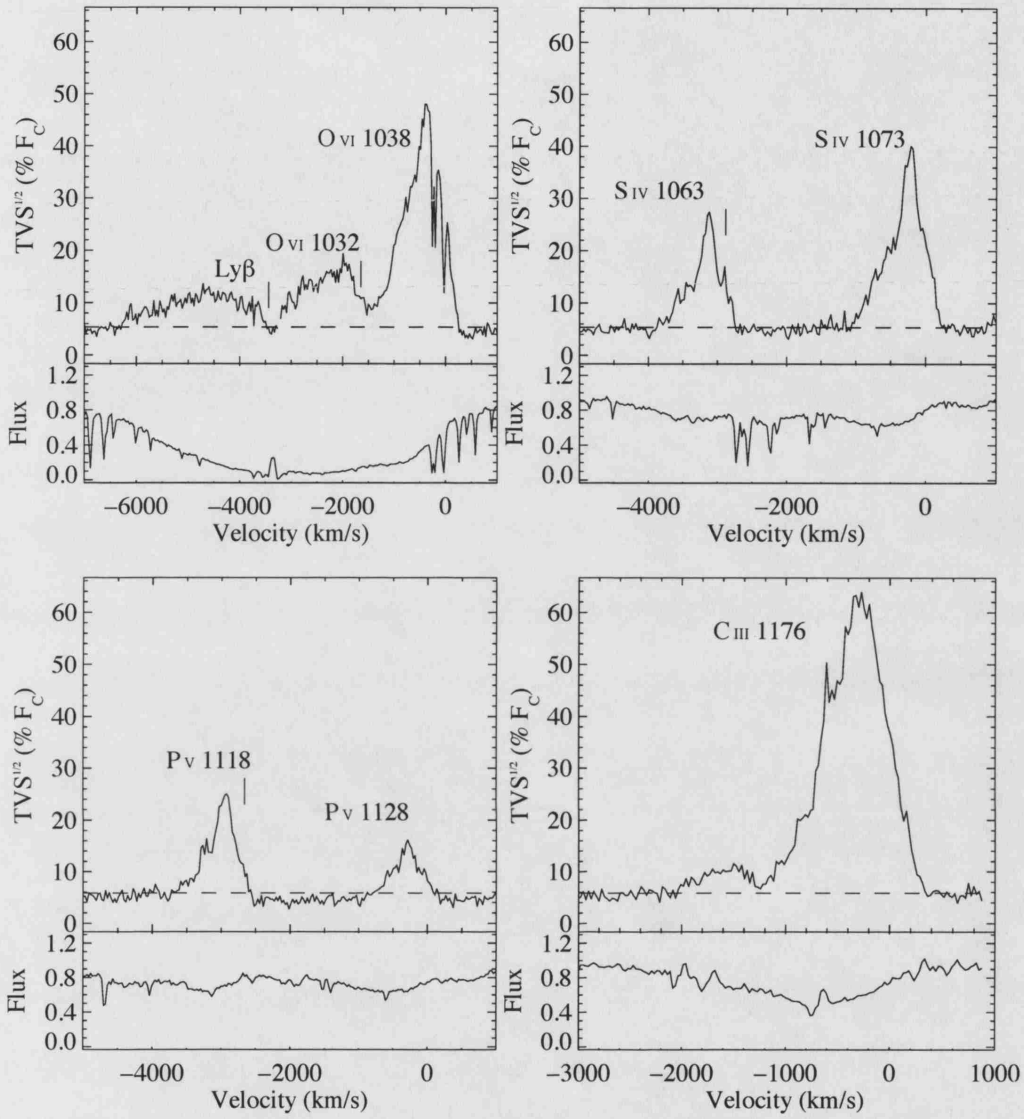

Figure 3.9: Temporal variance spectra for four selected regions from the FUSE time-series of RW Sex; the plots are in order of increasing wavelength (left to right, top to bottom). The bottom panels of each plot are the mean spectra for the selected regions and the upper panel contains the variance spectrum (solid line) along with a 95% confidence level of no variability (the dotted line). The velocity scales are based upon the right-most feature in the selected regions although marks have been provided to indicate the line centres of the other lines. The top two selected regions originate from LiF1a data and the lower two selected regions originate from the LiF2a data.

gion) is extremely turbulent and, further from the disc (at greater velocities) the outflow stabilises. Secondly, for all lines the blue-shifted absorption extends to greater negative velocities than the TVS variance does, meaning that at these large velocities (and hence at great distances from the disc if the monotonic velocity law is subscribed to) the wind is extremely stable and fluctuations are not detectable with data of this signal to noise.

The similarity in the structure of the TVS spectra for the S IV and P V doublets is an expected feature of an optically thin line. In optically thin regions the line strength is proportional to the number density of absorbers and the oscillator strength (which gives the ratio in strength between the doublets). Therefore, when there are fluctuations in the number of absorbers it is expected that both lines in the doublet react in the same way. However, in optically thick regions the relationship between line strength and the number of absorbers breaks down and when there are fluctuations in the number of absorbers the reaction of the two lines in the doublet will not necessarily be the same. This is a small but important point which is revealed by the TVS spectrum.

The one spectral line which has yet to be discussed in detail is the Lyman β line. The observed variance profile of this line (seen enlarged in Fig. 3.10) is different from the lines already discussed; the profile is much flatter and extends to far greater velocities. The rise in variance towards a maximum (from the line centre) is still at a greater rate than the subsequent reduction but this variance remains above the confidence level to almost -3000 km/s rather than approx. -1000 km/s, as was seen for the other lines. This variance profile suggests that the hydrogen traces different parts of the wind, with different conditions from those traced by the metal resonance lines.

So far the TVS analysis of the FUSE time-series has concentrated on spectral lines in the LiF1a and LiF2a channels, leaving out all the spectral features in the SiC2a channel. This particular channel contains several important spectral lines (e.g. N IV 923 Å and C III 977 Å) but unfortunately analysis is hindered by a poorly defined continuum which makes it difficult to perform a reliable normalisation of the spectra. However, there is much information to be gained from data in this channel so the TVS of the entire channel has been included in a plot by itself (see Fig. 3.11). The coloured bars in the figure represent three key velocity ranges for each line: 0 to -500 km/s (red), -1000 to -500 km/s (blue) and -1500 to -1000 km/s (green). The dashed line indicates the 95% confidence level of no variability; note that the temporal variance of the continuum regions at the short wavelength end of the spectrum are slightly higher than the long wavelength

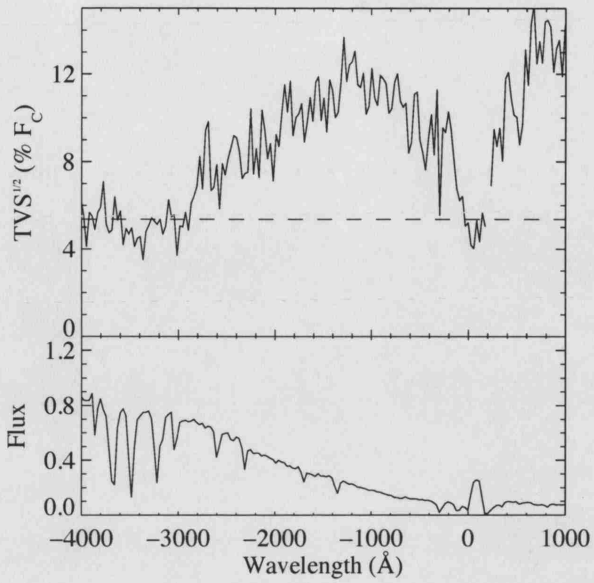

Figure 3.10: The temporal variance spectrum for Lyman β from the LiF1a section of the FUSE time-series of RW Sex. The bottom panel is the mean spectrum across the selected region and the top panel is the TVS; the dotted line in the TVS plot indicates the 95% confidence level of no variability.

continuum regions which is due to difficulties in normalising the short wavelength end of the spectrum.

The TVS of the SiC2a data reveals much the same results for the indicated lines as was seen for the LiF channel data; a complete lack of variance across the positive velocity sections and significant levels of variance at negative velocites. The peak in the variance for each line was measured to be close to -500 km/s in the LiF data but in this channel an increased level of noise means the peak in variance cannot be so clearly located. For most of the lines the variance seems to drop below the confidence level at ∼-1000 km/s which is also what was seen for most of the lines in the LiF data, although the N III and C III lines do show some variance above the confidence level beyond this range. The shape of the TVS profiles are relatively similar to each other but they are not identical. The variance profiles of those species at the same ionisation level seem to be the closest in shape, suggesting that there is some ionisation structure to the wind.

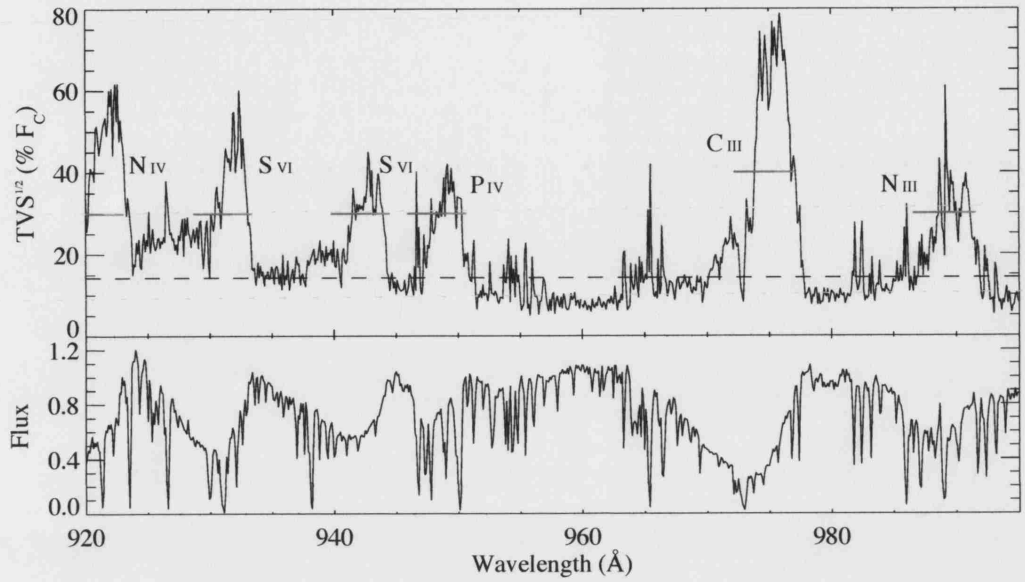

Figure 3.11: The temporal variance spectrum of the SiC2a section of the FUSE time-series for RW Sex. For the lines which have been marked, indications of the velocity regions have been given using coloured bars; red represents from 0 velocity to -500 km/s, blue represents from -1000 to -500 km/s from the line centre, and green represents from -1500 to -1000 km/s from the line centre. The dotted line indicates the 95% confidence level of no variability.

3.5.4 Comparing the Behaviour of Spectral Lines

In § 3.5.3 the temporal variance spectrum was calculated for each line and the resulting variance profiles was described. It was mentioned in § 3.5.2 that the simultaneous changes to different spectral lines inferred that they behave in phase with each other. In this section the behaviour of the different spectral lines in relation to each other is analysed in more detail to determine whether this is truly the case.

The following analysis concentrates on the following pairs of ions: N III 990 Å and N IV 923 Å, P IV 951 Å and P V 1128 Å and, S IV Å 1073 and S VI 945 Å. Two notes should be made about the N IV 923 Å line; it is an excited transition and it is very weak and close to the end of the FUSE data, thus measurements from it result in enhanced scatter in comparison to measurements from the other lines. For each line listed above, the mean flux was calculated in a strip between -1000 and 0 km/s from the line centre; this was deemed to provide a suitable estimate of the overall strength of the wind on each

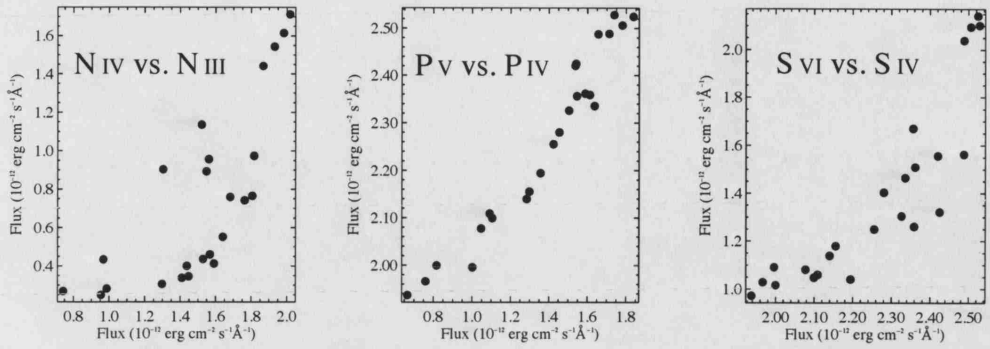

Figure 3.12: A comparison between the mean flux measured between -1000 and 0 km/s for pairs of ions from the elements N, P and S. The measurements were made from the FUSE time-series.

occasion.

Fig. 3.12 is a plot comparing the mean flux measured between -1000 and 0 km/s for pairs of ions of the elements N, P, S (from the FUSE time-series). Comparing the measurements of ions of the same elements can reveal the ionisation conditions in the disc wind rather than demonstrating the variable abundance of the elements at different points in the wind. All three plots show a clear linear correlation in the mean flux between the pairs of lines, although the degree of correlation does vary; the correlation between the mean fluxes for the phosphorus lines appear to be much better than for the nitrogen or sulphur lines. An explanation can be provided for the differences in the degree of correlation though. In the plot of the two nitrogen lines, as previously explained, the measurements of the N IV would likely result in enhanced scatter and thus the degree of correlation is reduced. For the two sulphur lines, the problem is due to the S VI line, which at times becomes so deep it suffers from the effects of saturation resulting in a breakdown in the correlation when the saturation occurs. The good linear correlation between the pairs of ions of the same elements suggests that the ionisation mixture of the outflow is not detectably variable. Thus, large changes in the spectral line profiles is most likely due to changes in the velocity profile and density of the outflowing material.

The comparison of ions of the same element has shown that there is correlated behaviour between different ionisation stages; what follows is a comparison of the wind of different species. If the comparison shows there to be no linear correlation between the two ions then it could signify some abundance effects or a differing in the origin of the

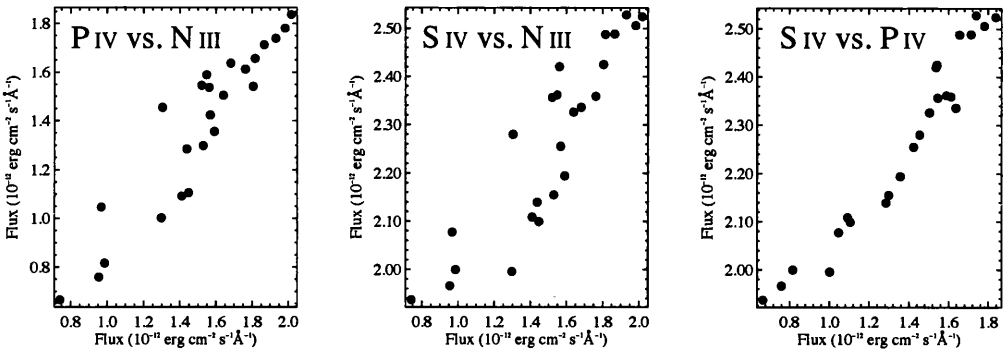

Figure 3.13: A comparison between the mean flux measured between -1000 and 0 km/s for pairs of ions of different elements. The measurements were made from the FUSE time-series.

disc winds on the face of the accretion disc. If the latter is the case then it is possible that an orbital modulation would be found within those measurements. Fig. 3.13 is a plot comparing the mean fluxes measured in the -1000 to 0 km/s range for N III and P IV, N III and S IV, and P IV and S IV. This particular combination of comparisons was selected because all three lines are of similar ionisation levels and none of them suffer from saturation effects or weakness. As was found in comparing ions of the same species, there is a strong linear correlation in the mean flux for the ions of different species. These comparisons show that any variation in the mean flux of the disc wind for one ion of one species, is echoed through all wind diagnostic lines and, that there is no lag in these changes between the lines. This reinforces the concept that the variability in the blue-shifted absorption of the lines is due to changes in the density and velocity profile of the outflowing material.

3.5.5 Fourier 2D Analysis of the Blue-Shifted Absorption

So far, the presence of a highly variable blue-shifted absorption has been established for several wind diagnostic lines in the far-UV spectrum of RW Sex. As yet, no attempt has been made to determine whether the observed variability is seemingly random, or modulated on some time-scale such as the orbital period of the system. A superficial analysis of whether the absorption is modulated can be made using Fourier 2D analysis which is where a Fourier transform is perfomed on every wavelength or velocity bin of a spectrum (Fourier analysis is described in more detail in § 2.2.3). Hence, this procedure indicates whether the flux along any portion of a spectrum is modulated, within the realms

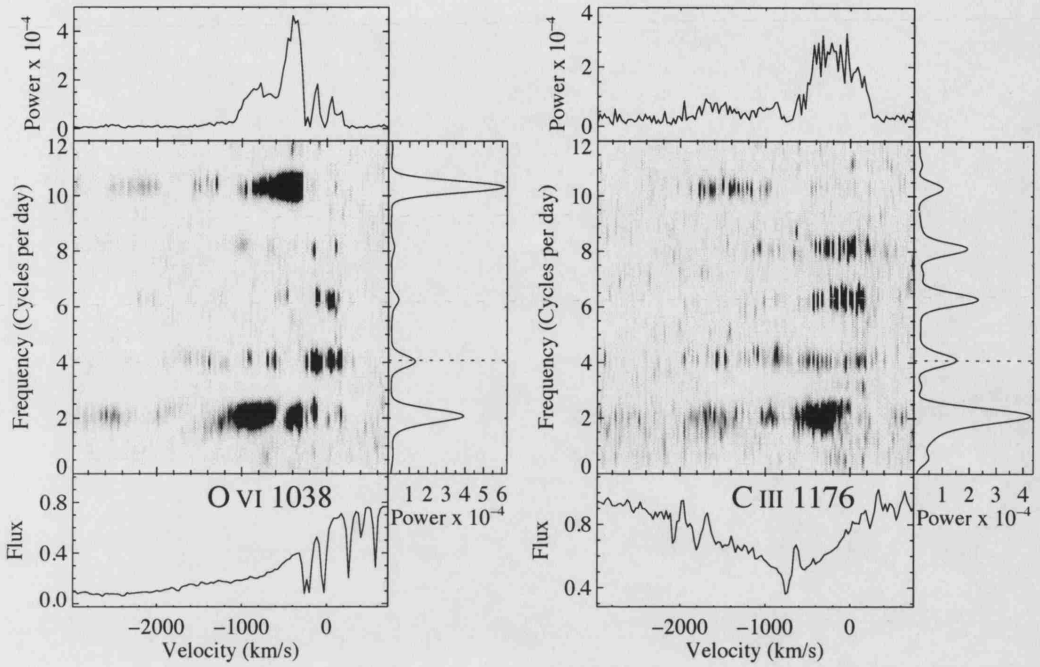

Figure 3.14: Fourier 2-dimensional plots of the O VI 1038 Å and C III 1176 Å lines from the FUSE time-series. In these plots the dark areas represent signals in the Fourier power spectra. Summations of the power in velocity and frequency space are shown to the top and to the right of the plot; the dotted line on the frequency summation plots indicates the frequency of the orbital period of RW Sex (approx. 0.245 days).

of the quality, spectral and temporal resolution of the data, and subject to the parameters supplied to the Fourier transform routine. The seemingly correlated behaviour between the lines means that it is unnecessary to show Fourier 2D plots of every line analysed so far; in this occasion, only the Fourier 2D plots of the O VI 1038 Å and C III 1176 Å lines are shown. These two lines were chosen specifically because they had the strongest TVS signals; the Fourier 2D plots are shown in Fig. 3.14 where dark areas indicate signals in the power spectra. In both plots, signals in the power spectra are discovered at frequencies of 2.1, 4.1 (the orbital frequency), 6.3, 8.1 and 10.3 d^{-1}; these frequencies approximately correspond to the periods, 0.48, 0.24 (the spectroscopically determined orbital period), 0.16, 0.12 and 0.097 days, respectively. This modulated behaviour generally appears to be strongest between ~ -1500 and ~ 0 km/s and for both lines there is some strength at even greater velocities from the line centre.

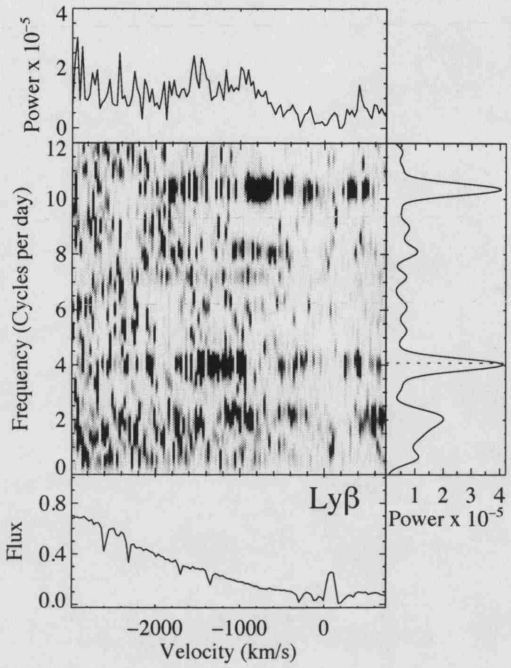

Figure 3.15: Fourier 2-dimensional plot of the Lyβ line from the FUSE time-series. In this plot the dark areas represent signals in the Fourier power spectra. Summations of the power in velocity and frequency space are shown to the top and to the right of the plot; the dotted line on the frequency summation plot indicates the frequency of the orbital period of RW Sex (approx. 0.245 days).

Fig. 3.15 is a Fourier 2D plot of the Lyβ line; it has been demonstrated that the blue-shifted absorption of this line is variable, but it has yet to be established whether this variability is modulated or not. The plot yields a similar result for this line as for the O VI 1038 Å and the C III 1176 Å lines in Fig. 3.14; across negative velocities of the Lyβ line, there are strong signals of modulation on the orbital period, and on the same series frequencies as was seen for the other two lines. The Fourier 2D plot does show some signals on the orbital frequency (and additional frequencies) at positive velocities but it is thought that this originates from the O VI 1032 Å line, although this cannot be confirmed.

In summary, the Fourier 2D analysis revealed the blue-shifted absorption flux (for the wind diagnostic and Lyβ lines) to have significant signals of variability on the orbital period although the strongest signals were in fact at the frequencies of 2.1 and 10.3 d^{-1}, which are separated from the orbital period in frequency space by approximately 2 and

6 d^{-1}, respectively. The analysis did not reveal any significant modulation (orbital or not) at positive velocities, with respect to the rest wavelengths of the relevant lines. The search for non-orbital modulation was limited to a maximum frequency of 21 d^{-1}, which corresponds to the exposure time of the frames used.

3.5.6 Equivalent Width's of the Blue Shifted Absorption

The Fourier 2D plots revealed the blue-shifted absorption to be modulated on the orbital period (or an alias of that period) but, no further information can be obtained from these plots as to the nature of this variability. The Fourier 2D analysis performed an inverse Fourier transform across 0.1 Å bins of the spectrum and it would be possible to "fold" each of these bins to determine the nature of the variability but, the noise of the data would not support a reliable analysis in this manner. By measuring the equivalent width of the blue-shifted absorption instead, there is a great loss in spectral resolution but the noise within each measurement is vastly reduced and thus the end results are more reliable. These equivalent widths measurements are presented in this section.

The plots shown in Fig. 3.16 are of the dirty and clean Fourier power spectra of equivalent width measurements for a select set of lines from the FUSE time-series; the equivalent width of the absorption was measured in the velocity range of -1000 to 0 km/s for all lines and the dashed line indicates RW Sex's orbital frequency. For all the lines apart from Lyβ, the strongest signal in the Fourier power spectrum is on the orbital frequency and, even in the power spectrum of the Lyβ line, significant power is shown on one of the aliases of the orbital frequency. The temporal coverage of this data means that it is not extensive enough to determine whether something is modulated on the orbital frequency or one of the aliases but, given the power spectra shown in Fig. 3.16, it no longer seems necessary.

The Fourier 2D plots in Figs. 3.14 and 3.15 showed the strongest indications of orbital modulation across a velocity band between -1000 and 0 km/s (hence the selected velocity bands for the equivalent width measurements just discussed). However, for all three lines there was some indication of orbital modulation of the absorption at velocities greater than this. To analyse this "high" velocity behaviour, equivalent width measurements were made in the -2000 to -1000 km/s velocity band for the C III 1176 Å line; this spectral line was chosen because it has no close features to contaminate the high velocity portions of the absorption and, the observed variability of the line is very high. Fig. 3.17 is a plot

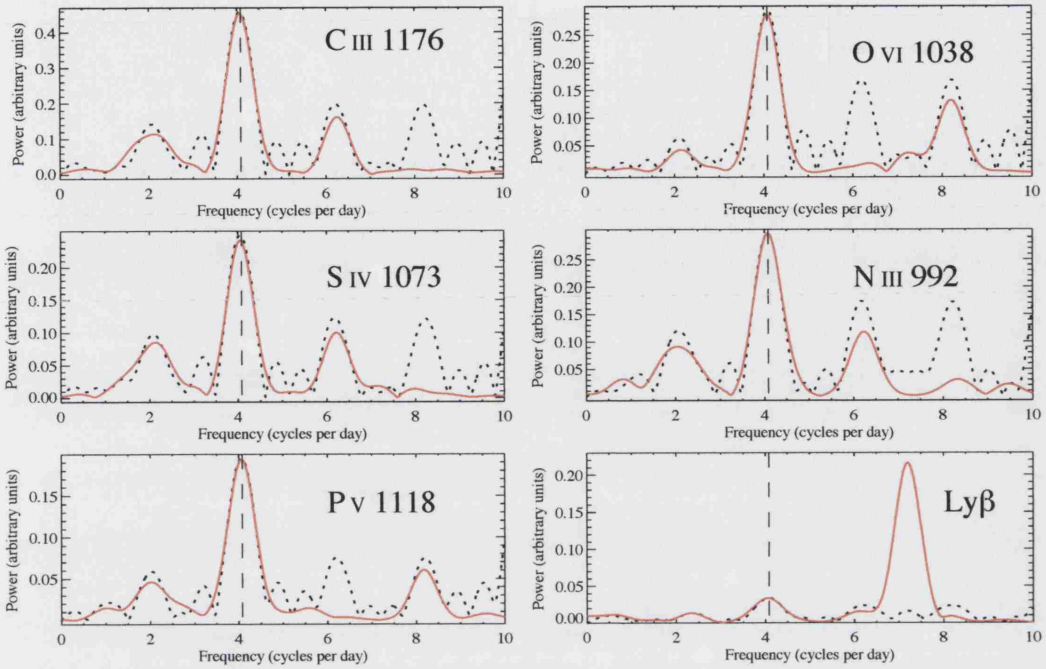

Figure 3.16: Fourier power spectra of absorption equivalent widths from the FUSE time-series. The black dotted lines represent the Fourier dirty spectra and the red solid lines represent the cleaned Fourier spectra (the gain was 0.2 for 200 iterations). The dashed vertical line represents the systems orbital period (0.245 days). For all lines the equivalent width was measured in the -1000 to 0 km/s range.

of the dirty Fourier power spectrum (black dotted line) and the cleaned Fourier power spectrum (red solid line) of these additional measurements. The dirty power spectrum shows a signal on just the orbital frequency while the cleaned spectrum shows signals on the orbital frequency and, an additional frequency at around 7.2 cycles per day. Given that this additional signal was not present in the original dirty spectrum, it is likely that the cleaning routine has distributed power incorrectly. Thus, the equivalent width measurements of the high velocity section of the C III line appears to be modulated on the orbital period of RW Sex. These "high velocity measurements" are analysed in more detail, later in this section.

Fig. 3.18 is a plot showing each set of absorption equivalent widths folded on the orbital period of 0.245 days. Unfortunately, none of the ephemeris provided in papers (such as Beuermann *et al.* 1992) were accurate enough to provide absolute phases for

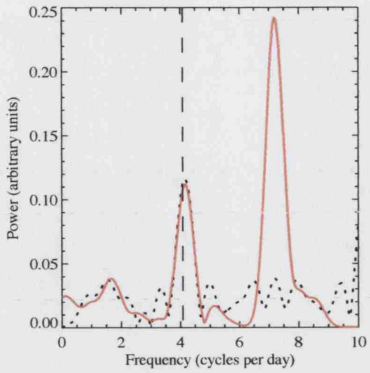

Figure 3.17: Fourier power spectrum of the equivalent width of a section of the FUSE time series, -2000 to -1000 km/s from the central velocity of the C III 1176 Å line. The black dotted line represents the Fourier dirty spectrum and the red solid line represents the cleaned Fourier spectrum (the gain was 0.2 for 200 iterations). The dashed vertical line represent the systems orbital period (0.245 days).

these data, so an arbitrary phase is adopted, where $\phi = 0$ is defined to be the time of the C III spectrum with the maximum line absorption strength. For most lines demonstrated (excluding Lyβ) the pattern demonstrated by the equivalent width measurements is very similar and the amplitude of these variations are similar in magnitude (between 0.5 and 2.4 Å). The pattern of the absorption strength can be broken down into two discrete sections. From $\phi = 0$ to $\phi = 0.6 - 0.7$, the absorption reduces in strength to a minimum at the end of this phase range. Subsequently, from $\phi = 0.6 - 0.7$ to $\phi = 1.0$ the absorption increases again to a maximum at the end of the phase range. There are several key points to be made from these measurements. Firstly, the reduction in strength of the absorption to a minimum is much slower than the subsequent increase in strength. This results in the asymmetric, absorption strength function observed in Fig. 3.18. Secondly, to a good approximation, the reduction in the strength of the absorption and the subsequent increase occurs linearly for all lines apart from O VI 1038Å. The reason for the non-linearity of the O VI absorption changes is probably due to the line becoming extremely deep and saturated. Thirdly, there is no detectable phase lag between absorption strength functions for any of the measurement sets shown.

Fig. 3.19 is a plot comparing the equivalent width measurements taken from C III 1176 Å line, from the -2000 to -1000 km/s velocity range and the -1000 to 0 km/s velocity range.

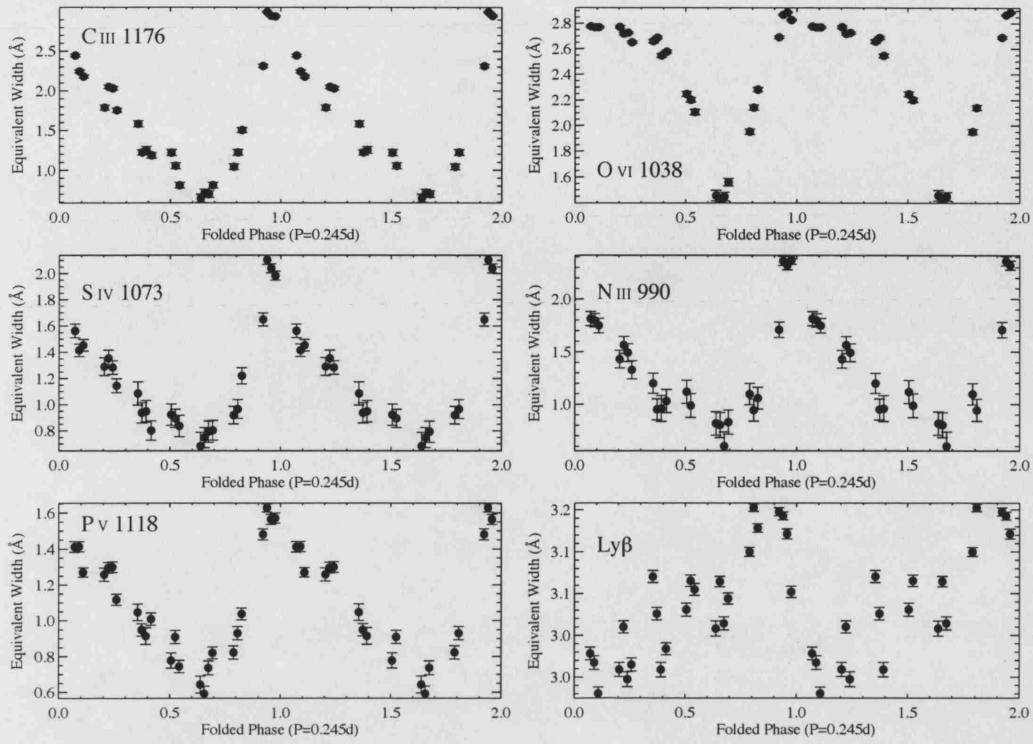

Figure 3.18: Absorption equivalent widths for key FUSE lines, folded on the spectroscopically determined orbital period and repeated for two cycles. $\phi = 0$ has been defined to be the time of the C III spectrum with the maximum line absorption strength.

The measurements have been been folded on the spectroscopically defined orbital period and $\phi = 0.0$ has been defined as in Fig. 3.18. The measurements from the higher velocity range (-2000 to -1000 km/s) almost appear to be a mirror image of the measurements from the low velocity range (-1000 to 0 km/s). For example, from $\phi = 0$ to $\phi = 0.65$ the absorption in the low velocity range decreases in strength (as described earlier) but in the high velocity range, an increase in absorption strength is seen over the same phase range. Similarly, from $\phi = 0.65$ to $\phi = 1.0$ the absorption in the low velocity range increases in strength to a maximum while the absorption in the higher velocity range decreases to a minimum. Interpretation of this behaviour is difficult without having a clear idea of the method of accelerating the wind. If a monotonic velocity law was assumed (as it has been previously in this chapter) then it would suggest that these measurements have sampled the same mass of wind at two locations from the disc. However, it has yet to be confirmed that the monotonic velocity law is the correct prescription for what is being observed so

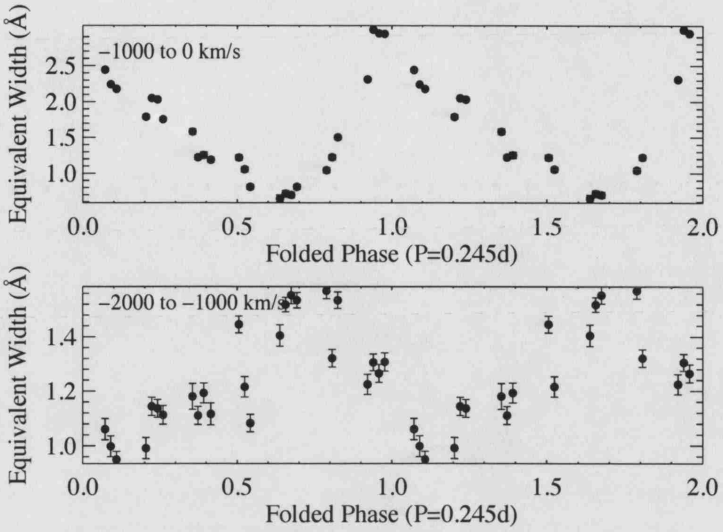

Figure 3.19: Absorption equivalent width measurements for two velocity ranges with respect to the C III 1176Å line; -2000 to -1000 km/s and -1000 to 0 km/s for comparison. The measurements have been folded on the spectroscopically determined orbital period and repeated for two cycles. $\phi = 0$ has been defined to be the time of the C III spectrum with the maximum line absorption strength (for the -1000 to 0 km/s range).

further interpretation would be mere speculation, without more information.

The equivalent width measurements of the blue-shifted absorption have provided additional proof that the strength of the absorption is orbitally modulated. The strength of the absorption varies approximately linearly, with a decrease in absorption strength to a minimum taking around $\Delta\phi \approx 0.6$, followed by an increase in absorption strength to a maximum, taking $\Delta\phi \approx 0.4$ (for the arbitrary phasing shown). This behaviour is repeated in all lines analysed and there is no apparent phase lag between them.

3.5.7 The Changing Morphology of the Blue-Shifted Absorption

Figs. 3.20, 3.21 and 3.22 are plots demonstrating the morphology of the C III, S IV and O VI lines. For the plot of the O VI lines, a particularly large section is shown so that the morphology of the Lyβ can be seen. Each figure consists of two panels, a left one and a right one. The right hand panel of each plot is the greyscale representation of the spectra, normalised by the overall mean of the time-series. In these greyscale plots, the black areas represent flux deficit and the white areas represent enhanced flux, with

respect to the mean profile. The horizontal black bars are the gaps in the data and it can be seen from this that there are seven distinct bands of data across the whole cycle. For each band of data shown in the greyscale plot, the mid point phase was determined and the mean of the spectra within the band was calculated; the resulting seven mean spectra are plotted in the left hand panels with their continuums shifted to the relevant mid-point phases (the mean spectra shown for the O VI line were normalised by the mean for contrast reasons). This method was used to display the data because plotting all 25 spectra would've resulted in a figure which is difficult to interpret and binning the data within specific phase bands would not have represented the data correctly, given the spread of the data along the orbital cycle. In all plots, $\phi = 0$ is defined as the time of the C III 1176 Å spectrum with the maximum line absorption strength.

Fig. 3.20 clearly shows how the morphology of the C III 1176 Å line changes as RW Sex rotates. $\phi = 0$ was defined as when this line shows the strongest absorption and from this plot it is clear that this is the case. Between $\phi = 0$ to $\phi = 0.3$, the absorption broadens as the blue edge moves to slightly more negative velocities and the red edge moves slightly closer to the line centre. During this time, the absorption becomes shallower as the blue and the red edges of the profile become less steep; the absorption is observed to decrease in strength during this time. From $\phi \sim 0.3 - 0.6$ the blue edge of the absorption trough remains relatively static while the red edge moves to more negative velocities, resulting in the absorption becoming even weaker. Some of the greatest changes to the absorption profile are observed between $\phi = 0.6$ and $\phi = 0.9$. From $\phi = 0.6$ and $\phi = 0.7$ the blue edge of the absorption suddenly becomes much shorter and the red edge becomes much longer; this gives the impression that the whole absorption has shifted significantly to more negative velocities. However, from $\phi = 0.7$ and $\phi = 0.9$ the C III absorption appears to return to a shape and strength very similar to the profile at $\phi = 0.6$.

Figs. 3.21 and 3.20 demonstrate the orbitally modulated morphology of the S IV doublet at 1063 and 1073 Å, and the O VI doublet at 1032 and 1038 Å, respectively; the Lyβ line is also shown in the second of the two figures. The observed changes to the morphology of these five lines is consistent with the description of the changes provided for the C III line and importantly they are still within phase. These plots do provide important insights to the changes that occur to the blue-shifted absorption during the orbital cycle but they are limited in their usefulness because firstly, the absolute phase of the system is not known, and secondly the driving mechanism for the wind is unknown.

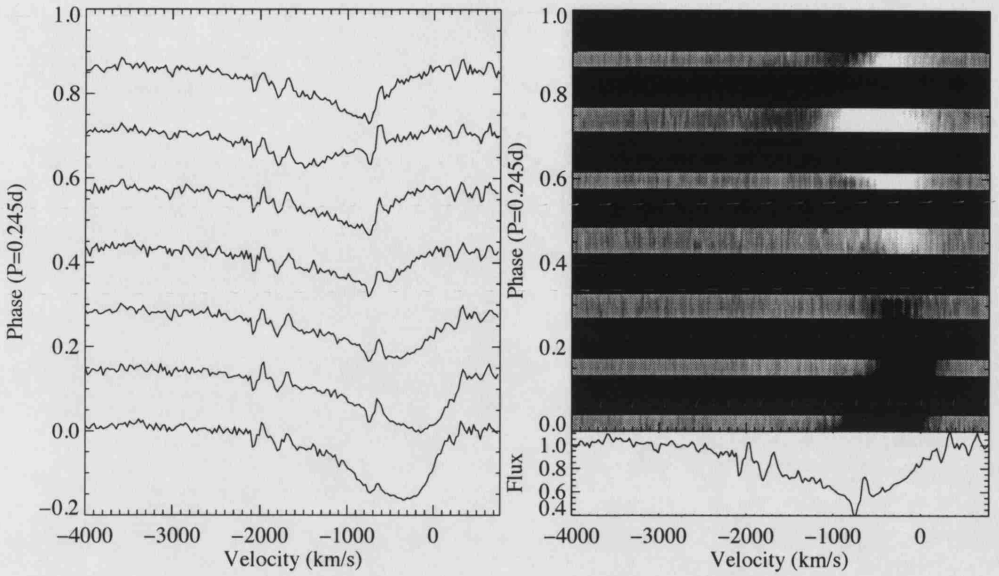

Figure 3.20: Plots showing the characteristics of the orbitally modulated behaviour of the C III 1176 Å line. The right hand panel shows the greyscale representation of the spectra, where each spectrum has been normalised by the mean of the whole time-series. The white areas represent enhanced flux and the black areas represent reduced flux, with respect to the mean profile. The black horizontal bars are gaps in the data, leaving seven distinct data bands. The mean spectrum and mid-point phase has been calculated for the relevant spectra in each of these data bands and the results are shown in the left hand panel. $\phi = 0$ is defined as the time of the C III 1176 Å spectrum with the maximum line absorption strength.

Assumptions can be made about the latter but for these plots to become extremely useful it is necessary to know the location of the components of the system (e.g. the secondary star and the accretion stream) at any given time and this cannot be determined without additional observations.

3.5.8 Analysing the Behaviour of the Absorption Velocity

It is useful to have information about the changing velocity of the blue-shifted absorption as it reveals further aspects about the behaviour of the outflow. One method for measuring this velocity would be to perform a least-squares fit to the absorption with a Gaussian profile which would then provide information about the central velocity and width (or

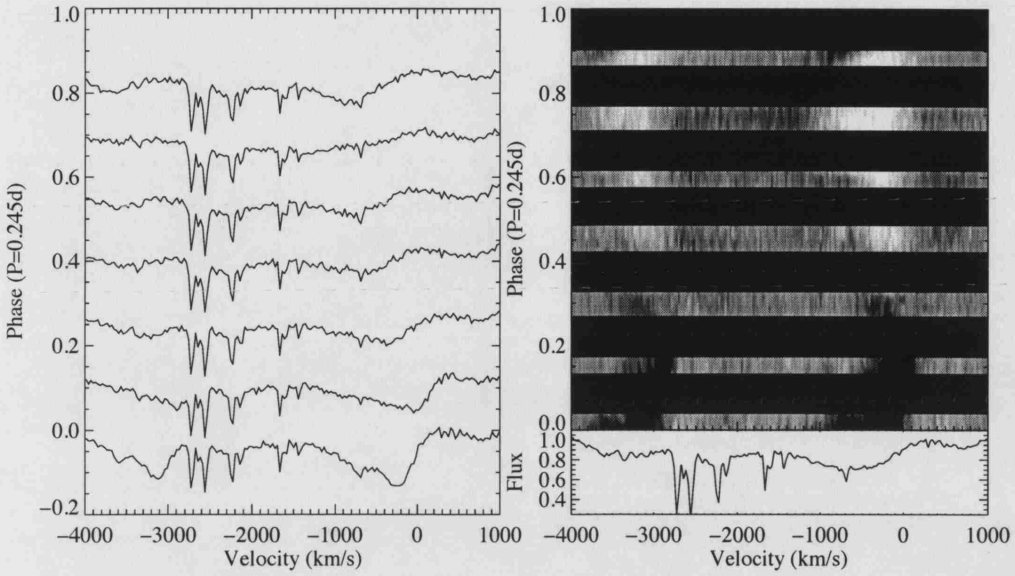

Figure 3.21: Plots showing the characteristics of the orbitally modulated behaviour of the S IV 1073 Å line (the S IV 1063 Å line can be seen at ~ -2800 km/s). The right hand panel shows the greyscale representation of the spectra, where each spectrum has been normalised by the mean of the whole time-series. The white areas represent enhanced flux and the black areas represent reduced flux, with respect to the mean profile. The black horizontal bars are gaps in the data, leaving seven distinct data bands. The mean spectrum and mid-point phase has been calculated for the relevant spectra in each of these data bands and the results are shown in the left hand panel. $\phi = 0$ is defined as the time of the C III 1176 Å spectrum with the maximum line absorption strength.

velocity spread) of the absorption. This method was tried but it was found to be very unreliable in the sense that the input parameters had to be very heavily constrained before the absorption would be found by the routine. The other major flaw with this method was that the resulting Gaussian profiles did not represent the profiles accurately; the vastly inconsistent absorption shape described in § 3.5.7 reveals why this is the case. Instead of attempting to fit a Gaussian profile to the absorption, the velocity of the deepest point of the absorption was measured using a simple search routine. Although this method does not provide the width of the profile as well as the velocity, it was inherently more stable to the changing profile shape and it did not make any assumptions as to the shape of the absorption. These measurements hereafter referred to as v_{abs} were made for C III 1176

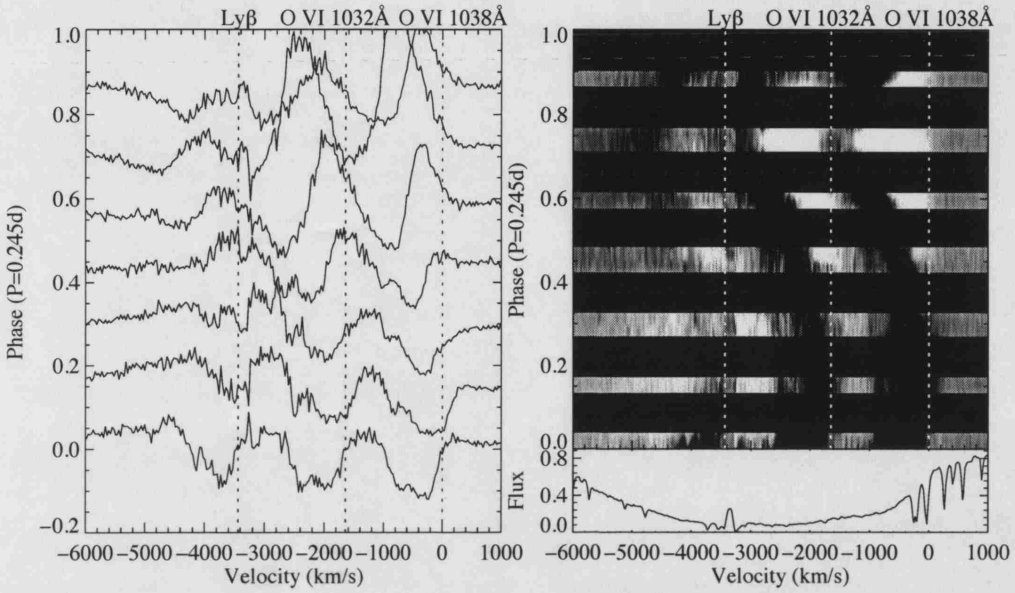

Figure 3.22: Plots showing the characteristics of the orbitally modulated behaviour of the O VI 1038 Å line. The right hand panel shows the greyscale representation of the spectra, where each spectrum has been normalised by the mean of the whole time-series. The white areas represent enhanced flux and the black areas represent reduced flux, with respect to the mean profile. The black horizontal bars are gaps in the data, leaving seven distinct data bands. For each of these data bands, the mean profile was calculated and the mid-point phase was determined; the results are plotted in the left hand panel. $\phi = 0$ is defined as the time of the C III 1176 Å spectrum with the maximum line absorption strength. The dotted vertical lines in both plots indicate the rest velocities of the O VI lines and the Lyβ line

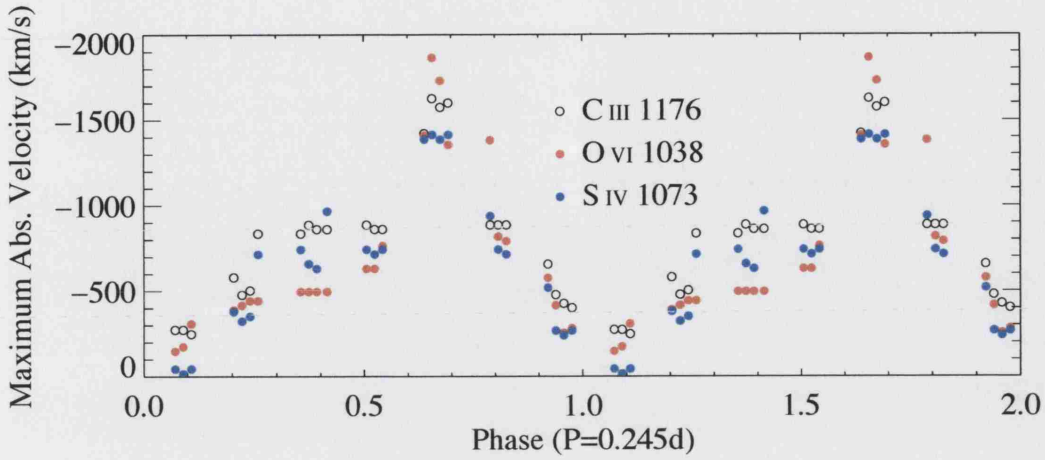

Figure 3.23: v_{abs} plotted against orbital phase (P=0.245d) for C III 1176 Å, O VI 1038 Å, and S IV 1073Å. $\phi = 0$ has been defined as the time of the C III 1176 Å spectrum with the maximum line absorption strength.

Å, O VI 1038 Å, and S IV 1073Å.

Fig. 3.23 is a plot of v_{abs} for C III 1176 Å, O VI 1038 Å, and S IV 1073Å, folded on the orbital period of RW Sex (P=0.245d) and repeated for two orbits; $\phi = 0$ has been consistently defined as the time of the C III 1176 Å spectrum with the maximum line absorption strength. The non-sinusoidal, cyclic variations to v_{abs} are well matched by all three ions; it has been consistently found that there is little difference to the behaviour of the blue-shifted absorption between any of the key lines. The amplitude of v_{abs} for P V is slightly greater ($\sim$ 1700 km/s) than for C III and S IV ($\sim$ 1400 km/s) although it is unknown why this would be the case. However, these amplitudes are still between seven and nine times greater than the amplitudes of $v_{absorption}$ and $v_{emission}$ for the Balmer lines ($\sim$ 200 km/s), as recorded by Beuermann *et al.* (1992).

One observation of Fig. 3.23 is that the point of maximum v_{abs} occurs at between $\phi = 0.6$ and $\phi = 0.7$ which is the approximate time when the equivalent width of the absorption reaches a minimum (see Fig. 3.16). This would infer that the velocity of the deepest point of the absorption and, the equivalent width of the absorption are somehow correlated in their behaviour. Fig. 3.24 is a plot of the equivalent width measurements against v_{abs} for the three ions to test whether there is in fact a correlation in the behaviour of the two values. There is some scatter to the measurements in Fig. 3.24 but overall there does appear to be a correlation between the equivalent width and v_{abs} whereby the latter

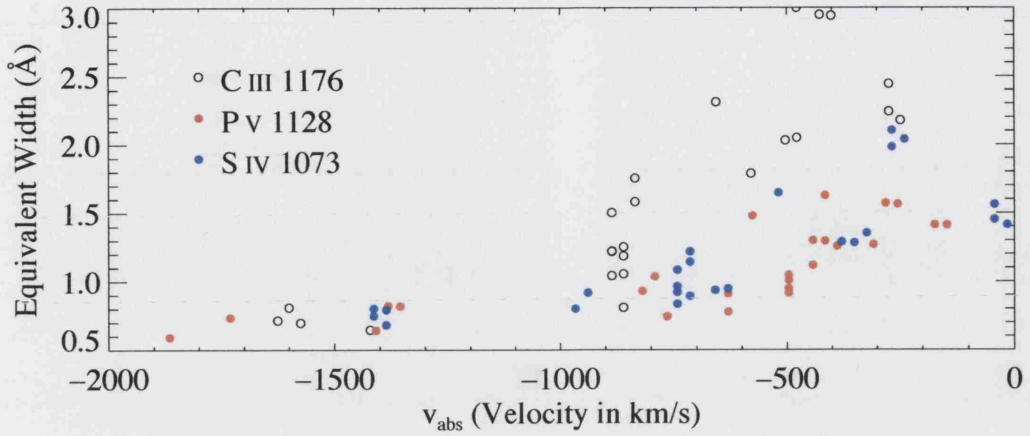

Figure 3.24: v_{abs} in km/s, plotted against equivalent width in Å, for C III 1176 Å, O VI 1038 Å, and S IV 1073Å.

is least negative when the former is strongest (there is some degree of curvature to the correlation which suggests that a linear solution would not be accurate).

The excellent correlation in behaviour between different ions and, the changing velocity of the blue-shifted absorption is shown for the entire wavelength range in Fig. 3.25. This plot is a greyscale representation of the time-series, which has been folded on the orbital period and $\phi = 0.0$ has been defined as before. The plot is similar to that of Fig. 3.21 in that the spectra have been normalised by the mean and the spectra have been folded on the orbital period but, unlike Fig. 3.21, the gaps in the data have been linearly interpolated across, giving a slightly artificial but clearer view of the absorption behaviour. The repetition in behaviour of all of the spectral lines visible in the spectrum (including the Lyβ line) is astounding. The same modulated variation to the absorption is observed, in phase, for every ion. The point of highest v_{abs} and lowest equivalent width (at $\phi = 0.7$ or $\phi = 0.7$) can also be seen quite clearly; at that time the absorption seems to extend to the greatest velocity but there also seems to be the greatest amount of flux excess.

In this section, further characterisation of the orbitally modulated changes of the blue-shifted absorption have been provided through the measurement of v_{abs} (the velocity of the deepest point of absorption). The excellent agreement between all the ions has been further demonstrated, along with the discovery that the equivalent width and v_{abs} are inversely correlated. In this study of the absorption there is little more information that can be easily extracted from this FUSE data. In the following section (§ 3.6), the analysis

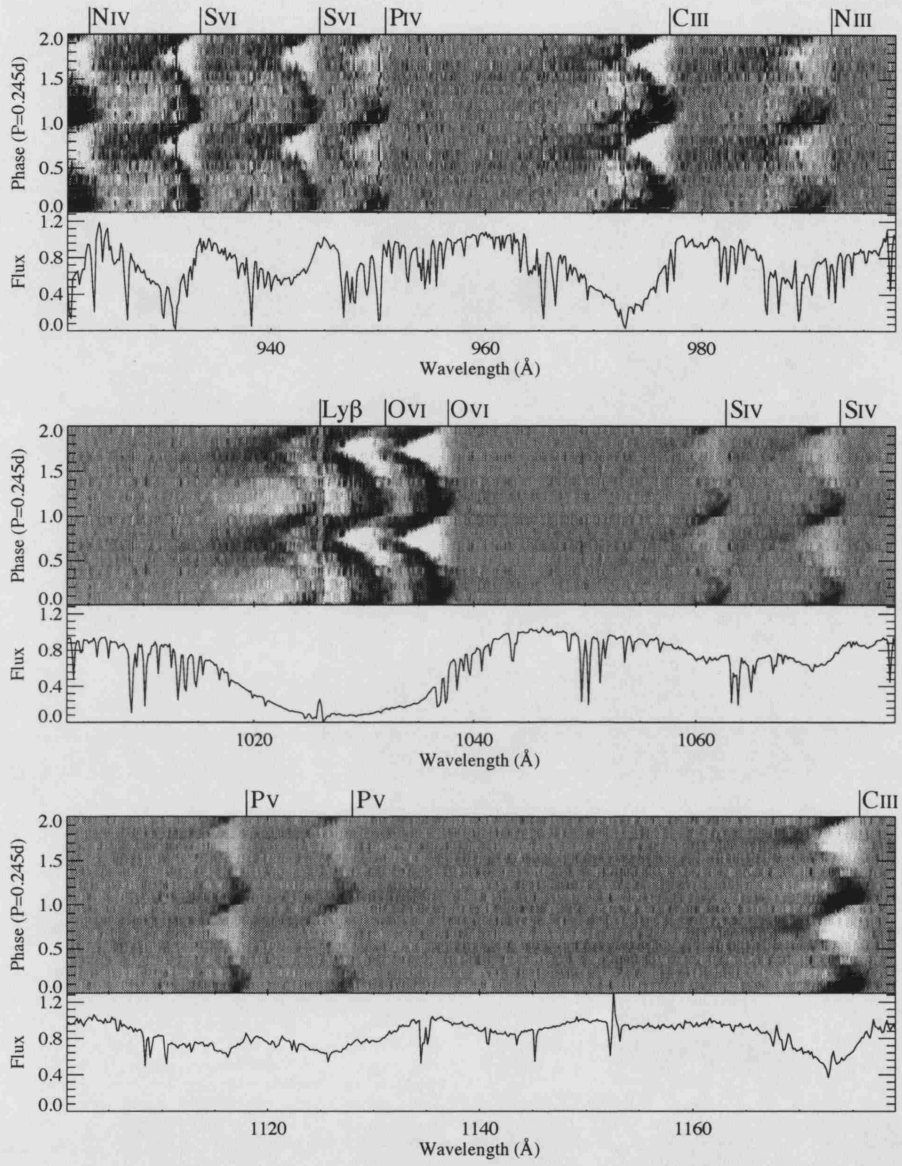

Figure 3.25: A greyscale representation of the entire FUSE time-series, folded on the orbital period of RW Sex (P=0.245d) and repeated for two cycles. The spectra have been normalised by the mean spectrum to demonstrate the changes to the absorption (black for a deficit in flux and white for enhancement of flux, with respect to the mean) and the data gaps have been linearly interpolated across.

of the HST time-series is presented.

3.6 Analysis of the HST Time-Series

The HST time-series (described in § 3.4.2), which was secured using the GHRS instrument, covers a longer wavelength range than the FUSE time-series. This means that the study into the accretion disc wind can include the additional UV resonance lines in that range. The HST observations were also secured 5 years earlier than the FUSE observations so it becomes possible to test whether the observed variations continue over different epochs. Unfortunately, the HST time-series only extends for 36% of an orbital period and RW Sex was only exposed for 41% of that time so the extent to which the orbital modulation can be analysed is limited. However, the HST time-series was originally acquired to search for small-scale structure in the wind so it has a good temporal resolution and a high signal-to-noise; in this section, a brief search to look for this small scale structure is presented.

Fig. 3.26 is a plot of the mean flux calibrated GHRS spectrum of RW Sex. The TUES spectrum shown in Fig. 3.4 was observed in the same year as this HST time-series and it overlaps in spectral range with the 'blue' sub-exposures so it is a useful comparison with which to start this analysis. It is comforting to find that across the overlapping wavelength range the continuum luminosity is well matched between the two data sets. As might be expected given the observations of the blue-shifted absorption in the FUSE time-series (see § 3.5) it is unsurprising to find some variations between the mean absorption profile in the TUES and HST time-series (for example, the Lyα absorption is much stronger in the HST spectrum than it is in the TUES spectrum) although some differences are as a result of different resolutions and signal-to-noise levels. The spectral range of the short-wavelength spectrum of IUE is also large enough to encompass both the red and the blue sub exposures of the HST time-series and so some comparison can also be made with that data (see § 3.3.2, the comparison is made with Fig. 3.2). The two spectra do not compare as well as the TUES and HST spectra; the IUE spectrum is noticeably weaker and the C IV profile is less pronounced. Since the IUE spectrum was observed 12 years before the HST time-series and cataclysmic variables are by their very nature variable, these differences are not unexpected.

Fig. 3.27 is a demonstration that the blue-shifted absorption is just as variable in

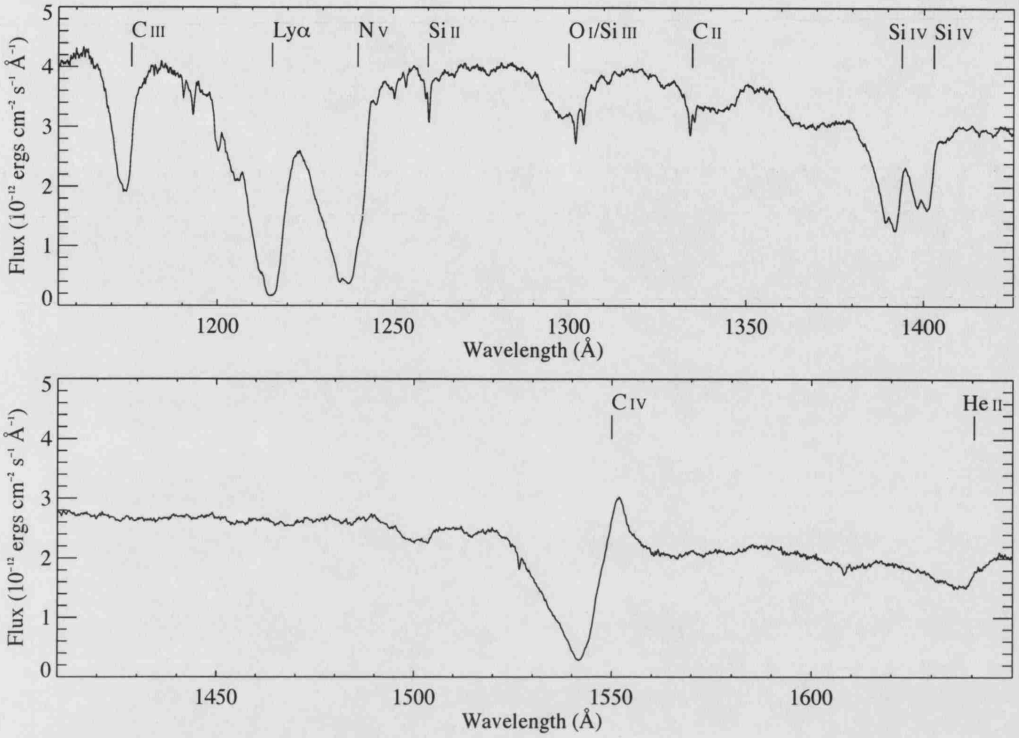

Figure 3.26: A plot of the mean flux calibrated spectrum of RW Sex from the HST time-series taken in 1996. The top panel shows the mean spectrum from the 'blue' sub-exposures and the bottom panel shows the mean spectrum from the 'red' sub-exposures. The main wind diagnostic lines have been identified.

this HST time-series as it is in the FUSE time-series; the figure shows simultaneous variations in the C III 1176 Å line and the Si IV 1400Å doublet. The behaviour of the two lines between the two spectra is relatively similar in that we see the absorption move significantly red-wards over a period of 1.3 hours but while the C III absorption seems to undergo a significant increase in strength during this shift to less negative velocities, the Si IV lines do not (at least not on the same scale). Fig. 3.28 similarly demonstrates large scale variability to the C IV 1550 Å line. The left hand panel shows that the variability of the absorption is enormous and significant changes are observed to the overall profile (over a 1.7 hour period). The right hand panel shows two spectra which are much less separated in time ($\sim$ 19 minutes). The purpose of this plot is to show that although there is a marked increase in the absorption strength and position between the two spectra, the emission seemingly remains static (in both velocity and strength). The lack of correlation in behaviour between the absorption and the emission suggests that the emission actually

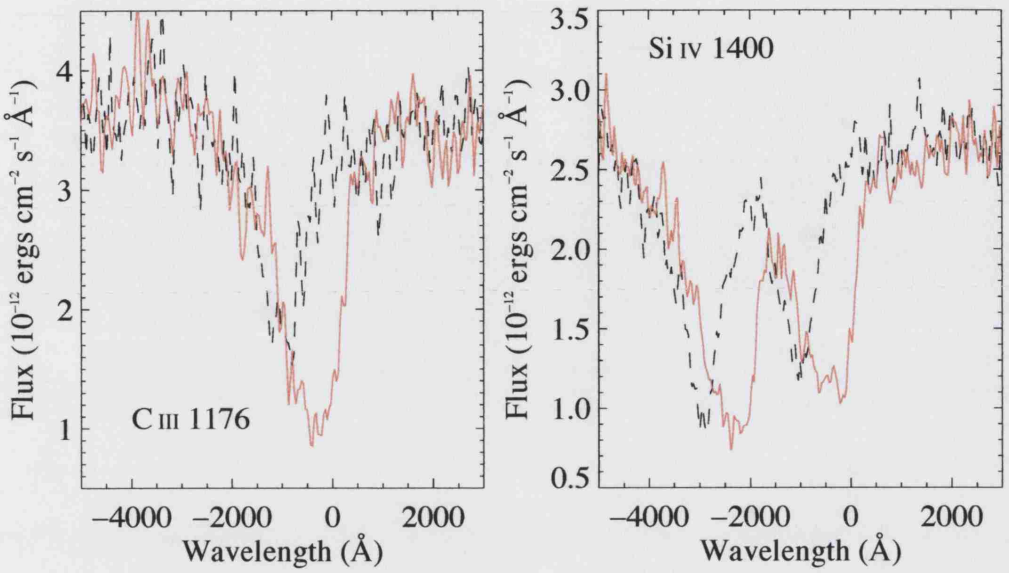

Figure 3.27: Pairs of HST spectra showing the simultaneous variations in the C III 1176 and Si IV 1400 profiles; the two spectra (black dashed line and red solid line) are separated in time by ~1.3 hours. The velocity scale of the Si IV doublet is based on the red-ward 1402.77 Å line.

originates from a non-scattering source (perhaps thermal) close to the accretion disc. The large scale, probably orbitally modulated, changes to the blue-shifted absorption are further demonstrated in a greyscale plot of the data (see Fig. 3.29). Large scale variability in the absorption is observed for many but, not all of the lines (e.g. Si II 1260Å, O I/Si III 1300Å and C II 1335Å). Since these non-varying lines are also relatively narrow and not shifted in velocity space, it is likely that they are formed close to the accretion disc, before the wind actually begins (e.g. an accretion disc photosphere).

The existence of the large scale variations to the blue-shifted absorption is consistent with the analysis of the FUSE data but the way that they vary is actually different. It can be seen in Figs. 3.27 and 3.28 that the absorption appear to become stronger as it heads towards lower velocities which is the opposite to what was analysed in considerable detail § 3.5.8. Unfortunately, the relatively small phase coverage means that this data set is unlikely to yield the reasons for these differences and indeed, any more information about the orbital modulated behaviour of the blue-shifted absorption. What this time-series can provide that the FUSE time-series couldn't, is high temporal resolution data which allows for the search for variability on a short time-scale. A search through the blue and the red

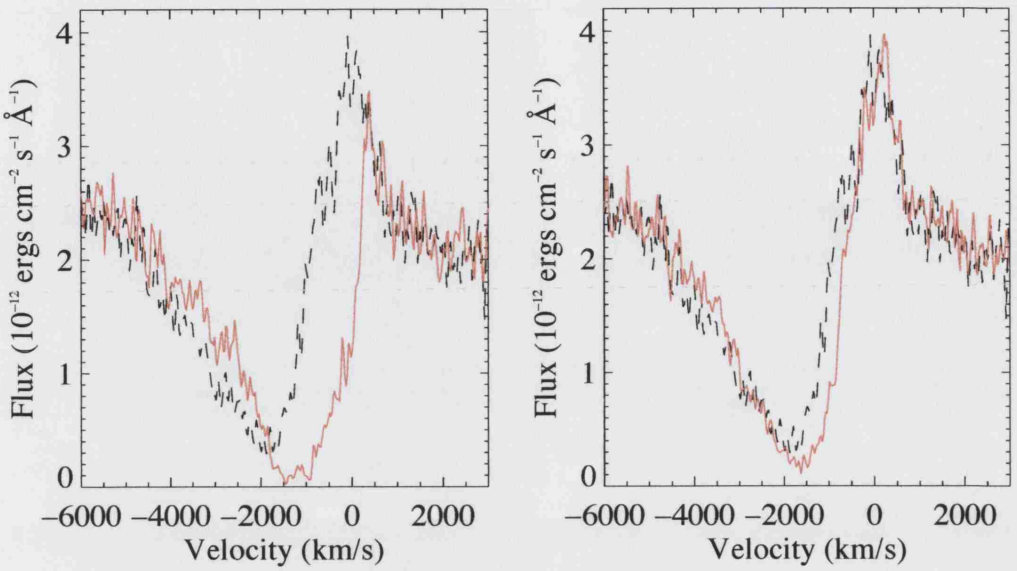

Figure 3.28: Pairs of HST spectra demonstrating large scale variations to the C IV 1550Å line. The two spectra in the left plot are separated in time by ~ 1.7 hours while the two spectra in the right panel are separated in time by ~ 19 minutes. The black dashed spectrum is identical between the left panel and the right panel.

channel reveals that the absorption of the wind diagnostic lines is highly variable on short time-scales. In the red channel, small fluctuations are observed in the absorption of the C IV 1550 Å doublet but unfortunately the two lines of the doublet are too close together to easily confirm these small variations and the He II line is not strong enough for those small variations to be detectable. Small fluctuations are also observed in the resonance lines of the blue channel and lines are more favourable for a comparative check to be made. In particular, the Si IV 1400Å doublet shows multiple simultaneous rapid fluctuations to the line profile; Fig. 3.30 demonstrates this by displaying two different views across the same data. In the left panel, three consecutive plots of the Si IV doublet are shown; the time frame starting at t=0 is based upon the first spectrum selected (black-dashed line). Within ~ 30 seconds, a small flux enhancement has formed at ~ -750 km/s and a flux deficit has occured, centered on ~ -250 km/s, simultaneously in both lines of the doublet. Individually, the two regions undergo a $\sim 20\%$ change in the mean flux but collectively there is no overall change. These fluctuations are also shown on the right hand panel, which is a greyscale (colour enhanced) view of the silicon lines, around about the time

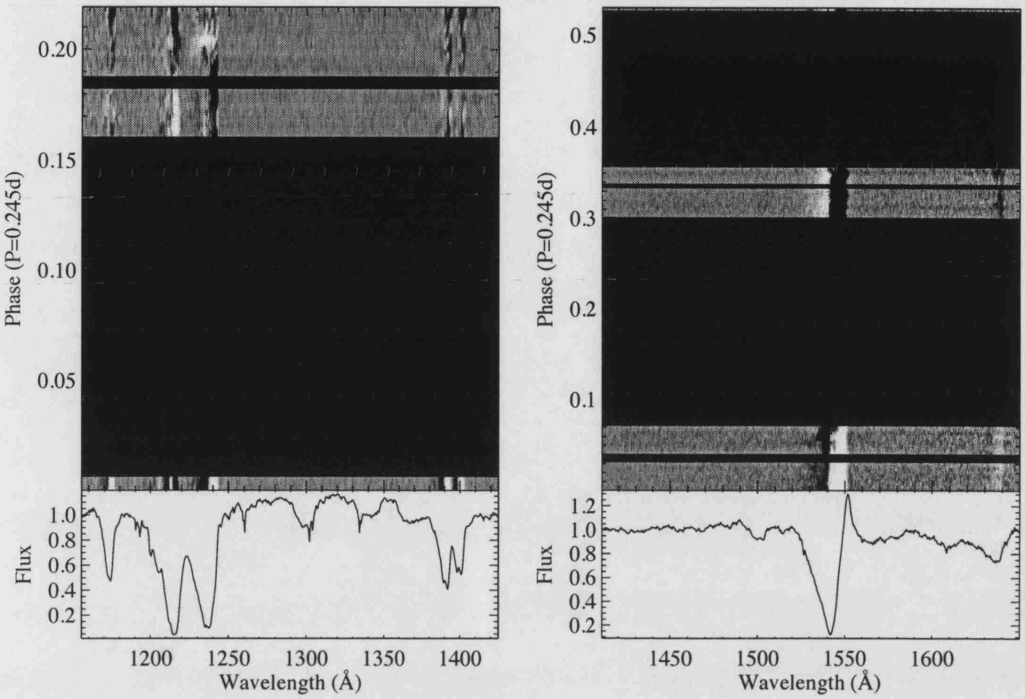

Figure 3.29: Greyscale represensations of the HST time-series of RW Sex for the blue (left panel) and red (right panel) channels. The data has been phased on the orbital period of RW Sex (0.245 days) and has been ratioed with respect to the mean profile. In the greyscale plot, black represents flux deficiency and white represents flux excess with respect to the mean profile. The black horizontal bands are due to gaps in the data over the phase regions. For each plot, $\phi = 0.0$ has been defined as the first spectrum in the selected time-series.

of the spectra in the left hand panel (they have been indicated with horizontal, black, dashed lines). These specific enhancements in flux can be clearly seen, along with other, multiple fluctuations in the absorption shape observed simultaneously in both lines (of special note is the sudden reduction in the absorption width from t=0.016 onwards).

Given that the greyscale view of the Si IV doublet in Fig. 3.30 covers only $\sim$ 18 minutes, the degree and numeracy of the fluctuations to the absorption would suggest that the wind of RW Sex is very unsteady on short time-scales. No evidence could be found in this time-series, that the observed fluctuations are regular in any way but, even with the impressive time sampling of this data, it is difficult to track the individuals features of the absorption. Thus, without further evidence to the contrary, these fluctuations are thought to relate

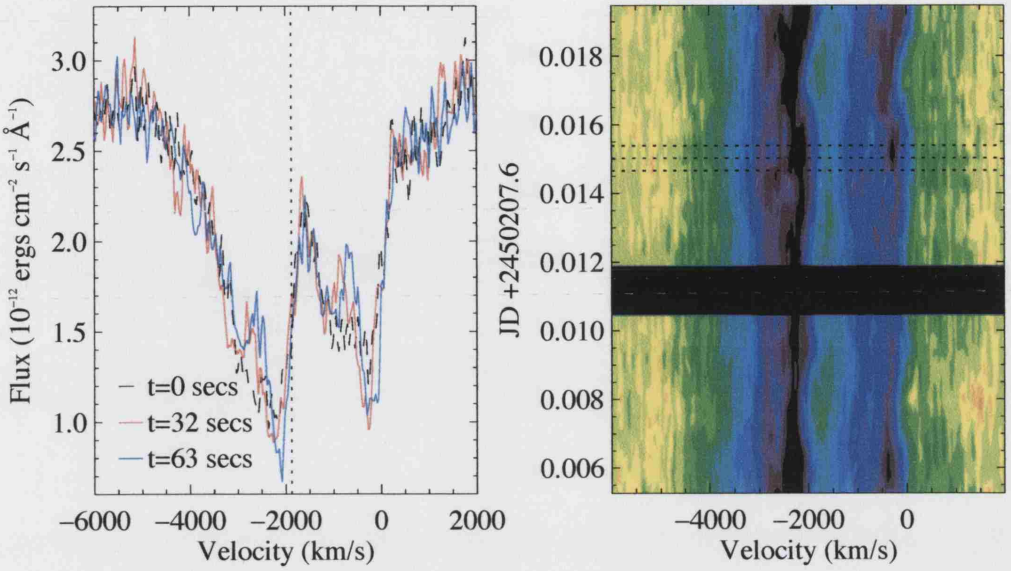

Figure 3.30: Plots demonstrating the rapid fluctuations of the Si IV 1400Å doublet. The left hand panel contains three consecutive spectra of the Si IV doublet, showing an example fluctuation in the blue-shifted absorption. The right hand panel shows the greyscale view of the Si IV doublet around the same time as the three consecutive spectra of in the left hand panel (the position of the three spectra is shown as horizontal dashed black lines). In this colour enhanced plot, black represents absorption and red/white represents emission.

to stochastic processes.

3.7 Discussion

Using UV and far-UV spectroscopy, the line profile characteristics of RW Sex has been established. The measurements show that for multiple wind diagnostic lines, a strong, blue-shifted absorption is observed which most probably originates from some kind of disc outflow (to be discussed later in this section). The observations paint a picture of an outflow which is variable on two different time-scales. On time-scales as small as 30 seconds (and maybe even smaller), apparently stochastic processes result in enhances and deficits in the flux strength at numerous points in the absorption trough. On longer time-scales there is the orbitally modulated (P=0.245d) behaviour of the absorption, resulting in significant changes to the strength and velocity which are consistently observed and

repeated in every observable outflow driven line. No evidence was found to suggest that the observed changes were due to contamination from a varying (in flux, radial velocity, or both) emission source, localised to the accretion disc.

The dominance of absorption features in the UV spectrum of RW Sex is consistent (from observations of other systems and models such as Knigge *et al.* 1995) with the general belief that it is a low inclination system; the lack of observed eclipsing for this system provides further evidence of this fact. This is an important constraining factor to the disc wind because for the observed orbital modulation to occur for an essentially face on disc, there must be a significant break in the axi-symmetry which must present itself through the column of outflow that the observer is looking through, as the system rotates.

The dwarf novae YZ Cnc (in outburst), was one of the first CVs in which the ultraviolet resonance lines were observed to be strongly varying in a periodical way. Drew & Verbunt (1988) described observations showing this phenomenon and hypothesised that a break in axi-symmetry could occur if the hot inner disc region is not rotationally symmetric or the outflowing wind makes an angle with the normal to the accretion disc. The solution to the latter of these two concepts would be to have the outflow seated on a warped or tilted disc. Thus, if there was a degree of collimation to the outflow, the resulting absorption may show orbital modulation in strength and velocity.

Having the outflow seated on a warped or tilted disc is a sensible solution to the observations but it is not flawless. One potential problem arises with the phenomenom of superhumping. Superhumps are best explained as the beat between the orbital period and the precession of the accretion disc; either apsidal precession in the case of positive superhump, where the photometrically determined period is slightly longer than the spectroscopically determined orbital period, or nodal precession in the case of negative superhumps, where the photometrically determined period is slightly shorter than the spectroscopically determined orbital period. Positive superhumps are believed to occur when an accretion disc extends beyond the radius at which the Keplerian period is one third of the orbital period. When this happens the disc becomes eccentric and undergoes a slow prograde precession and the relative positions of the secondary star and eccentric disc repeat on a period slightly longer than the orbital period i.e. the positive superhump period. In contrast, negative superhumps are thought to arise from a warped or tilted accretion disc (Patterson *et al.* 1993), which results in a nodal precession; so far,

no negative (or positive) superhump period has been detected for RW Sex. It would not be true to say that because no superhump period has been detected for RW Sex, it does not possess a warped or tilted disc but, assuming that negative superhumps do arise from such systems, it means that one potentially useful piece of evidence is not present.

With the outflow seated on a warped or tilted disc, it has already been mentioned that to produce the observed changes to the absorption as the system rotates would require there to be a certain degree of beaming/collimation of that wind. Thus, if as might be expected that the tilted section of the disc undergoes nodal precession, then it might also be expected that the wind would show evidence of that precession in the form of a negative superhump period; this has been found in the case of precessing jets for systems such as SS433 (Abell & Margon 1979). The question must arise from this as to whether the FUSE or HST time-series are suitable for distinguishing between a negative superhump period and the true orbital period. Although there is no known negative superhump period for RW Sex, one could be estimated based on the negative superhump detected for another system; for V592 Cas the negative superhump period is $\sim$ 3 % less than the orbital period which when translated to RW Sex would result in a negative superhump period of 0.238 days which corresponds to 4.2 d^{-1}, compared with 4.1 d^{-1} for the spectroscopically determined orbital period. It is possible to estimate the ability of a data set to resolve such differences (taking into account not only the temporal resolution but also the length of the time-series) by measuring the FWHM of the signals in the Fourier power spectra derived from the data. In the case of the FUSE time-series, measurements from the Fourier power spectra presented in Fig. 3.16 reveal a FWHM of 0.71 d^{-1} which clearly indicates that the FUSE data simply does not have a sufficiently long baseline to distinguish between the orbital period and a superhump period. With a temporal resolution of as low as $\sim$ 30 seconds, the HST time-series has good enough time-sampling to distinguish the two periods but it unfortunately lacks the phase coverage. What this means for RW Sex is that the wind may still be modulated on a negative superhump period but it cannot be confirmed whether this is the case or not with the data presented in this study. It should be made very clear that although some references have been made with respect to a collimated flow and jets, it is in no way being suggested that the disc wind of RW Sex is in fact a jet (although there may be some connection between the two); CVs remain the only accretion disc setting in which jets have not been discovered and a recent study of RW Sex by Hillwig *et al.* (2004) in

the search of satellite features to stellar lines (indicative of jets) found no such evidence.

Before the tilted disc theory can be accepted as a possible scenario for RW Sex, it must first be asked whether it is actually possible to create a tilted disc, how the tilt is formed and whether it is a stable feature of the disc. Pringle (1996) hypothesised that an accretion disc may be warped by radiation from the central source if the disc is not illuminated in a uniform way. Such a situation is suitable for systems with strong central sources such as active galactic nuclei and X-ray binaries (where warped discs are generally accepted) but cataclysmic variables struggle to provide an efficient enough accretion process to make this work; it would require an extremely efficient accretion process and a particularly large disc making this scenario highly unlikely (Ogilvie & Dubus 2001). Murray & Armitage (1998) used smoothed particle hydrodynamics to test whether gravitational tilt instabilities can grow fast enough in the accretion disc fluid so as to create a measurable tilt in the disc but they conclude from their results that it is not possible.

Lai (1999) provide a solution to the tilted disc problem in the form of magnetic fields. They showed that the magnetic field of a sufficiently magnetised central object can induce warping in the accretion disc and make it precess around the spin axis if the magnetic dipole is inclined to the system plane; the magnetic field strength of the white dwarf in a non-magnetic cataclysmic variable is still relatively high compared to many astrophysical situations ($B \leq 10^5 G$ compared with $B \sim 1500G$ for sunspots). The only problem with this idea is that the white dwarf typically spins several times faster than the orbital system so it may be expected that the observed modulation is on the white dwarf rotation period. If the warping of the disc is instead induced by the magnetic field of the secondary star, as suggested by Murray *et al.* (2002), then because the secondary star is tidally locked and co-rotates with the system, the modulated variability may in fact be on the orbital period (or a negative superhump period assuming that nodal precession would still occur).

The tilted disc scenario not only explains the general orbital modulation of the disc wind, it also provides a possible reason why the equivalent width and velocity measurements were variable in the way observed for the FUSE resonance lines. It is first assumed that the disc outflow is monotonically increasing along the radial distance. At the starting phase, the viewing angle through the disc outflow material is such that only the very lower sections of the disc wind are projected against the UV emitting inner disc; see the left hand diagram in Fig. 3.31. At this phase, only the low velocity portions of the outflow are seen and the observed optical depth (and therefore equivalent width) is at its highest

because the number density of absorbers is likely to be greatest close to the accretion disc. At $\phi = 0.5$ (see the right hand diagram in Fig. 3.31) the high velocity portions of the disc outflow are being seen projected against the inner disc so in the absorption profiles the absorption is seen to move to the blue but the reduced number density of absorbers means that optical depth and therefore the equivalent width is reduced. Again, there are a few flaws with this idea. Firstly, at $\phi = 0.5$ in the simplified model, both the high and low velocity portions of the wind are being observed so significant absorption would still be expected at low velocities and this is not what is seen. This flaw may be resolved with a more complex outlook of the scenario. Secondly, some of the lines such as C III, C IV and Si IV showed much smaller variability in the line strength than some lines such as S IV and P V. A possible resolution to this flaw would be if there was an ion stratification to the outflow, where some ions such as C III, C IV and Si IV were present in large concentrations at all velocities while other ions such as S IV and P V were confined, close to the accretion disc.

There have been many steps to identify the driving mechanism for CV disc winds and many have been based around the idea of line driven winds such as that of Proga (2000) and Long & Knigge (2002). With the idea of a radiation driven wind in mind, the point rises as to whether some of the large scale variability observed along the line profiles can be related to instabilities in line-driven winds. The orbital modulation of the wind driven absorption lines says that this cannot be the mechanism. It is possible that the small scale instabilities observed in the disc wind (features that are typically observable in both lines of the S IV doublet on time scales of less than a minute - see § 3.6) are related to instabilities in the wind due to variability in radiation pressure, outflow density etc. but, this variability would not be expected to be orbitally modulated. However, there are other factors to consider when large and small scale variability are referred to because it is likely that line driving cannot support a CV outflow by itself and other mechanisms such as magneto-hydrodynamics much be taken into account.

The purpose of this thesis is to present a multi-wavelength study of low inclination cataclysmic variable stars. In this chapter the disc wind from RW Sex has been presented using information gathered from far-UV and UV spectroscopy of the system. In the following two chapters, both optical and UV observations of V592 Cassiopeiae are analysed and presented to show the evidence of its accretion disc outflow. In the following chapter, optical observations of a third system, BZ Camelopardalis, are presented and discussed

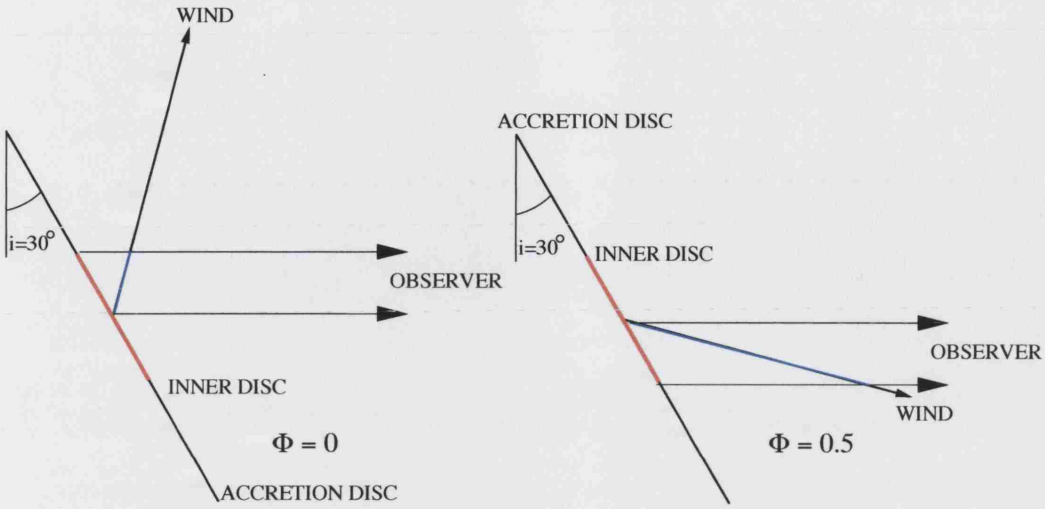

Figure 3.31: A demonstration of the possible explanation to the orbitally modulated change in the equivalent width. The diagrams are simplifications of the accretion disc (solid black line) which is placed at an inclination angle of 30 degrees (within the accepted inclination range for RW Sex). The red, middle section of the disc represents the inner accretion disc from the middle of which the disc outflow originates. The wind is assumed to originate from a tilted inner disc and so it has been placed at an angle of 45 degrees with respect to the orbital plane. The blue, inner section of the wind depicts the range of the outflowing wind which if projected against the UV emitting section of the disc through the observers line of site (indicated). The diagram is drawn for $\phi = 0$ and $\phi = 0.5$.

with respect to its accretion disc wind.

CHAPTER 4

Optical Spectroscopy of V592 Cassiopeiae

The results from an optical study of V592 Cas published in Witherick *et al.* (2003) are presented and greatly expanded upon. The study uses a new optical time-series taken with the 2.3-metre telescope at Kitt Peak National Observatory (or KPNO) in the autumn of 2001.

4.1 Introduction

V592 Cas is a low inclination CV of the sub-group UX UMa; broad Balmer absorption in the spectra is one characteristic of this sub-group. With a V magnitude of $\sim$ 12.7, it is not as bright as RW Sex (see § 3) and as such it has not been studied to the same degree. V592 Cas has, however, remained an object of some interest after the discovery within IUE spectra that it has a disc wind. After an initial literary review of V592 Cas, this chapter concentrates on the optical aspects of the wind by presenting an optical time-series taken with the 2.3-metre Bok telescope at KPNO in October of 2001. In chapter 5 the far-UV aspects of the wind are discussed with the presentation of a new FUSE time-series of V592 Cas.

4.2 Literature Review

On initial discovery, V592 Cas was described as a blue, luminous object and was given the designation LS I +55°8. It was in Greenstein *et al.* (1970) that spectroscopic evidence was presented to suggest that V592 Cas is some type of contact binary star (e.g. broad Balmer lines in absorption with weak emission cores) although it was Warner in (1976) who first proposed that it is a UX UMa type CV. The variable star designation of V592 Cas was introduced by Kholopov *et al.* (1981) after results presented in Africano & Quigley (1978) showed the system to be photometrically variable (by ~ 0.4 magnitudes).

Photometrically, V592 Cas is an interesting system as its light curve shows variability on three periods. The two longest of these periods are the positive and negative superhumps, which are thought to be 2.934 ± 0.001 and 2.686 ± 0.001 hours respectively (Taylor *et al.* 1998). Although the positive superhump was clearly present, the signal indicating the presence of the negative superhump was very weak and it has not yet been confirmed. The third period on which the modulation of the light curve was detected, was a ~ 22 minute period presented in Kato & Starkey (2002), although there has been no additional published attempts that verify this period. The photometric light-curve of V592 Cas shown in Taylor *et al.* (1998) also, did not reveal any detectable eclipse which at the very least confirms that the system is not a high inclination one (i.e. $i \lesssim 70°$).

The orbital period of V592 Cas remains a moot point as radial velocity analysis from time-series spectroscopy has revealed periods of both ~ 2.76 (Taylor *et al.* 1998) and ~ 2.47 hours (from Huber *et al.* 1998); if the latter of these two periods is correct then it brings into question the validity of the negative superhump period. Whichever period is the true one (this is discussed in more detail, later in this chapter) it cannot be ignored that V592 Cas is one of the few systems to be placed inside of the infamous 2-3 hour period gap (see § 1.3.1). Spectroscopy also provides additional evidence of V592 Cas's low inclination in the form of single peaked emission and low radial velocity amplitudes; using the latter parameter, Huber *et al.* (1998) estimate the inclination angle of V592 Cas to be $\sim 28°$ which means that it is nearly face-on. Table 4.2 summarises the orbital and superhump periods.

Although most studies of V592 Cas have used optical data, there have been some studies using data from outside of this band. Ciardi *et al.* (1998) used a spectral energy distribution (or SED) model with near-infrared photometry to determine the contribution

Parameter	Value	Ref.
$P_{\rm orb}$ (spectroscopic)	0.115063 ± 0.000001 or $0.103^{+0.040}_{-0.020}$ days	1/2
$P_{\rm orb}$ (positive superhump)	0.12226 ± 0.00003 days	1
$P_{\rm orb}$ (negative superhump)	0.11193 ± 0.00005 days	1
Inclination Angle	$28^{\circ}{}^{+11}_{-10}$	2

(1) Taylor *et al.* (1998) (2) Huber *et al.* (1998)

Table 4.1: A summary of orbital modulation and the inclination angle of V592 Cas.

of various CV components to the continuum. They found that between the extreme-UV and UV wavelengths, the white dwarf contributed over 50% of the continuum flux (this would be an unusually high contribution from the white dwarf) but, at longer wavelengths the accretion disc dominates; overall the secondary star (with an estimated temperature of 3200K) contributes very little flux. The SED model also inferred an accretion rate of $\sim 10^{-8}$ $M_{\odot}$ yr^{-1} and a distance of 63 parsecs, which is much smaller than the 330 parsecs estimated by Taylor *et al.* (1998).

The first ultraviolet observations of V592 Cas were made with the International Ultraviolet Explorer (IUE) in 1981, as part of a study by Guinan and Sion (of Villanova University) to observe nine, close binary systems containing accretion discs. The disc wind of V592 Cas was discovered in short wavelength spectra by Guinan & Sion (1982) in the form of the characteristic P-Cygni profile, for the C IV resonance doublet and as blue-shifted absorption for the high temperature ions; the degree of variability they saw for the C IV line was significant. Hoare & Drew (1993) later used the IUE observations of V592 Cas to aid in the creation of a grid of photo-ionisation models for the stellar winds of non-magnetic CVs. More recently, V592 Cas has been the subject of a far-UV study into its wind using time-series spectroscopy collected with FUSE; the results of this study are presented in § 5.

4.3 IUE Observations of V592 Cas

A search through the Multi-mission Archive at the Space Telescope Science Institute (or MAST) reveals that only seven exposures were made of V592 Cas with IUE and, they were all taken in low dispersion mode; Table 4.2 summarises these seven exposures.

Data ID	Exp. Time (secs)	Start Time
SWP15658	900	18:48
SWP15658	1800	19:12
SWP15659	3600	21:20
SWP15659	3600	20:16
LWR12085	1680	22:24
LWR12084	1200	19:48

Table 4.2: A summary of the IUE observations of V592 Cas. All spectra were exposed on the 5th December, 1981 using the low resolution modes of the relevant spectrographs.

Fig. 4.1 is a plot of one of the short wavelength IUE exposures (data ID: SWP15659) with several resonance lines marked. The presence of the blue-shifted absorption for each of the marked lines is a strong indication that an outflow is being driven from this system; the C IV 1550Å line is the only observed line with any detectable emission which is the same as was seen for the IUE spectrum of RW Sex (see Fig. 3.2).

Fig. 4.2 is an enlarged view of the C IV 1550 Å profile in velocity space (taken from the short wavelength IUE exposure shown in Fig. 4.1). The red solid line, which has been plotted over the real exposure, is the best fit simulation to the C IV profile using the Sobolev code developed by Drew (1987). The fit is not very good and although the code has been superseded by others (e.g. Long & Knigge 2002), it does demonstrate the difficulty in not only understanding the processes which drive the wind, but also in just simulating the shape of the profile. To fit the profile, it was necessary to set v_{max} to 3500 km/s and, set the inclination to 50°, which is much higher than the angle estimated by Huber *et al.* (1998) ($\sim 28°$) but, it would still class the system as being a low inclination one. This best fit also yielded an estimate of the mass loss, as a product with the C^{3+} ion fraction, of $\dot{m}q \approx 10^{-9}$ $M_{\odot}$ yr^{-1}; unfortunately the C^{3+} ion fraction is essentially unknown.

Although the IUE long wavelength spectra, with a wavelength range of 1900—3300Å, lack the resonance lines from which the disc outflow can be examined, the presence of a relatively strong 2200 Å interstellar absorption feature does allow the interstellar extinction towards V592 Cas to be estimated (see Fig. 4.3). The *f*m_unred command (from the

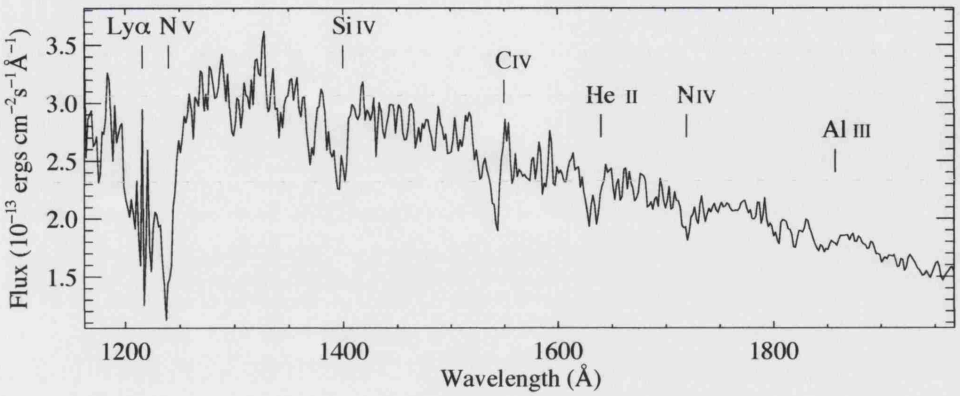

Figure 4.1: The IUE ultraviolet spectrum of V592 Cas with resonance lines marked (SWP15659). The exposure was taken on the 5th December, 1981.

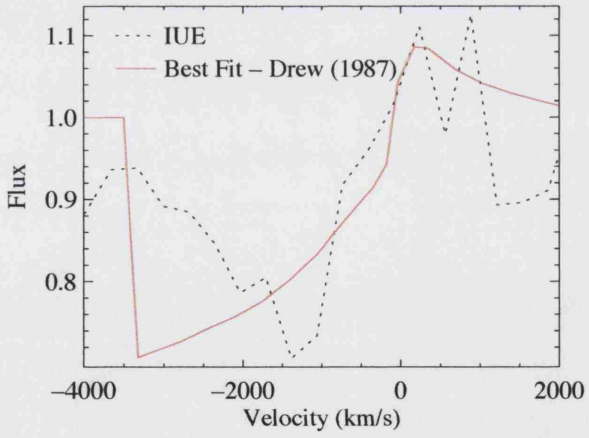

Figure 4.2: A plot of the C iv 1550Å profile in velocity space (black, dotted line) and the best attempt at fitting the profile using the Sobolev code by Drew (1987) (red, solid line; the parameters of the fit were: $v_{max} = 3500$ km/s and $i = 50°$). The spectrum is from exposure SWP15659 of the IUE data-set.

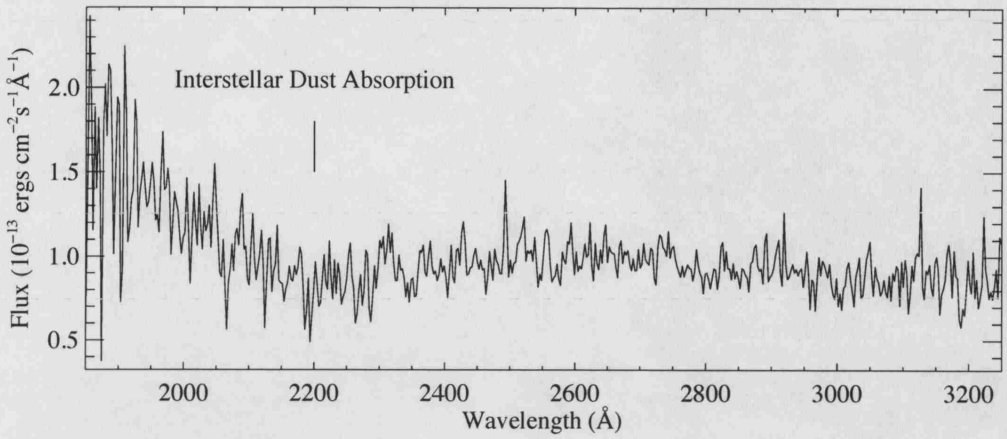

Figure 4.3: The IUE long wavelength spectrum of V592 Cas with the 2200 Å interstellar absorption feature marked (LWR12085). The exposure was taken on the 5th December, 1981.

NASA IDL astronomer's library) was used to remove the interstellar absorption from the spectrum, resulting in an estimated $E(B-V)$ of 0.25; this is the same as the compromised value listed in Taylor *et al.* (1998). If it is assumed that the mean ratio of total neutral hydrogen to colour excess is 5.8×10^{21} atoms cm^{-2} mag^{-1} (Bohlin *et al.* 1978), then the column density of neutral hydrogen towards the star is calculated to be 1.3×10^{21} atoms cm^{-2} mag^{-1} or $\log(N(cm^{-2})) = 21.1$.

4.4 The Optical Observations

The time-series of optical spectra used in this study were taken with the 2.3-m Bok Telescope of the Steward Observatory, based at Kitt Peak National Observatory, USA; the author was one of the observers. The observing run consisted of three consecutive nights, running from 2001 October 23 to 25 UT, which will hereafter be referred to as nights 1 to 3, respectively. A Bollers and Chivens spectrograph with a grating of 1200 lines mm^{-1} was used with a 1200×800 pixel CCD; the dispersion axis was parallel to the long axis of the CCD. The spectrograph slit was set to an angle of 1.5 arcsec which was sufficiently large so that most of the star light passed through the slit but, there was some loss of light at the edges, making the photometric calibration unreliable. The resulting spectra had a wavelength coverage of 3900 to 5000 Å with a spectral resolution of 1.9 Å, which was suitable for studying the following lines: the key Balmer lines from Hβ to Hϵ;

	Start Date (UT)	Start Time (UT)	End Time (UT)	No. of Exposures
Night 1	23rd October 2001	06:34	09:46	40
Night 2	24th October 2001	06:29	09:38	40
Night 3	25th October 2001	06:01	09:24	41

Table 4.3: A summary of the optical time-series of V592 Cas, taken with the 2.3-m Bok telescope, in October 2001.

He I lines at 4471 and 4922 Å; and the He II line at 4686 Å.

The exposures were grouped into banks of five and, between these banks a He-Ar arc frame was taken to ensure that object frames had accurate wavelength calibration throughout the observing run. Each object exposure lasted for 240 seconds which resulted in a signal-to-noise at the continuum of around 90. In total, over the three nights, 121 usable exposures of V592 Cas were taken. Table 4.3 is a summary of these exposures.

The exposures taken during the Bok observing run were reduced using IRAF and, the following analysis was undertaken using both IRAF and IDL. The extracted spectra were corrected for heliocentric velocity but not for systemic since the latter is not accurately known for V592 Cas. Nightly exposures were also made of the star Feige 110 (a white dwarf of spectral type DA) for photometric calibration purposes although as already stated, the loss of light either on side of the slit during the observations resulted in unreliable photometric calibration.

4.5 Analysis of the Optical Observations

4.5.1 The Spectrum

Fig. 4.4 is the time-averaged optical spectrum of V592 Cas from the October 2001 observing run; the key lines have been identified. On close inspection, the Balmer lines reveal themselves to be composed of more than one component. The Balmer profiles appear to comprise from a strong, but narrow emission and a underlying absorption. The two largest sources of Balmer emission for a non-magnetic CV are the accretion disc chromosphere, and the bright/hot spot, which is the shock heated region of the disc where the accretion stream impacts; it is possible that there would be a small emission contribution from a disc outflow. Possible sources of Balmer absorption would be the accretion disc,

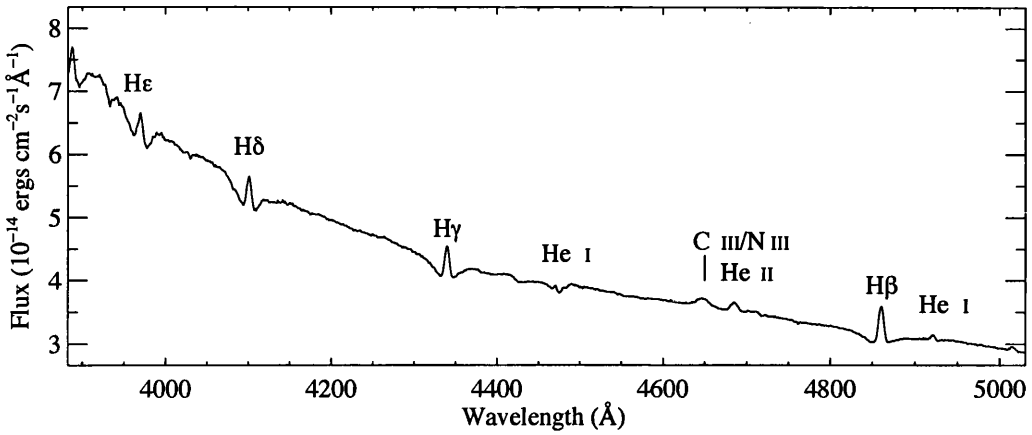

Figure 4.4: The average of 121 flux-calibrated V592 Cas optical spectra from the October 2001 observing run. Owing to losses of light either side of the slit, the flux levels are likely to be uncertain by 10-15 percent. The key lines have been identified.

the white dwarf and a disc outflow.

Helium is well represented in Fig. 4.4, with a narrow emission core superimposed on a broader absorption. The He I 4471Å is similar in profile to the Balmer lines, although it is much weaker than any of the Balmer lines observed in this spectrum. In contrast, the remaining two helium lines (the He I 4922 Å line and the He II 4686Å line) are both dominated by emission. Potentially, the He II 4686Å line (along with its UV counterpart at 1640 Å) have a special purpose in this study into accretion disc winds because it is believed that a significant contribution to the flux of this line could originate from a strong wind (Hoare 1994); this would make it an important wind diagnostic line.

The variability of a selection of optical lines is demonstrated in Fig. 4.5. The plots compare two extreme examples from night 1, separated in time by $\sim$ 1.8 hours. The pair of Hβ spectra show striking changes to the blue ward side of the absorption but, the two spectra vary very little along the red ward side of absorption; there is also some small-scale shift in the velocity of the emission. The pattern of behaviour observed in these two spectra for Hβ were found in the other Balmer lines but, to a lesser degree. The differential behaviour between the blue and red side absorption provides some evidence for a multi-component absorption.

The variability of two of the helium lines is also demonstrated in Fig. 4.5, although

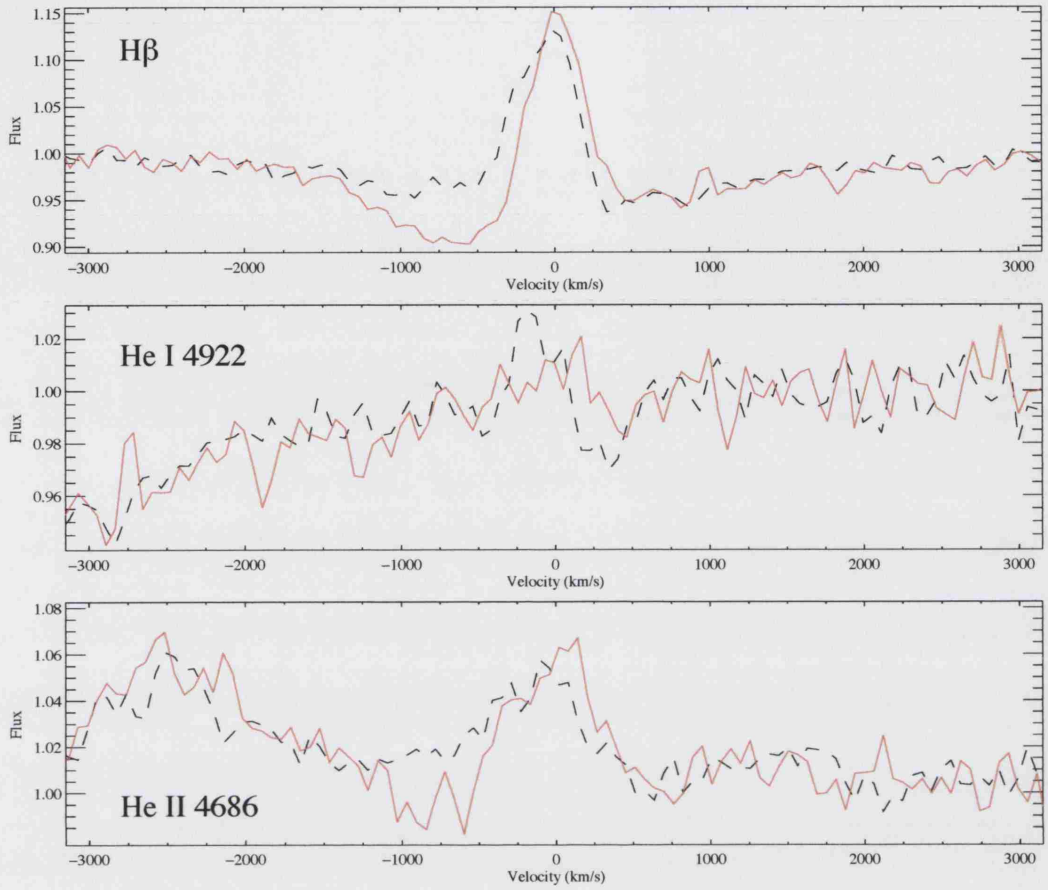

Figure 4.5: A demonstration of the line profile variability of the Hβ, He I 4922 Å and He II 4686 Å lines. The two spectra (red solid line and black dashed line) are separated in time by ~ 1.8 hours.

they are not variable to the same degree as is seen for the Balmer lines. Both the He I 4922Å and He II 4686Å lines undergo a slight shift to the red between the black dashed spectrum and the red solid line spectrum. However, for the He II 4686Å line there appears to be a slight decrease in flux across the blue-ward side of the profile which mimics what was seen for the Balmer line. If the strengthening blue-ward absorption of the Balmer lines is related to an increase in the perceived strength of the wind, then this apparent absorption along the blue-ward side of the He II 4686Å line may also originate from the wind. Confirmation that the observed changes to the He II 4686Å line are real and not an artefact of the data reduction process are provided by the Bowen blend, centered on ~ -2500Å, which shows no detectable variability above that of the noise.

Fig. 4.6 is a grey-scale representation of the time-series for the Hβ, Hγ, He I 4922 Å

and He II 4686 Å lines. To enhance the visualisation of the variability characteristics, each spectrum was normalised by the mean profile before being used to construct the image. For the two Balmer lines and the He I line, regions of reduced (black) and enhanced (white) flux, with respect to the mean, are seen to switch from the blue to red (and vice-versa) over the course of the three nights. It cannot be ruled out that the He II emission is also undergoing this pattern of variability but, data with a greater signal-to-noise level would be necessary to detect it; this would be possible by time-binning the data but except for this line the loss in temporal resolution would be too great. Although this core pattern of variability is very weak for the He I 4922Å line, it does appear to be acting in phase with the two Balmer lines.

Fig. 4.6 provides some evidence towards identifying the origin of the Balmer emission. If the emission originated from the accretion disc then it is expected that it would be broad and double peaked, although given the low inclination angle of the system, it is expected that the separation of the peaks would be small (e.g. Horne & Marsh 1986). If the emission came from the bright spot instead, then it is expected that the profile would be narrow and follow a sinusoidal path (or s-wave) in the velocity-time plane, because of the rotation of the binary system. Views of the Balmer lines from both Figs. 4.4 and 4.6 suggest that the bright spot origin more accurately represents the observations, although the disc probably contributes some flux to the line. The only caveat to this interpretation is that the observed amplitude of the emission (from Fig. 4.6) is uncharacteristically small for the bright spot.

The grey-scale representations of the two Balmer lines in Fig. 4.6 reveal more information at extended distances from the line centre. On several occasions during the three nights, broad decreases in the flux strength are observed across the blue-ward side of the absorption. The three strongest features have been labelled as 'a', 'b' and 'c' although more of these features do exist in these plots. These flux changes are seen to extend to a maximum velocity of ~ -3000 km/s; at this distance from the line centre the influence to the line profile from the emission must be small (if not non-existent) so it must be concluded that these changes to the profile are as a result of increases in the absorption strength rather than reductions in the emission strength. It is evident that the labelled changes to the blue-ward Balmer absorption in Fig. 4.6 most likely originate from the accretion disc wind since if it were due to changes to the accretion disc chromosphere, variability would be observed on both sides of the profile.

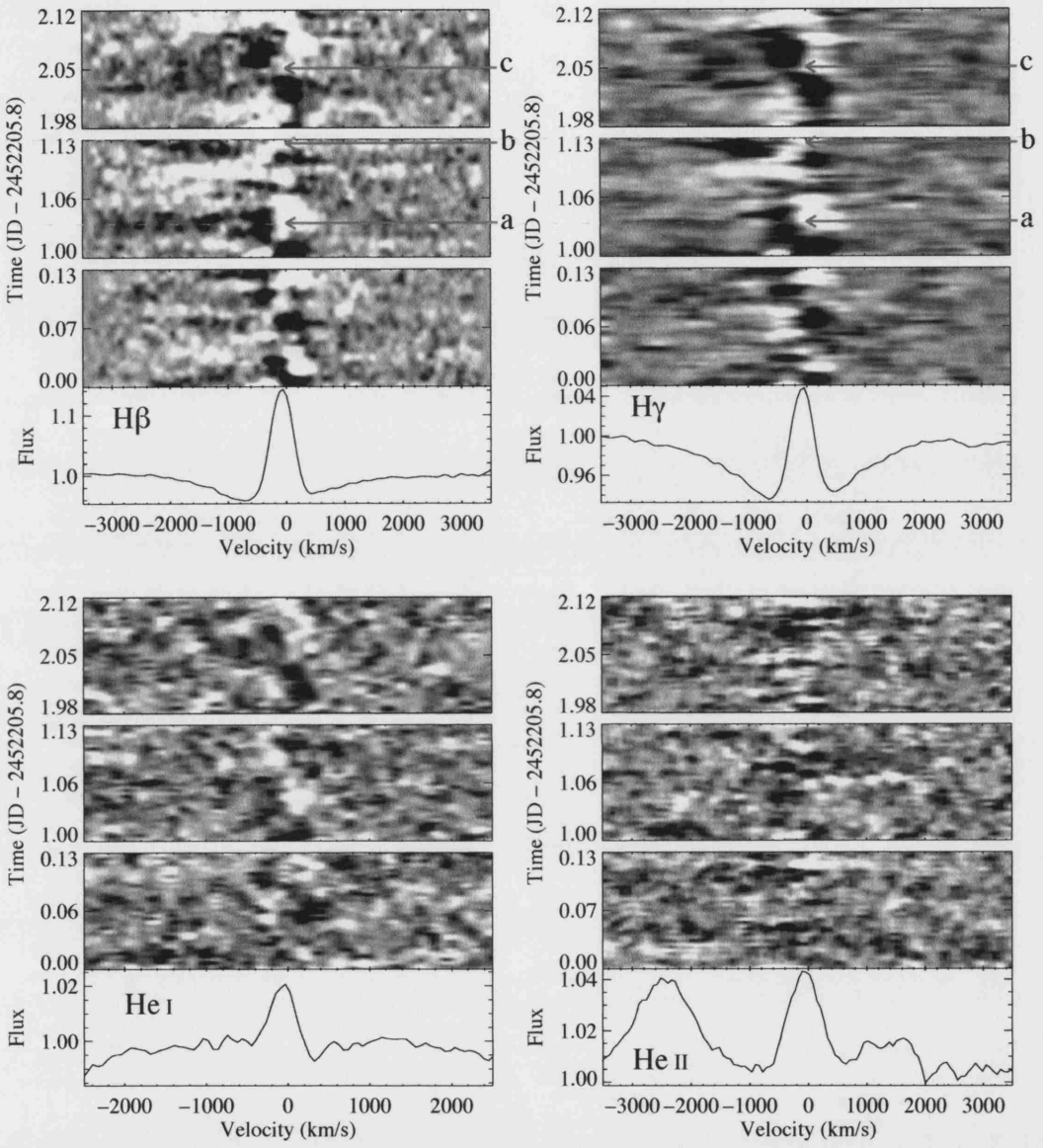

Figure 4.6: Grey-scale representations of the Hβ, Hγ, He I 4922 Å and He II 4686 Å lines; successive nights have been stacked on top of each other, so the bottom frames are night 1, the middle frames are night 2 and the top frames are night 3. To improve the contrast of the variability, the individual spectra were divided by the mean, the results of which were used to construct the images. In these plots, white represents enhanced flux and black represents reduced flux, with respect to the mean profile.

4.5.2 Temporal Variance Spectra of Wind Formed Optical Lines

The temporal variance spectrum (or TVS) is a powerful tool in time-series analysis; the TVS is described in more detail in § 2.2.2. In Fig. 4.7, TVS based on the Bok optical time-series are shown for Hβ, Hγ, He I 4922 Å, and He II 4686 Å. The greyscale representations of individual lines in Fig. 4.6 are broadly consistent with the TVS spectra. For the four lines shown, there is significant variance between ~ -1000 and $\sim +1000$ km/s although the variance for the two Balmer lines is much greater than for the helium lines. Rather than peaking at a single point, the four lines show twin peaks in the variance (this is much clearer for the Balmer lines than it is for the helium lines) which are a result of the sinusoidal s-wave motion of the emission.

One aspect of the Balmer line TVS profiles which could have been easily overlooked is that they are not symmetric with respect to the line centre. The drop in variance towards the blue from the line centre, is not nearly as rapid as the drop in variance towards the red. The result of this is that while the variance along the red wing of the TVS profile reduces to the 95% confidence level (the horizontal dotted line in Fig. 4.7) at $\sim +1000$ km/s, the variance along the blue wing does not drop to the confidence level until nearly ~ -2500 km/s. It is not an unreasonable assumption that the variance due to the sinusoidal emission is only significant within -500 to +500 km/s, meaning that variance beyond this range (such as the variance across the blue side of the line centre) is probably from another source. The most logical source of this blue-ward variance is the variable extended absorption described in § 4.5.1 and shown in Fig 4.6. Unfortunately, the strength of the helium lines in comparison to the observed noise do not support a similar investigation as to whether the TVS of those lines is also asymmetric in the same way.

In § 4.5.1 the Balmer lines were shown to have two distinct regions of variability, across the core of the line from the radial velocity shifting of the emission and, at extended regions across the blue side of the lines which is possibly due to a disc outflow. The TVS of the Balmer lines in this section showed that along the blue side of the spectrum the variability extends to ~ -2500 km/s while across the red side of the spectrum the variability was shown to extend only as far as is expected for the shifting emission. In the following section, the Balmer line profile is decomposed and the central velocity of each component is measured to help in understanding their behaviour.

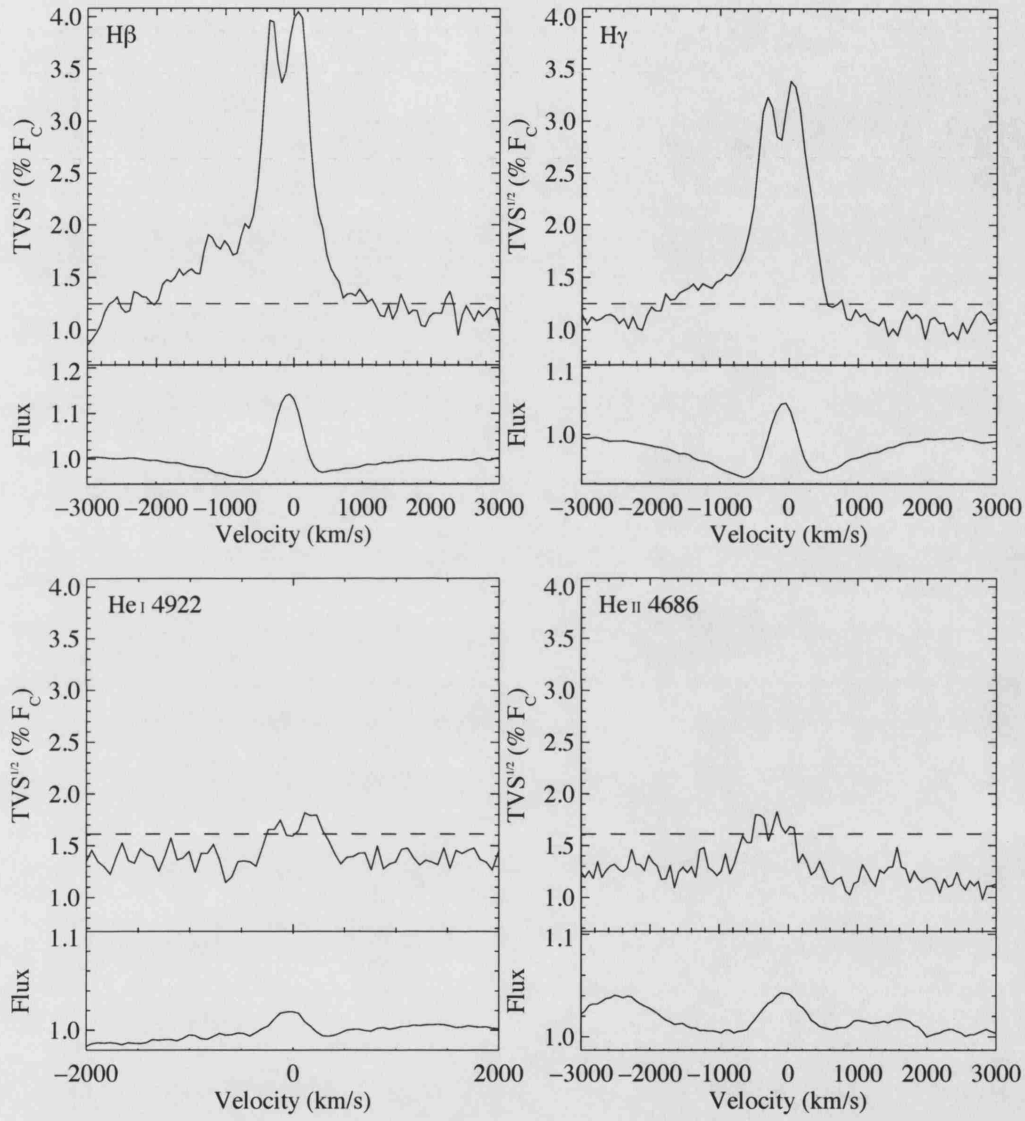

Figure 4.7: The temporal variance spectra (upper frames) for the Hβ, Hγ, He I 4922 Å and He II 4686 Å lines. The lower frames (in each panel) are the mean profiles of the selected regions and the dashed lines indicate a 95 percent confidence level of no variability.

4.5.3 Measuring the Radial Velocities of the Balmer Line Components

An inspection of the individual Balmer profiles of the Bok time-series suggests an empirical interpretation such that the profiles are composed of the following three distinct components. (i) There is a broad, shallow absorption component which likely corresponds to the optically thick disc or white dwarf. This weak absorption may be variable but, the signal-to-noise of the individual spectra is too low to permit an analysis of its temporal behaviour. It is therefore assumed that the said feature is static and can be assumed to be a Gaussian profile with a FWHM of $\sim$ 2800 and, a central intensity of ~ -0.04 (the equivalent width is $\sim$ 1.8 Å); these parameters are based on a mean spectrum created from a dozen spectra, showing similar strength in both the blue and red wings of the absorption. The remaining two components are also assumed to be Gaussian in shape and are: (ii) a variable (in velocity and flux) emission component which may arise from the hot spot or the accretion disc as a thermal wind emission source; and (iii) a variable disc-wind absorption component which extends blue-ward to Doppler shifted velocities of ~ -2000 km/s. It is not impossible that the disc-wind absorption component may have some strength at positive velocities.

The central velocity, full-width at half maximum and core depth were all entered as free parameters to the Gaussian profiles used to fit the emission and blue-shifted absorption. Each individual Balmer profile was fitted using a least-squares routine with the above three Gaussian components; Fig. 4.8 shows an example, by comparing a real Hβ profile with its three Gaussian fit. Keeping one of the three Gaussian profiles fixed in shape meant that the least-squares routine had less problems converging to a sensible solution. Measuring the radial velocity of the emission allowed for a new test of the orbital period of the system, in the hope that the results will firmly point to a period of either 0.103 or 0.115 days. Huber *et al.* (1998) measured the radial velocity motion of the emission without decomposing the profile into its individual components so it was also hoped that more accurate values of the K velocity amplitude and γ systemic velocity than those presented in Huber *et al.* (1998), could be derived. Measuring the central velocity of the absorption can potentially trace either a variable radial velocity shift or a variable profile width, and therefore could be used to help determine whether the absorption is modulated.

The lack of clear detection of an additional absorption component meant that the

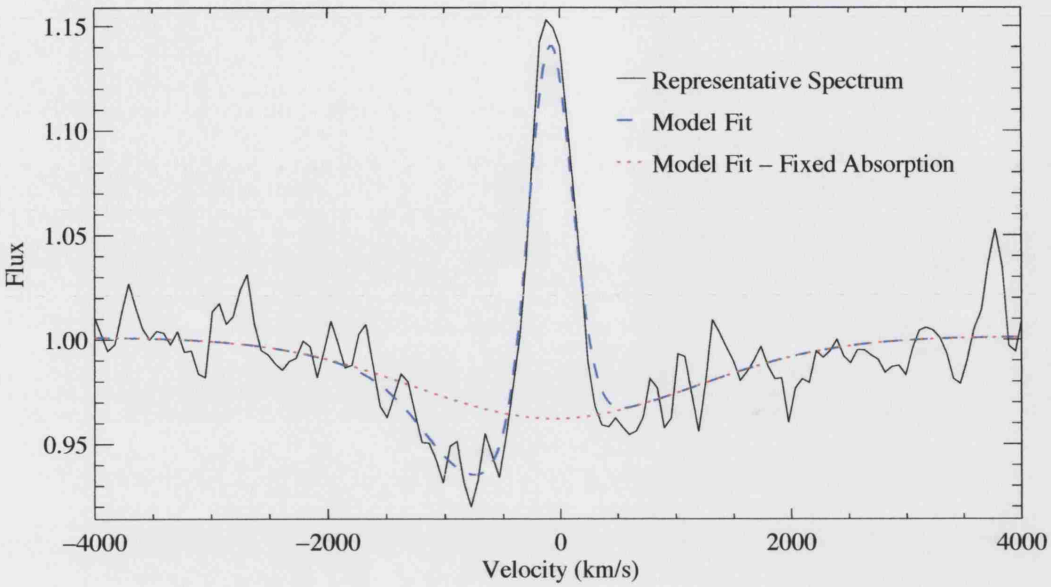

Figure 4.8: A comparison between an example Hβ profile and the fit to it, based on the three Gaussian model described in the text. The black solid line is the observation, the blue dashed line is the overall fit and red dotted line is the adopted broad underlying disc/white dwarf absorption, which has been assumed to be constant for all fits.

triple Gaussian formulation was not suitable for tracking the motion of the helium lines and the Bowen blend (at 4640Å). In fact, the signal-to-noise of the data prohibited fitting Gaussian profiles to the Bowen blend and the He II 4686Å line, so only the He I 4922 Å line was fitted, using a simple one Gaussian profile. It was fortunate that this helium line was strong enough to fit a Gaussian to because its motion in Fig 4.6 appeared to mimic (in phase) the central emission of the Balmer lines and it did not appear to be affected by variable absorption. However, it was still relatively weak so it was necessary to co-add the spectra into bins of 15 minutes in a compromise between obtaining usable fits to the line and preserving the temporal resolution of the data.

Before any results are presented, it is useful to be reminded of the periods associated both spectroscopically and photometrically, with V592 Cas. Firstly, there is the spectroscopically determined orbital period which has been found to be 0.103 days by Huber *et al.* (1998) and 0.115 days by Taylor *et al.* (1998). Secondly, there are the three photometrically determined periods, consisting of the positive and negative superhump periods of 0.122 and 0.112 days respectively (see Taylor *et al.* 1998) and the 22 minute

modulation discovered by Kato & Starkey (2002) (who suggest that this modulation is due to a weakly magnetised white dwarf). As far as it is known, the superhump periods have not been confirmed spectroscopically but, if V592 Cas really does have a warped or tilted disc and it also has a wind seated on this disc, then it is possible that the radial velocity measurements of the absorption are modulated on the negative superhump period (further discussion related to this can be found in § 3.7). The separation in time between the 0.115 day period and the 0.112 day period is $\sim$ 4 minutes which is close to the temporal resolution of the time-series. This would suggest that it would not be possible to distinguish between the two periods from this time-series except that the phase lag between the two periods over just 24 hours would be $\Delta\phi \sim 0.25$ which would definitely be detectable. Therefore it should be possible to distinguish between the orbital period and the negative superhump period with this data.

A search was made of the radial velocity measurements for modulation (on any period within reason) by passing them through a Fourier transform algorithm. Initially, the search was performed for frequencies between 0 and 15 cycles per day, which corresponds to a period range of infinity to $\sim$ 1.6 hours. Fig. 4.9 is a plot of the dirty and CLEAN power spectra (Roberts *et al.* 1987) of the radial velocity measurements, for the Balmer line emission and absorption and, the He I 4922Å radial velocity measurements; initially the dirty power spectra are discussed. For all dirty power spectra presented, there are strong signals close to or on both the 0.103 and 0.115 days periods. In all cases, the signals of these two periods are flanked by signals of similar width but decreasing strength, separated in frequency by approximately 1 cycle per day. Since the separation of the two suggested orbital period signals is also approximately 1 cycles per day, it is most likely possible that one of the suggested periods is an alias of the other. It should be noted that the separation of the 0.115 day orbital period and the negative superhump period is close to the half-width at half maximum of the Fourier power spectrum which means that it would not be possible to distinguish between the orbital period and negative superhump period using this method.

By passing the dirty power spectra through a CLEAN algorithm it was hoped that some of the 1-day aliases would be removed and the true orbital frequency would be revealed. The cleaned power spectra for each set of radial velocity measurements is shown in Fig. 4.9 as dot-dashed red lines; 200 iterations were used, with a gain of 0.2. For all of the dirty power spectra, the majority of the 1-day alias periods have been removed by the algorithm

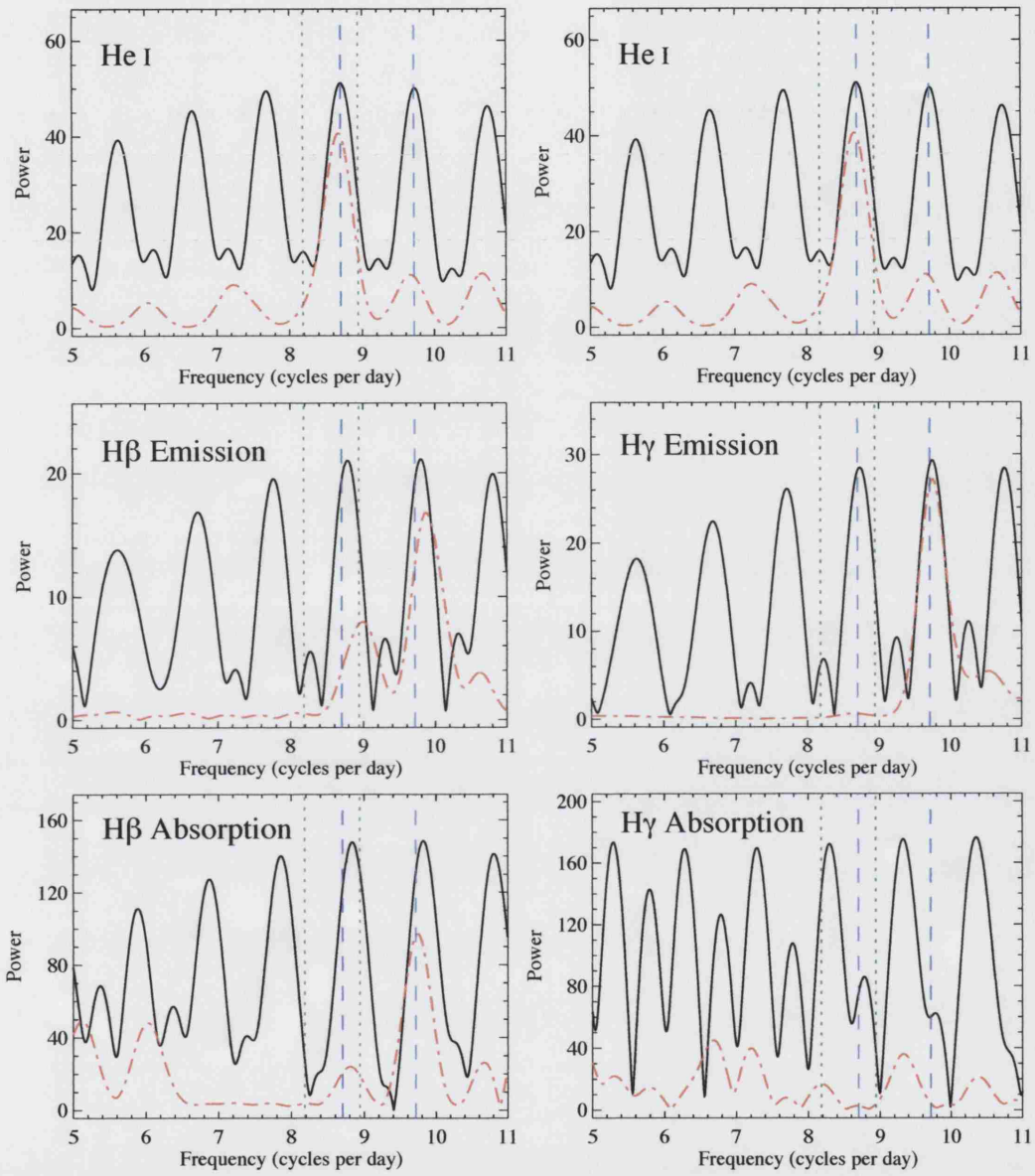

Figure 4.9: Fourier dirty (black line) and CLEAN (red dot-dashed line) power spectra for the He I 4922 Å line and the absorption and emission measurements for Hβ and Hγ. The left-most vertical blue dashed line marks the frequency of the 0.115 day period from Taylor *et al.* (1998) and the right-hand blue dashed vertical line marks the frequency of the 0.103 day period from Huber *et al.* (1998). The left and right green dotted lines indicate the frequencies of the positive and negative superhumps, respectively.

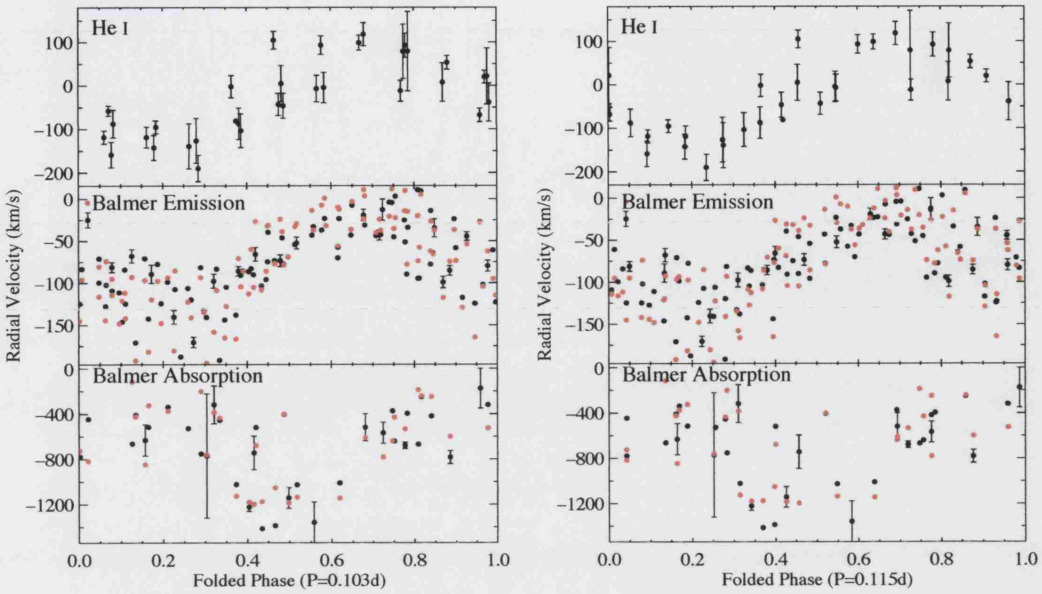

Figure 4.10: Radial velocities for He I 4922Å, and Balmer absorption and emission, phased on the periods of 0.103 (left-hand panel) and 0.115 days (right-hand panel). The black circles of the two sets of Balmer plots are Hβ measurements and the red data points are for Hγ; sample errors have been provided for Hβ. Phase 0.5 has been arbitrarily defined as when the Balmer absorption reaches a maximum blue-ward velocity. It should be noted that in non-wind cases, the Balmer absorption wind velocities have been excluded.

but, the puzzle of which period is the correct one does not appear to be solved in these plots. The strongest signal in the CLEAN power spectra for the absorption and emission of the Balmer lines is on the 0.103 day period but, in at least the Hβ measurements there is still a weak but detectable signal on the 0.115 day period. The strongest signal in the cleaned power spectrum of the He I 4922Å line is instead on the 0.115 day period and there is still some signal strength on the 0.103 day period. From these results it becomes understandable why the debate regarding the spectroscopically defined orbital period arose in the first place.

Fig. 4.10 is a plot of the radial velocity measurements against orbital phase for both the 0.103 and 0.115 day periods. By plotting the data in this way it was hoped that it might be possible to distinguish between the true period and the alias period with the assumption that the data points phased against the incorrect period maybe slightly more scattered than those phased on the true orbital period. The ephemerides provided

by Taylor *et al.* (1998) and Huber *et al.* (1998) could not be used in this circumstance because they are not accurate enough; instead, $\phi = 0.5$ has been arbitrarily defined as when the Balmer absorption reaches maximum blue-ward velocity. However, other than minor variations in the location of individual data points, the two plots look identical and it is not possible to identify the correct orbital period between them. What these plots do show is that there is a phase lag between the emission measurements (of both the Balmer lines and the He I line) and the Balmer absorption measurements; this phase lag is between a factor of 0.2 and 0.3 of the orbital period and is considered as significant.

It has proved to be impossible to determine the correct orbital period from the 1-day alias with this optical time-series. Given the similarity in radial velocity curves in Fig. 4.10 it is unlikely that further analysis of these measurements will be greatly affected by whichever period is chosen but, to investigate the orbital modulation of the data it is still necessary to make a decision as to which period should be used.

There are several arguments as to why the 0.115 day period should be the preferred choice of orbital period. Firstly, the strongest signal in the cleaned power spectrum of the He I line radial velocities (see Fig. 4.9) was on or near the 0.115 day period. Since the He I line did not appear to be contaminated by any additional components, it is likely that the radial velocity measurements of this line are more reliable than the radial velocity measurements of the Balmer emission, and therefore it could be inferred from this that the power spectrum of the He I radial velocities is likely to be more reliable than the power spectrum of the Balmer emission radial velocities. Secondly, with 264 spectra spread over a 410 day period, compared with just 41 spectra over 332 days, the data set used by Taylor *et al.* (1998) proves to have the better temporal coverage than the data set used by Huber *et al.* (1998), which considerably favours the choice of the 0.115 day period over the 0.103 day period. Not only was the Taylor *et al.* (1998) data set more extensively sampled but, they also use the Monte Carlo test of Thorstensen & Freed (1985) to confirm that they had selected the correct period. Evidence other than what has been discovered from this time-series does point to the 0.115 day period as the correct one and therefore it is this period which is the accepted orbital period for the remainder of this study.

The radial velocity measurements were fitted with a least squares routine of the form

$$v(t) = \gamma + K sin[2\pi p^{-1}(\phi - \phi_0)] \tag{4.1}$$

	γ^a (km/s)	K^b (km/s)	$P^c_{spec}(days)$
He I λ4922	-11.0±7.6	108±11	0.1145±0.0003
Hβ Ems	-75.0±2.9	44.2±4.3	0.1146±0.0002
Hγ Ems	-75.3±3.5	63.5±4.9	0.1144±0.0003
Hβ Wind Abs	-748±76	460±130	0.1145±0.0001†
Hγ Wind Abs	-770±110	580±190	0.1145±0.0001†

[a] Systemic velocity

[b] Semi-amplitude velocity

[c] Cyclic period of data

[†] The relatively poor quality of the Balmer absorption radial velocity measurements, meant that Eqn. 4.1 was fit to the data using a fixed period (shown), derived from the weighted mean period of the He I, Hβ emission and Hγ emission fits.

Table 4.4: Summary of radial velocity solutions for V592 Cas.

where γ is the systemic velocity, K is the semi-amplitude velocity, p is the period and ϕ_0 is the epoch for $\phi = 0.0$. γ, K, p and ϕ_0 were all specified as free parameters with appropriate starting values; the starting value for p was 0.115 days. Table 4.4 summarises the best fit parameters and the corresponding errors for the least-squares fit to the Balmer and He I radial velocities.

The most reliable estimates to the orbital period of V592 Cas are provided by the Balmer and the He I 4922 Å emission so it is fortunate that the best fit periods for these three sets of emission radial velocities are within 1-σ of each other. The mean weighted period based on these results is 0.1145±0.0001 days which is adopted as the orbital period of V592 Cas from here on. The relatively large error on the Balmer absorption measurements meant that attempting to perform the sinusoidal fit to the radial velocities with the period as a free parameter was not possible, so instead the period was fixed at the mean weighted period defined above.

When reviewing the best fit velocity solutions it is necessary to consider the absorption and emission results separately since they were ultimately measured for different reasons (the emission was measured to track the orbital motion of V592 Cas and the absorption was measured to track the behaviour of the disc outflow). Table 4.4 shows there to be

some discrepancies in the systemic and semi-amplitude velocities between the Balmer lines and the He I line but, not between Hβ and Hγ. The best fit semi-amplitude velocities of the two Balmer lines are statistically not of the same population since they are beyond 3-σ from each other but, they are still relatively close and these differences are small in comparison to the differences between the Balmer and He I semi-amplitude velocities. Similarly for the systemic velocities, the best fit solution for the two Balmer lines are within 1-σ of each other but, the He I systemic velocity is nearly twice that of the two Balmer lines. The discrepancies between the Balmer and He I could signify a difference in the formation location of the two lines but it could also be due to an oversimplification of the shape of the line profiles. This cannot be resolved without a greater understanding of the underlying physical processes involved.

Figs. 4.6 and 4.10 suggest that the amplitude of the central absorption velocity would be much larger than the amplitude of the emission velocity and, that is what the best fit solutions to the Balmer absorption reveal. The amplitude of the Hβ and Hγ absorption (the solutions are within 1-σ of each other) are nearly five times the amplitude observed for both the Balmer and He I emission. It should be stressed that these solutions are attempts to parameterise and simplify the behaviour of the blue-shifted absorption in terms of a Gaussian profile and are unlikely to represents its true morphology.

So far, the analysis of the radial velocity measurements has catered towards the search for modulation close to the orbital period. This is not an unreasonable approach since most of the periods associated with this system are close to the orbital period (e.g. the two candidate orbital periods and the positive and negative superhump periods). Fig. 4.9 shows dirty and CLEAN Fourier power spectra across a selected frequency range, to search for the 22 minute period (or $\sim$ 66 cycles per day) discovered photometrically by Kato & Starkey (2002); the corresponding frequency is indicated with the vertical blue dashed line. These Fourier power spectra do not reveal any strong evidence that there is modulation within the data on that 22 minute period. So far, the 22 minute modulation has only been observed photometrically so a lack of detection does not mean that it does not exist. If, as Kato & Starkey suggested, that the 22 minute period is indicative of a weakly magnetised white dwarf, then the spectroscopic detection of it within the blue-shifted absorption measurements would infer that the outflow is being confined (at least in part) by the magnetic field of the white dwarf, although this is an unlikely scenario. However, since there has been no detection of the 22 minute modulation, it appears as though this

is not the case.

In this section the determined radial velocities from performing a multi-component fit to the Hβ and Hγ profiles have been presented. Using the emission radial velocity measurements it has not been possible to determine whether the correct orbital period is 0.103 or 0.115 days but, it was discovered that the absorption is modulated on the orbital period and varies slightly out of phase with the emission. In the following section the nature of the orbital modulation is discussed in more detail.

4.5.4 The Orbitally Modulated Behaviour of the Blue-Shifted Absorption

Fig. 4.12 is a greyscale representation of the Hβ line (the He I 4922 Å line can be found at $\sim$ +3700 km/s), folded on a period of 0.1145 days and co-added into bins of width $\Delta\phi = 0.029$. For consistency with previous plots, $\phi = 0.5$ has been defined as when the blue-shifted absorption reaches its maximum blue-ward velocity, as indicated from the Gaussian fitting results. There are four key observations to be made from this figure. Firstly, the blue-edge of the wind absorption etches a sinusoidal line into the continuum. Secondly, no corresponding sinusoidal line is observed for the red edge of the absorption, although it does admittedly coincide with the Balmer emission, making it a little difficult to clearly see what is happening. From these two observations it can be inferred that the red edge of the absorption is anchored close to the line centre and the sinusoidal line of the blue-edge of the absorption is formed by the constantly changing width of the profile. Thus, since the radial velocity measurements of the absorption, presented in § 4.5.3, measure the centre point between the two wings of the absorption, those measurements actually track the width of the profile and not the motion of it. The third key observation of Fig. 4.12 is the phase lag between the emission and the absorption (see also Fig. 4.10). In this figure, the absorption peaks in maximum negative velocity at the arbitrarily defined $\phi = 0.5$ while the emission of Hβ and the He I line, peak in blue-ward velocity at $\phi \approx 0.2$. Finally, the features which were originally flagged in nights 2 and 3 (see Fig. 4.6) are no longer distinct but instead fit within the overall cyclic absorption behaviour. These key observations of the wind absorption are discussed in more detail in § 4.6.

Fig. 4.13 shows the two-dimensional Fourier spectrum of Hβ and Hγ with the aim of demonstrating the velocity range of the orbital modulation more clearly; for both

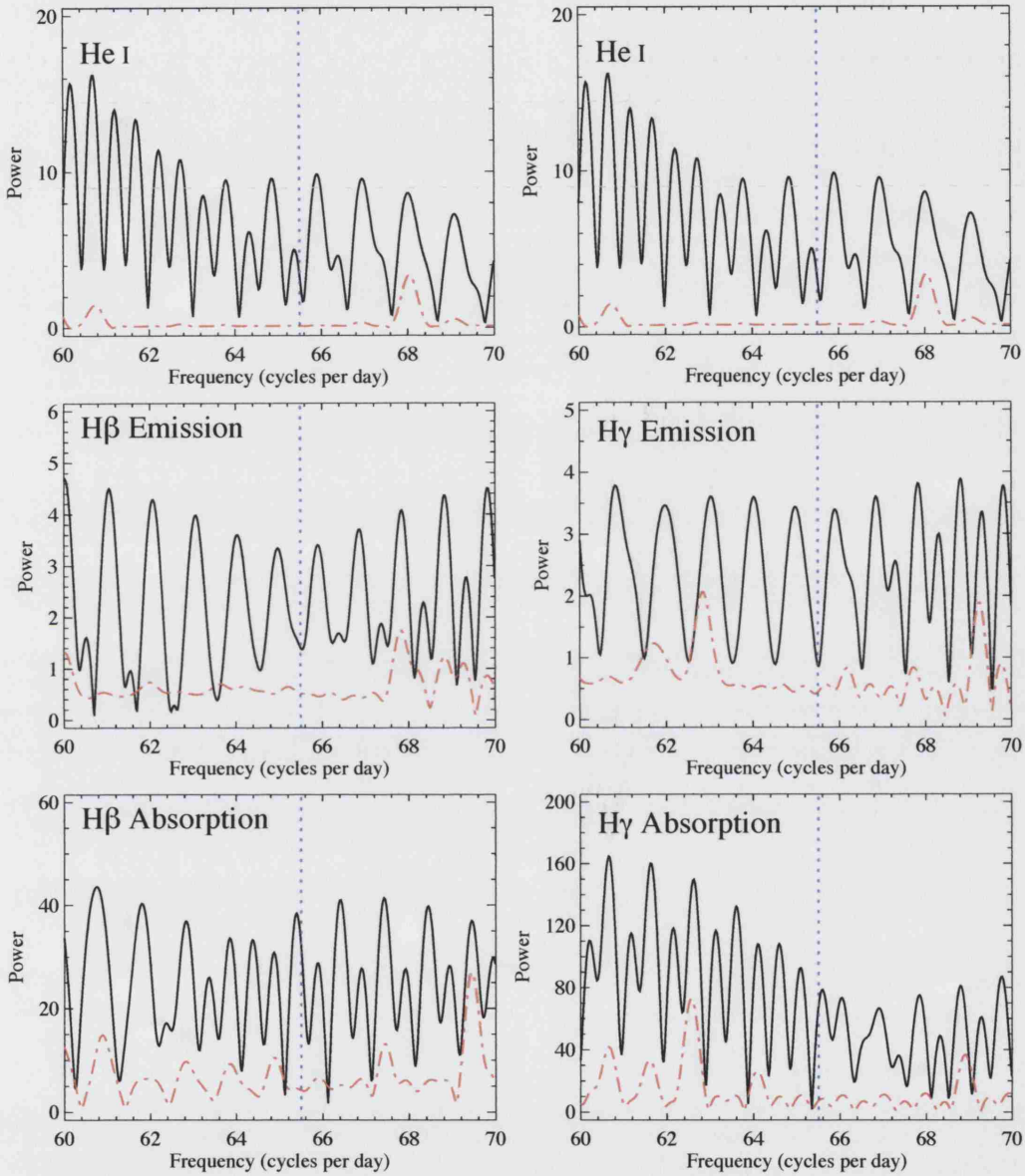

Figure 4.11: Fourier dirty (black line) and clean (red dot-dashed line) power spectra for the He I 4922 Å line and the absorption and emission measurements for Hβ and Hγ. This plot centres around the Kato & Starkey (2002) period of 22 minutes (or 0.015 cycles per day), which is indicated by a vertical blue dashed line in each plot.

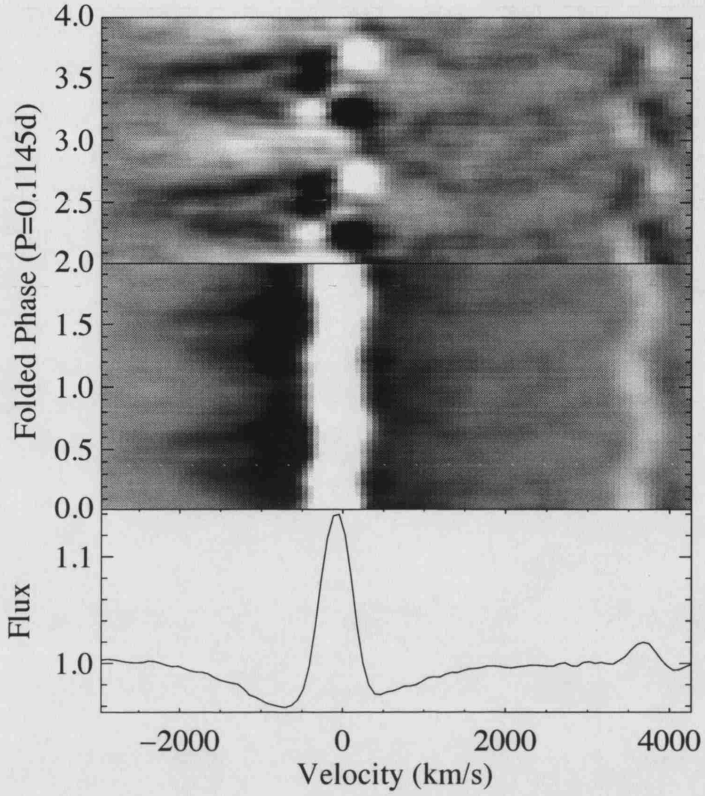

Figure 4.12: A grey-scale representation of Hβ, folded on a period of 0.1145 days, placed into 35 bins and repeated for two cycles (the feature at $\sim +3700$ km/s is the He I 4922 Å line). The bottom frame, spanning from $\phi = 0$ to 2 is the original data and the top frame, spanning from $\phi = 2$ to 4, is the residual data where each spectrum has been divided by the overall mean. $\phi = 0.5$ has been set to when the Balmer wind absorption reaches its maximum blue-ward velocity.

Balmer lines there is considerable signal strength along the indicated orbital frequency. For Hβ, the strong signal is between ~ -2500 and ~ -1000 km/s but, for Hγ the signal extends from ~ -2000 km/s to approximately the line centre; there is unlikely to be any significance to this slight difference in location. It appears that there is a weak signal extending red-wards from the line centre on the orbital frequency, but since it is not very strong and was not observed in Fig. 4.12, there is little that can be concluded from it.

The equivalent width was measured for each Hβ profile across two velocity ranges, the purpose being to directly compare and quantify the behaviour between the blue and the red wings. Across the blue wing the selected velocity range was from -2500 to

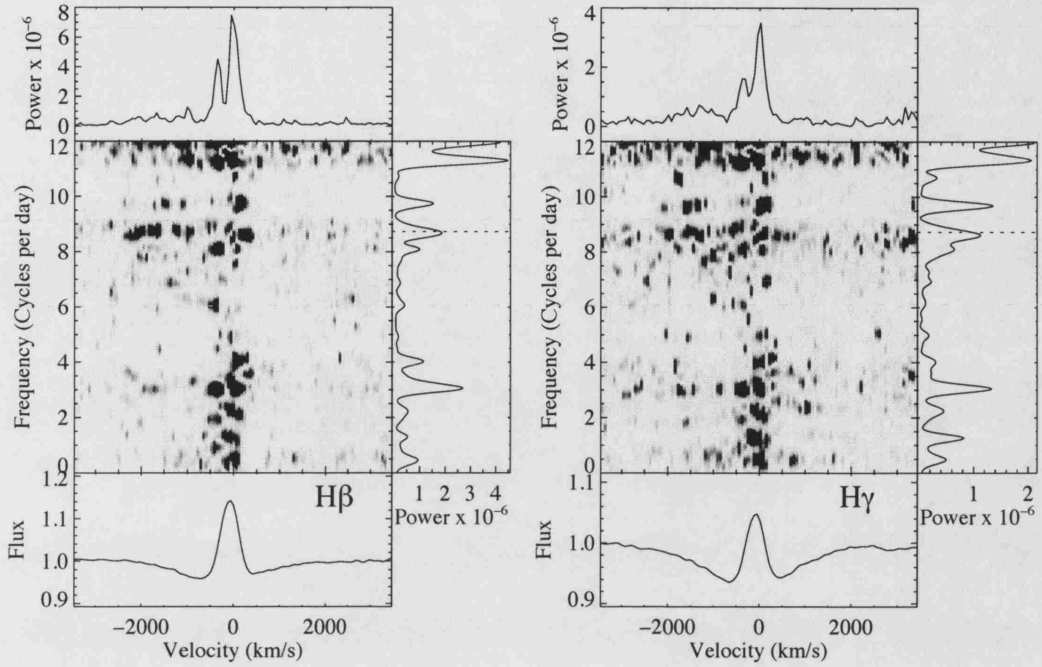

Figure 4.13: Fourier 2-D plots of the Hβ and Hγ lines; the black areas indicate peaks in the power spectrum although it is the black horizontal bands which are significant. Summations of the power (in arbitrary units) are shown at the top and right hand side. The dotted line on the frequency summation plot (right hand side) indicates the believed orbital period for the system.

-1500 km/s and across the red wing the velocity range was 1500 to 2500 km/s; these regions were selected because it is believed that at these distances from the line centre the emission contributes little variable flux. The equivalent width is typically reserved for quantifying the strength of an entire line but, in this circumstance it has been utilised to measure the strength of the two selected regions. Fig. 4.14 compares the equivalent width measurements from these two regions to try and determine whether a correlation exists between them. The data points within this plot are very scattered and there is little evidence of correlation. A linear correlation test performed on the pair of values yielded a probability that there isn't a linear correlation of 92% ($r = 0.075$).

Fig. 4.14 proves that there is no detectable correlation between the strength of the blue and red wings of the Balmer profile but it does show the red wing undergoing fluctations in strength. Fig. 4.15 is a plot of the dirty and clean Fourier power spectra for the red wing equivalent widths. In the dirty power spectrum there are a multitude of peaks and

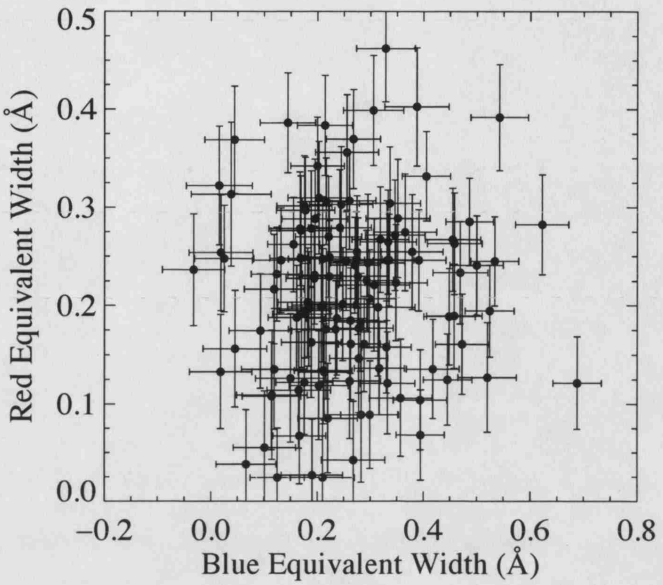

Figure 4.14: A plot of red absorption wing equivalent widths (1500 to 2500 km/s) against the blue absorption wing equivalent widths (-2500 to -1500 km/s).

it is unclear from just this plot whether any are due to a real modulation. However, the cleaned power spectrum shows a weak but significant signal close to the orbital period suggesting that these red wing fluctuations may in fact be modulated on the orbital period. Given the lack of correlation between the blue and the red wing measurements it is unlikely (but not impossible) that these red wing fluctuations are related to the wind absorption; it is more likely that the fluctuations belong to a weak red-ward component.

It was already mentioned in § 4.5.1 that the He II 4686Å line has the potential to diagnose accretion disc winds in CVs (e.g. Hoare 1994). In the spectrum of V592 Cas, the feature is weak and mostly in emission but, it is variable and at times it is observed to dip into absorption along the blue-ward side (see Fig. 4.16). At its greatest strength, the blue-ward He II 4686Å reaches a strength of ~ 0.08 Å which is likely to be a lower limit since there is some infill from the emission and some contamination from the Bowen blend. Using this single measurement and Table 1 of Hoare (1994) , the mass-loss rate from the disc is crudely estimated to be $\sim 10^{-9} M_{\odot}$ yr^{-1}; the line profiles were simulated using the Sobolev approximation and level populations taken from non-local thermodynamic equilibrium which matched the observed strengths of the C IV and N V UV resonance lines. This rough estimate agrees with the theoretical calculations of Howell *et al.* (2001) for a system with an orbital period such as V592 Cas, assuming that it has only just come

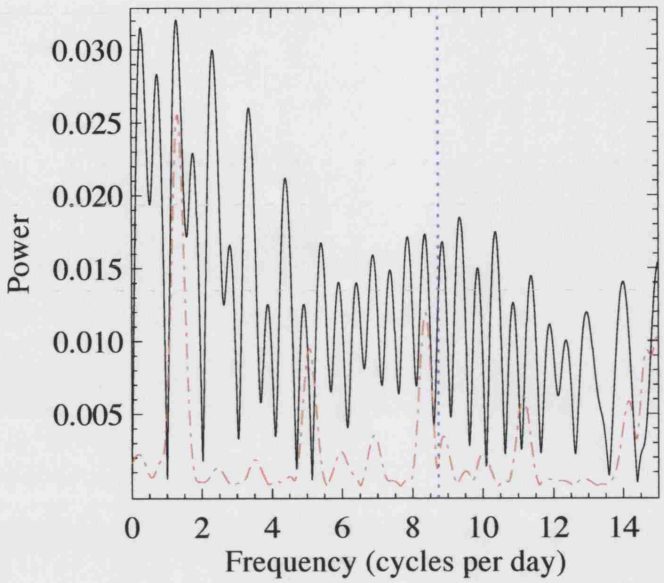

Figure 4.15: Fourier dirty (black solid line) and clean (red dot-dashed line) power spectra for the equivalent width measurements taken across the red velocity range of the Hβ line (between 1500 and 2500 km/s). The vertical blue dotted line indicates the frequency of the orbital period.

into contact within the period gap; this value also agrees with the estimated $\dot{m}q$ in § 4.3 if it is assumed that $qC^{3+} \sim 1$.

In this section, the behavioural characteristics of the disc wind absorption have been described in detail. The orbital modulation of the disc wind absorption is best explained as a varying width with the red-edge (of this blue-shifted absorption) fixed in location, close to the line centre. A modulated fluctuation in the strength of the red side of the Balmer lines is presented but the nature and cause of this variability is uncertain and would require a higher signal-to-noise data for further investigation. The strength of the disc wind outflow is estimated to be $\sim 10^{-9} \mathrm{M}_{\odot}\ \mathrm{yr}^{-1}$ using some assumptions from Hoare (1994) about the He II 4686Å line. However, since the exact nature of the disc outflow is not known, it is unlikely that the method used to calculate the mass-loss rate will give an accurate estimate. In the following section, some system parameters for V592 Cas are calculated using the same methods as Huber *et al.* (1998) but, using the radial velocity solutions presented in § 4.5.3.

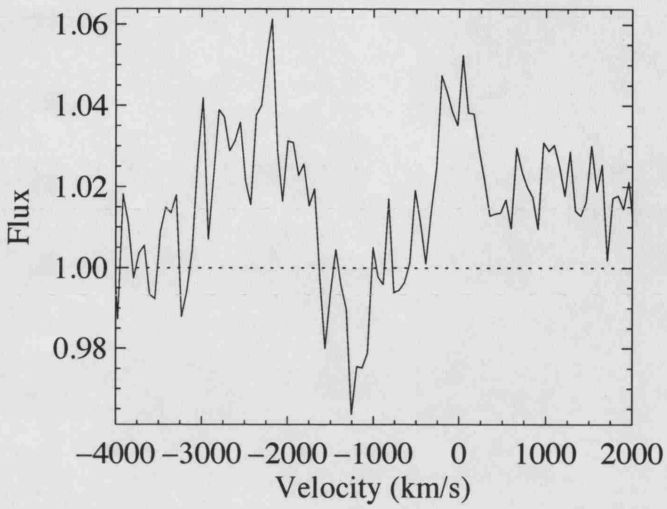

Figure 4.16: An example plot of the He II 4686 Å line, showing when the blue-shifted absorption is present. The horizontal dotted line indicates the position of the continuum.

4.5.5 System Parameters

Using their radial velocity solutions for V592 Cas, Huber *et al.* (1998) derive several system parameters including the inclination angle and the mass of the two stars. Their calculations are based on the methods presented in Warner (1973) for determining the mass of component stars and, they make many assumptions to complete the calculations such as the secondary being a zero-age main sequence star; there are obviously many caveats to their methods and equations used (which they admit to) but the estimates provided are invaluable. The system parameters that they derived were based upon radial velocity measurements of the Balmer emission using a single Gaussian fit and an orbital period which is believed to be incorrect. In this section, the system parameters are recalculated using radial velocity measurements from the multi-component fit presented in § 4.5.3 and, (what is believed to be) the correct orbital period; it should be noted that quoted errors are calculated on a statistical basis and do not take into account systematic errors in the inputted measurements.

The three input values into the following equations are: the orbital period (P), the projected rotational velocity of the disc ($v \sin i$), and the amplitude of the radial velocity curve of the primary star (K_1). The orbital period which will be used is the mean average value derived from the radial velocity measurements of the emission features

(P=0.1145 days). It is assumed that $v \sin i$ can be estimated from the full-width at half maximum (FWHM) of the Balmer emission; this is not an unreasonable assumption since the width of the Balmer emission for Hβ and Hγ is observed to be approximately the same. The mean full width at half maximum of the two Balmer lines (derived from the multi-component fit to the Balmer lines) was 480.486 ± 0.002 km/s. Finally, a suitable estimate of K_1 can be derived from the radial velocity amplitudes of the Balmer emission in Table 4.4. Taking the mean value of K from both Hβ and Hγ produces an estimated value for K_1 of 53.9 ± 6.5 km/s.

The first system parameter to be derived is the mass ratio of the two stars or

$$q = \frac{M_2}{M_1} \tag{4.2}$$

where M_2 and M_1 are the masses of the secondary (red dwarf) and primary stars (white dwarf), respectively. q may be calculated by solving for it with the following equation

$$\frac{K_1}{v \sin i} = q f(q)^2 \tag{4.3}$$

which originally came from Warner (1973). $f(q)$ is the distance between the centre of the primary star and the inner Lagrangian point, and it can be estimated with the formulation provided by Plavec & Kratochvil (1964) for systems with $0.1 \leq q \leq 10$ i.e.

$$f(q) = 0.5 - 0.227 \log q \tag{4.4}$$

The mass ratio between the two stars is obtained by entering K_1 and $v \sin i$ into Eqn. 4.3 and solving for q; the mass ratio is thus determined to be 0.289 ± 0.035.

The mass of the secondary star may be derive using the newly determined value of q and the equation (Shafter 1983)

$$\frac{M_2}{M_\odot} = 0.998 \times 10^{-4} \left(\frac{1+q}{q}\right)^{\frac{1}{2}} P \beta^{-\frac{3}{2}} \left(\frac{R_2}{a}\right)^{\frac{3}{2}} \tag{4.5}$$

where P is the orbital period, β is the factor of deviation of a spherical approximation to a Roche geometry of the secondary star (this is assumed to be 0.96, just as Huber *et al.* (1998) did), R_2 is the radius of the secondary star and a is the separation of the two

stars. At this stage, R_2 and a are unknown quantities but the ratio between them can be estimated using the equation (from Paczyński 1971), this is only suitable for systems where $0 \leq q \leq 0.5$

$$\frac{R_2}{a} = 0.462 \left(\frac{q}{1+q} \right)^{\frac{1}{3}}. \tag{4.6}$$

Using $q = 0.289$ results in $R_2/a = 0.281$ and the mass of the secondary star is then estimated to be 0.33 ± 0.02 $M_\odot$; the mass of the primary star is calculated from these results to be 1.14 ± 0.16 $M_\odot$. Using this mass for the secondary, assuming that it is a zero age main sequence star and the equation (Patterson 1984)

$$\frac{R}{R_\odot} = \left(\frac{M}{M_\odot} \right)^{0.88} \tag{4.7}$$

provides an estimate of the radius of the secondary star (R_2) of 0.38 ± 0.02 $R_\odot$. The ratio $R_2/a = 0.281$ so the separation between the two stars is determined to be 1.34 ± 0.10 $R_\odot$.

In this study of accretion disc outflows from CVs, the three most important parameters to know about a system are probably the orbital period, the inclination angle and the absolute phase. The absolute phase cannot be determined using the data provided in this time-series but since the radial velocity amplitude, the mass ratio of the two stars, the mass of the secondary star and the orbital period, are known, it is possible to calculate the orbital inclination angle using the equation (Downes *et al.* 1986)

$$\sin^3 i = \frac{K_1^3 P}{2\pi G M_2} \left(\frac{q+1}{q} \right)^2. \tag{4.8}$$

Thus, the inclination angle is estimated to be $28.8 \pm 4.1°$, which is extremey close to the estimate provided by Huber *et al.* (1998) ($28°^{+11}_{-10}$) and well within the errors.

In this section, the system parameters for V592 Cas, originally derived by Huber *et al.* (1998), have been updated using new radial velocity solutions and a different orbital period; Table 4.5 summarises these system parameters and compares them to those presented in Huber *et al.* (1998). Using a different orbital period and different estimates for K_1 and $v \sin i$ did result in slightly different system properties (e.g. a larger mass ratio) but these changes had little effect on the systems inclination angle and V592 Cas remains a very low inclination CV. However, there are caveats to this method of determining the system parameters which should be considered before these results are fully

Parameter	Value from Huber *et al.* (1998)	Newly Derived Value
Spectroscopic Period (Days)	$0.103^{+0.040}_{-0.020}$	0.1145 ± 0.0001
M_1 ($M_\odot$)	$1.4^{+1.0}_{-0.6}$	1.14 ± 0.16
M_2 ($M_\odot$)	0.30	0.33 ± 0.02
q	$0.19^{+0.1}_{-0.6}$	0.29 ± 0.03
R_2 ($R_\odot$)	0.34	0.28 ± 0.01
a ($R_\odot$)	1.4	1.34 ± 0.10
i	$28^{+11\circ}_{-10}$	$28.8 \pm 4.1^\circ$

Table 4.5: A comparison of system parameters for V592 Cas derived by Huber *et al.* (1998) and newly derived in this thesis. The errors on the newly derived values listed above are statistical errors only and do not take into account any systematic errors on the measurements used to derive the values.

accepted. The two most important caveats in this method relate to the measurements from the data used as input values. Firstly, it has been assumed that the Balmer emission accurately traces the motion of the white dwarf and this is not necessarily the case; this would of course affect any values dependent on K_1. Secondly, the FWHM of the Balmer lines was used as an estimate for $v \sin i$ of the accretion disc but, this FWHM is only representative of the disc at an unknown average radius; this of course brings into question all results dependent on $v \sin i$. Thus, all derived system parameters in this section should be considered with some care.

4.6 Discussion

Using time-series spectroscopy, it has been possible to establish the optical wind characteristics of the low inclination nova-like CV, V592 Cas. An in-depth study into the Balmer line profiles reveals that they can be considered as the sum of three distinct features: a broad, shallow underlying absorption, a strong but narrow absorption and a blue-shifted absorption. The velocity shift of the emission and the blue-shifted absorption for each spectrum in the time-series were measured by fitting the entire Balmer line profile with a triple Gaussian function. The emission was found to move in a s-wave in velocity space, a motion which is shown to be modulated on or close to the orbital period. An analysis of

the changing morphology of the blue-shifted absorption revealed that it undergoes asymmetric broadening, whereby just the blue edge of the absorption varies in location and, the red edge remains close to the line centre. This asymmetric broadening extends to a maximum velocity of ~ -2000 km/s and is modulated on a period close to or on the orbital period. There is a phase lag of a factor of ~ 0.3 of the orbital period between the emission reaching maximum blue-ward velocity and, the blue-shifted absorption expanding to its greatest width.

At times during this chapter the blue-shifted absorption has been described as resulting from a disc outflow or wind. This is not an unreasonable assumption and it is true that there is much evidence in the UV wave band that V592 Cas is driving a wind (see § 4.3) but it is not necessarily the case that this blue-shifted absorption is due to such an outflow. One alternative (but plausible?) explanation for the observations arises if V592 Cas is an SW Sex star. The SW Sex class was originally created by Thorstensen *et al.* (1991) and was based upon the following observed characteristics: eclipses, single-peaked lines, orbital periods between 3 and 4 hours, strong He II 4686 Å emission (typically around half the strength of the Hβ emission) and absorption in the He I and Balmer lines opposite the eclipse (also referred to as phase 0.5 absorption). It was suggested by Patterson *et al.* (2002) that the phenomenon of the SW Sex stars may be linked to nodal precession of the accretion disc because many of the positively confirmed systems posses signals related to negative superhumps (Harvey *et al.* 1995). This may or may not be a defining characteristic but since many other systems exhibit negative superhump periods it would be dangerous to classify a system based on this one discovery alone.

The most successful explanation for the SW Sex phenomenon yet to appear, is that the accretion stream is overflowing the initial point of impact and continues over the accretion disc until it impacts closer to the white dwarf (Hellier & Robinson 1994). When this happens it is believed that the phase dependent absorption can originate from the free-falling accretion stream above the inner portions of the disc. The velocity amplitude of this phase dependent absorption for high inclination systems is typically on the order of 1000 km/s but, for low inclination systems the $\sin i$ effect is likely to compress this amplitude to much lower values. For the low inclination systems, the phase dependent absorption would also be expected to remain throughout the orbital period (at varying intensities) because there is much more disc to project against, with respect to the line of site to the observer.

Some of the accepted characteristics for SW Sex stars are dependent on the orbital inclination of the system with respect to the line of site to the observer; this is the only classification of non-magnetic CVs which is seemingly dependent on i since they typically depend on light curve characteristics. V592 Cas is not a high inclination system so this would normally rule it out for such a classification but, there have been a few cases where low inclination systems are thought to be SW Sex stars such as V442 Oph (Hoard *et al.* 2000) and LS Peg (Taylor *et al.* 1999) and, have been suggested as such from just a subset of these characteristics. The question is whether there is sufficient evidence to classify V592 Cas as a SW Sex star given the evidence already presented. In the spectrum of V592 Cas there are single peaked emission lines, effectively phase dependent absorption and an orbital period close to 3 hours ($\sim$ 2.75 hours). However, the He II emission is not excessively strong for a nova-like system and the phase dependent absorption is not actually within the core of the line as you should expect for SW Sex systems.

Another, less well accepted scenario for SW Sex stars is that they have a magnetic white dwarf whose field lines disrupt the inner regions of the accretion disc (Horne 1999); evidence presented by Rodríguez-Gil *et al.* (2001) based on a study of LS Peg (a low inclination SW Sex star) indicated that the white dwarfs of SW Sex stars probably have strong magnetic fields. These field lines rotate with the white dwarf and the accreting gas which comes into contact with them are threaded along the field lines and hence stripped from the accretion disc; the phase dependent absorption is believed to be the result of these accretion "curtains" which form above the accretion disc. If a 22 minute signal had been detected for the blue-shifted absorption, then this would not only have reinforced the detection by Kato & Starkey (2002), it would also have added towards the evidence that V592 Cas was an SW Sex star. However, given the available evidence it appears unlikely that V592 Cas is an SW Sex star and so the most plausible explanation for the blue-shifted absorption remains a disc wind.

If the blue-shifted Balmer absorption is due to an outflow/disc wind then a method for modulating the wind as the system rotates must be found. Phase related changes to UV wind lines have been observed in several other low inclination systems such as YZ CNC, IR Gem, V3885 Sgr (Drew & Verbunt 1988; Woods *et al.* 1992) and V795 Her (Prinja *et al.* 1992; Prinja & Rosen 1993), although there is evidence to suggest that V795 Her may be an SW Sex system (Casares *et al.* 1996) which would therefore exclude it from this

group. An orbitally modulated wind was also found for RW Sex using far-UV data; the similarities between what was observed for RW Sex (see § 3) and what has been observed for V592 Cas are admittedly between the UV and optical wavebands but they cannot be ignored. For RW Sex, the suggested method for causing a break in axi-symmetry was to assume that the wind was seated on a warped or tilted disc but, no evidence was found for that deformation of the disc in the form of negative superhumping. This prescription may be more successful for V592 Cas as Taylor *et al.* (1998) discovered (albeit weak) evidence of a negative superhump period photometrically although it has admittedly not been verified spectroscopically.

There are clearly some strong similarities between RW Sex and V592 Cas (e.g. the modulated wind, the inclination angle) which must be addressed. A complete comparison cannot be made between the observations presented in this chapter and those presented in § 3 because one time-series is in the optical and one time-series is in the ultraviolet. To address this problem, in the following chapter the wind of V592 Cas is analysed using far-UV spectroscopy taken with FUSE in 2003.

CHAPTER 5

FUSE Observations of V592 Cassiopeiae

5.1 Introduction

The purpose of this study is to compliment the optical investigation into the accretion disc wind of V592 Cas presented in § 4, using far-UV observations. Some similarities exist between the far-UV characteristics of RW Sex's disc wind and the optical characteristics of V592 Cas' disc wind and it was hoped that by analysing this far-UV time-series, further similarities may arise which could lead to the conclusion of a common mechanism.

V592 Cas is a low inclination, UX UMa system with a period of 0.1145 days. The system has been shown to exhibit positive and negative superhumps with periods of 0.1223 and 0.1119 days, respectively (Taylor *et al.* 1998). The negative superhump period is associated with a tilted or warped accretion disc which could be a source of a broken axi-symmetry to the wind if this is the cause of the orbital modulation; if the far-UV disc wind is observed to be modulated on the negative superhump period then this would be key evidence to support this notion. Proof that V592 Cas has a disc outflow was first shown in the UV using IUE observations (see § 4.3), and in § 4 it was shown that the wind can be seen at optical wavelengths. See § 4.2 for a more complete introduction and literature review of V592 Cas.

5.2 The FUSE Observations

The purpose of the FUSE observations was to explore the time-dependent behaviour of the disc wind in the far-UV, following its discovery at optical wavelengths. It was hoped

Data ID	UT Start Time	Exposure Length (seconds)	No. of Exposures
D1140101000	Aug 5th 2003 21:22	23734	12
D1140102000	Aug 7th 2003 00:05	19972	12
D1140103000	Aug 8th 2003 03:28	14514	9

Table 5.1: A summary of each night of the FUSE observations of V592 Cas (program ID: D114). All exposures were taken in time-tag (TTAG) mode with the large aperture (LWRS).

that ground based optical observations of V592 Cas would be obtained simultaneously with the FUSE observations, but unfortunately it was not possible to obtain observing time on a suitable telescope before the FUSE observing run commenced.

The FUSE observations were recorded in TTAG mode through the LWRS aperture (see § 3.4.1 for details regarding FUSE), on the 5th, 7th and 8th August, 2003. The target was observed on three separate occassions to ensure that sufficient data was available across several orbits so that orbital modulation or near orbital modulation (in the case of the superhump phenomena) could be resolved. In total, there was 16 hours of on source exposure time spread across the three days; Table 5.1 summarises these exposures.

The spectra were pipeline reduced and calibrated using version 2.23 of CALFUSE (Dixon & Sahnow 2003). Each spectrum used is a combination of all FUSE channels where the worm distortion in LiF1B has been masked and the LiF1B has been scaled to match the flux strength of LiF2A. The wavelength range of < 1000 Å in LiF2B proved to be extremely noisy so this was masked during the co-adding of the spectra. In the processing logs of Detector 1, warning flags were given for exposures 8-12 of the second nights observations so for these spectra, only Detector 2 channels were co-added.

Two different versions of the time-series are presented in this chapter. Firstly, there are the original exposures, of which there were 33, ranging in exposure times from ~ 450 to nearly ~ 4000 seconds (see Table 5.1). The second version of the time-series is a 100 second sub-set spectra of the original exposures, resulting in 653 spectra with a far greater temporal resolution but, a much lower signal to noise. In both data sets the spectral resolution was ~ 0.1Å. This analysis primarily concentrates on the 100 second data but where stated, the original exposures are used.

5.3 Analysis of the FUSE Observations

5.3.1 The Spectrum

Fig. 5.1 is the time-averaged spectrum of V592 Cas from the combined channels of the FUSE time-series; the spectrum has been de-reddened with the assumption that $E(B-V) = 0.25$ (Taylor *et al.* 1998). The spectrum is clearly dominated by interstellar components of atomic and molecular hydrogen. Fig. 5.2 is a plot comparing a small section of the FUSE spectrum with a theoretical interstellar, molecular hydrogen transmission spectrum based on a column density of $\log(N(cm^{-2})) = 21.1$ and generated by McCandliss (2003); no attempt has been made to actually fit the molecular hydrogen in the V592 Cas spectrum, it is merely shown for demonstrative purposes.

The abundance of interstellar features makes it difficult, but not impossible, to identify the wind features and as such it has been possible to identify the wind diagnostic lines of C III 1176Å, P V 1118 and 1128Å, S IV 1063 and 1073Å, O VI 1032 and 1038Å, and Lyβ (the rest wavelengths have been identified in Fig. 5.1). In comparing the time-averaged FUSE spectrum of RW Sex and V592 Cas it is found that although the low ions of C III and S IV are of similar strength, the higher ions of P V and O VI are much deeper for RW Sex.

It is unfortunate that there are no archive spectra with which the time-averaged FUSE spectrum can be compared with since this would allow a long term test of profile stability to be performed. However, a comparison of continuum strength between these FUSE observations, archive IUE spectra and the optical observations presented in § 4 does reveal it to be relatively stable over the long time-span (approximately 20 years) covering the three sets of observations (see Fig. 5.3). At the very least, this means that the high mass transfer rate and accretion disc are stable.

5.3.2 Line Profile Variablity

The key observational disc wind characteristics of RW Sex (far-UV, see § 3) and V592 Cas (optical, see § 4), was the presence of a blue-shifted variable absorption. Fig. 5.4 demonstrates that this highly, variable, blue-shifted absorption is also present in the FUSE spectrum of V592 Cas, by showing the changes that occur to five selected wind diagnostic lines. For each plot, the same two spectra (which are separated in time by 18 hours) are shown indicating that this variability is not only detectably strong but, it also appears

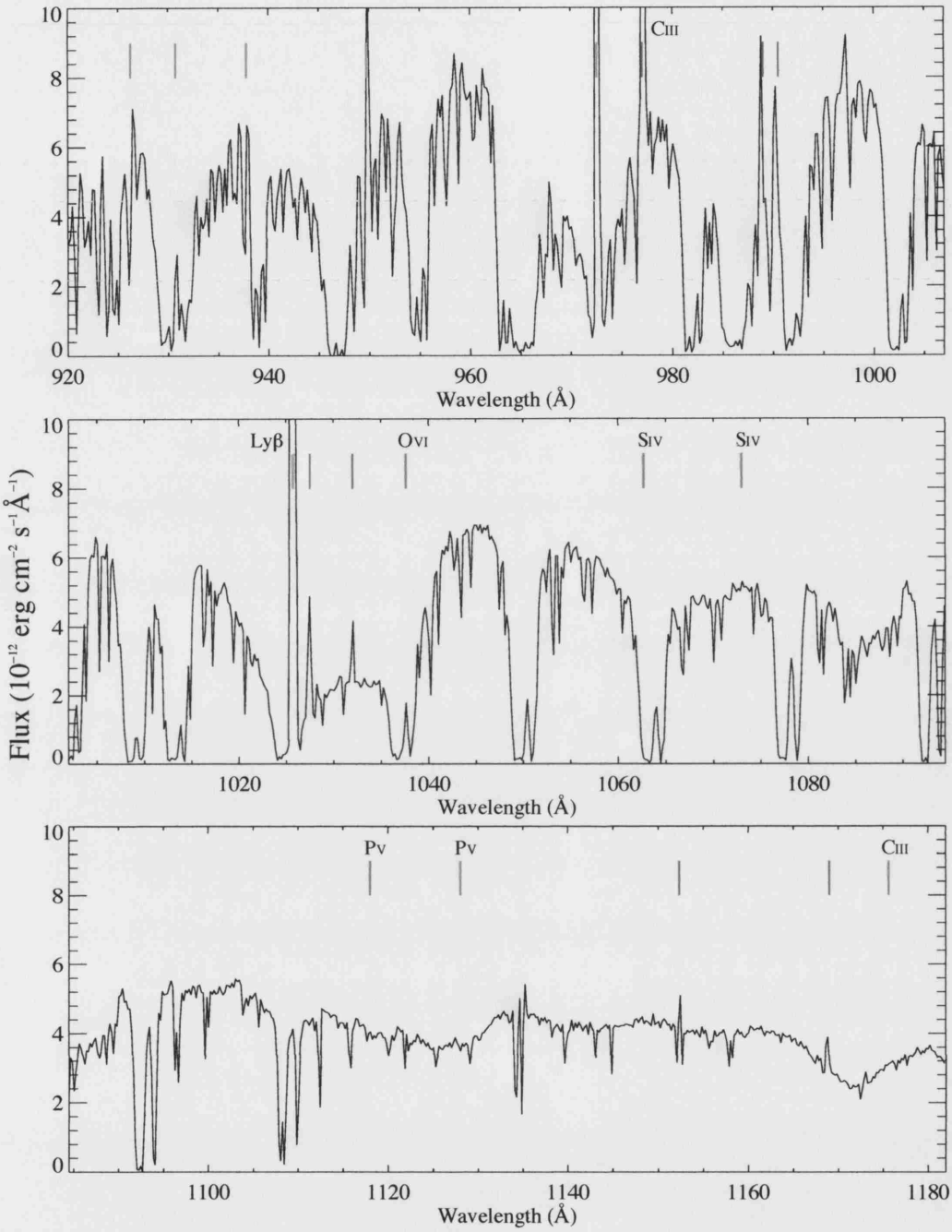

Figure 5.1: The time-averaged spectrum of V592 Cas from the combined FUSE channels; the spectrum has been dereddened based on an $E(B-V) = 0.25$. The rest wavelengths of the hydrogen Lyman lines (in red) and several other key lines (in green and blue) have been marked with vertical lines. The features which have been marked in green are highly variable and are most likely contaminated by airglow due to the low orbit of FUSE. This spectrum has been binned to 0.02Å.

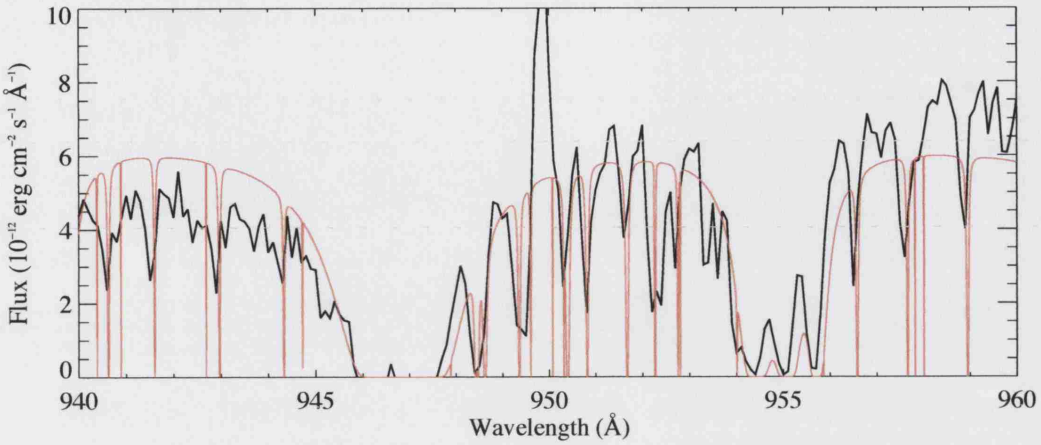

Figure 5.2: A plot comparing a small section of the FUSE mean spectrum of V592 Cas, with a synthetic interstellar molecular hydrogen transmission spectrum.

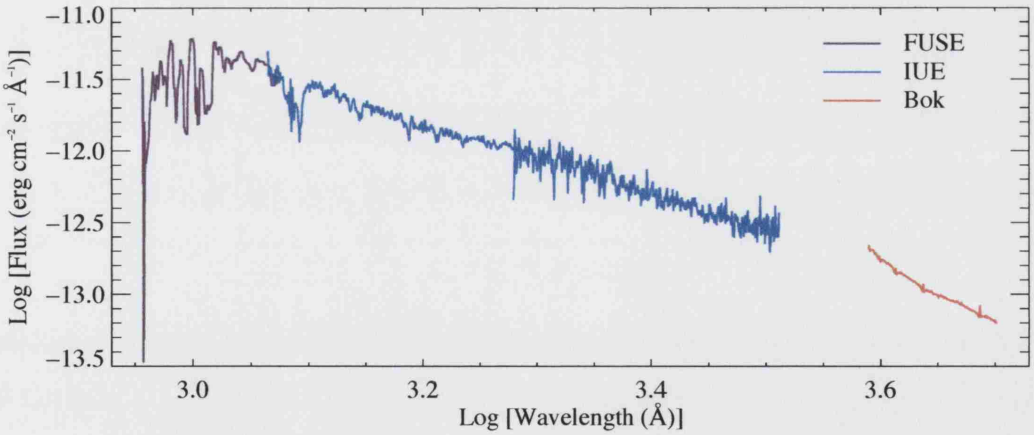

Figure 5.3: The de-reddened combined FUSE (purple line), IUE (blue line) and optical (red line) spectrum of V592 Cas. The IUE exposure was taken in 1982, the optical spectrum was taken in 2001 and the FUSE observations were taken in 2003, demonstrating that the continuum has remained stable in strength over a 20 year period.

to be simultaneous between all the lines. From the black to the red spectrum, there is a large increase in the depth of the blue-ward absorption but there does not appear to be any comparative change in the red-ward side of the profiles (other than the simultaneous blue-ward changes of a doublet companion). The changes to the S IV and P V lines are much weaker than the changes to the Lyβ and C III lines.

Fig. 5.5 is a plot of the temporal variance spectra for the P V doublet and the C III 1176Å line. These two lines were chosen to demonstrate the variance of the resonance lines because they were the lines least affected by additional components such as interstellar lines. As might be expected given the line comparisons in Fig. 5.4, the vast majority of the variance for both lines is at negative or blue-ward velocities. Using the 95% confidence level as a reference point, the variance at positive velocities is up to $\sim$ 500 km/s for the P V doublet and up to $\sim$ 750 km/s for the C III line but, towards negative velocities the P V doublet extends to over -1000km/s (the proximity of the shorter wavelength doublet and the relative strength of the noise in comparison to the variance makes this difficult to judge) and the C III variance extends to ~ -3500km/s, clearly showing the blue-ward dominance of the variance. The velocity at which the variance peaks is not so easy to tell from these plots. For the P V doublet, the TVS would suggest that the greatest variance is very close to the line centre but, given the noise it is not possible to tell whether this is an accurate observation. The peak in the variance profile for C III is between -1500 and -1000 km/s; the airglow feature at ~ -2000km/s is of course, excluded from this analysis. One further observation of both TVS plots is the large reduction of variance at ~ -250km/s which appears to be a greater change in variance than the general scatter of the data points. There is little that can be told about the variance drop from just these plots but they may indicate either a stable velocity range within the wind (unlikely) or a two component wind.

5.3.3 Modulation Analysis

So far, the analysis of the FUSE resonance lines has revealed the presence of highly variable blue-shifted absorption. These results are similar to that of the Balmer lines of V592 Cas (see § 4) and, the far-UV resonance lines of RW Sex (see § 3). One of the most important characteristics discovered for these two sets of observations was that the absorption is modulated close to or on the orbital period; modulation has yet to be established for these FUSE observations of V592 Cas. As a test of modulation for multiple

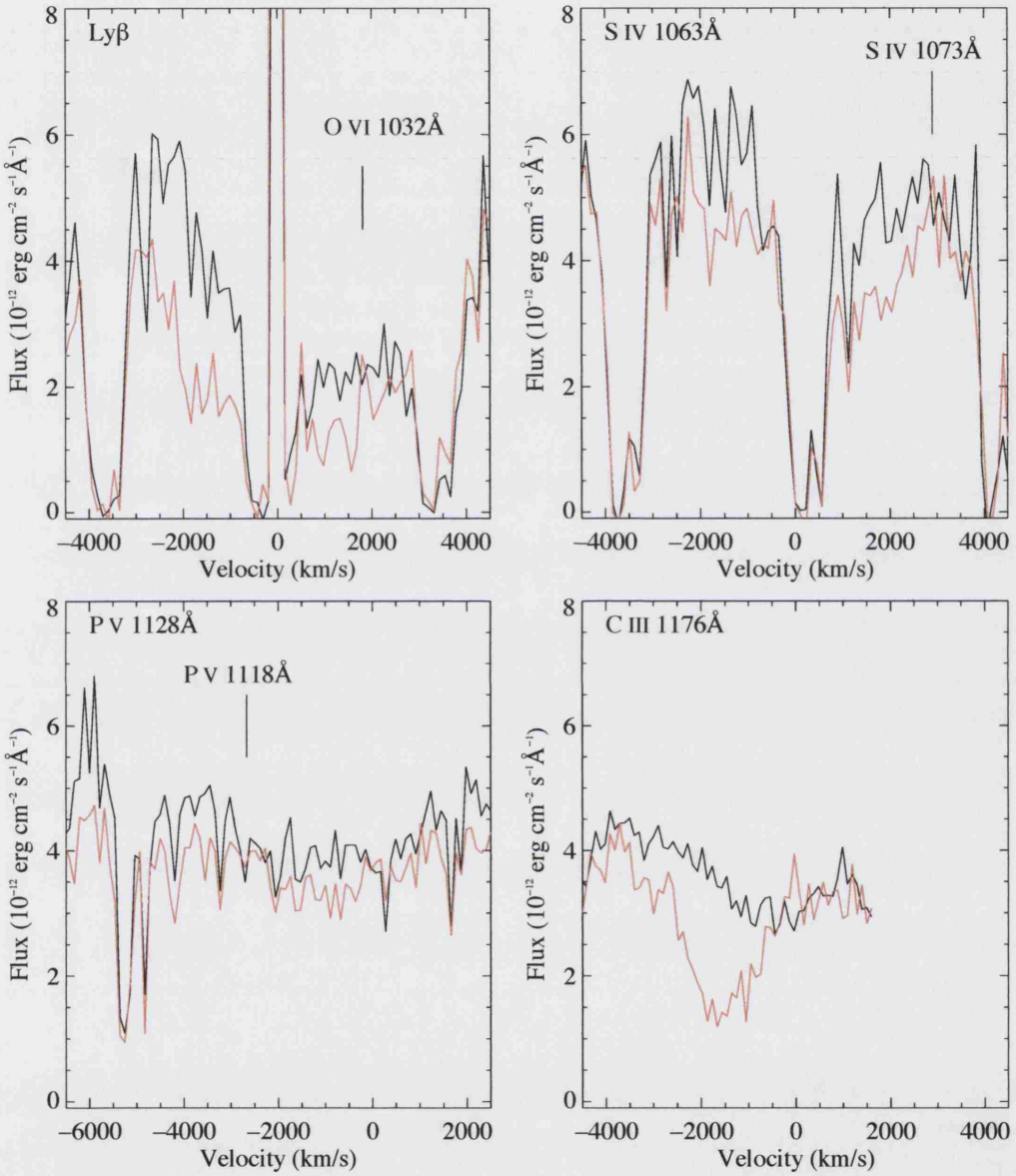

Figure 5.4: A demonstration of the line profile variability of Lyβ, O VI, the S IV doublet, the P V doublet and the C III lines. The two spectra (from the original exposures), which are separated in time by $\sim$ 18 hours, have been re-binned to a spectral resolution of 0.4 for this illustration Å.

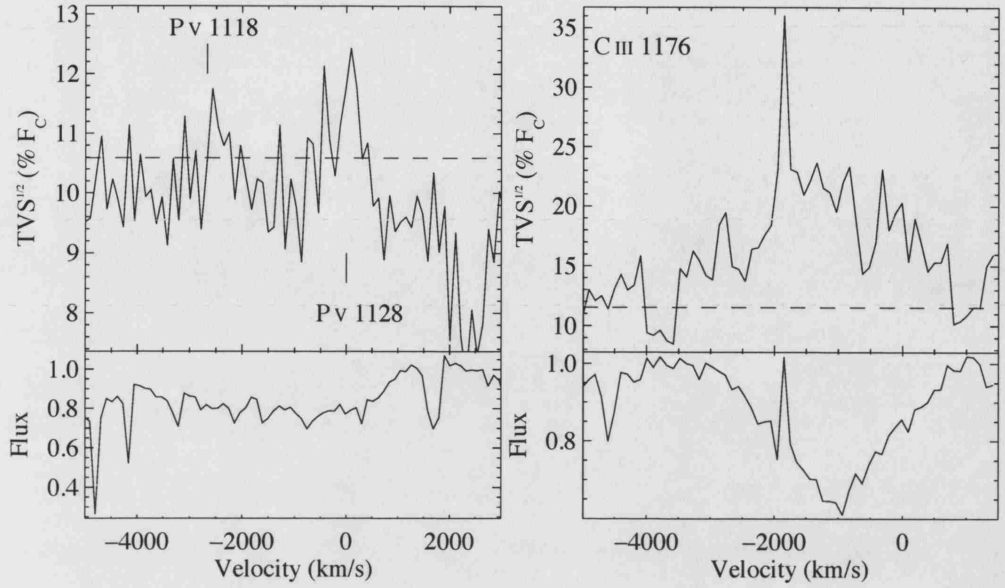

Figure 5.5: Temporal variance spectra of the P v doublet (zero velocity located on P v 1128Å) and the C III 1176Å line, from the FUSE time-series of V592 Cas. The spectra have been binned to 0.4Å and the horizontal dotted line indicates the 95% confidence level of no variability.

periods, Fig. 5.6 is a Fourier 2D plot of the C III 1176Å line. The frequency range shown has been selected to allow the identification of modulation close to the orbital period (such as the positive and negative superhumps) and also on other, shorter periods, such as the 22 minute period presented by Kato & Starkey (2002).

By far the strongest, most obvious signal of modulation in Fig. 5.6 is on a frequency of 8.675 cycles per day or a period of 0.1153 days. This strong signal spans from ~ -2500km/s to $\sim$ 500km/s and there is a small gap in the signal between ~ -1000 and ~ -500km/s; a gap which is close to (but does not exactly coincide with) the drop in variance noted for Fig. 5.5. A scan across the plot at greater velocities reveals no signal on the 22 minute period or on any other frequency other than that of the orbital period (or close to it). This is a significant result because it indicates that this blue-shifted absorption is orbitally modulated (or close to), just as was found in the optical observations of V592 Cas and, in the FUSE observations of RW Sex. The half-width at half-maximum of this fourier signal would indicate an uncertainty on this frequency of $\pm \sim 0.003$ days, which is borderline to distinguish whether the modulation is on the orbital period or the negative superhump period (this period is 0.112 days).

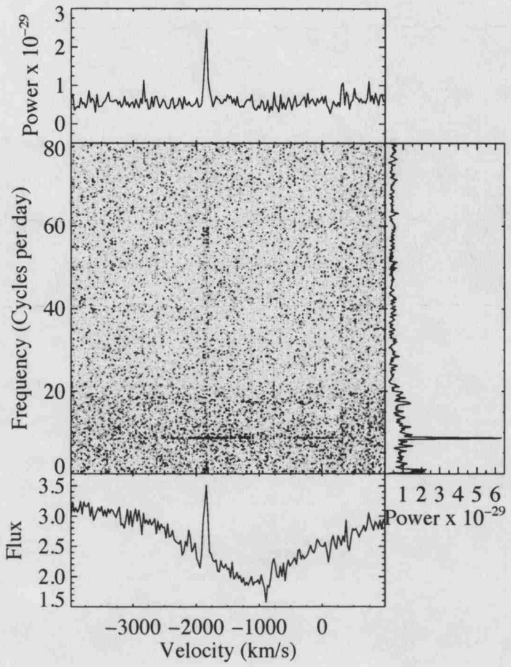

Figure 5.6: The Fourier 2D plot of the C III 1176Å line, from the FUSE observations of V592 Cas. The line plots to the top and right hand side are summations of power in the frequency and velocity domain. The Fourier transforms were performed on data which has been co-added into bins of 0.01 days.

Fig. 5.6 suggests that variability of the blue-shifted absorption is modulated on the orbital period rather than either of the superhump periods but the errors on these Fourier peaks means a clear-cut answer is not given. To provide a more definitive test, equivalent width measurements were taken from the C III 1176Å line, between a velocity of -2000 and -1000 km/s (to provide a good sample of the wind) and then folded on each of the three periods; the results are shown in Fig. 5.7. Unfortunately the ephemeris used in § 4 is not accurate enough to provide reliable phases for these data. The coherence in the data points when they are folded on both superhump periods is much lower in comparison to when they are folded on the system orbital period. This is a clear indication that the modulation to the wind is on the orbital period and definitely not on either of the superhump periods; this is discussed further in § 5.4.

As well as being modulated on the orbital period, Fig. 5.7 shows that the strength of the absorption does not vary sinusoidally and therefore not symmetrically. The peak in the absorption strength conveniently occurs at $\phi \approx 0$ and is followed by a gradual reduction

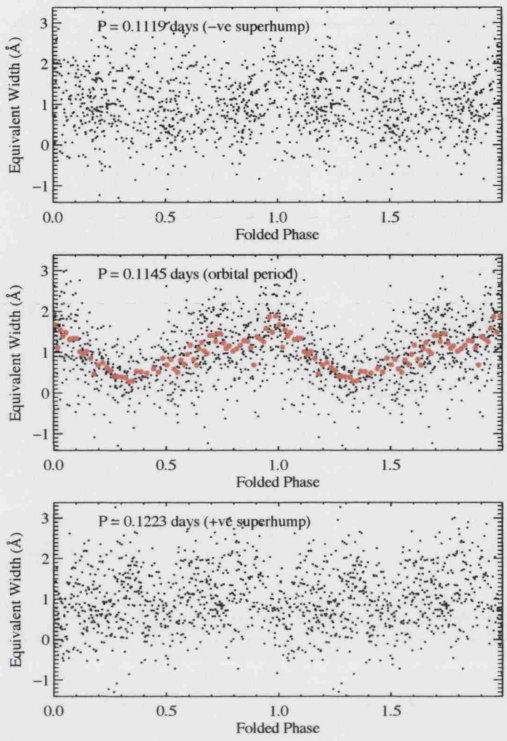

Figure 5.7: The C III 1176Å equivalent width between -2000 and -1000 km/s, folded on the orbital period and, the positive and negative superhumps. $\phi = 0.0$ has been arbitrarily defined from the date of the first spectrum in the series. The red data points for the orbitally modulated data are the original measurements (see e.g. Table 5.1) binned by a ratio of 10:1 to show how the equivalent width varies more clearly.

to a minimum at $\phi \approx 0.3$. The subsequent rise to maximum absorption strength continues until $\phi \approx 1.0$ although, there is a small bump in favour of a stronger absorption at $\phi \approx 0.7$. Fig. 5.8 is a plot showing the Gaussian central velocity and FWHM of the C III 1176Å line against orbital phase from single Gaussian fits to the profile (the Gaussian profile proved to be a reasonable approximation to the C III 1176Å line); the measurements were taken from spectra co-added into bins of width $\Delta\phi = 0.1$ to improve the accuracy of the results. Just as with the equivalent width measurements the variability of the central velocity is not symmetric. To a reasonable estimation, the phase at which the velocity is least blue-wards coincides with the phase of the weakest absorption. A similar relation is found between the phase of the most blue-ward velocity and the phase of the strongest absorption. The plot of FWHM against orbital phase does demonstrate some variability

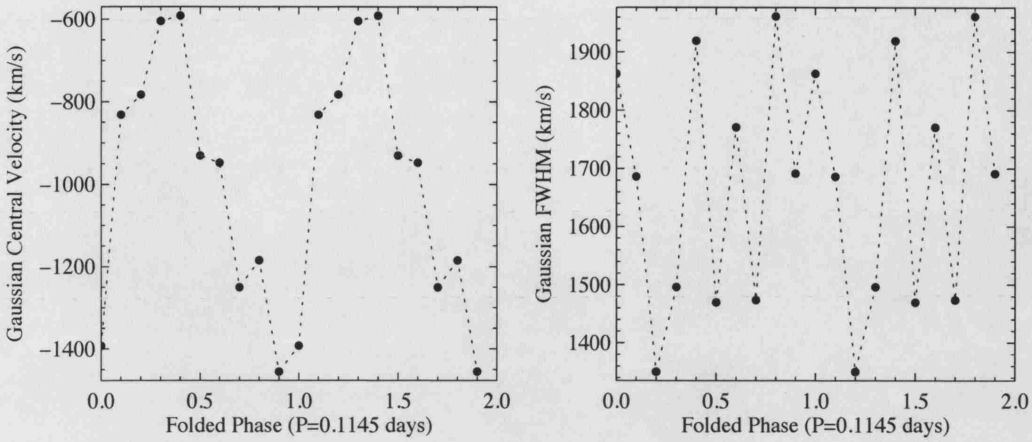

Figure 5.8: The Gaussian central velocity and full width at half maximum of the C III 1176Å line against folded phase (where P=0.1145 days). The measurements were taken from FUSE spectra, co-added into bins of width $\Delta\phi = 0.1$.

in the line-of-site velocity dispersion (the dispersion ranges from 1350 km/s to 1960 km/s) but, there is no clear pattern to this variability.

Measurements of the velocity and the equivalent width across the -2000 to -1000 km/s band of the C III 1176Å line were also taken for RW Sex (see § 3.5.6 and § 3.5.8). With many similarities, such as an orbitally modulated wind, already existing between the two stars, a unique opportunity is presented to make a comparison. A comparison between these measurements of V592 Cas and the same measurements of RW Sex (see Figs. 3.17 and 3.23) reveals that for both stars, a minimum in absorption equivalent width (between -2000 and -1000 km/s) coincides with the least blue velocity. It is also discovered that, the orbital modulation of the two quantities for the two stars is not symmetric although in the case of RW Sex, it is the reduction to absorption minimum which is fastest, rather than the rise to absorption maximum like it is with V592 Cas. Despite the weakness of the variability of V592 Cas' wind in comparison to that of RW Sex's (the C III 1176Å TVS for RW Sex peaked at over 55% above the background level while the same plot for V592 Cas only peaked at 15% above the background level) there are clearly very strong similarities between them and, without knowing the reasons for the asymmetry it is unknown whether this slight difference in orbital modulation characteristic is significant or not.

Fig. 5.9 further demonstrates the clear orbital modulation of the disc outflow (and its confinement to blue-ward velocities) with greyscale representations of the C III 1176Å,

S IV 1073Å and O VI 1038Å lines. If the spectra had been folded on a period a few percent shorter or longer (i.e. negative or positive superhump periods) then with data of this temporal sampling, the observed coherence in data points would not be seen. The relative weakness of the variability in all lines apart from C III 1176Å has made it difficult to confirm with some certainty, whether the variability in all lines is acting synchronously or out of phase. Fig. 5.9 shows that for a range of ionisation states, the orbital modulation is closely in phase with each other. The one key difference which is observed between the lines is that the orbital modulation of the low ionisation C III line extends to greater velocities (~ -3000 km/s) than the higher ionisation S IV lines (closer to -2000 km/s) although this is probably just an optical depth effect. Regardless of the spectral line involved, the orbital modulation is characterised by an initial rapid reduction in the velocity of the absorption, followed by a more gradual return to larger blue velocities; the effect of this modulation is to "draw" a series of asymmetric patterns. This is notably different from the optical observations where the pattern of modulation was more symmetric (see Fig. 4.12).

In this section, the analysis that reveals the orbital modulation of the disc outflow, along with the nature of the modulation, has been presented. Apart from a swap in the asymmetry at which the central velocity reaches a maximum and a minimum, remarkable similarities have been demonstrated between these FUSE observations of V592 Cas and the FUSE observations of RW Sex presented in § 3 and, it is most likely that the same mechanism operates in both systems. In the following section, the orbital modulation of the outflow is discussed in greater detail, with reference to RW Sex and other CVs showing UV orbital modulations.

5.4 Discussion

This analysis of the FUSE observations of V592 Cas has revealed the presence of a strong, blue-shifted absorption for the far-UV resonance lines. Time-series analysis of the absorption shows it to be modulated on the system orbital period (P=0.1145 days) and not, on either the negative superhump period (P=0.112 days - this was only a weak detection by Taylor *et al.* (1998) and there has been no further attempt to confirm its presence) or on the positive superhump period (P=0.122 days). If it is true that a negative superhump is indicative of a warped or tilted disc and a positive superhump is indicative of an eccentric

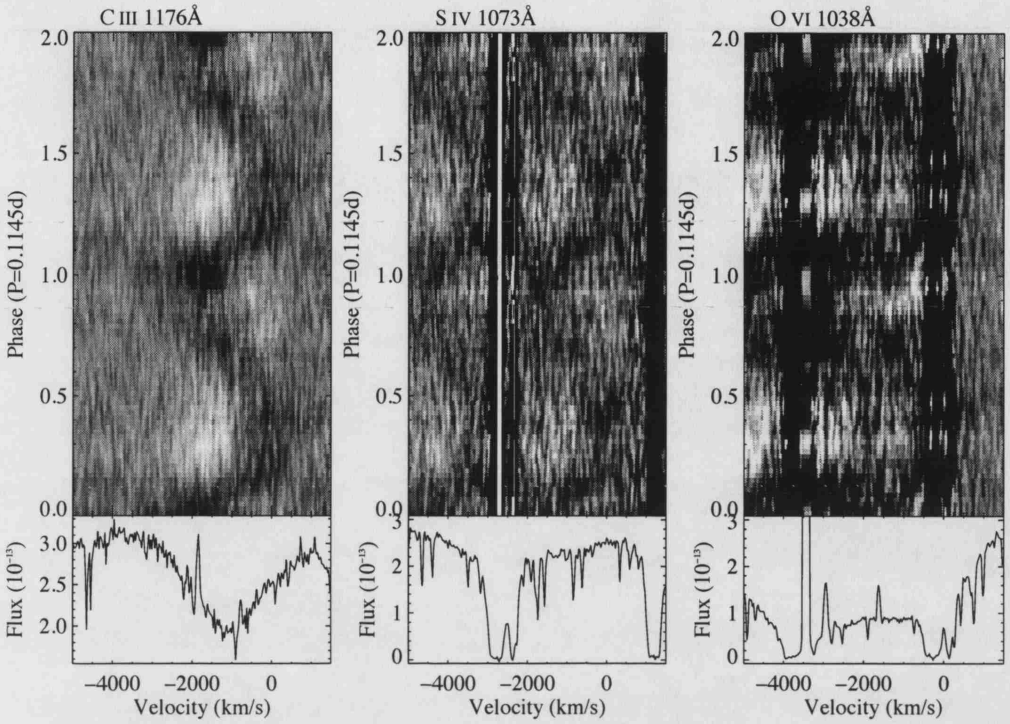

Figure 5.9: Greyscale representations of the orbitally modulated behaviour of the C III 1176Å, S IV 1073Å and O VI 1038Å lines from the FUSE time-series of V592 Cas. The spectra were co-added into bins of width $\Delta\phi = 0.02$, normalised by the mean, and repeated for two cycles.

disc, then the lack of detection of the absorption modulation on either period would infer that neither characteristic has an effect on the observed variability. The clear similarities shown between this system and RW Sex (see § 5.3.3) further bolster this claim since there has been no superhump detection for the latter (e.g. Prinja *et al.* 2004).

The advent of the IUE and other far-UV/UV telescopes has resulted in the discovery of a number of CVs whose UV resonance absorption lines exhibit orbital modulation and now, with the analysis of far-UV time-series of both RW Sex and V592 Cas, two more systems can be added to the list; Table 5.2 is thought to be a comprehensive list of these systems. It is extremely helpful in understanding the cause of the orbital modulation to have multiple systems exhibiting these properties but, when systems are to be grouped together, the characteristics of the orbital modulation must also be considered. The studies cited in Table 5.2 which describe the orbital modulation, use time-series from FUSE, HST and IUE. Ideally, a comparison between the studies would use a common set of

spectral lines and, this is possible for limited number of the studies since lines of N V, Si IV and C IV are present in both IUE and HST spectra. However in reality, such a comparison would have to rely on the theory that common characteristics would be observed in all of the UV resonance lines. It should also be noted that for the superhumping CVs listed, it is not necessarily true that the modulation is not on either superhump period since for many of the studies there has been no indication as to whether this was tested (or whether the time sampling of the data supported a test).

In comparing the disc wind orbital modulation characteristics of the CVs listed in Table 5.2 it is clear that there are some systems showing very similar characteristics and therefore can be grouped together. These groups are:

1. CVs who's blue-shifted absorption undergoes shifts in velocity but no apparent change in strength; the manner of the velocity is well matched by a sinusoid. The CVs which belong to this group are AH Her, DX And and IX Vel.

2. CVs who's blue-shifted absorption undergoes significant variation in strength which when quantified with either mean flux or equivalent width, is well matched by a sinusoid. This is the largest of these groups and it contains V3885 Sgr, SU UMa, V603 Aql and AH Men and, could potentially contain TT Ari and Z Cam but the temporal sampling of the data used did not support a test of sinusoidal variation of the absorption strength.

3. CVs who's blue-shifted absorption not only undergoes significant variation in strength but also undergoes velocity shifting, both quantities of which are well matched by a sinusoid. The CVs which belong to this group are IR Gem and YZ Cnc and, at least for IR Gem it was mentioned that the velocity shift of the line profile was at a minimum when the absorption was at its deepest.

4. CVs who's blue-shifted absorption undergoes significant variation in strength and velocity shift but both quantities are not well matched by a sinusoid and in fact vary with an asymmetric function. The CVs which have been added into this group are V592 Cas and RW Sex and, the only strong differences in the modulation between them is in the specific pattern to this modulation.

5. This final group holds just one system, V795 Her. The observations of it's blue-shifted absorption indicate a strong variation in its strength but it appears to be

Table 5.2: A list of cataclysmic variables which are shown to exhibit orbital modulation of UV absorption. The table has been sorted by type (NL = Nova-Like, DN = Dwarf Novae, Na = Fast Nova and IP = Intermediate Polar) and then by period. The dwarf novae listed in the table below would have been observed during outburst since it is only during outburst that the wind is present.

Star	Type	Period (days)	Inclination (degrees)	Orbital Variability Reference	Superhumps?
V795 Her	NL	0.108	—	Rosen *et al.* (1998)	Yes (Patterson & Skillman 1994)
V592 Cas	NL	0.115	$28^{\circ}{}^{+11}_{-10}$	This chapter	Yes (Taylor *et al.* 1998)
TT Ari	NL	0.138	—	Stringfellow *et al.* (1993)	Yes (Skillman *et al.* 1998)
IX Vel	NL	0.194	< 60	Mauche (1991)	—
V3885 Sgr	NL	0.216	< 50	Woods *et al.* (1992)	—
RW Sex	NL	0.245	$32^{\circ} \leq i \leq 52^{\circ}$	See § 3	No (Patterson, private comm.)
IR Gem	DN	0.068	—	Woods *et al.* (1992)	Yes (Kato 2001)
SU UMa	DN	0.076	—	Woods *et al.* (1990)	Yes (Kato 2002)
YZ Cnc	DN	0.087	$38 \pm 3^{\circ}$	Woods *et al.* (1992)	Yes (Patterson 1979)
AH Her	DN	0.258	$46 \pm 3^{\circ}$	Knigge *et al.* (1994)	—
Z Cam	DN	0.290	$51^{\circ} \leq i \leq 61^{\circ}$	Szkody & Mateo (1986)	—
DX And	DN	0.441	$45 \pm 12^{\circ}$	Drew *et al.* (1991)	—
V603 Aql	Na	0.138	$13 \pm 2^{\circ}$	Borczyk *et al.* (2003)	Yes (Patterson *et al.* 1997)
AH Men	NL	0.139	—	Mouchet *et al.* (1996)	Yes (Patterson 1995)

due to the rise and decline of an emission peak centred on -600 km/s and not from the absorption changing in strength. Also, this change occurs across a very limited phase range of the orbit ($\Delta\phi = 0.4$) and is therefore not well matched by a symmetric function such as a sinusoid.

The modulation characteristics for which the CVs have been grouped are obviously very rough interpretations of the descriptions provided in the studies. Given new data and a new study, it would also be possible for a CV to be reclassified into another group. For example, several of the systems show sinusoidal variability in either velocity or flux, but this detected sinusoidal behaviour may be related to the low time resolution of the data used (such as IUE) and the variability may in fact be asymmetric, as it was for V592 Cas and RW Sex; data with better temporal resolution would reveal whether this is the case. Also, some of the CVs show only one variable parameter of the blue-shifted absorption (either the velocity or strength), data with a better signal to noise and higher temporal resolution would reveal whether the other parameter is in fact variable as well.

The advantages of studying blue-shifted absorption troughs (and also orbitally modulation of this absorption where it exists) is the hope that a pattern in system parameters may be discovered leading to some insight into the reasons for the observed behaviour. It is true that all the systems listed in Table 5.2 have a non-eclipsing or low inclination angle (for those systems for which the inclination angle is known) but, this is most likely an observational selection effect of a bi-polar outflow against an accretion disc. There are similarities to be found between the CVs in some of the groups. For example, the two CVs whose orbital modulation shows sinusoidal variation in flux strength and velocity shift (IR Gem and YZ Cnc), are both relatively short period dwarf novae. Drew (1993) suggest that short period dwarf novae are more likely to demonstrate orbitally modulated disc winds if the location of the line emission source is determined by the mass of the primary star and the disc radius, meaning that for short period systems the shadowing of the emission source is more significant. However, when a comparison of those systems only demonstrating a variation in absorption strength is made, this does not seem to hold true since a range of periods (and CV types) is seen for these systems. It is also interesting to note that four of the six systems which were categorised into this group are known to be superhumping, although what this means in the context of a sinusoidally varying absorption strength is unclear. It is clear that a far larger sample of CVs exhibiting or-

bitally modulated UV absorption is required before a pattern can be properly searched for (if one does in fact exist) although with the failure of the Space Telescope Imaging Spectrograph (or STIS) on HST, FUSE is now the only UV spectrograph left so this may not be possible.

In all of the orbital modulation studies listed in Table 5.2, the biggest problem has been in identifying a suitable mechanism for breaking the axi-symmetry of the disc outflow. Given the similarity in behaviour between RW Sex and V592 Cas, it is believed that the same mechanism is responsible for breaking the axi-symmetry in both CVs although it is not yet clear what that mechanism may be. Suggestions of stream overflow, magnetic confinement by the white dwarf or accretion disc and, a warped or tilted disc have all been made (see § 3.7 and § 4.6) and although the latter suggestion is the preferred one, the lack of detection of a negative superhump period has made it less favourable and more difficult to explain. The favoured mechanisms described in the studies listed in Table 5.2 seem to prefer an axi-symmetric outflow and an asymmetric line emission source rather than an outflow with a break in axi-symmetry. An asymmetric emission source could occur on the disc if it originated from a single location such as an impact region. The most obvious impact region on an accretion disc is the bright spot, where the accretion stream collides with the side of the accretion disc. For a low inclination CV, the velocity amplitudes at the edge of the disc would be on the order of a few hundred km/s which are much lower than the velocity amplitudes observed for the wind absorption of RW Sex and V592 Cas. Perhaps a more suitable source of line emission would occur if the system were undergoing stream overflow (as in the case of SW Sex stars), in which case the re-impact point would be much closer to the white dwarf, resulting in higher velocity amplitudes which could act as the suitable emission line source (Lubow 1989; Marsh *et al.* 1990) although it should be noted that the optical characteristics of V592 Cas do not agree with this interpretation (see § 4.6). One final possibility for creating an asymmetric emission source are spiral shocks in the accretion disc. Numerical simulations show that these spiral shocks can grow to the size of the accretion disc and there is a potential for them to be long-lived. Such shocks are likely to be fixed in the binary rotation frame and thus the potential exists for the non-axisymmetric structure to pervade not only the disc but perhaps the outflow itself (Spruit 1989*a*; Spruit 1989*b*). However, although these spiral shocks have been detected in some CVs (e.g. U Gem, Neustroev *et al.* 2004) it still proves difficult to simulate their behaviour and hence they are not fully understood (e.g. Godon *et al.* 1998).

It is possible to conceive methods by which an accretion disc wind can be orbitally modulated, even for systems with low inclination but, what is lacking is definite proof of any one mechanism. For the majority of systems in which absorption strength or velocity varies sinusoidally, the mechanisms in which either the outflow or the line emission source are asymmetric can provide a suitable and understandable solution but, for V592 Cas and RW Sex an added complication arises in explaining the asymmetric velocity and flux curves. Do V592 Cas and RW Sex posses a modified version of the outflow mechanism employed by those systems whose quantities vary sinusoidally or are there fundamental differences? It is interesting to note that the optical observations of V592 Cas (see § 4) do reveal a sinusoidally varying blue-shifted absorption but how does this fit in with the asymmetrically varying absorption observed at far-UV wavelengths? Is the same phenomenom being observed? These are some of the important questions being raised by the study of disc winds from CVs. Although as yet there are no clear solutions as to how the disc winds are driven and why they present certain characteristics, the work in this thesis is helping to contribute to a solution by providing detailed individual accounts (or case studies) of the wind driving characteristics of several CVs.

CHAPTER 6

Optical Spectroscopy of BZ Camelopardalis

This chapter presents the results from time-series optical spectroscopy of the low-inclination, nova-like cataclysmic variable, BZ Camelopardalis. This case study focuses on the re-analysis of observations taken with the William Herschel Telescope (or WHT) and continues with the analysis of a previously unreleased set of observations, taken at the McDonald Obsevatory in Texas. The case study concludes with a discussion of these results in context with data which has already been published.

6.1 Introduction

RW Sex and V592 Cas are two relatively similar, UX UMa CVs and as it was shown in § 4 they also have similar disc wind characteristics (i.e. the orbitally modulated wind). In this chapter, the optical disc wind characteristics of a slightly different CV, BZ Cam, are studied. Just like RW Sex and V592 Cas, BZ Cam is a high-state, low inclination nova-like CV but it is a VY Scl nova-like system rather than a UX UMa system. In this case study, the results of analysing an optical time-series of BZ Cam taken with the 2.2-m telescope at the McDonald Observatory in Texas are presented, along with the re-analysis of an optical time-series taken with the 3.6-m William Herschel Telescope at La Palma and originally published by Ringwald & Naylor (1998).

6.2 Literature Review

BZ Cam has an orbital period of 3.68 hours or 0.153693 days (Patterson *et al.* 1996), which puts it well above the 2-3 hour period gap for CVs (see § 1.3.2). On timescales small enough to resolve the orbital period, the light-curve of BZ Cam is complex with a variety of small and large amplitude variations. Patterson *et al.* (1996) suggest the discovery of weak, transient signals in these light-curves above and below the orbital period which could be evidence for superhumping; Kato & Uemura (2001) published photometric evidence of a positive superhump with a period of 0.15634 days although they suggest that this is only detectable when BZ Cam is in a low state. Light-curves covering much longer time-scales demonstrate why BZ Cam belongs to the VY Scl subgroup of CVs. VY Scl CVs are sometimes referred to as anti-dwarf novae because for the most part they are in a state of constant outburst, fed by a high mass-accretion rate but, occasionally they enter a state of quiescence which for BZ Cam, means a drop in visual brightness of $\sim 1.5 - 2.0$ magnitudes. The first observed occurrence of BZ Cam entering a state of quiescence was in 1928 and was reported by Garnavich & Szkody (1988), who used light-curves derived from the Harvard Plate Collection. The plates recorded the visual magnitude dropping from $B = 12.5$ to $B = 14.1$ mag; unfortunately no spectra exist to detail the changes which occurred to the spectral lines during this period. Observations of BZ Cam entering a state of quiescence were made one other time, between 1999 and 2000, which was reported by Greiner *et al.* (2001) using observations mostly taken from the Variable Star Network (or VSNET). Fortunately on this occassion, spectra were taken both before and during the quiescence; stark differences were observed between the two states such as a flatter spectral slope, stronger emission lines and the notable omission of P-Cygni profiles (a feature indicative of a wind), as the system decreased in brightness.

A rare feature of BZ Cam is that it lies at the apex of a "bow-shock-like" nebula (see Fig. 6.1). The faint emission nebula around BZ Cam was originally identified by Ellis *et al.* (1984) on Palomar Sky Survey Prints. They suggested that the nebula could actually be an ejected shell from a nova eruption but this idea was later discounted in a more detailed study by Krautter *et al.* (1987). They provide two alternate explanations for the observed phenomenon; it is in fact a true planetary nebula or, the nebula was formed by an interaction between a stellar wind from BZ Cam and the surrounding interstellar medium. The blue-shifted absorption evidence (albeit intermittent) of BZ Cam's disc wind

Figure 6.1: The bow shock of BZ Cam. Credit: R. Casalegno, C. Conselice et al., WIYN, NOAO, MURST, NSF

was first discovered by Thorstensen in 1993 and later published by Patterson *et al.* (1996). Ringwald & Naylor (1998) suggested in a more detailed study of the "intermittent" disc wind, that it is unlikely to be due to blob ejection and is more likely a "normal" wind which switches on and off. They characterised the wind with a linear acceleration up to ~ -3000 km/s over a timespan of around 6 minutes followed by a linear deceleration over a 30-40 minutes period. The wind was not found to be modulated on any detectable period.

So far this literature review has focussed on optical studies of BZ Cam but, there have also been multiple studies of BZ Cam at UV and far-UV wavelengths. Griffith *et al.* (1995) performed a detailed study of the wind in the far-UV using data from the IUE archive (see Fig. 6.2 for an example short-wavelength IUE line). Although there were only 15 low resolution spectra (spread over a 28-hour time line) they found that the P-Cygni profiles varied considerably with time, especially C IV 1550Å and, they raised the possibility of an orbital modulation within these lines. The IUE data used by Griffith *et al.* (1995) lacked the temporal and spectral resolution necessary for a more detailed study. A more detailed data set collected using the Goddard High Resolution Spectrograph on board HST was presented by Prinja *et al.* (2000*b*); they discovered the wind of BZ Cam to be highly variable and that the resulting large changes to the profile were entirely constrained to

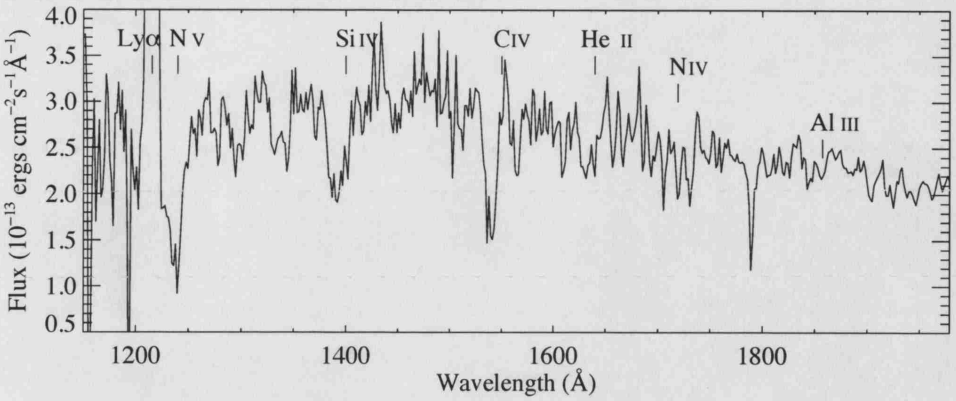

Figure 6.2: The IUE ultraviolet spectrum of BZ Cam with resonance lines marked (SWP13372). The exposure was taken on the 26th February, 1981.

the blue-ward absorption although the data set was not designed to search for the orbital modulation suggested by Griffith *et al.* (1995).

6.3 The Observations

6.3.1 The WHT Observations

The William Herschel data set analysed here was kindly provided in a reduced form by Fred Ringwald; the data was originally presented in (Ringwald & Naylor 1998). A brief description of the original observations are provided here.

This time-series of optical spectra was collected using the Intermediate dispersion Spectrograph and Imaging System (ISIS) on the 4.2-m William Herschel Telescope, La Palma. The observations were made on 1995 February 6/7 and 7/8 UT which will hereafter be referred to as nights 1 and 2 (see Table 6.1 for a summary of the observations). ISIS is a double armed spectrograph; for these observations it was configured with the blue arm centred on He I 5876 Å and the red arm centred on Hα. The R1200B and R1200R gratings were used with the blue and red arms respectively, giving a dispersion for all spectra of 0.4Å pixel^{-1}. In total there were around 650 usable spectra which are split between the two arms and the two nights. Each exposure lasted 20 seconds; the data provided was already reduced and co-added in pairs resulting in a temporal resolution of 60 seconds and a signal-to-noise ratio at the continuum of $\sim$ 48 for the blue arm and

	No. of Spectra	$T_{\rm start}$ (HJD)	$T_{\rm end}$ (HJD)	ΔT (days)	$\Delta\phi$
Night 1	155	2449755.40	2449755.56	0.161	1.05
Night 2	178	2449756.36	2449756.55	0.192	1.25

Table 6.1: A summary of each night of the WHT observing run for BZ Cam. The information provided for each night are the number of spectra, the start and end times as Heliocentric Julian Dates, and the phase coverage provided by the data.

~ 40 for the red arm. The data provided was flux calibrated and corrected for heliocentric velocity but not systemic velocity; the following analysis was carried out using the Interactive Data Language (or IDL) software package.

6.3.2 The McDonald Observatory Observations

This time-series of optical spectra was collected by F. Ringwald and R. Prinja using the Cassegrain spectrometer on the 2.1 metre Otto Struve telescope at the McDonald Observatory, Texas. The observations were secured during 7 nights between the 26th December 1998 and the 3rd January 1999, see Table 6.2 for a summary of observations. The resulting spectra covers a range of approximately 4300 to 5000 Å with a dispersion of ~ 0.9 Å per pixel. This range includes: the Balmer lines Hβ and Hγ; He I lines at 4471 Å and 4922 Å; the He II line at 4686 Å; the C III/N III Bowen blend at 4650 Å. Each exposure lasted for 180 seconds resulting in approximately 500 spectra covering seven nights, each with a S/N at the continuum of around 30. The frames were reduced with IRAF and the analysis was implemented in IDL by the author.

6.4 Analysis of the Optical Time-Series

6.4.1 The Spectra

This analysis of the BZ Cam optical spectrum begins with a look at the WHT data set. Fig. 6.3 is the mean average He I 5876 Å profile from the blue arm spectra. To the red of the He I profile are two Na D lines at 5889.95 Å and 5895.92 Å, which are mostly likely interstellar in origin. The He I profile is very much dominated by emission but there is a weak blue shifted absorption from the disc wind giving the profile a weakly P-Cygni

	No. of Spectra	$T_{\rm start}$ (HJD)	$T_{\rm end}$ (HJD)	ΔT (days)	$\Delta\phi$
Night 1	70	2451173.79	2451174.01	0.22	1.48
Night 2	96	2451175.61	2451175.97	0.36	2.36
Night 3	70	2451176.56	2451176.94	0.38	2.45
Night 4	52	2451177.68	2451177.91	0.23	1.51
Night 5	42	2451179.81	2451179.96	0.15	1.00
Night 6	57	2451180.72	2451180.93	0.21	1.39
Night 7	104	2451181.57	2451181.94	0.38	2.45

Table 6.2: A summary of each night of the McDonald observing run for BZ Cam. The information provided for each night are, the number of spectra, the start and end times as Heliocentric Julian Dates, and the phase coverage provided by the data.

shape. Fig. 6.4 is the time-averaged Hα and He I 6678 Å profiles from the red arm spectra. The Hα profile is heavily dominated by emission and no dip into absorption is observed as it was for the He I 5876 Å line. However, the line profile is asymmetric with a less steep decline in strength towards the red wing than towards the blue wing. The He I 6678 Å profile appears reasonably symmetric with no apparent evidence of an absorption component, unlike He I 5876 Å, although they are similar in core strength.

Fig. 6.5 is the time-averaged flux calibrated optical spectrum of BZ Cam from the McDonald Observatory time-series. The recent optical low state in 1999/2000 was estimated by Greiner *et al.* (2001) to have begun around May 1999 which is at least 5 months after this time-series was observed meaning that BZ Cam was still in a high optical state; Fig. 6.5 demonstrates this with a similar flux level to that observed during the documented optical high states such as Fig. 1 of Patterson *et al.* (1996). It is fortunate that the observations were taken before BZ Cam optical low state because the nature of disc winds suggests that the system needs to have a high mass transfer rate and therefore be in an optically high state; such events, although rare, have proved to be unpredictable. The main observation to be made from Fig. 6.5 is that the Hβ and Hγ lines both show similar asymmetry to their profile shapes as is seen for the WHT observations of Hα, which does infer that BZ Cam was in a similar level of high state between the two sets of observations.

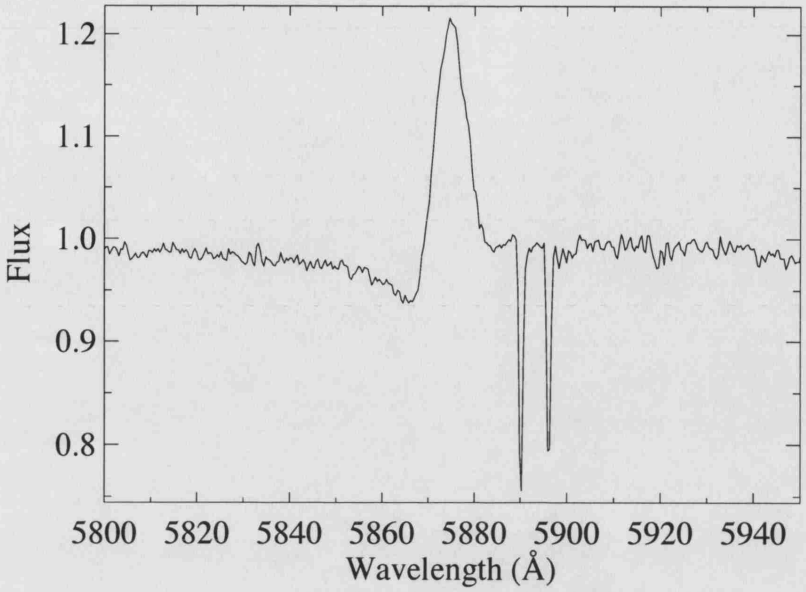

Figure 6.3: The mean normalised He I 5876 Å profile of BZ Cam from the 1995 WHT time-series. The two absorption lines red-wards of the He I profile are the Na D lines at 5889.95 Å and 5895.92 Å. The spectrum is an average of 328 ISIS blue arm spectra.

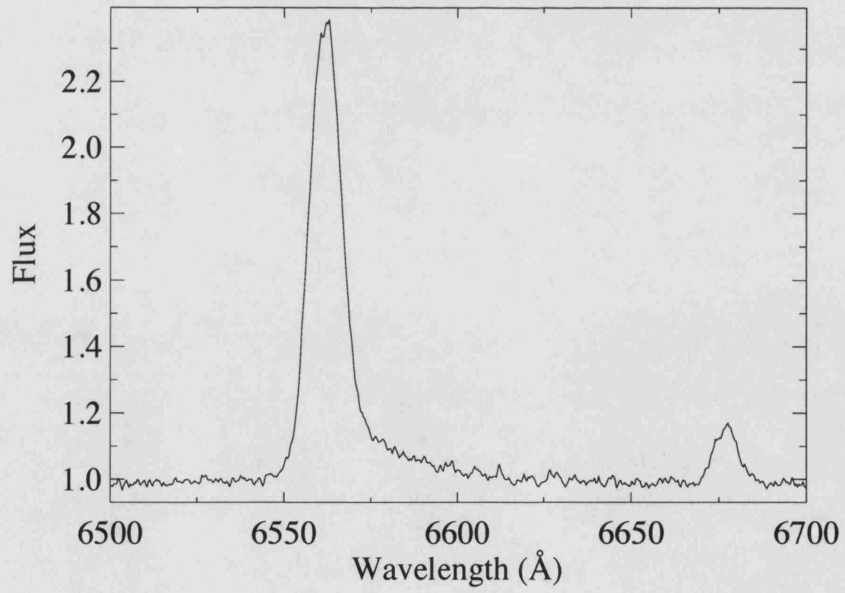

Figure 6.4: The mean normalised Hα (left) and He I 6678 Å (right) profiles of BZ Cam, from the 1995 WHT time-series. The spectrum is an average of 329 ISIS red arm spectra.

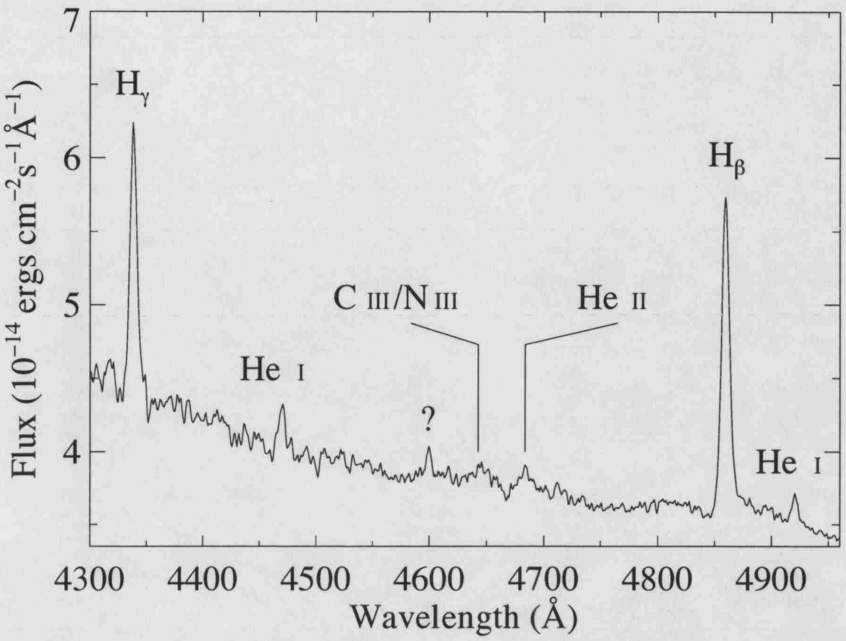

Figure 6.5: The mean flux calibrated optical spectrum of BZ Cam, from the 1998/1999 McDonald time-series. The feature marked '?' (at a wavelength of ~4600Å) has so far remained unidentified.

Fig. 6.6 demonstrates the variability of the He I 5876 Å line by displaying two extreme ISIS blue-arm profiles from the WHT time-series. The first difference to note is the slight blue shifting of the dotted profile in comparison to the solid line profile which is due to the binary motion of the stars within the CV system. Regardless of this, there is an enormous difference in the strength of the absorption and emission between the two profiles. In the solid line profile of Fig. 6.6, there is a very strong, blue-shifted absorption component to the overall line profile but in the dotted line profile the absorption component is almost non-existent and the emission is much stronger. These observations, which are separated in phase by $\Delta\phi = 0.40$, show that there is at least one variable component to the He I 5876 Å but they do not indicate whether the emission, the blue-shifted absorption or another component which has not been considered is variable.

Each pair of profiles shown in Figs. 6.6 and 6.7 represent the most extreme cases in both the red and blue arm data. Although the pair of spectra from Fig. 6.6 were not observed at the same time as the pair of spectra from Fig. 6.7, the two pairs of spectra do approximately correspond in orbital phase meaning that a phase dependent comparison can be made between the Hα and He I 5876 Å lines; the inference from comparing these

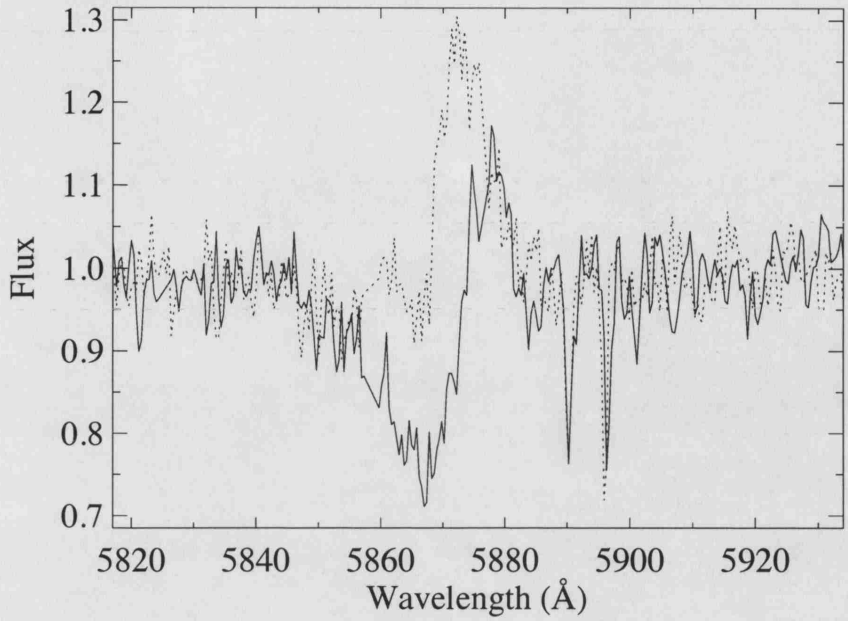

Figure 6.6: A demonstration of the line profile variability of the He I 5876 Å line using spectra from the WHT time-series. The spectrum with the solid line was exposed during night 1 and the dotted line spectrum was exposed during night 2. These two spectra are separated in time by 1.14 days, corresponding to a phase difference (based on an orbital period of 0.154 days) $\Delta\phi = 0.4$.

figures is that the change in strength and velocity is co-ordinated in phase between these two lines.

Fig. 6.8 is a demonstration of the variability of the Hβ line using spectra from the McDonald time-series. A velocity shift in the emission component is again observed as it was for Hα and the He I 5876 Å line from the WHT observations; this velocity shift is probably related to the orbital motion of the binary components. The observed changes to the shape of the Hβ line between the observations shows characteristics relating to both the He I 5876Å line and the Hα line. Other than the change in strength and velocity shift of the emission, the dotted-line profile has a strong blue-shifted absorption component which is not observed in the solid-line profile; this is similar to what was observed for the He I 5876Å line. From the dotted line profile to the solid line profile an excess of flux forms along the red wing of the line, (between 4870Å and 4885Å) this was also observed for the Hα line.

Figs. 6.6, 6.7 and 6.8 show considerable variability in the He I 5876Å and Balmer lines.

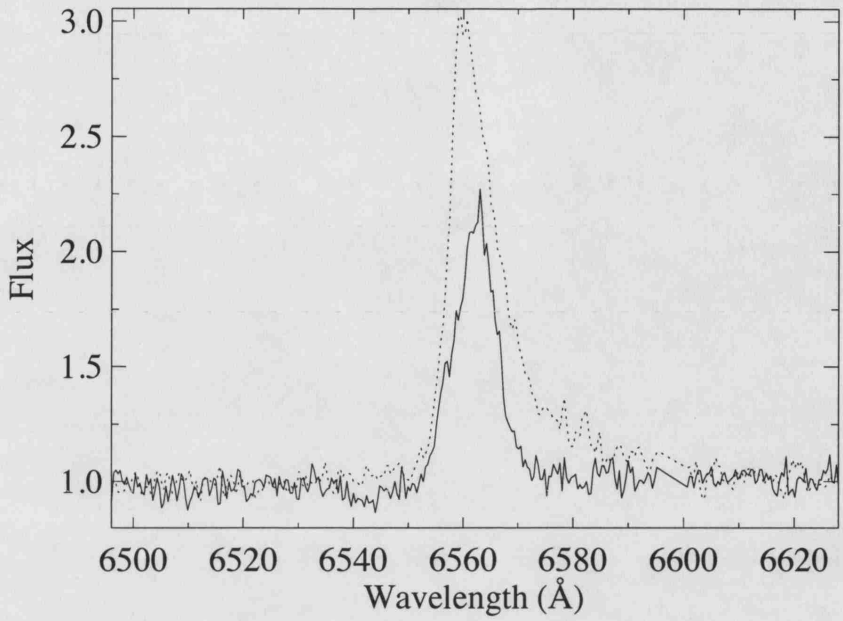

Figure 6.7: A demonstration of the line profile variability of the Hα line using spectra from the WHT time-series. The spectrum with the dotted line was exposed during night 1 and the solid line spectrum was exposed during night 2. These two spectra are separated in time by 0.84 days, corresponding to a phase difference (based on an orbital period of 0.154 days) $\Delta\phi = 0.47$.

The He I 5876Å and Hβ lines have at least shown the presence of a blue-shifted absorption component which can be best explained as originating from some kind of outflow. However, it is not clear from just these plots that a lack of blue-shifted absorption indicates that the outflow has stopped as the contribution from the emission to the disappearance of the absorption is still not clear. What these profile comparisons do inherently show is that these profiles do need to be studied on a temporal basis.

6.4.2 Greyscale Representations of the Optical Time-Series

Fig. 6.9 shows greyscale representations of the He I 5876 Å Hα and He I 6678 Å lines from the WHT time-series. To enhance the visualisation of the variability characteristics, each spectrum was normalised by the mean profile before being used to construct the images. The strongest feature in both sets of greyscales plots is the presence of a strong but narrow flux deficit and excess located at the rest wavelengths of the three spectral lines; during the course of each night, the respective flux deficit and excess are observed

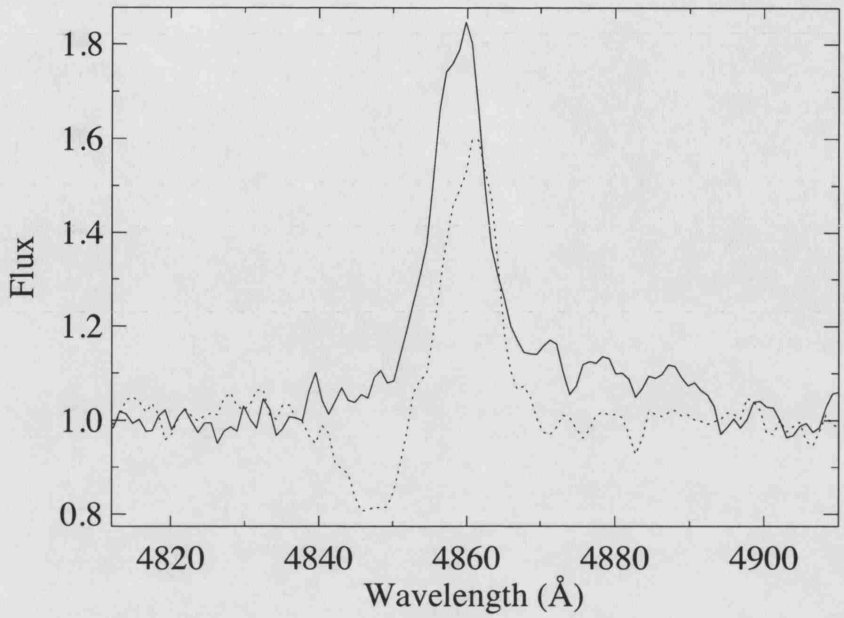

Figure 6.8: A demonstration of the line profile variability of the Hβ line using spectra from the McDonald time-series. The solid line spectrum was exposed on the 26th December 1998 and the dotted line spectrum was exposed on the 28th December which are effectively nights 1 and 2 of the time-series. These two spectra are separated in time by 1.74 days, corresponding to a phase difference (based on an orbital period of 0.154 days) $\Delta\phi = 0.32$.

to switch sides. These features are most likely representative of the observed velocity shifting of the emission and the simplest explanation to this is that it is due to the orbital motion of the two stars.

When the velocity motion of the He I 5876 Å and 6678Å lines are compared with the velocity motion of the Hα line, it is clear that there are some differences. Assuming that the behaviour is orbital in origin then, the difference in velocity motion may be due to a phase offset between the two lines. To test this theory, a simulated time-series of the Hα and He I 6678Å lines (from the ISIS red arm data) was generated in an attempt to reproduce the core behaviour of the lines. The time-sampling of this simulated data was identical to that of the original WHT time-series and the two spectral lines were assumed to be single Gaussian profiles with FWHM of 300 km/s and core intensities of 1.40 and 0.18 for Hα and He I 6678 Å respectively. The velocity shift of both lines was assumed to be sinusoidal in the velocity-time plane, with a period of 0.154 days and an amplitude

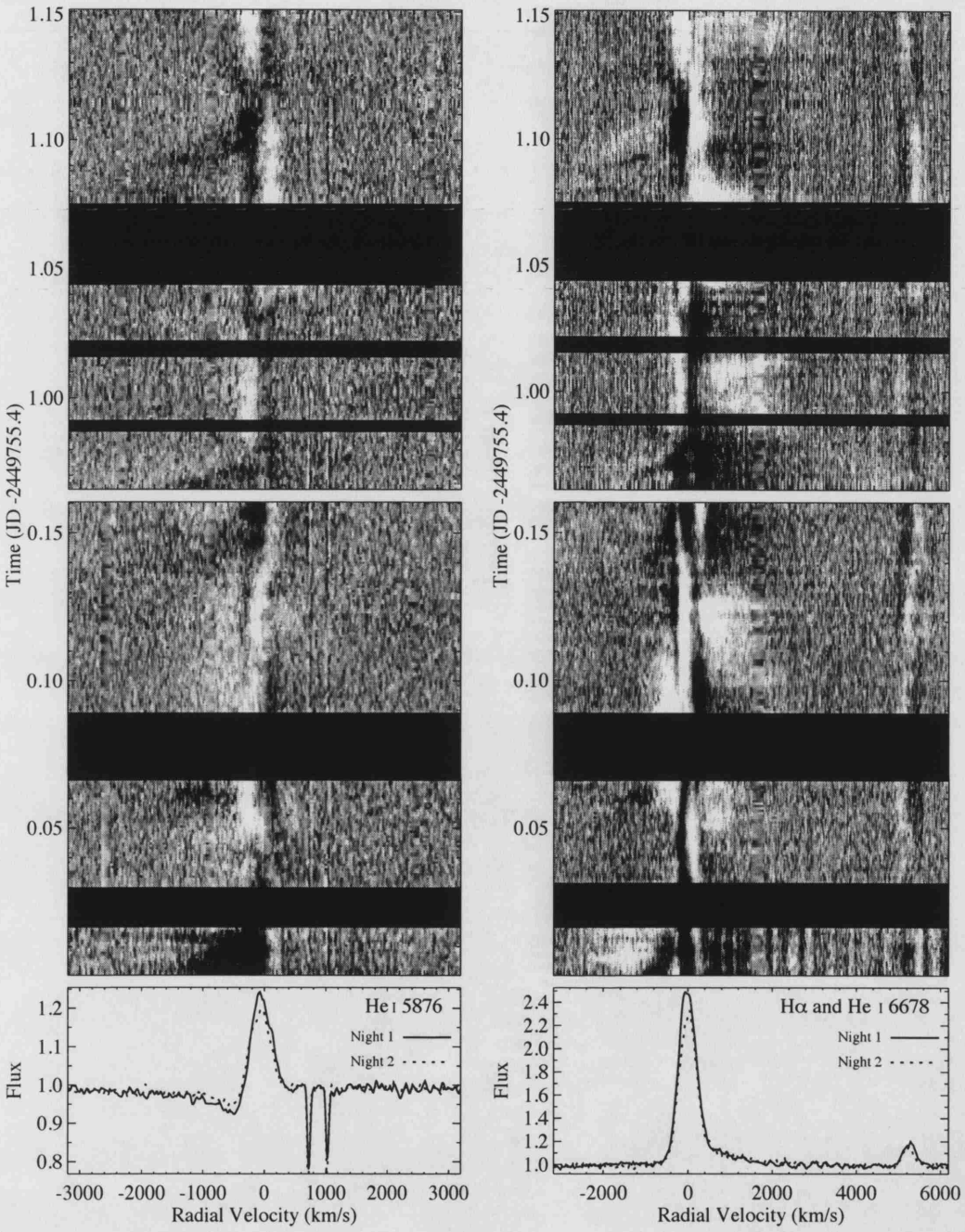

Figure 6.9: Greyscale representations of the He I 5876 Å (left), Hα and He I 6678 Å lines (right) for night one (bottom) and night two (top) using the WHT time-series, the mean profiles of the two nights are shown underneath. To improve the contrast of the variability, individual spectra were divided by the mean and the results were used to construct these images. In these plots white represents enhanced flux and black represents reduced flux with respect to the mean profile; the black and white cut levels are set to 0.93 and 1.07 respectively.

of 50 km/s. Fig. 6.10 is a comparison figure of the real red arm WHT time-series against our simulated profiles. The simulation is a close match for the real observations; for this to be achieved the phase offset between the two lines was $\Delta\phi = 0.23$. This is a significant and noticeable offset between the two species and suggests a difference in their origins.

The main aim of this study is of course to present the optical disc wind characteristics of BZ Cam. In the greyscale representations of the WHT time-series (see Fig. 6.9), evidence for the disc wind comes in the form of flux deficit events (i.e. black areas) which occur simultaneously in both He I 5876Å and Hα. Although the corresponding events for He I 5876Å and Hα are very similar in shape, they are not identical and for Hα these events have a corresponding strong flux deficit at red-ward velocities, extending as far as $\sim +2000$ km/s. Hα differs even further from the He I 5876Å line by undergoing times of enhanced flux at red-ward velocities, with no corresponding blue-ward enhancement. At this stage in the analysis it is unclear exactly how these regions of enhanced red-ward flux are related to the disc wind, if at all, and why they are not seen for the He I 5876Å line.

In each night shown in Fig. 6.9 there are three distinct blue-shifted wind events which are observed simultaneously for both lines; these events were also identified by Ringwald & Naylor (1998). To investigate the behaviour of these wind events on their own merits, and to investigate how they differ between the two lines, velocity and date measurements were taken from them to record how they change with time. Each event is denoted by the channel it was observed in (B for blue, R for red), the day it was observed (1 for night 1 and, 2 for night 2) and a consecutively running letter to indicate which event it was (i.e. a, b, or c). Thus, the first blue-shifted wind event observed for Hα is referred to as *R1a* and its corresponding event for He I 5876Å is *B1a*. For every event, date (as an offset from the first spectrum) and velocity measurements were taken at the beginning and end of the blue or left most edge of the wind event. In some cases it was clear that the wind event was not connected to the line centre, in which case it was possible to make measurements from the red edge of the wind event as well. From these measurements, the elapsed time of an event and the acceleration of an edge could be calculated. For the He I 5876Å the measurements are recorded in Table 6.3 and the measurements from the Hα line are recorded in Table 6.4; Fig. 6.11 is a repetition of the greyscale representations of the WHT time-series but with the wind event measurements marked.

Although each wind event is slightly different, in general (apart from *B2c* and *R2c*) they do have the same basic characteristic of a blue-edge which begins at a velocity

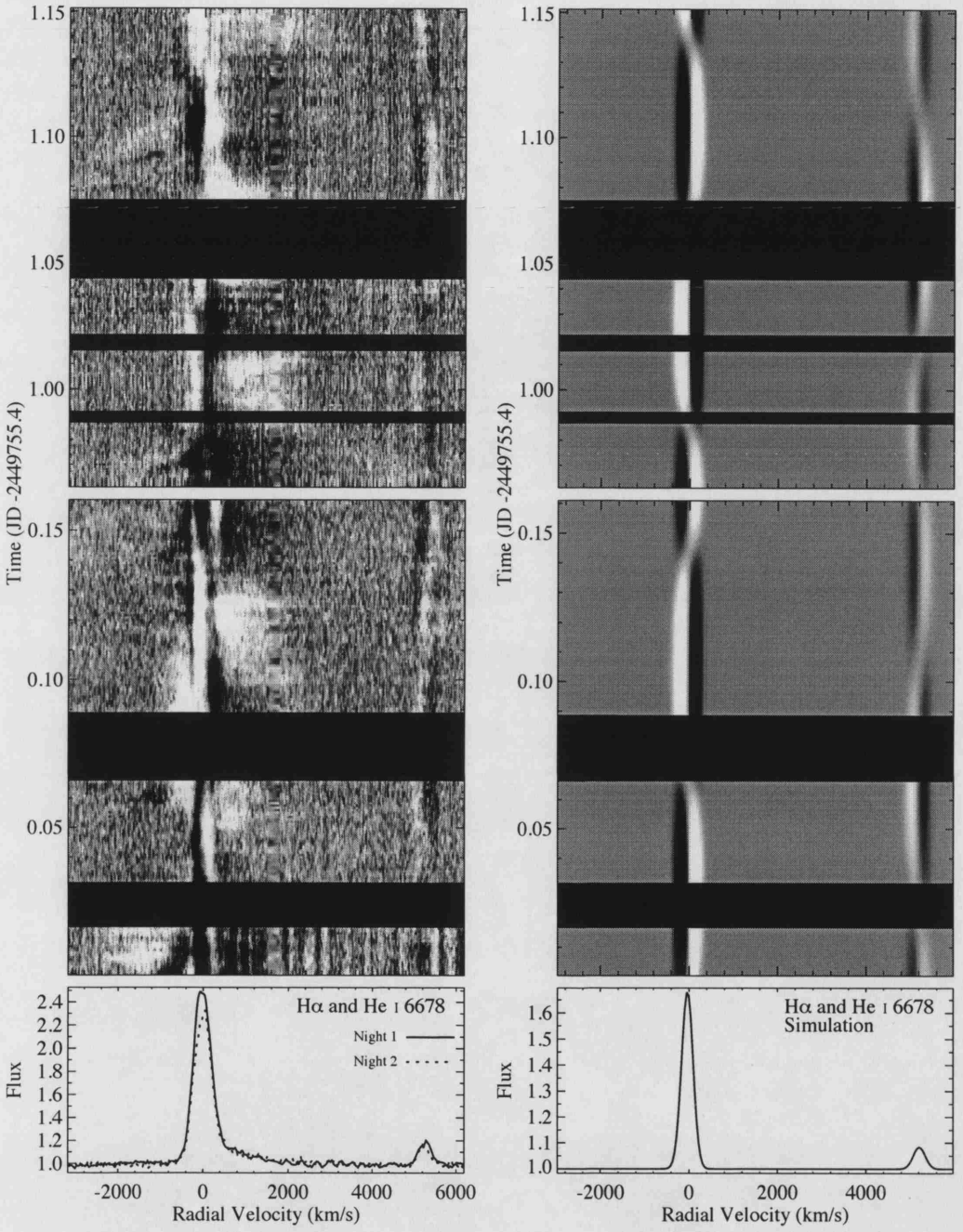

Figure 6.10: Greyscale representations of Hα and He I 6678 Å and their simulated profiles for nights one and two of the WHT time-series. To improve the contrast of the variability, each individual spectrum was divided by the mean profile and the results were used to construct these images. In these plots, white represents flux enhancement and black represents flux deficit with respect to the mean profile; the black and white levels are set to 0.93 and 1.07 respectively. To achieve an accurate representation of the observations, the phase offset between Hα and He I 6678 Å was $\Delta\phi = 0.23$.

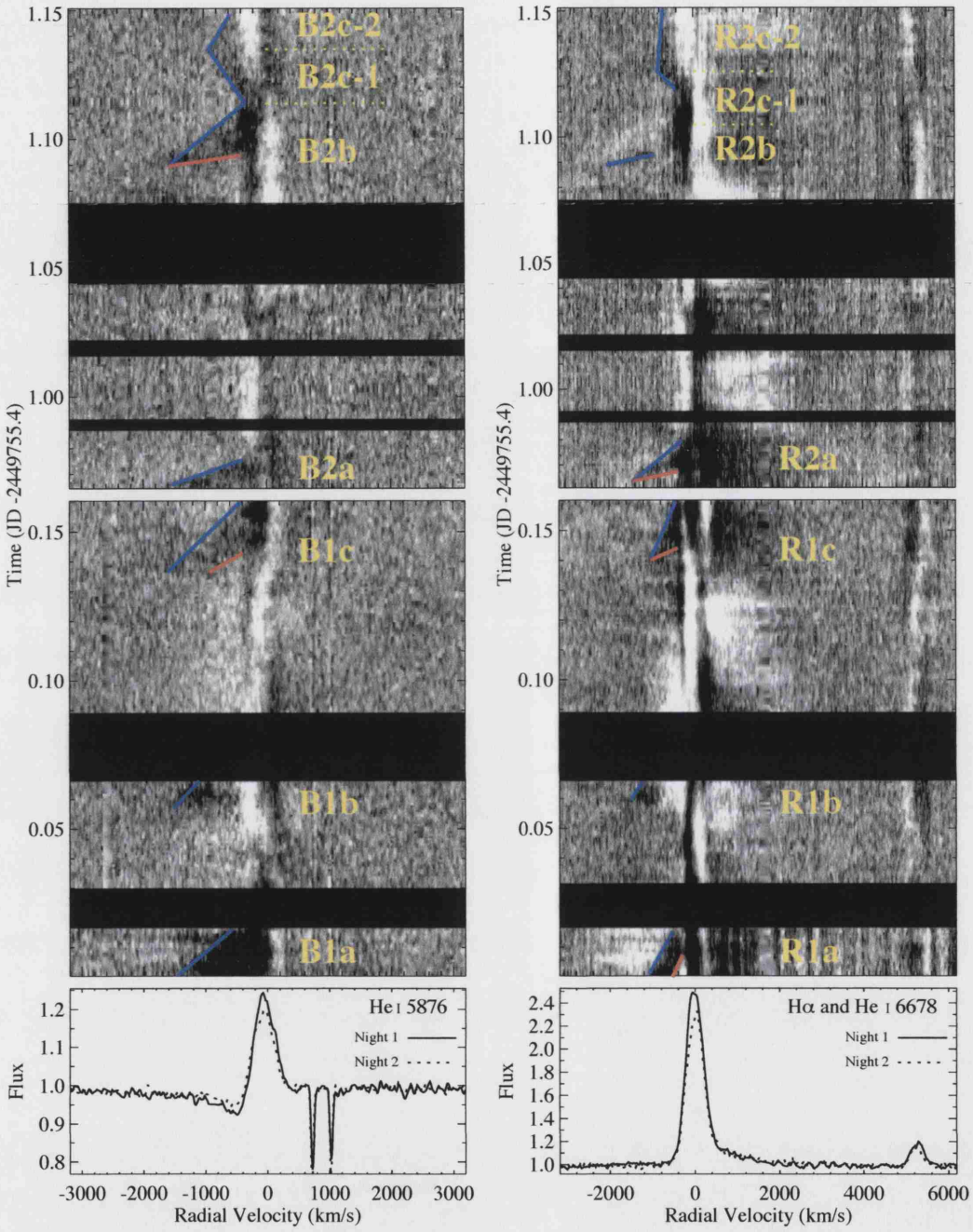

Figure 6.11: Greyscale representations of the He I 5876 Å (left), Hα and He I 6678 Å lines (right) for night one (bottom) and night two (top) using the WHT time-series, the mean profiles of the two nights are shown underneath and the blue-shifted absorption events have been marked (the blue lines indicate the location of the blue edge measurements and the red lines indicate the red edge measurements where it has been possible. To improve the contrast of the variability, individual spectra were divided by the mean and the results were used to construct these images.

Event	*B1a*	*B1b*	*B1c*	*B2a*	*B2b*	*B2c-1*	*B2c-2*
$T_{\rm start}$ (days)	0.000	0.057	0.137	0.966	1.090	1.114	1.134
Blue Edge $v_{\rm start}$ (km/s)	-1450	-1510	-1610	-1530	-1580	-340	-920
Blue Edge $v_{\rm end}$ (km/s)	-560	-1100	-420	-390	-400	-920	-570
Blue Edge ΔT (mins)	22.2	13.4	33.7	14.0	35.1	30.1	19.4
Blue Edge $\dot{v}$ (km/s^2)	0.67	0.51	0.59	1.37	0.59	-0.17	0.30
Red Edge $v_{\rm start}$ (km/s)	—	—	-920	-1530	-1580	—	—
Red Edge $v_{\rm end}$ (km/s)	—	—	-390	-390	-400	—	—
Red Edge ΔT (mins)	—	—	—	14.0	35.1	—	—
Red Edge $\dot{v}$ (km/s^2)	—	—	0.97	1.37	0.59	—	—

Table 6.3: Measurements of time and velocity of the blue-shifted absorption for the He I 5876Å line. For each event, measurements were taken from the blue edge of the absorption event and where possible, from the red edge of the absorption event (where this has not been possible, has been indicated with —); these absorption events are shown more clearly in Fig. 6.11. The length of time between the beginning and end of the absorption events (ΔT) and the average acceleration ($\dot{v}$) across each absorption event have also been calculated and are shown here.

between -1500 – -1000 km/s and subsequently decreases in velocity towards the line centre at an approximately linear deceleration on the order of 1 km/s^2. The inference from events such as *B1c* and *B2b* is that this wind absorption actually forms at these high velocities and then subsequently in-fills towards the line centre. Since the formation of these events at high velocities is not observed, the mechanism for creating them must be acting on a shorter time-scale than the temporal resolution of this data i.e. on the order of seconds to minutes. Although this is not observed for all the events, some have been cropped by gaps in the time-series so this could be a recurring feature of the wind. The occurrence of these events initially appears to be regularly spaced but the time span between them is actually between $\sim$ 80 minutes and $\sim$ 180 minutes which rules out the possibility of an orbital modulation ($p_{\rm orb} \approx 221$ minutes). The events referred to as *B2c* and *R2c* are slightly different to all the other wind events. These simultaneous events occur at the same time as *B2b* and *R2b* finish and unlike the other events, the expansion of the flux

Event	*R1a*	*R1b*	*R1c*	*R2a*	*R2b*	*R2c-1*	*R2c-2*
T_{start} (days)	0.000	0.059	0.140	0.964	1.089	1.119	1.126
Blue Edge v_{start} (km/s)	-1080	-1500	-1050	-1430	-2050	-420	-850
Blue Edge v_{end} (km/s)	-530	-1230	-440	-300	-920	-850	-720
Blue Edge ΔT (mins)	20.2	9.0	28.3	23.2	6.2	9.8	35.7
Blue Edge $\dot{v}$ (km/s^2)	0.45	0.51	0.36	0.82	3.03	-1.31	0.060
Red Edge v_{start} (km/s)	-530	—	-1050	-1430	—	—	—
Red Edge v_{end} (km/s)	-300	—	-390	-370	—	—	—
Red Edge ΔT (mins)	10.6	—	5.9	5.4	—	—	—
Red Edge $\dot{v}$ (km/s^2)	0.37	—	1.87	3.31	—	—	—

Table 6.4: Measurements of time and velocity of the blue-shifted absorption for the Hα line. For each event, measurements were taken from the blue edge of the absorption event and where possible, from the red edge of the absorption event (where this has not been possible, has been indicated with —); these absorption events are shown more clearly in Fig. 6.11. The length of time between the beginning and end of the absorption events (ΔT) and the average acceleration ($\dot{v}$) across each absorption event have also been calculated and are shown here.

deficits to high velocities is observed. They do not, however, expand to as high velocities as is observed for the other wind events. Why *B2b* and *R2b* should be so much different to the other wind events is unclear although it is probably just a different form of the same phenomenon.

The wind events occur approximately simultaneously for both Hα and He I 5876Å but there are strong differences between them. When comparing the first night events between both lines, it is notable that the velocity at which the wind event forms for Hα is typically lower than it is for He I and since the events last for approximately the same amount of time, the deceleration for the Hα events is slightly lower than the deceleration for He I 5876Å. *R1a* is of course affected by an additional flux excess extending between the blue edge and ~ -2000 which would have affected these measurements, possibly resulting in a lower initial velocity than expected. However, *R1c* is definitely not affected by any flux excess and it is clearly measured to have a slower deceleration. During the second night of the observing run, the wind events are similar in their behaviour but not identical to

the first night. For example, the blue edge of event *B2a* starts off at a velocity of -1530 km/s which is similar to the other events from night 1 but, the subsequent deceleration is more than double than what has been previously observed. Similarly for Hα, the events observed in night 2 undergo a much greater deceleration than has been observed in the previous night.

The wind events referred to as *B1a*, *B1b*, *B1c*, *B2a* and *B2b* for the He I 5876Å line, and *R1a*, *R1b*, *R1c*, *R2a* and *R2b* for the Hα show some strong generic similarities but they are not identical between events of the same line or, simultaneous events between lines or even between the two nights; it should be noted that the time-averaged profiles for each night shown in Fig. 6.11 indicate that both Hα and He I 5876Å had stronger flux during night 2 which could be the source of the noted differences between the nights. There is no evidence of an orbital modulation but they do occur on approximately regular time-scales so this suggests that it is not a continuous outflow which is being observed at different angles as the system rotates. Clearly, what ever is generating these variations is acting on an extremely short time-scale. Of additional interest is the flux excess observed at red-ward velocities for the Hα line but not for the He I 5876Å line. It should be noted that these flux excess events do not occur at the same time as the wind absorption events and typically it is observed that the former ends when the latter begins.

What the McDonald series lacks in temporal and spectral resolution (in comparison to the WHT time-series) it more than makes up for in spectral and temporal coverage. The aim of the McDonald time-series was to observe many more cases of the disc outflow over multiple nights and across multiple spectral lines, than had been observed in the WHT time-series. Fig. 6.12 is a greyscale representation of the McDonald time-series across the entire spectral range. In these greyscale representations it is clear to see the variability in the Hβ line and the slightly weaker Hγ line; variability is likely to be present for the other lines but the signal to noise ratio of the data is too low to bring this variability out of the data. It is important to note that the changes that occur to the Hβ, are seen to happen simultaneously in the Hγ line although to a lesser degree. Fig. 6.13 is a greyscale representation of the McDonald time-series, expanded across the Hβ and He I 4922 Å lines to investigate these wind events.

In Fig. 6.13, He I 4922Å is understandably much weaker than Hβ and therefore so is its observed variability. It would have been useful if the sinusoidal path generated by the He I line as the CV rotated were visible in these greyscale maps but unfortunately the line

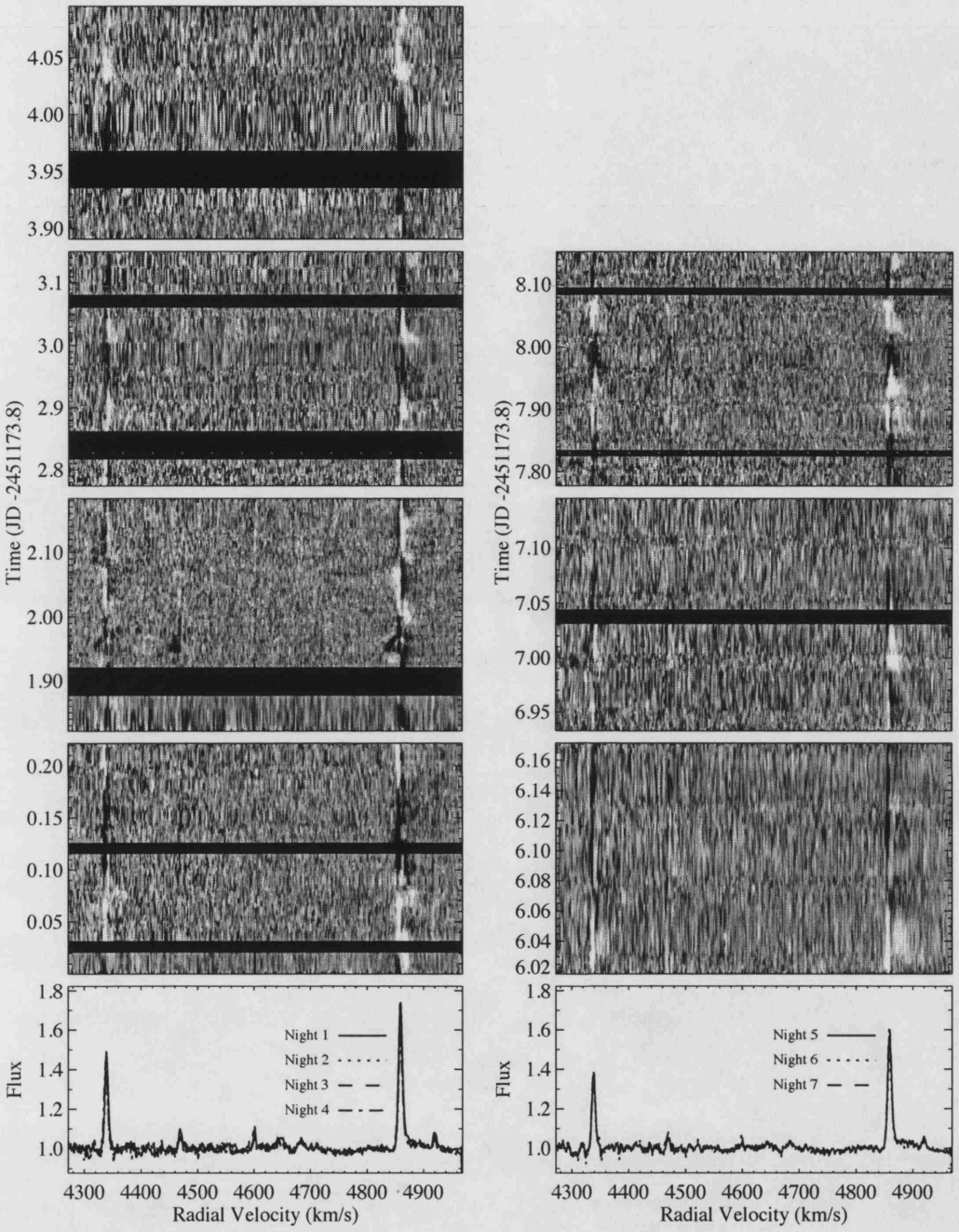

Figure 6.12: Greyscale representations of the entire optical spectrum from the McDonald time-series. Nights 1-4 are in the left figure and nights 5-7 are on the right figure. These plots were constructed from the residual of dividing each spectrum by the mean profile; white represents enhanced flux and black represents reduced flux with respect to the mean (cut levels were 0.93 and 1.07 for black and white respectively). Horizontal bars represent large gaps in the time-series. Mean profiles are shown underneath.

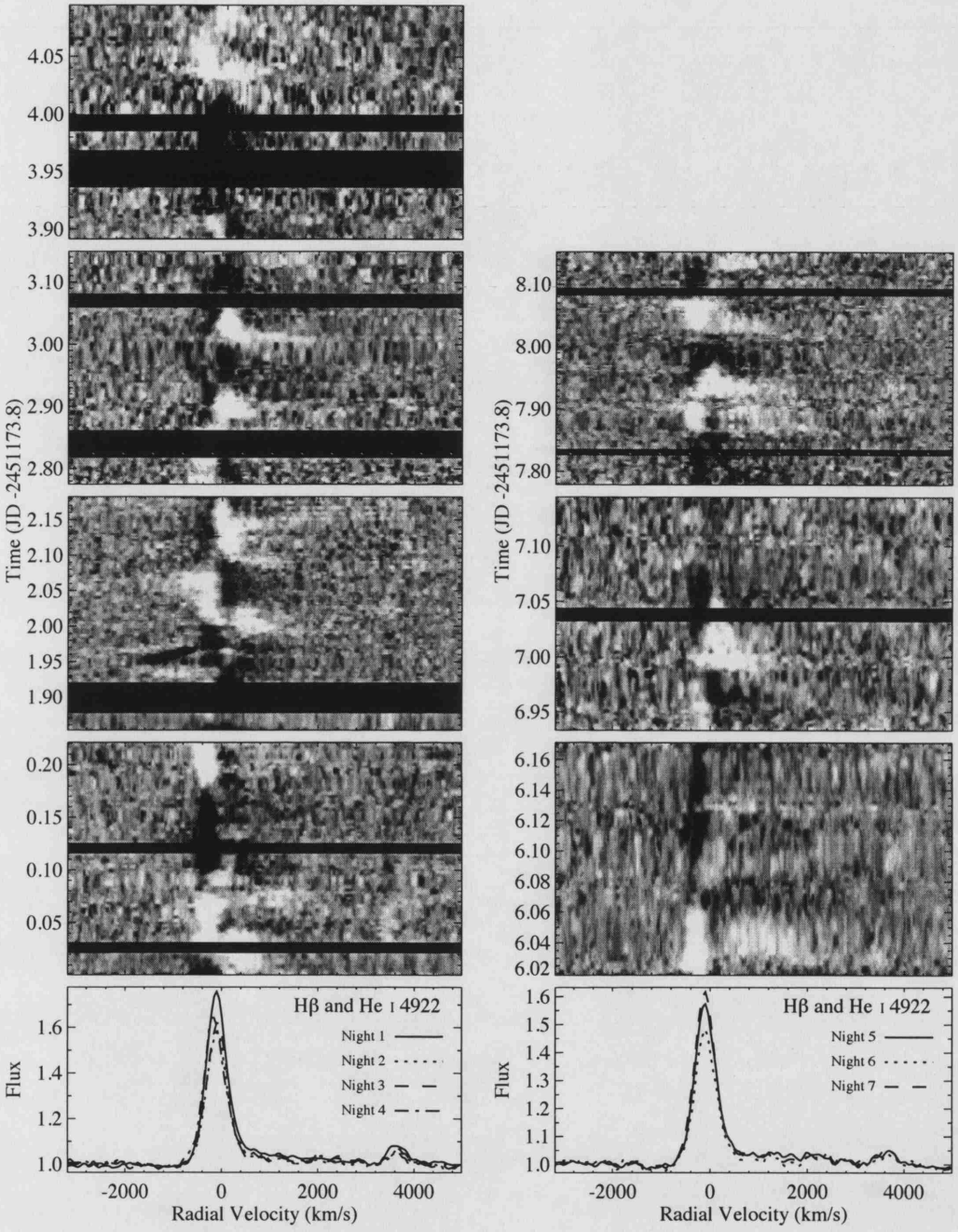

Figure 6.13: Greyscale representations of the Hβ and He I 4922 Å lines from the McDonald time-series. Nights 1-4 are in the left figure and nights 5-7 are on the right figure. These plots were constructed from the residual of dividing each spectrum by the mean profile; white represents enhanced flux and black represents reduced flux with respect to the mean (cut levels were 0.93 and 1.07 for black and white respectively). Horizontal bars represent large gaps in the time-series. Mean profiles are shown underneath.

is too weak in these representations to see this. Based on the Hα observations from the WHT time-series, the predicted behaviour of the Hβ line would be regularly repeating blue-shifted wind events and enhancements of flux at red-ward velocities. With respect to the blue-shifted absorption events, quite surprisingly only one event is observed during all 7 days of the observing run; this single event can be seen in night 2 at a time offset of 1.945. The blue edge of this event starts at a velocity of -1810 km/s and decelerates to -600 km/s over 40.6 minutes, the resulting deceleration was 0.50 km/s^2. The red edge of this wind event started at a velocity of -1250 km/s and decelerated to -550 km/s over 26.2 minutes, the resulting deceleration was 0.45 km/s^2. Although the wind event formed further from the line centre than was seen for any events in the WHT time-series, overall the event is very similar, with the initial formation at high velocities and the subsequent deceleration towards the line centre at ~ 0.5 km/s^2.

This single wind absorption event is the only major blue-shifted wind absorption event observed during the entire 7 night observing run and the question arises as to why this might be. It is entirely possible that the reason events are not seen is because the signal to noise ratio of the data is too low to detect the events, bearing in mind that there was only one very strong event in the (*B1a* and *R1a*) WHT time-series. However, a more likely scenario is that the optical component to the wind is simply less active than before. The comparison of flux levels in Fig. 6.5 with previous observations indicated that BZ Cam had not yet entered a state of quiescence which means that the mass transfer rate between the two stars should still be relatively high. If the system is truly less active in this time-series than the WHT time-series (with respect to the wind) then it raises the possibility that this optical component to the disc outflow is not entirely constrained by the mass transfer rate.

As already mentioned, the red-ward flux enhancements observed in the WHT observations of the Hα line are also observed in these McDonald observations of the Hβ line. These flux enhancements are very similar to those observed for the Hα in that they extend as far as +1500 km/s and there is no indication of an orbital modulation to them from these plots. In the WHT observations it was noted that these flux enhancements did not occur at the same time as the blue-shifted wind events suggesting some kind of connection. In the McDonald observations only one wind event is actually seen, while these red-ward flux enhancements occur relatively regularly suggesting that there is no link between the two. One potential explanation for these observed changes to the emission are

that they are actually due to mini absorption events across the red-wing but spanning a lower velocity domain than is observed for the blue-shifted wind events. Further analysis may yet reveal their nature.

6.4.3 Temporal Variance Spectrum

Fig. 6.14 are plots of the temporal variance spectra for He I 5876 Å and Hα (He I 6678 Å is also included at positive velocities); temporal variance spectra are described in § 2.2.2. The plots of He I 5876 Å were created from the entire blue-arm spectra of the WHT time-series. Note the presence of the Na D lines at 5889.95 Å and 5895.92Å; the variance across these two line profiles is particularly strong and given the twin peaks, would suggest a binary motion. However, closer investigation of the time-series revealed that the lines are in fact stationary (and therefore interstellar); large variance is observed across the two lines because they are very narrow (typically covered by three or four pixel) and minor variations in their strength created this large variance.

The profile of the He I 5876Å TVS in Fig. 6.14 is consistent with the descriptions provided in § 6.4.2 of its behaviour. There is a strong variance along the core of the line which is due to several factors; the binary motion of the CV and an apparent variability in the strength of the emission (to be investigated in more detail later). The variance is also observed to be asymmetric with respect to the line centre; the reduction in variance away from the line centre is much quicker towards the red-wing than it is towards the blue-wing. For example, the variance along the red wing of the profile reaches the 95 percent confidence level at a velocity of $\sim$ 450 km/s, while over the blue wing of the line profile, the variance doesn't go below the 95 percent confidence level until a velocity of ~ -1500 km/s, over three times further from the line centre. This TVS profile of the He I 5876Å line is indicative of the strongly variable blue-shifted wind and a lack of any comparable activity at red-ward velocities.

The TVS profile of the Hα line (Fig. 6.14) is also consistent with the description provided of its behaviour in § 6.4.2. As with the He I 5876Å, the variance profile is strongly asymmetric but this time the asymmetry is the opposite way around, with the drop in variance more rapid towards the blue than towards the red. The source of the variance at red-ward velocities is of course the strong and regular flux enhancements observed for the Hα line. The variance along the blue wing does briefly rise above the 95% confidence level and subsequently reduces back below it again. The source of this variance is likely

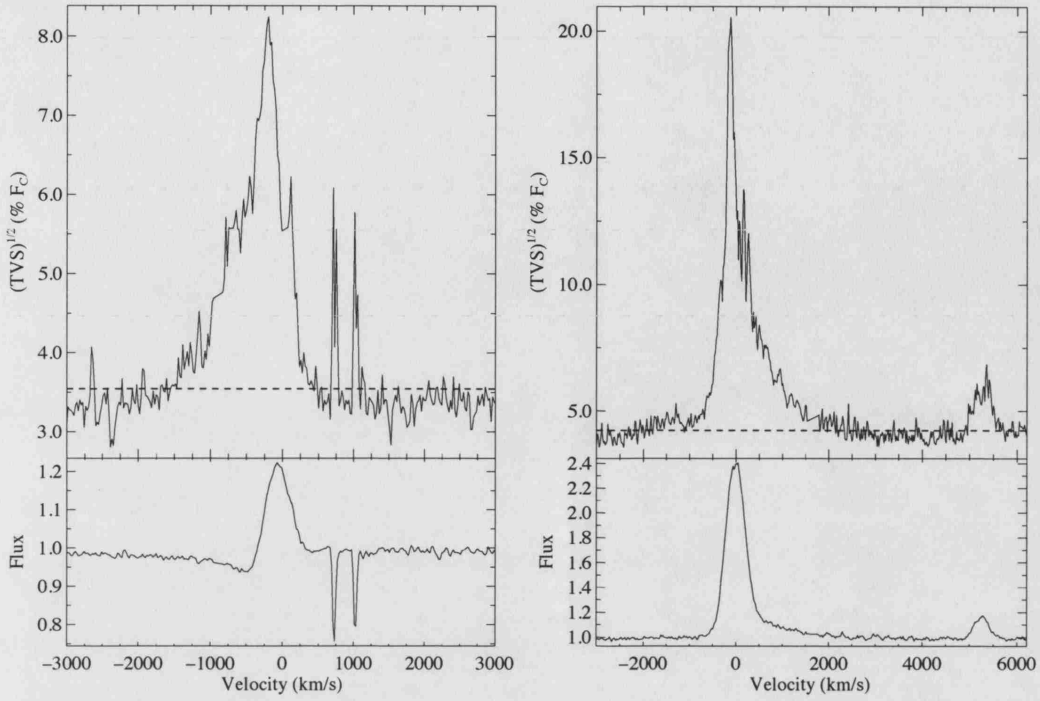

Figure 6.14: Temporal variance spectrum of He I 5876 Å (left) and Hα (right), from the WHT time-series. The peaks in variance of the Na D lines at 5889.95 Å and 5895.92Å (left figure) are caused by small fluctuations in their strength and their narrow profile, and not by the binary motion of the cataclysmic variable; hence they are thought to be interstellar in origin. The lower frames are the mean profiles of the selected regions and the dashed lines indicate a 95 percent confidence level of no variability.

to be the blue-shifted absorption events which, although they were observed for the Hα line, they were by no means as strong as they were for the He I 5876Å line.

Fig. 6.15 is a plot of the temporal variance spectra of the Hβ and Hγ lines from the McDonald time-series. It is unfortunate that the signal to noise of the time-series is not high enough to produce useful temporal variance plots of the helium lines. The resulting TVS profiles are similar to the Hα TVS profile from the WHT data in that a strong asymmetric peak in variance is observed, although the degree of asymmetry is not as strong as it was observed for the Hα line. It is indicative of the strong flux enhancements observed along the red wing of the profiles in Fig. 6.13. For Hγ some indications of this asymmetry are seen along the profile but it is not very clear and the variance intercepts the 95 percent confidence level at similar velocities either side of the line centre.

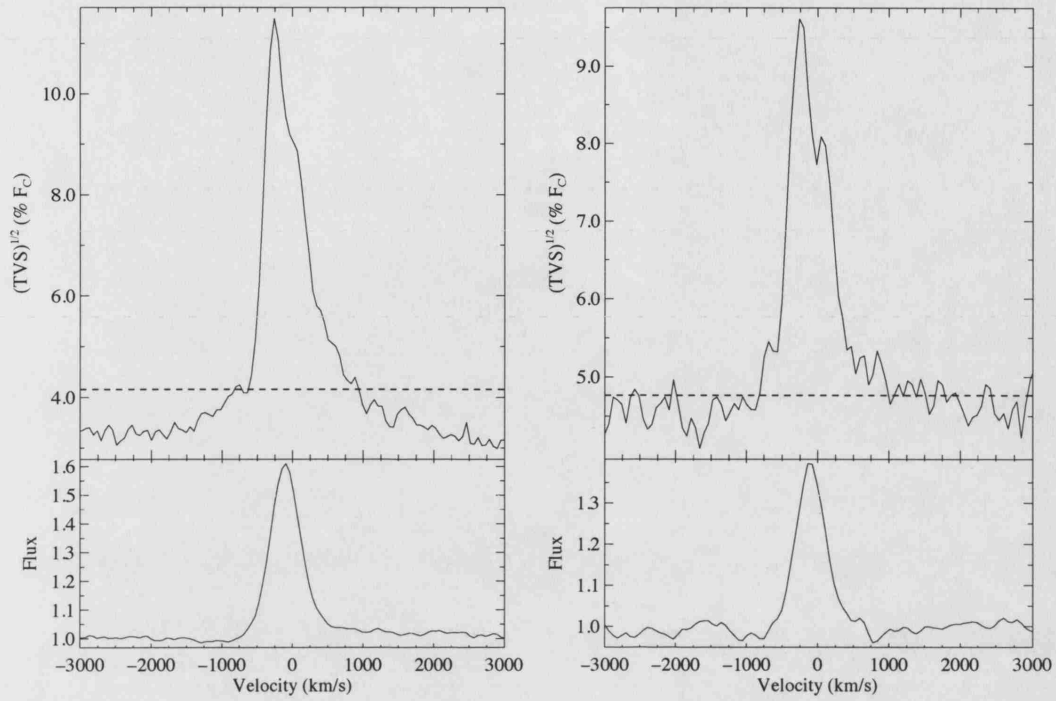

Figure 6.15: Temporal variance spectrum of Hβ (left) and Hγ (right) from the McDonald time-series. The lower frames are the mean profiles of the selected regions and the dashed lines indicate a 95 percent confidence level of no variability.

These plots of temporal variance have been useful in showing the degree of activity along the line profile and also showing the extent to which the activity is biased to either side. However, more detailed analysis is needed before anything can be said for certain about the nature of this activity.

6.4.4 Radial Velocity Measurements

Providing an orbital solution for BZ Cam is less of an issue than it was for V592 Cas for two reasons; the orbital period is reasonably well know and for the purposes of making radial velocity measurements, the line profiles can be reasonably estimated by a simple single Gaussian profile. The two time-series in this study provide an ideal opportunity to provide a new and more accurate value for the orbital period. By determining the orbital periods for both Balmer lines and helium lines, orbital discrepancies between the two lines (if any exist) may be revealed. The emission lines of the Balmer lines Hβ and Hγ in the McDonald time-series, and of Hα and the He I lines at 5876 Å and 6678 Å in

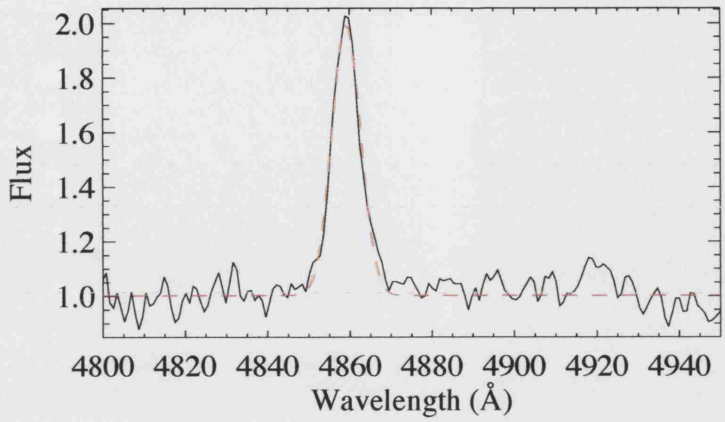

Figure 6.16: An example line fit to Hβ from the McDonald observations of BZ Cam, using a single Gaussian solution.

the WHT data set were fit using the assumption that they conformed to a simple single Gaussian, see § 2.2.1 for more information about fitting line profiles and see Fig. 6.16 for an example of one of these fits. The line centre measurements from these Gaussian fits are representative of the radial velocity shifts of each emission profile.

The initial analysis of the radial velocity measurements was to pass them through a Fourier transform algorithm and then to subsequently pass the resulting dirty power spectra through a Fourier clean algorithm (200 cleaning iterations were performed, with the gain set to 0.2); see § 2.2.1 for more information about Fourier transforms and Fourier cleaning. Figs. 6.17 and 6.18 are plots of the dirty and clean power spectra for all measured lines in both time-series (for WHT: Hα, He I 5876 Å and He I 6678 Å and, for McDonald: Hβ and Hγ). The most notable difference between the Fourier power spectra generated from McDonald observations and those generated from the WHT observations is that in the former, the profiles are much narrower than in the latter which is due to sheer length and number of spectra that were taken in the McDonald observations in comparison to the WHT time-series. Table 6.5 is a list of the three strongest signals in each of the dirty power spectra presented in Figs. 6.17 and 6.18; in all dirty power spectra apart from Hα, the strongest signal corresponds with the orbital period ($p_{\rm orb}$ is equivalent to 6.52 cycles per day). The strong signals observed either side of the orbital period are 1-day aliases.

Table 6.6 is a list of the strongest signals in each of the cleaned power spectra (as presented in Figs. 6.17 and 6.18). Each cleaned power spectrum clearly shows a strong

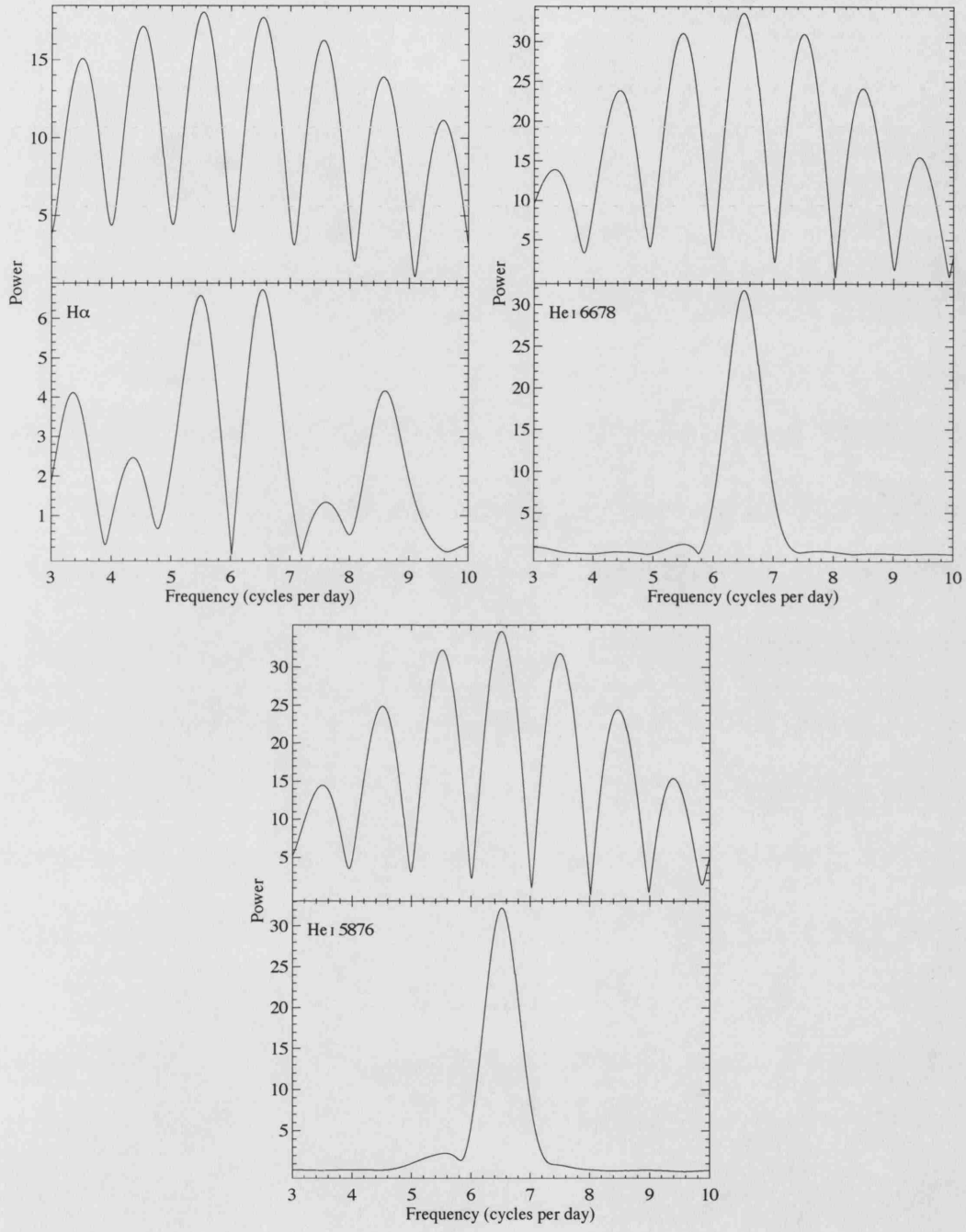

Figure 6.17: Fourier dirty (upper panels) and clean (lower panels) power spectra for the radial velocity measurements of Hα (top left), He I 6678 Å (top right) and He I 5876 Å (bottom) in the WHT time-series.

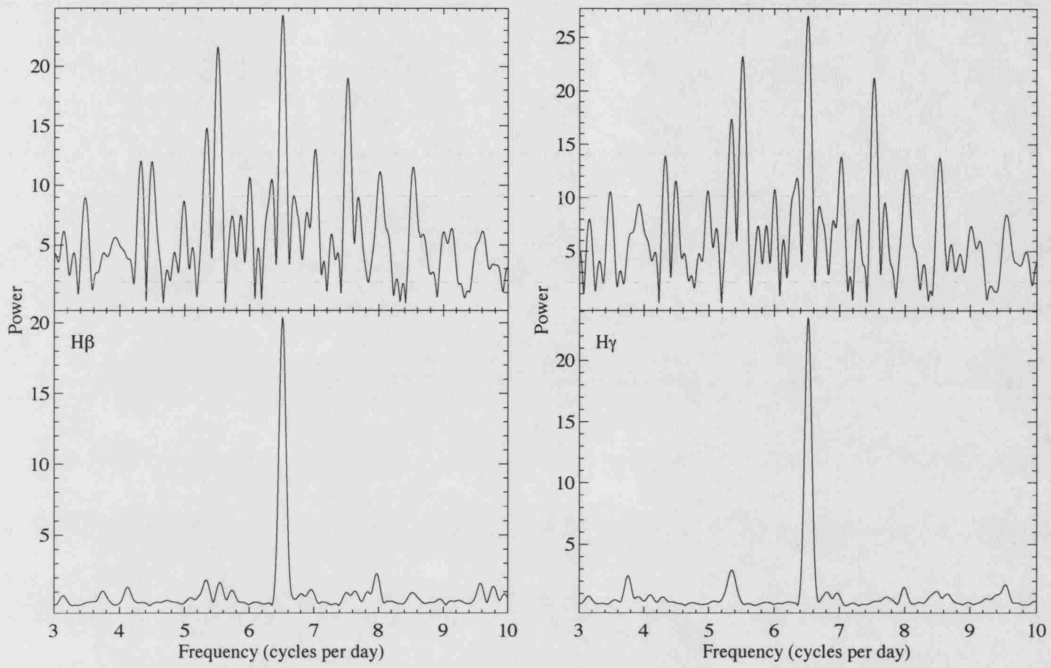

Figure 6.18: Fourier dirty (upper panels) and clean (lower panels) power spectra for the radial velocity measurements of Hβ and Hγ in the McDonald time-series.

Line	Three Strongest Signals (days)		
Hα	0.153	0.181	0.221
He I 5876	0.133	0.153	0.181
He I 6678	0.133	0.154	0.182
Hβ	0.1329	0.1535	0.1816
Hγ	0.1328	0.1533	0.1815

Table 6.5: A table of the three strongest signals in the dirty Fourier power spectra of all measured lines from all measured BZ Cam lines. The table has been separated into results from the WHT time-series (top values) and results from the McDonald time-series (bottom panel). Estimated errors on these values based on the FWHM measured from the Fourier profiles are ± 0.015 cycles per day for the power spectra from the WHT time-series and ± 0.0010 cycles per day for the power spectra from the McDonald data.

Line	Strongest Signal (days)
Hα	0.1528
He I 5876 Å	0.153
He I 6678 Å	0.154
Hβ	0.1533
Hγ	0.1534

Table 6.6: A table of the strongest signal in the clean Fourier power spectra of all measured BZ Cam lines. The table has been separated into results from the WHT time-series (top values) and results from the McDonald time-series. The dirty spectra were cleaned with a gain of 0.2 and 200 iterations. Estimated errors on these values based on the FWHM measured from the Fourier profiles are ± 0.015 cycles per day for the power spectra from the WHT time-series and ± 0.0010 cycles per day for the power spectra from the McDonald data.

period on or around the orbital period and only for Hα is there any suggestion of an additional period. This stability in displaying the orbital period as the strongest signal suggests that the Gaussian interpretation is at the very least adequate for these purposes. The reason that the Hα measurements did not show the orbital period to be as strong as it was for all the other lines is probably due to a slight asymmetry of the profile from the flux enhancements that occur over the red-ward side; the more asymmetric the profile becomes the more it deviates from the Gaussian formulation meaning that any fit to the line using the Gaussian formulation would give slightly inaccurate line centre measurements. However, once the radial velocity measurements were passed through the cleaning algorithm, the orbital period still showed itself to be the strongest signal indicating that the Gaussian formulation still proved to be a reasonable estimation to the profile shape.

The next stage of the radial velocity analysis was to actually find a sinusoidal solution for each line. Each radial velocity curve was fitted in IDL using Craig Markwardt's fitting routine, using the entered formula of

$$v(t) = \gamma + K sin[2\pi p^{-1}(\phi - \phi_0)] \tag{6.1}$$

Line	Period (days)	K (kms^{-1})	γ (kms^{-1})
Hα	0.1533±0.0002	39.4±1.1	-39.3±0.9
He I 5876	0.1533±0.0002	68.7±2.0	-30.0±1.4
He I 6678	0.1535±0.0002	67.1±1.6	-46.6±1.2
Hβ	0.15350±0.00004	51.5±1.6	-94.0±1.1
Hγ	0.15350±0.00005	57.3±2.2	-125.5±1.6

Table 6.7: A summary of radial velocity solutions for the BZ Cam measurements. Resulting phases have been omitted since the solutions were calculated in period space as well. The results have been divided into those obtained from the WHT time-series (upper panel) and those obtained from the McDonald time-series (lower panel).

where γ is the systemic velocity, K is the semi-amplitude velocity, p is the period and ϕ_0 is the epoch for $\phi = 0.0$; Table 6.7 shows the results of these fits (phase differences are omitted from this table since the curves were fitted in period space as well, making the phase of the fits relatively meaningless). Surprisingly the derived errors on the K and γ parameters, which are calculated from the covariance matrix generated within the least squares routine, are only on the order of 2% which is unexpectedly very small. The small errors are likely the result of the large number of data points which are used in the fitting process (e.g. more data points equals smaller errors) so these errors will be treated with some scepticism.

It has been repeated numerous times that the orbital period of BZ Cam is well known and therefore not brought into question. Therefore the orbital period can be used as a consistency check between the line measurements and between the time-series. It is fortunate that the period solutions presented in Table 6.7 are very close, either 0.1533 or 0.1535 days. Even statistically (using the error of the WHT values) the periods are within 1 standard deviation unit of each other. It should also be noted that the error on the periods of the McDonald values are about a factor of 4 smaller than the WHT errors which is due to not only the McDonald time-series being much longer, but also because of there being many more spectra. The mean weighted period obtained by combining all of these results is 0.15348±0.00003 days; the lower errors for the McDonald values means that this result is more heavily weighted towards those values. The most accurate orbital

Spectral Line	γ (km/s)
He I 4471Å	-109 ± 16
He I 4922Å	-82 ± 15
He II 4686Å	-83 ± 29

Table 6.8: γ velocities measured from the helium lines in the time-averaged McDonald spectrum of BZ Cam.

period for BZ Cam quoted to date is 0.153693 days by Patterson *et al.* (1996). There is a slight discrepancy between the two values but this only amounts to $\sim 0.1\%$ proving that the orbital period derived here is realistic.

The reasons why the solutions for K and γ are significantly different is unclear. It is entirely conceivable that two different species could have different K velocities due to a difference in origin on the accretion disc; a Keplerian accretion disc would mean that the closer the origin of the species was to the white dwarf, the faster it would be moving and the greater the measured velocity amplitude or K would be. However, large differences are also observed in K for Balmer lines between the WHT and McDonald time-series. The derived γ velocities should be roughly the same for each line since the system is receding from Earth at a specific velocity but again, significant differences are discovered with these values between lines and between the WHT and McDonald time-series. Fortunately for the McDonald time-series, it is possible to provide a consistency check for γ with the other lines present in the spectrum by determining their line centres through a single Gaussian fit to the time-averaged spectrum; it should be noted that the signal to noise ratio of these additional lines was too low in the individual spectra to support a time-series analysis. The resulting γ velocities are shown in Table 6.8 and also show some spread in their values but they are somewhat closer in value to the McDonald solutions than to the WHT solutions.

This newly determined and more accurate orbital period can be used to determine whether there is a phase shift between certain lines which helps in determining whether they originate from different parts of the disc. It is possible for example, to make this comparison between the lines measured in the WHT time-series or the lines measured in the McDonald time-series but it would be unsafe to make the comparison between the two time-series since although the derived error on the period is relatively small, over

the four year period (which is the time between the two data sets) the resulting error on phase becomes ± 0.3 which is significant.

Fig. 6.19 is a plot of the WHT central velocity measurements folded on the orbital period of 0.1535 days. Overall the suggested period is suitable for the data and all three plots show periodic radial velocity motion. The radial velocities of the helium lines clearly shows the sinusoidal motion expected for the lines of a binary star. The Hα line also shows a sinusoidal motion but this is not as clear as additional structure is found in the radial velocity curves. It is noted that although all of the lines were fitted with single Gaussian profiles, there were many times during the WHT time-series where the line profiles diverted from the Gaussian shape; this appeared to be due to the flux excess along the red wing. Therefore many of the line profile fits gave slightly incorrect indications of the line centre and either should have been more red (i.e. more positive velocties, indicated by diamonds in Fig. 6.19) or more blue (i.e. more negative velocities, indicated by crosses in Fig. 6.19). These inaccuracies in the line profile fitting suggest that the amplitude of the Hα radial velocity curve should be greater than that determined and it also adds a degree of uncertainty to the phase of the sinusoid. This is important because a clear feature of Fig. 6.19 is the phase shift between the helium lines and Hα which from this figure appears to be $\Delta\phi \approx 0.15$. This is slightly less than the phase shift estimated from the profile simulation in § 6.4.1.

Fig. 6.20 is a plot of the McDonald radial velocity measurements folded on the period of 0.1535 days. The scatter of the radial velocity measurements is much larger than what was seen in Fig. 6.19 for the WHT data, which is probably due to the lower S/N of the data. The folding of the data demonstrates the periodic radial velocity motion of the binary system although it cannot be determined whether there is any fine structure to this periodic motion such as what was seen for Hα because of the spread of the data. The radial velocity curves are approximately in phase.

Fig 6.21 is a greyscale representation of the lines available in the WHT time-series, folded on the orbital period of 0.1535 days. Folding the spectra on this period shows periodic behaviour in the cores of all three lines; the patterns created are less clear for Hα than they are for the two helium lines. The phase lag of the Hα core motion behind the helium lines is now seen more clearly, proving that it was not merely an artefact of the method used to measure the central velocities. Caution should be used in assuming too much more about the activity of these lines from these plots because only two nights

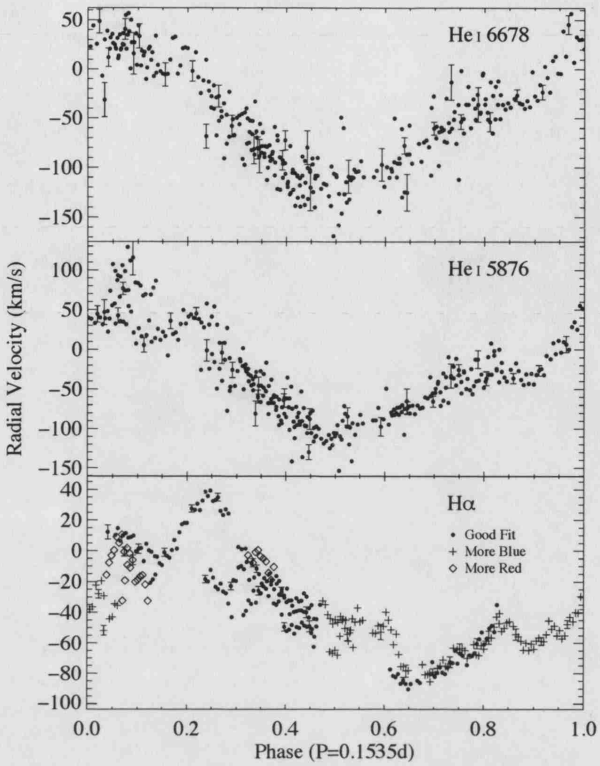

Figure 6.19: Radial velocities for Hα (bottom panel), He I 5876 (middle panel) and He I 6678 (top panel), folded on a period of 0.1535 days. Phase 0.5 has been arbitrarly defined as when the helium lines reach their most negative velocity. The Hα line profile did not always conform well to a Gaussian profile so indications have been given where the determined radial velocity should've been more blue (crosses) or more red (diamonds). Sample errors are provided for all three lines. Measurements are from the WHT time-series.

data is available so any events which are particularly out of character with the general behaviour of the system would still appear relatively strong. This means that although the blue-ward wind absorption events are observed very strongly in Fig. 6.21, it does not mean that they are periodic features.

The situation is slightly different for the McDonald data in Fig. 6.22 (the greyscale representations of Hβ and He I 4471 Å) because there is 7 nights worth of data so when the spectra are folded on the orbital period the sporadic features are more suppressed, although there aren't many of these features in this data. The Balmer lines again show the expected sinusoidal motion although unlike what was seen for the WHT time-series,

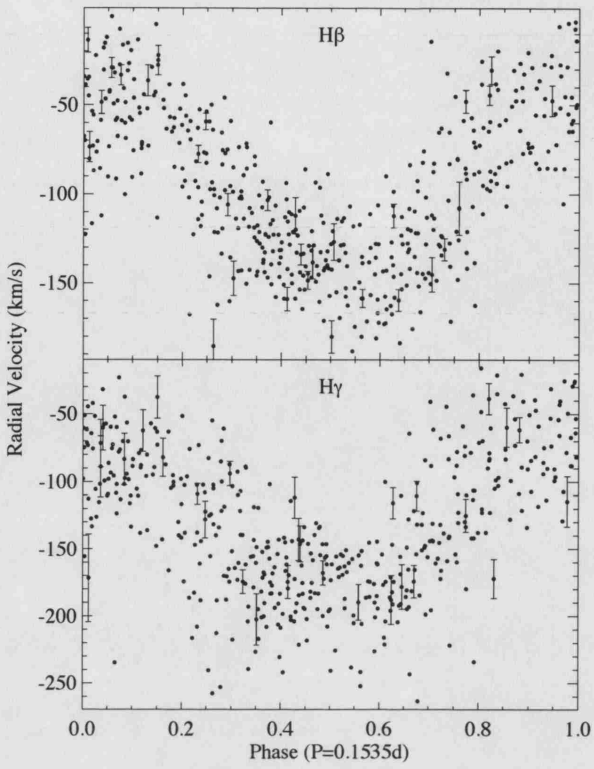

Figure 6.20: Radial velocities for Hγ (bottom panel) and Hβ (top panel) folded on a period of 0.1535 days. Phase 0 has been arbitrarily defined as when the Balmer lines reach their least negative velocity. Sample errors are provided for both lines. Measurements are from the McDonald time-series.

there appears to be a slight asymmetry in this sinusoidal motion, having a stronger impact on the blue-ward side of the line centre than the red-ward side (note how the blue-ward absorption excesses in the residual plot are much weaker than on the red-ward side). This may indicate the presence of an underlying emission source which is weighted more towards the red-ward side than the blue-ward side. Note also the presence of the He I 4922 Å line at approximately 3700 km/s with respect to the rest velocity of Hβ; it is very faint in comparison to Hβ but it is still possible to see the sinusoidal motion.

In the greyscale representation of the He I 4471 Å shown in Fig. 6.22, a behaviour is observed which is not seen in any of the other studied lines so far. In the normal greyscale images the two edges of the emission are observed to behave slightly differently; both edges move to the red much quicker than they move to the blue; this motion is out of phase and the blue edge moves much further than the red edge. The net result is that

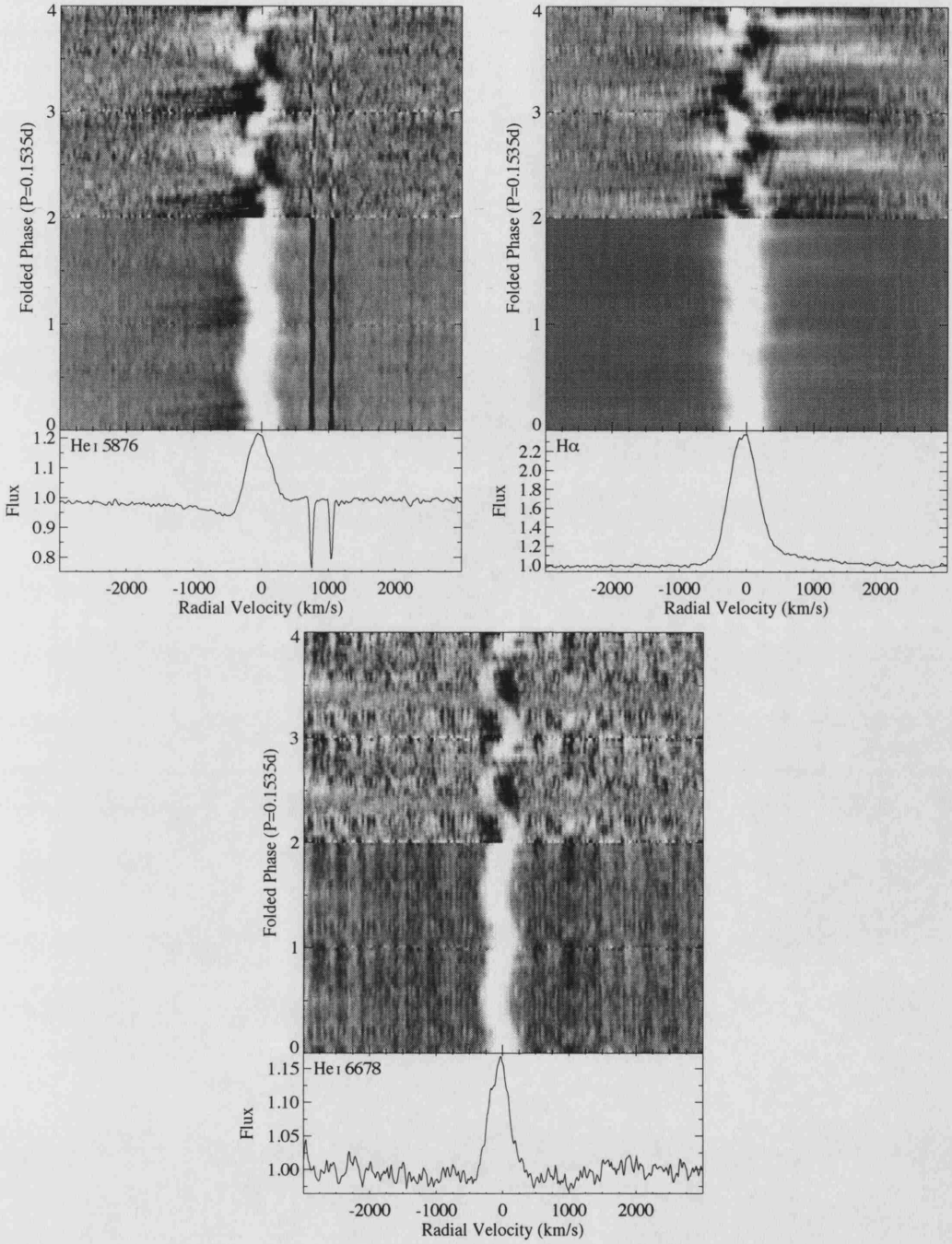

Figure 6.21: Greyscale representations of He I 5876 (top left), Hα (top right) and He I 6678 Å (bottom) folded on a period of 0.1535 days, placed into 40 bins and repeated for two cycles. The data spanning from 0 to 2 cycles is the original data while the data spanning from 2 to 4 cycles is the residual data where each spectrum has been divided by the mean profile. Phase 0.5 has been arbitrarily defined as when the helium lines reach their maximum blueward velocity.

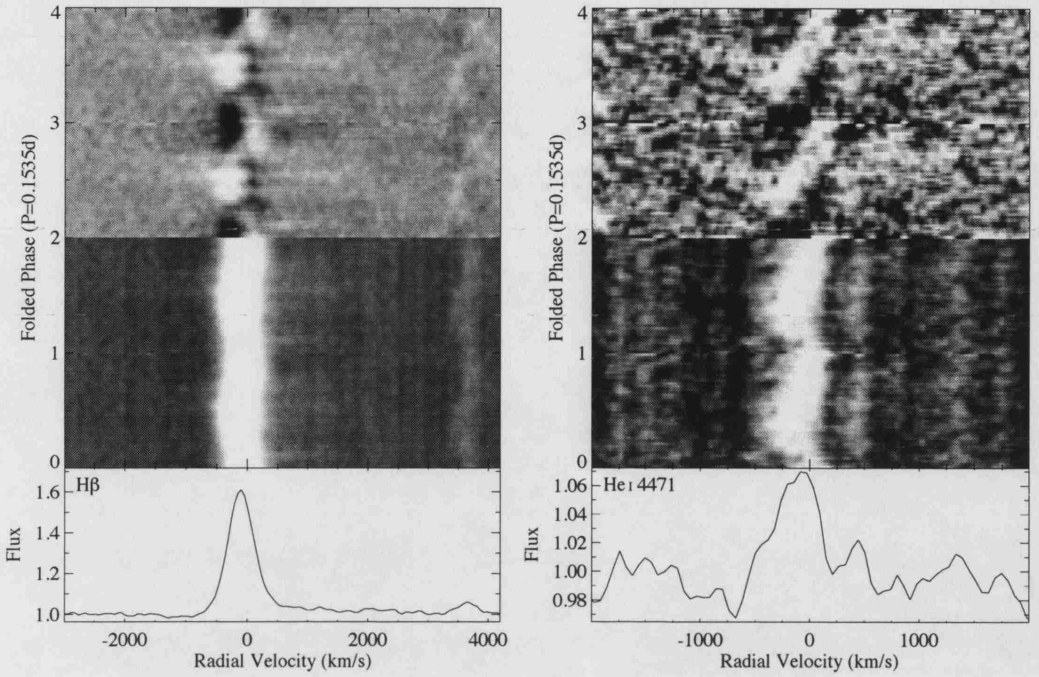

Figure 6.22: Greyscale representations of the Hβ and He I 4471 line (from the McDonald time-series), folded on a period of 0.1535 days, placed into 40 bins and repeated for two cycles (the feature at a velocity of $\sim$ 3700 km/s is He I 4922 Å). The data spanning from 0 to 2 cycles is the original data, where white represents emission and black represents absorption and the data spanning from 2 to 4 cycles is the residual data where each spectrum has been divided by the mean profile. Phase 0.5 has been arbitrarily defined as when the emission reaches maximum blue-ward velocity.

the core emission actually changes in width. This behaviour is observed in the residual plot as a series of black and white stripes (flux excesses and deficits) moving from the blue to the red as time progresses.

6.5 The Disc Wind

Evidence for an optical component to the disc wind of BZ Cam comes in the form of the blue-shifted wind events described in § 6.4.2. The brief analysis presented in § 6.4.2 consisted of measurements taken directly from the spectra and no attempt was made to decompose the emission and the blue-shifted wind absorption so as to more accurately

record the behaviour of the wind during each event. In this section, such a process is described.

6.5.1 He I 5876Å

The analysis of the He I 5876Å profile in § 6.4 suggests that the spectral line is convolution of two components, a strong emission whose observed behaviour (i.e. the sinusoidal velocity motion) most likely originates from the bright spot and, an intermittent blue-shifted absorption which is believed to originate from the disc outflow. With an additionally variable red-ward flux excess component, the Hα profile is somewhat more complicated to decompose than the He I 5876Å. Since the aim is to record the behaviour of the blue-shifted wind absorption, there is also little point in attempting to decompose the Hβ profile from the McDonald time-series since only one clear blue-shifted wind event was observed in that data. He I 5876Å is therefore the perfect candidate for studying these wind events in more detail. In this study of the disc wind, the measurements that will be retrieved by the process of fitting each He I 5876Å line in the time-series are the central velocity and the full-width at half maximum (or FWHM) of each wind profile. These two properties provide measures of the average velocity and the velocity spread of the material which is coming from the accretion disc.

The most obvious way of decomposing the emission and wind absorption for the He I 5876Å line would be to repeat the method used in § 4.5.3 for V592 Cas, whereby each Balmer line was fitted with a triple Gaussian formula. This method of separating the three components of the line profile was successful because however variable in strength the wind was, it was always present. However, for BZ Cam the wind is not always present meaning that the least-squares routine used to perform the fit would try and decompose the profile into two components when at times, only one was present. Therefore, a slightly different method is used whereby the emission component of the He I line is initially removed before any further measurements are taken from the blue-shifted absorption events. The method for removing the emission from the He I line is discussed in § 6.5.2 and the results of fitting the remaining wind absorption are presented in § 6.5.3. It should be noted that measurements from the wind events were made from the WHT time-series by Ringwald & Naylor (1998) but, they did not attempt to remove the emission during the fitting process so the measurements presented here should give a more accurate representation of the wind behaviour.

6.5.2 Removing the Emission from the He I 5876Å Line

The procedure for removing the emission from the He I 5876Å profile required two major assumptions: the emission is fixed in strength and the blue-shifted wind absorption does not extend as far as the red-side of the line centre. With respect to the first of these assumptions, the mean profile of He I 5876Å from the individual nights (see Fig.6.9) has already indicated that there is some variability in the strength of the emission and that this variability seems somewhat sporadic; it is unclear whether this variability is related to an underlying absorption component or that the emission is actually changing in strength. Nevertheless, although this variability exists, it is still relatively small and the main aim of this procedure is of course to observe the blue-shifted absorption in its entirety so for these purposes the emission is stable enough to be considered as static.

It is not immediately obvious that the assumption that the red wing of the absorption does not extend as far as positive velocities is valid so the logical step is to confirm whether this is the case. As it has already been stated, many of the He I 5876Å spectra contain little to no evidence of the blue-shifted wind absorption so, the spectra were grouped into those systems showing a strong wind event and those systems that weren't, and then a comparison was made between the mean spectra of each group; Fig. 6.23 is a plot of this comparison, whereby the red-wing has been mirrored onto the blue-side for clarity. To construct these two mean spectra, each profile had to be shifted onto the rest frame using the radial velocity solutions presented in § 6.4.4. The wings and emission peaks of the wind driven and non-wind driven profiles are very similar in strength suggesting that if there is any contamination of the red wing from the blue-shifted absorption, the degree of contamination is very small. An additional benefit to creating these mirror images of the red wing of the emission is that these constructed profiles provide suitable estimates of the shape and size of the emission so the mean of these two mirror images was calculated for the later use of removal from the wind driven spectra.

The method for subtracting the emission from each wind-driven profile was relatively simple. The mean emission profile described above was shifted by the relevant velocity given by the radial velocity solutions in § 6.4.4; this correctly shifted emission profile was then simply subtracted from the appropriate wind driven profile. Fig. 6.23 contains mean plots of the wind driven and non wind driven spectra with the emission removed. The method proves to be relatively successful but it is not perfect since for the non-wind

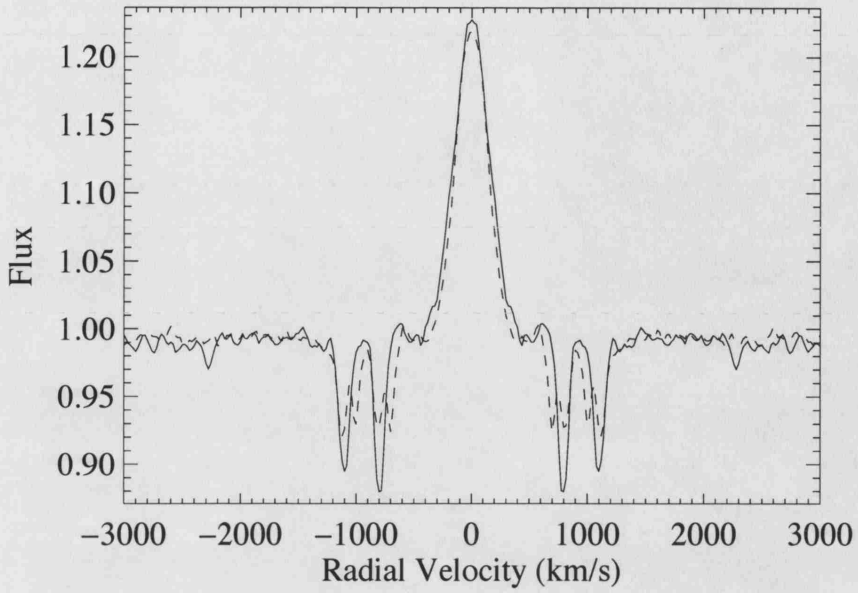

Figure 6.23: Plots of the red wing of the He I 5876 Å emission, mirrored onto the blue-side in the zero velocity axis. The solid line is a plot of the emission from the non-wind driven spectrum and the dashed line is a plot of the emission from the wind driven spectrum. All data are from the WHT data-set

driven profiles, some emission remains across the line centre. It is also interesting to note from the non-wind driven profiles that there is still a weak absorption component present at blue-shifted velocities, indicating that there is a minimum absorption contribution to every profile in the time-series, even if it is not clearly visible in the individual profiles of the time-series. The emission subtraction from the wind driven profiles is however very successful as it appears as though it has been completely removed, leaving just a strong blue-shifted absorption feature.

6.5.3 Analysing the Remaining Absorption Components

After the successful removal of the emission from the wind-driven profiles, the next step was to fit each blue-shifted absorption with a Gaussian profile to determine the central velocity and velocity spread of the absorbing material. A small minority of the wind profiles were not suitably fit with a Gaussian so these results had to be discarded. However, in general the fitting provided realistic values for the behaviour of the wind events *B1a*, *B1c*, *B2a*, *B2b* and *B1c* shown in Fig. 6.11 and described in § 6.4.2.

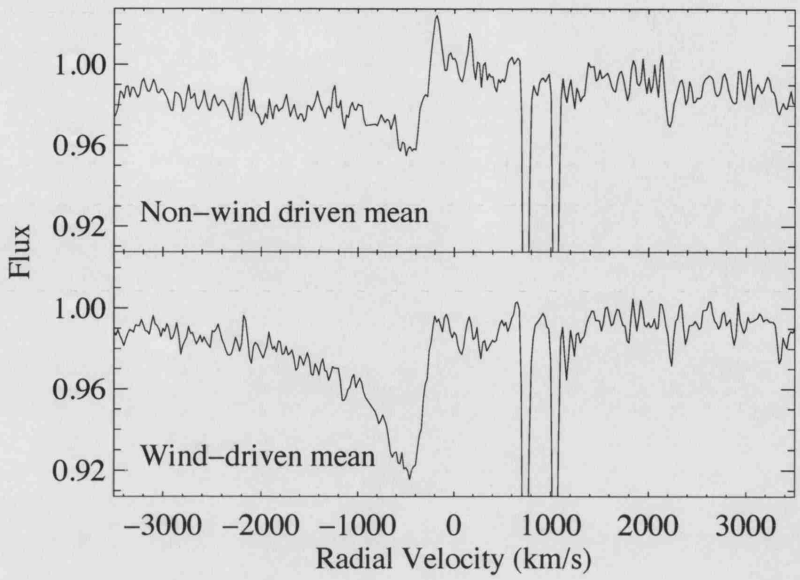

Figure 6.24: Plots of the mean He I 5876 Å profile from the WHT time-series, with the emission removed using the technique described in the text. The upper plot is the mean of the non-wind driven profiles and the lower plot is the mean of the wind driven profiles.

The derived central velocities and FWHM of the wind events *B1a*, *B1c*, *B2a*, *B2b* are presented in Figs. 6.25, 6.26, 6.27 and 6.28; these measurements have been plotted against time offset from the first data point and, orbital phase just for completeness. When comparing the phase of the beginning and end of each wind event it is clear that the binary rotation of BZ Cam is not a factor in these events and how they appear. It is also clear from these plots that there is no connection between the measured central velocities and the FWHM (or velocity spread) of the material. In all of the events shown, there is some variability in the FWHM of the blue-shifted wind event but this variability is not correlated with the general deceleration of the line velocities. A comparison between the FWHM and central velocities does however indicate that at the beginning of each event the absorption is completely detached from the line centre, providing further evidence that the wind absorption forms at high velocities.

An important characteristic of each decelerating wind event is that the deceleration is approximately linear (this of course excludes the data points marked in grey in Fig. 6.25). The linear deceleration was noted in § 6.4.2 but the calculated deceleration of each event

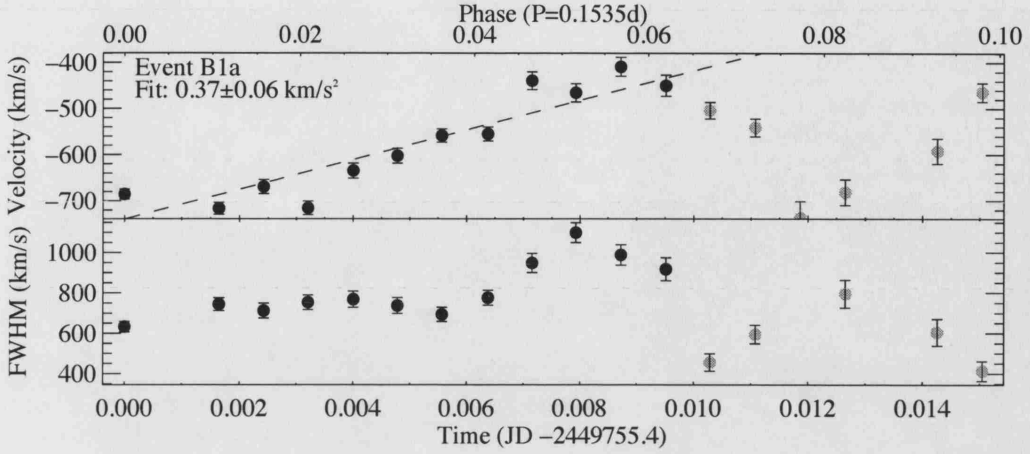

Figure 6.25: Plots of the central velocities and FWHM of the best fit single Gaussian profiles to the wind driven blue-shifted absorption in event *B1a* (from the WHT time-series); each data point is shown with a 1-σ error bar. A linear fit was performed to the initial decelerating central velocities, the result of which is shown on the plot; the data points marked in grey were neglected from the fit because the interest was purely with the initial deceleration.

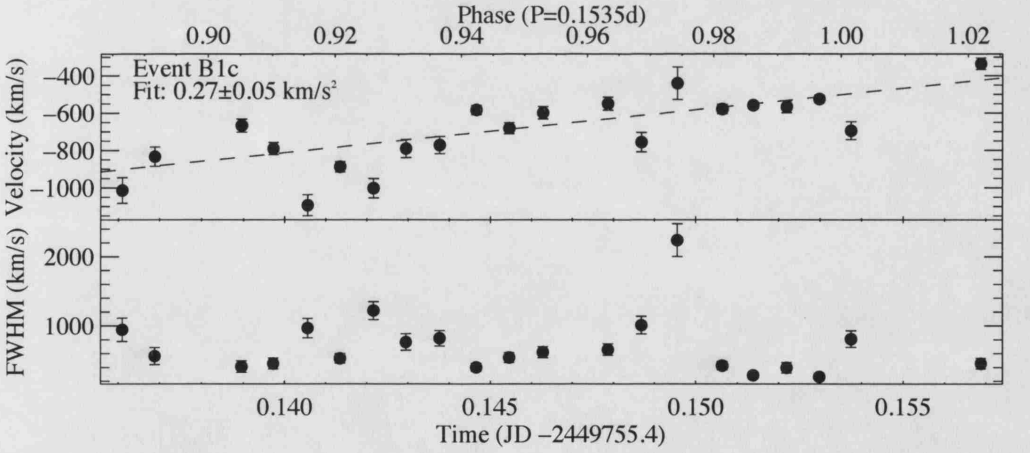

Figure 6.26: Plots of the central velocities and FWHM of the best fit single Gaussian profiles to the wind driven blue-shifted absorption in event *B1c* (from the WHT time-series); each data point is shown with a 1-σ error bar. A linear fit was performed to the decelerating central velocities, the result of which is shown on the plot.

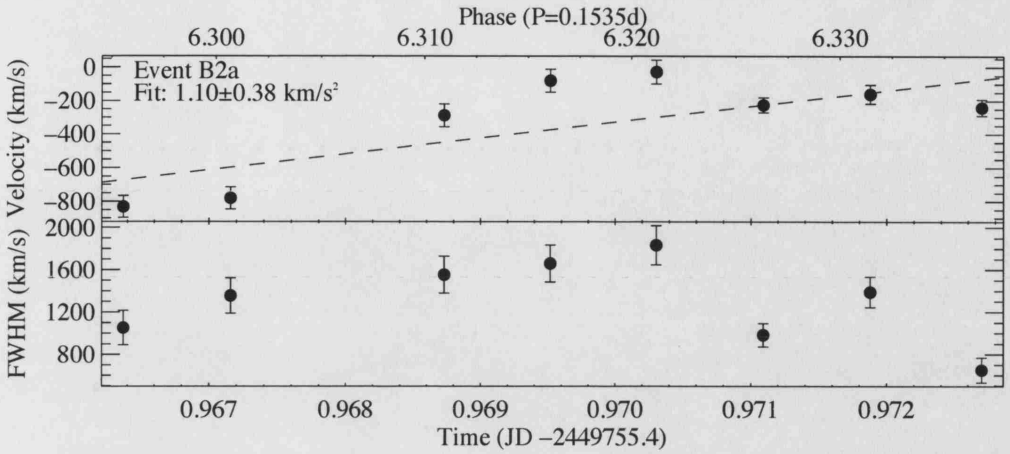

Figure 6.27: Plots of the central velocities and FWHM of the best fit single Gaussian profiles to the wind driven blue-shifted absorption in event *B2a* (from the WHT time-series); each data point is shown with a 1-σ error bar. A linear fit was performed to the decelerating central velocities, the result of which is shown on the plot.

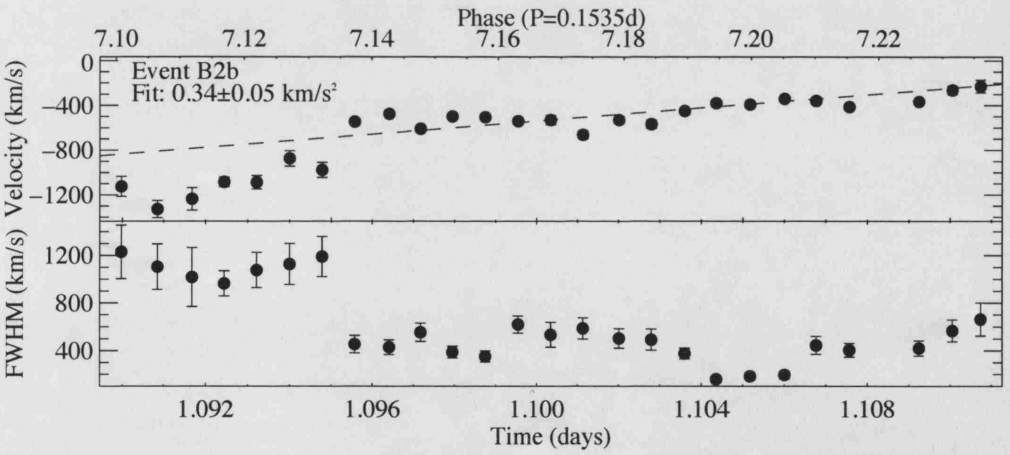

Figure 6.28: Plots of the central velocities and FWHM of the best fit single Gaussian profiles to the wind driven blue-shifted absorption in event B2b (from the WHT time-series); each data point is shown with a 1-σ error bar. A linear fit was performed to the decelerating central velocities, the result of which is shown on the plot.

Event	Deceleration (km/s^2)
B1a	0.37±0.06
B1c	0.27±0.05
B2a	1.10±0.38
B2b	0.34±0.05
B2c	-0.12±0.02

Table 6.9: A summary of the decelerations of the measured central velocities from the blue-shifted wind events of the He I 5876Å.

was taken from two measurements, from the blue edge of the absorption, one at the beginning of the event and one at the end of the event. Measuring the linear decelerations from the central velocities determined in this section would however provide a more accurate value for the deceleration of these features; the decelerations were calculated by performing a linear least-squares fit to each set of central velocity measurements, and the gradient of each solution is the deceleration (these decelerations are summarised in Table 6.5.3). The deceleration of events *B1a*, *B1c* and *B2b* are found to be within 1.7-σ of each other; the mean weighted deceleration based on these three events is 0.32±0.03 km/s^2. Such consistency in the deceleration of wind events spread over two days infers the presence of a repeatable mechanism in generating these winds. The deceleration for event *B2a* is noticeably much larger (1.10±0.38 km/s^2) than these other events but the relatively large error it has still puts it within 2.2-σ of the other calculated decelerations.

Event B2c (Fig. 6.29) was unique in that it was the only one of the events where the wind absorption was actually observed to accelerate from the line centre; the measured acceleration of this absorption is 0.12km/s^2. This acceleration of the line centre occurs for quite some time (nearly 35 minutes) before a sudden rapid acceleration, taking the line centre to a velocity of over -1200km/s, is seen. Given that this behaviour does not conform with any of the other wind events, it must be concluded that this was an unusual event.

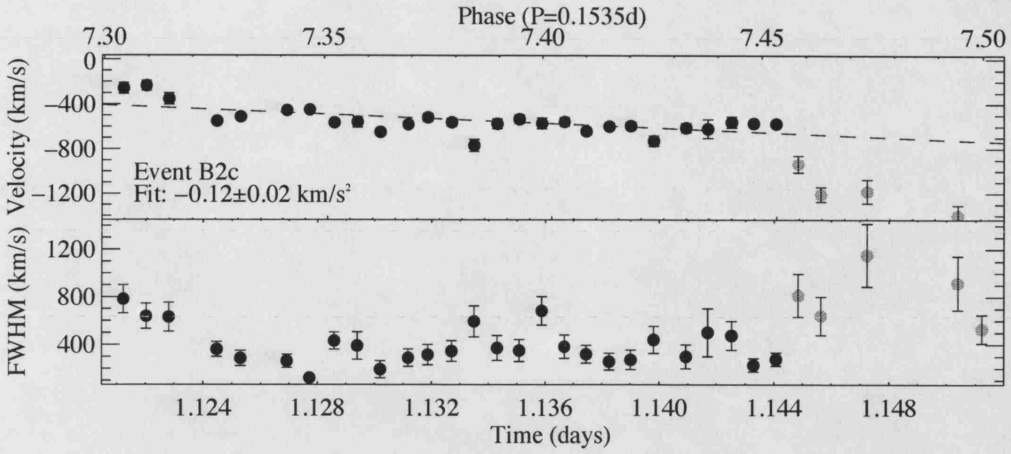

Figure 6.29: Plots of the central velocities and FWHM of the best fit single Gaussian profiles to the wind driven blue-shifted absorption in event B2c (from the WHT time-series); each data point is shown with a 1-σ error bar. A linear fit was performed to the initial accelerating central velocities, the result of which is shown on the plot; the latter velocities (shown in grey) were not included in the fit as they did not seem to conform to the linear acceleration.

6.6 Discussion

The analysis of optical time-series in this chapter has presented evidence for optical components of the accretion disc wind. The re-analysis of the WHT time-series (originally presented in Ringwald & Naylor 1998) showed the optical component to the wind to be blue-shifted absorption events for both the He I 5876Å and Hα lines, forming at a velocity of ~ -1500 km/s and gradually decelerating towards the line centre. These episodic events are only initially detected at these moderate to high blue-ward velocities and their progression from the low velocities is never seen, which raises the likelihood that this initial progression is very rapid. For example, the temporal resolution of the WHT time-series is 60 seconds meaning that for material to be accelerated to -1500 km/s between spectra would require an acceleration of at least 25 km/s^2. Measurements taken from the He I line, involving a process of removing the emission and fitting the remaining wind with a Gaussian profile, revealed the deceleration of this absorption to be ~ 0.3 km/s^2. The repetition of these wind events in the WHT time-series is between 80 and 120 minutes but, the repetition is far from regular and there is no evidence of a connection with the orbital period or, a superhump period (the presence of a positive superhump period of

0.15634 days was suggested by Kato & Uemura 2001).

The contribution of the McDonald time-series to the study of the disc wind was small but not insignificant. With only one recorded wind event, it was not possible to provide the detail study of the wind that it was hoped that the McDonald data would provide but it did importantly show that despite having similar flux levels to the WHT time-series (and hence similar mass-transfer rates) there was no regular occurrence of these wind events.

Ringwald & Naylor (1998) state that the P-Cygni absorption events (i.e. the blue-shifted wind events) trace out a sawtooth shapes in the continuum, but in this re-analysis of the WHT time-series the initial acceleration to the high velocities that this sawtooth shape implies, were not observed. If, as what appears to be the case, that the wind is accelerated to high velocities in a short space of time, then a suitable mechanism must be found to perform these rapid accelerations. The commonly believed mechanism for accelerating disc winds from CVs is line driving but for a wind to be driven in such a way, the blue-shifted absorption would perhaps be observed to gradually broaden from the line centre (this is dependent on whether a confinement mechanism is involved), as the mass is accelerated and hence would not be a suitable driving mechanism for these optical wind events. One theory to explain these observations which has been discounted by Ringwald & Naylor (1998) is that these wind events originate from pockets of gas which have been ballistically thrown from the accretion disc in such a way that its component of velocity along the line of sight decreases over time.

Using the concept of a ballistically accelerated pocket of gas provides some avenues for describing the observed linear deceleration. One possible solution for the observed deceleration is that a retarding force is acting on the pocket of gas to slow it down after it has been ballistically accelerated. The problem with such as concept is the need for the linear deceleration since a force such as gravity decreases with distance and thus so would the deceleration. A more plausible explanation for the linear deceleration is if the pocket of gas itself were not decelerating but its direction were changing with respect to the line of sight of the observer; maintaining such constant velocity in such a scenario would probably be very difficult but it will be assumed as though for the purposes of this example. A motion such as that described would perhaps be possible if the pocket of gas were following a magnetic field line. Blandford & Payne (1982) showed that a centrifugally driven disc wind may be formed if the magnetic field of the disc wind is

sufficiently strong enough and if the poloidal component of the magnetic field makes an angle of less than 60° with the disc surface (i.e. a magneto-centrifugal ejection). Thus magnetism could potentially provide both the confinement and launching mechanisms for these wind events. There is currently no evidence to suggest that BZ Cam has a strong magnetic field but there are two possibilities to consider with respect to this issue. Firstly, many VY Scl systems have also been found to be SW Sex systems so the possibility is that BZ Cam is also an SW Sex system, although there is currently no evidence to support this hypothesis. In the model of an SW Sex systems proposed in Horne (1999), a magnetic field is anchored in the inner disc and it propels material from it; this could be the source of the intermittent high velocity absorption observed for BZ Cam. Even if BZ Cam is not an SW Sex system, arguments using spectral features and timing properties of VY Scl have been put forward suggesting that this sub-group of nova-like systems have strongly magnetised white dwarfs (see Jameson *et al.* 1982; Hollander & van Paradijs 1992). In fact, calculations provided by Hameury & Lasota (2002) to determine the magnetic field strength of VY Scl system suggests that it may even be as high as that of an intermediate polar system.

Fig. 6.30 is a demonstration of the trajectory that a pocket of gas which has been ballistically thrown from an accretion disc might have assuming that the gas is travelling at 1500 km/s and has a line of sight deceleration of 0.32 km/s^2. The simulation of this trajectory (which is for demonstrative purposes only) assumes that the pocket of gas is initially thrown in a direction normal to the accretion disc and that the inclination angle of the disc is 0°. This trajectory demonstration is not unlike the path that a mass might follow if it were confined to magnetic field lines. There is however one caveat to this demonstration. The binary separation between the two stars of a CV ranges from 0.5-3R$_\odot$ (Warner 1995) or from 0.4-2.1×10^{6}km. Using the trajectory presented in Fig. 6.30, by the time the line of sight velocity of the pocket of gas has reached -700 km/s, the distance it would have travelled perpendicular to the disc would be at the upper end of this binary separation range and would therefore no longer be an absorbing component. This trajectory path is however very simplified since a pocket of gas thrown ballistically from the disc would still be influenced by the gravity field of white dwarf and thus would not be able to maintain this fixed velocity.

How does the idea of gas being ballistically thrown from a disc affect the other results? The observations of Hα are similar to He I 5876Å but, there is also the presence of a regular

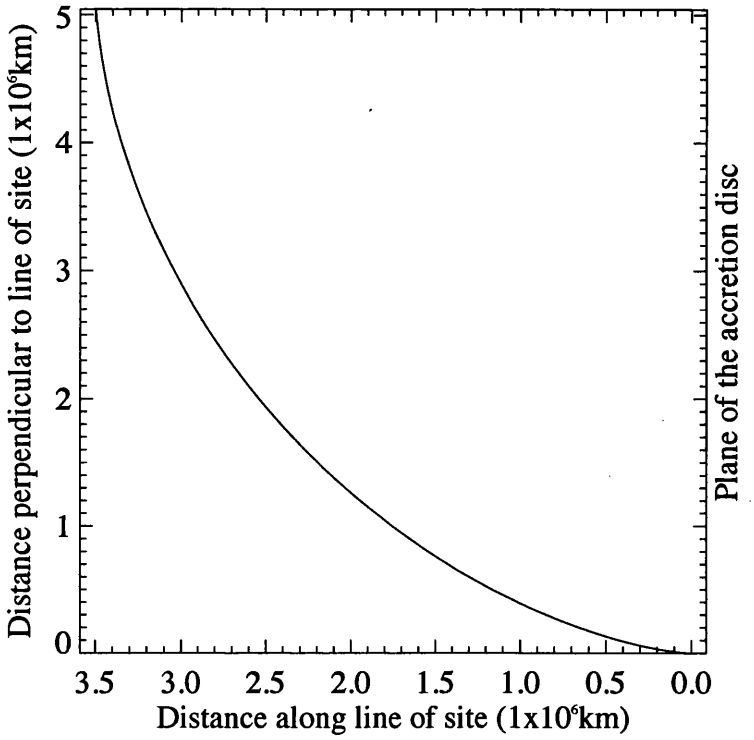

Figure 6.30: Calculated trajectory of a pocket of gas with a fixed velocity of 1500 km/s and a projected deceleration along the line of sight of 0.32 km/s^2. It is assumed that the disc of the cataclysmic variable has an inclination of 0 degrees and that the gas is initially thrown directly towards the observer.

excess of flux over the red-ward side of the line centre. Ringwald & Naylor (1998) suggest that it may be the result of a rotating outflow although they concede that the lack of correlation with the P-Cygni events make this idea somewhat flawed. The source of this red-ward emission excess remains unknown. It is also necessary to be able to explain why only one event was observed in the 7 nights of the McDonald time-series. These events are obviously strong enough to be visible in the Balmer lines other than Hα because that single event is observed in the second night of the observing run for the Hβ line. It is also important to restate that BZ Cam had not yet entered a state of quiescence during the McDonald observations (although it was relatively close) so the change in the occurrence of the events cannot be related to the mass transfer rate. If these wind events are however related to magnetic field strength then perhaps they reveal a reduction in the field strength before the system enters the state of quiescence.

The UV and far-UV studies of BZ Cam (Griffith *et al.* 1995; Prinja *et al.* 2000*b*)

provide clear evidence that this CV is driving an accelerating outflow from the accretion disc. The 'picture' presented by these UV observations is of an erratic and chaotic wind which shows no obvious modulation; this is essentially the same view provided of the episodic wind events in the WHT He I 5876Å and Hα data. Since the UV and optical continua form at different locations along the accretion disc and the line diagnostics used in the optical analysis are different to those in the ultraviolet, it is easy to understand why differences may exist between their behaviour although it also cannot be ruled out that the phenomenon observed at UV and optical wavelengths are not of the same origins. Despite the lack of wind events in the McDonald time-series, for this optical wind component to be better understood it is necessary for additional optical time-series observations of BZ Cam to be taken.

CHAPTER 7

FUSE Survey of Disc Winds from CVs

7.1 Introduction

For the main bulk of this thesis, case studies of accretion disc winds from several, roughly similar, high state CVs have been presented. The case studies showed that two apparent similar systems (V592 Cas and RW Sex) can show very similar disc winds while another, apparently similar CV (BZ Cam) can show a significantly different and somewhat unpredictable disc wind. There are, of course, known differences between these systems such as the orbital period and, BZ Cam is a VY Scl system rather than a UX UMa system like the other two CVs but, it is not entirely clear how these factors relate to the disc winds. To understand how the known parameters of a system affect the accretion disc wind it is necessary to survey a number of wind driving systems using similar data (i.e. of the same wavelength range) and to log the similarities and differences. In this chapter, such a survey is presented.

This survey relies on far-UV data collected with the FUSE; all of the data to be presented are available to the public through the Multi-mission Archive at the Space Telescope Science Institute (or MAST). Far-UV spectroscopy has been selected for this survey because not only has such a survey not been performed before but, FUSE data had already shown itself to be very successful in the analysis of the disc winds from V592 Cas and RW Sex (see § 3 and § 5). It has been repeatedly stated that time-averaged spectra do not provide a complete picture of a disc wind and a time-dependent analysis of disc winds should always be performed. Despite this, time-averaged spectra are the focus of this survey because they can still reveal some important characteristics

of the disc wind and, a time-series analysis of all the systems in this survey would be large and unwieldy, especially when the size of just one of the individual case studies is taken into consideration; it is also likely that many of the CVs of interest do not have appropriate FUSE time-series data. This survey also focusses on orbital periods and their relationship with the disc wind because for many systems, the orbital period is the only known physical parameter and it does give indication of the system size. The relationship between inclination angle and disc wind is also discussed in some part because it can give valuable information about different streamlines through a wind from a variety of systems. However, for many of the systems to be presented, the inclination angle is not known to any accuracy which limits the extent to which it can be analysed.

7.2 Selecting Appropriate CVs and Processing the Archive Data

The selection criteria for this survey was relatively simple; nova-like or dwarf novae CVs which were known to be wind driving but had also been observed with FUSE, the data also had to be publicly available. The initial step was to produce a list of CVs observed with FUSE, this was an extremely easy task using the online search tool. This list of systems was considerably reduced in size by searching each target for evidence of a disc wind and rejecting those systems which did not show any. It would of course have been possible to search for evidence of the disc winds from the FUSE data itself but, the MAST online previews were not really suitable for this purpose and from the time the request for the data was put forward to the time the data was actually downloaded was on the order of one day. It was therefore more efficient and faster to perform a search through literature for evidence of a disc wind from a specific CV and failing that, a search for evidence proceeded to IUE archive data. The FUSE observed list of CVs was reduced to 24 systems, which are listed in Tables. 7.1 and 7.2.

There is an obvious caveat to including dwarf novae in a survey of disc winds, dwarf novae disc winds are only present during outburst. For several of the dwarf novae CVs listed in Table 7.2, IUE evidence has clearly indicated the presence of a strong wind but, these observations would have been taken when the system was in outburst and since these outbursts cannot be predicted, there is no guarantee that any of the FUSE observations were taken during outburst either (this can only be determined by actually viewing the

FUSE spectra of each dwarf nova CV). The primary purpose of this study is to investigate the disc winds properties and so one option would be to exclude from the survey, those dwarf novae which are found to be in a state of quiescence. However, the purpose of this survey is also to act as an archival resource so those systems which have been observed during quiescence will still be included in group line profile plots (and clearly indicated as so) but they will not be included in the detailed analysis.

The spectra for each of the 24 targets were downloaded from MAST. For each target there are numerous exposures which is dependent on the planned observing run for the target. For each of these exposures there were eight FITS (Flexible Image Transport System) files, one for each of the FUSE channels. As with the RW Sex and V592 Cas case studies, further analysis was limited to just three channels: LiF1a, LiF2a and SiC2a. Each exposure of each channel was imported into IDL and checked for quality purposes; the exposures from each channel which were not rejected were then combined into a single time-averaged spectra. Thus for each of the 24 target systems there were three spectra available for further analysis.

7.3 The Orbital Periods

From the 80 minute lower limit to the 2-3 hour period gap, the orbital period distribution of CVs is well studied (see § 1.3.2). The orbital period for a CV is usually well known but, there are occasions when it is measured photometrically and confused with the superhump period (see § 3.7 for more information on superhumping). Despite this, when an orbital period is known it is unlikely to be more than a few percent inaccurate. There has been no evidence presented so far to indicate that the orbital period distribution of wind driving CVs is any different from the general population of nova-like and dwarf novae systems, so this is an ideal opportunity to check this. Fig. 7.1 is a plot comparing the orbital period of all the CVs in this survey with all known nova-like and dwarf novae systems listed in Ritter & Kolb (2004). The one caveat of this comparison is that in the general population of CVs there are approximately equal numbers of nova-like and dwarf novae systems, while in this survey the dwarf novae are under represented. The reason that the dwarf novae are under represented in this survey is that dwarf novae disc winds are only visible during outburst which are unpredictable events meaning that it is extremely difficult to obtain observations of dwarf novae during outburst. Hence, the disc winds of

Name	Type	P_{orb} (days)	Wind Reference
AH Men	Nova-like/IP?	0.127	Gänsicke & Koester (1999)
BH Lyn	SW Sex	0.156	Hoard & Szkody (1997)
BP Lyn	UX Uma/SW Sex?	0.153	Hoard & Szkody (1996)
DI Lac	Classical Nova	0.544	Moyer *et al.* (2003)
IX Vel	UX Uma	0.194	IUE Archive data
LS Peg	SW Sex	0.175	IUE Archive data
MV Lyr	VY Scl	0.132	IUE Archive data
QU Car	UX Uma	0.454	Drew *et al.* (2003)
RW Sex	UX Uma	0.245	§ 3
RZ Gru	UX Uma	0.36	IUE Archive data
TW Pic	VY Scl	0.265	IUE Archive data
V3885 Sgr	UX Uma	0.216	Woods *et al.* (1992)
V592 Cas	UX Uma	0.115	§ 5
V751 Cyg	VY Scl	0.144	IUE Archive data
V795 Her	Nova-like/SW Sex?	0.108	Rosen *et al.* (1998)
WX Cen	V Sag	0.417	Diaz & Steiner (1995)

Table 7.1: A table of wind driving nova-like CVs whose FUSE archive spectra will be studied in this survey.

dwarf novae are rarely observed.

The comparison between the two orbital period distributions reveals three things. Firstly, in the general population of CVs there are a far greater proportion of systems below the period gap than is observed for the systems in this survey. This could be due to the under representation of the dwarf novae systems which do have a relatively high proportion of short period systems. Secondly, there is a complete lack of systems at the low end of the period gap but, at the upper end there appears to be a larger than normal population. Thirdly, the drop in the proportion of systems towards high orbital periods is observed but, it is not as clear as for the overall population of CVs and, there is a particularly strong peak in the histogram between 6-7 hours. These last two observations are probably a result of representing a general population of CVs with a small number of systems; some deviation from the general population would be expected. Thus all three

Name	Type	P_{orb} (days)	Wind Reference
EM Cyg	Z Cam	0.291	
RX And	Z Cam	0.210	IUE Archive data
SS Cyg	U Gem	0.275	
SW Uma	SU Uma	0.057	
U Gem	U Gem	0.177	
VW Hyi	SU Uma	0.074	IUE Archive data
WX Hyi	SU Uma	0.075	IUE Archive data
Z Cam	Z Cam	0.290	

Table 7.2: A table of wind driving dwarf-nova CVs whose FUSE archive spectra will be studied in this survey.

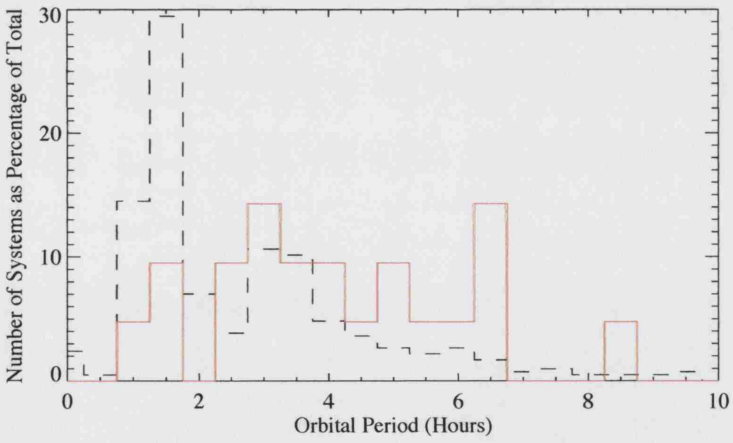

Figure 7.1: A histogram comparing the orbital period distribution of the wind driving CVs in this FUSE survey (the red, solid line) with the orbital period distribution of all known nova-like and dwarf novae systems listed in Ritter & Kolb (2004) (the black dashed lines).

observations are likely to be the result of the population sample used in comparison to the general population. The inference from this comparison is that the population of CVs used in this survey (and therefore probably for wind driving systems in general) is not unusual.

7.4 Inclination Angles

Although the inclination angle is not so much a physical parameter as an observational one, it is nonetheless extremely important. In the case of wind driving CVs, it is necessary for the column density of absorbers along the line of sight to be high enough to produce absorption on the spectrum of the CV; this does put constraints on the inclination angles at which wind driving systems can be observed at. If, for example, a CV is at a particularly high inclination then there many not actually be any disc for the wind to project against (the accretion disc emits in the UV in the inner disc regions). This could potentially result in an enhanced resonance emission but, the characteristic absorption would not be present. Another potential limit to the inclination angle comes from the actual opening angle of the wind. Using the assumption that the wind flows radially, then if the opening angle of the wind is not low enough then regardless of whether there is sufficient disc to project against, there may be no particles along the line of sight to resonantly scatter the photons. The issue of wind opening angle could also affect systems with very low inclination angles since it becomes an issue of how close to the accretion disc normal the wind flows at.

As with the general population of CVs, the inclination angle is not known to any accuracy for many of the systems in this survey. The known inclination angles (or limits in some cases) for the systems in this survey are listed for the systems in the survey in Tables 7.1 and 7.2; for completeness the superhumping status is also indicated. The mean inclination angle for the systems in this survey (where known) is $\sim 45°$, which compares well with the expected value for the general population, assuming a uniform distribution at all angles. However, the greatest inclined system in the survey is U Gem, which has an inclination angle of 69° which suggests that the issues relating to viewing a system at high inclination are likely to be true. The lowest inclined system in the survey is MV Lyr, which has an inclination angle of 12° but, most of the systems are greater than 30° which could be the result of difficulties in measuring the inclination angle of very low inclined

Name	P_{orb} (days)	i	Superhumping
AH Men	0.127	—	Yes (Patterson 1995)
BH Lyn	0.156	—	—
BP Lyn	0.153	low	—
DI Lac	0.544	low	—
IX Vel	0.194	60°	—
LS Peg	0.175	30°	—
MV Lyr	0.132	12°	—
QU Car	0.454	$< 60°$	—
RW Sex	0.245	34°	No (Patterson, private comm.)
RZ Gru	0.36	—	—
TW Pic	0.265	—	Yes (Norton *et al.* 2000)
V3885 Sgr	0.216	$< 50°$	—
V592 Cas	0.115	29°	Yes (Taylor *et al.* 1998)
V751 Cyg	0.144	—	—
V795 Her	0.108	—	Yes (Patterson & Skillman 1994)
WX Cen	0.417	—	—

Table 7.3: A list of the inclination angles (or i) and superhumping status of the nova-like CVs in this survey. Ritter & Kolb (2004) is the source of the inclination angles. A dash in the superhumping column indicates that no known test for superhumping has been performed.

systems.

7.5 Superhumping

In Tables 7.3 and 7.4 it has been indicated whether a systems is a known superhumper or not. It is noted that for the majority of systems the superhump status is unknown and, where it is known it is usually a positive result. RW Sex is the only system in the survey which is specifically known not to be a superhumper and this was only discovered through a private communication between Dr. Raman Prinja and Prof. J. Patterson. This suggests that in cases where a test for superhumping has been performed and the

Name	P_{orb} (days)	Inclination Angle	Superhumping
EM Cyg	0.291	67°	—
RX And	0.21	51°	—
SS Cyg	0.275	37°	—
SW Uma	0.057	45°	Yes (Kato 2002)
U Gem	0.177	69°	—
VW Hyi	0.074	60°	Yes (Vogt 1983)
WX Hyi	0.075	40°	Yes (Walker *et al.* 1976)
Z Cam	0.29	57°	—

Table 7.4: A list of the inclination angles (or i) and superhumping status of the dwarf novae CVs in this survey. Ritter & Kolb (2004) is the source of the inclination angles. A dash in the superhumping column indicates that no known test for superhumping has been performed.

result is negative, the result is not published, although for some of the systems it could simply be that no attempt was made to discover whether it is superhumping or not.

The tables show that 7 out of the 24 survey systems are known to be superhumpers. It is not known whether this is a particularly high result or not because there are no known population studies of the phenomena. It should be noted that there has been no evidence to link disc winds and superhumping; in the case of V592 Cas and RW Sex, superhumping was used as a possible solution for the observed orbital modulation. However, it is still useful to know whether any of the systems are superhumping because it could help to describe any observed behaviour.

7.6 A Spectral Comparison

The purpose of this survey is of course, to present the disc wind characteristics discovered in FUSE data. It would be possible to analyse and compare the entire far-UV spectra from the three FUSE channels (see Table 7.5 for a list of the key wind diagnostic lines in FUSE spectra) but, the survey will instead be more closely based on the successful analysis of the winds from V592 Cas and RW Sex and therefore analysis will be performed on just a small number of select lines. The lines that have been chosen for this analysis

Ion	λ_0(Å)	I.P. of Previous Ion (eV)	I.P of Ion (eV)
C III	977.020, 1125.65, 1175.6	24.4	47.9
N III	989.799	29.6	47.5
N IV *	923.06	47.5	77.5
P IV	950.657	30.2	51.4
S IV	1062.66, 1072.97	34.8	47.3
P V	1117.98, 1128.01	51.4	65.0
S VI	933.39, 944.52	72.7	88.0
O VI	1031.93, 1037.62	113.9	138.1

Table 7.5: This table lists the disc wind diagnostics lines present in the FUSE spectra. The table has been split into those lines which are considered to be low ionisation (upper panel) and those which are considered to be high ionisation for the conditions (lower panel). * N IV is an excited transition.

are: C III 1176Å, S IV 1073Å, P V 1118Å and O VI 1038Å. These four lines were selected because they provide a good range of elements and ionisation states and, in the analysis of V592 Cas and RW Sex, C III 1176Å in particular was shown to be very strong and relatively uncontaminated by interstellar and additional stellar features. The latter three lines are of course doublets but, there would be a duplicate of results if both lines in each doublet were analysed. The following analysis concentrates on the C III 1176Å line but later, comparisons are made between this line and the other three.

7.6.1 The C III 1176Å Line

Fig. 7.2 is a plot of the C III 1176Å profiles for all 24 target systems in this survey. Every time-averaged profile has been normalised to 1.0 and the spectral scales have been converted into velocity space. The plots are in order of increasing orbital period but, a * is used to indicate the dwarf novae systems, to distinguish between them and the nova-like systems. Those dwarf novae systems were are also observed during quiescence are additionally marked with a 'Q'.

The first observation to be made of these plots is that the signal-to-noise greatly varies between them. While some plots provide an unprecedented view of the C III line (IX Vel for example), in other plots it is difficult to ascertain whether there is even a feature at

1176Å (DI Lac for example). This factor of how noisy the data is, is essentially a function of the relative brightness of a CV and the total on source exposure time for all frames used. Unfortunately this issue of data quality is not resolvable without further FUSE observations and so DI Lac and WX Cen must be ruled out from further analysis. The second observation to be made of these plots is that V751 Cyg, TW Pic and RZ Gru show no evidence of any C III absorption. Reasons for this can be easily found for V751 Cyg and TW Pic because both CVs are VY Scl systems (or anti-dwarf novae) and therefore could be in a state of quiescence. For the third system, RZ Gru, there is no easy solution but, one possibility could be a case of incorrect classification. Since these systems cannot be analysed for a disc wind, they too, cannot undergo further analysis; this leaves 19 out of the original 24 systems.

The purpose of this survey is to be able to characterise the disc wind of each system and to monitor differences with respect to the orbital period, for example. It is not to investigate spectral peculiarities with respect to other wind driving systems and there are five systems which do show significant differences in comparison to the remaining systems: the dwarf novae SW UMa, WX Hyi and SS Cyg and, the nova-like systems BH Lyn and QU Car. For the dwarf novae, these peculiarities in the line profiles in comparison to the other CVs are most likely to be related to being in a state of quiescence and have therefore been marked with a 'Q'. BH Lyn is a confirmed SW Sex system so the possibility arises that this is also a VY Scl anti-dwarf novae CV, similar to V751 Cyg and TW Pic. QU Car is also an unusual CV in that it is extremely luminous and there is evidence to suggest that the companion star of the binary is a carbon star (Drew *et al.* 2003). It is perhaps these unusual properties which account for QU Car having a C III line profile unlike any of the other CVs in this survey. Although these systems do warrant further investigation, that is not the purpose of this survey and they are excluded from further detailed analysis of the C III profile. The remaining systems are: VW Hyi, V795 Her, V592 Cas, RW Sex, AH Men, MV Lyr, BP Lyn, LS Peg, U Gem, IX Vel, RX And, V3885 Sgr, EM Cyg and Z Cam.

One aspect of the disc wind profiles which was heavily studied in the V592 Cas, RW Sex and BZ Cam case studies was the relative strengths of the absorption at positive and negative velocities with respect to the line centre. In the (time-series based) case studies of these two systems it was discovered that the majority of the absorption was at negative velocities and therefore the line of sight velocity of the wind was predominantly towards

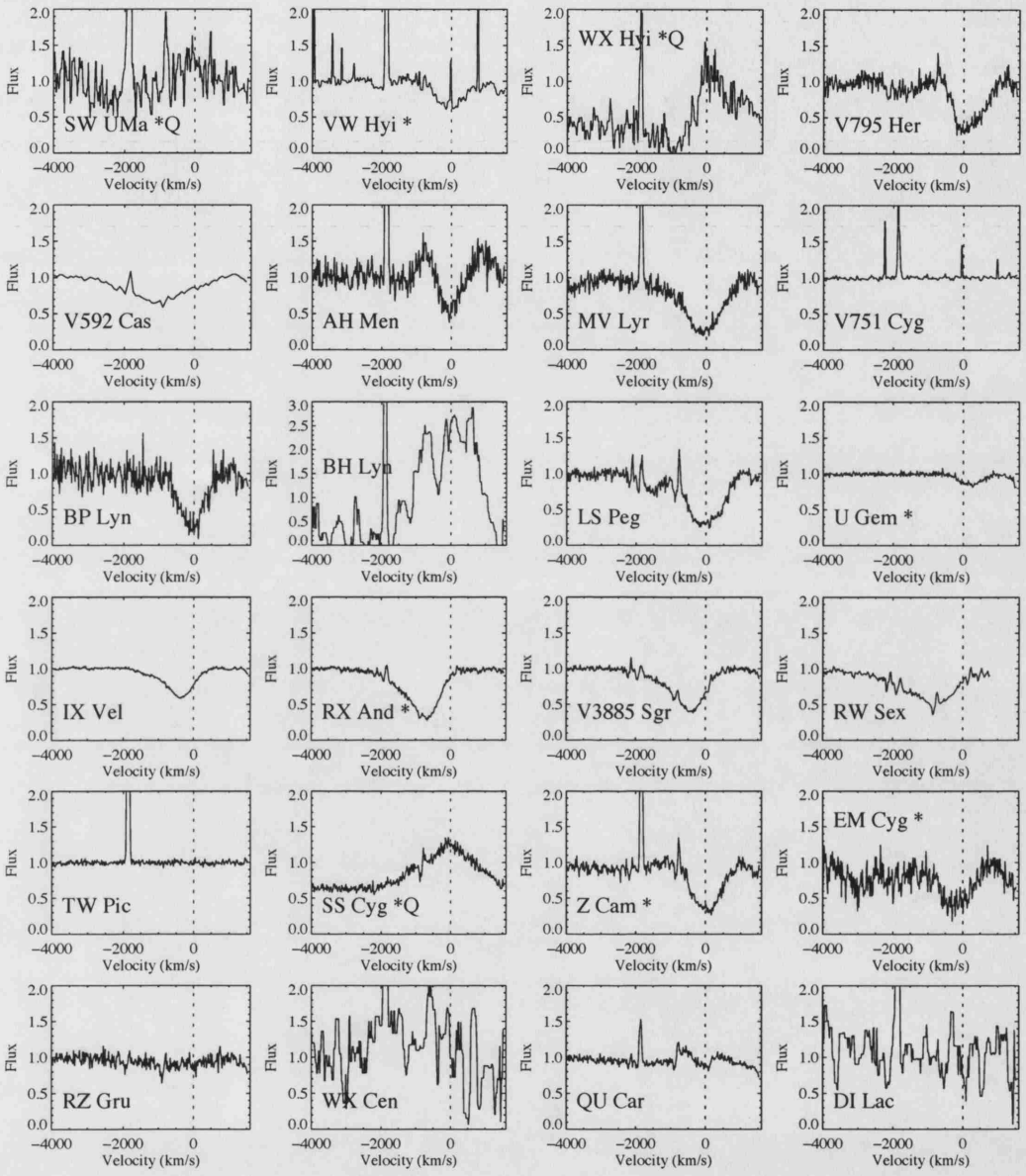

Figure 7.2: Normalised plots of the C III 1176Å line in velocity space, for the 24 target nova-like and dwarf novae (indicated with an * - an additional "Q" indicates that the dwarf novae is in quiescence) CVs in this survey. From left to right, top to bottom, the spectra are in order of increasing orbital period. Some of the spectra have been passed through a median filter to improve the clarity of the line profile.

the observer. This balance between absorption at blue-ward and red-ward velocities is important because it reveals information with respect to the nature of the disc winds. Absorption at blue-ward velocities is relatively easy to explain if it is assumed that the ouflow is accelerating from the disc, since the majority of absorbers in the line of sight between the observer and the disc would have a strong velocity component towards the observer. If an accelerating wind were still assumed, along with radial flows of wind, then red-ward moving material is more difficult to explain. It is conceivable that with high enough inclination angles, the wind which is flowing close to the plane of the accretion disc could provide red-ward absorbers along the line of sight; if the wind flows were not precisely radial and some other component of motion were added into the equation (such as a rotational component) then it is probable that a more plausible scenario could be conceived. Another possible source of significant red-ward absorption could result if the outflow were more ballistic in nature i.e. material is thrown up away from the plane of the disc and then fell back onto it, as discussed for BZ Cam (see § 6.6). The infalling material would have a strong red-ward velocity component but, there would also be a strong blue-ward signature from the material that was originally thrown up although the location of any resulting absorption would be dependent on what section of the disc the ballistic material projected against.

To quantitatively compare the blue/red absorption bias of the systems in this survey, equivalent width measurements were taken across both sides of the C III line centre and the ratio between the two measurements was calculated. These measurements, along with the calculated ratios, are shown in Table 7.6; a ratio of less than 1.0 indicates that the absorption is predominantly red-shifted and a ratio greater than 1.0 indicates that the absorption is predominantly blue-shifted. The one caveat to this technique is that a false asymmetry would be given if, for example, that the C III profile of a particular CV had a very shallow blue-ward absorption which extended to high velocities but, a very deep red-ward absorption. Even if there was in fact more absorption at blue-ward velocities it would still be possible for the ratio to give a red-ward bias. For this reason, measurements of the maximum blue-ward velocity are also made. The first system in the list (which has been placed in order of increasingly blue-shifted absorption) is AH Men, which unlike the other systems in the list, shows significant emission at either end of the absorption; this is why the ratio is negative. The next two systems in the list are U Gem and V795 Her and, these are the only two systems in the survey showing significantly red-shifted absorption.

This red-shifted absorption is clearly visible in Fig. 7.2 (especially for V795 Her) but, what is interesting about this result is that there are no other apparent characteristics to link these two systems. For example, the line profile shapes are very different (U Gem's C III profile is reasonably symmetric while V795 Her's is not) and they are not the same type of CV since U Gem is a dwarf nova and V795 Her is a nova-like system. It is highly probable that there is no common characteristics between these two systems which resulted in the predominantly red-shifted absorption.

Of the eleven remaining CVs in Table 7.6, three show an absorption which has roughly equal strength either side of the line centre. These three systems are Z Cam, VW Hyi and LS Peg and although the ratios calculated for them are not exactly 1.0, when errors are taken into consideration this approximation to the result is quite reasonable. However, the remaining eight systems (and therefore the majority) demonstrate a predominantly blue-shifted absorption as has already been observed for RW Sex and V592 Cas. It should be noted that there are several systems showing a more heavily blue-shifted absorption than RW Sex and V592 Cas, indicating that they are not extreme cases of blue-ward absorption.

Part of the focus of this survey is to search for relationships between the disc wind characteristics and, the orbital period and inclination angle. For the purposes of finding a relationship/correlation, Fig. 7.3 is a plot of the blue/red ratios listed in Table 7.6, against the orbital period and inclination angle. The inclination angle is not known or is only known as a limit for several systems in this survey which explains the reduction in the number of data points in comparison to the plot of orbital period against blue/red. However, regardless of the number of data points, Fig. 7.3 shows there to be no correlation between either inclination angle or orbital period and the blue/red ratio.

It was an interesting result that V795 Her and U Gem (a dwarf nova in outburst) both showed a redshifted C III absorption profile since although this would suggest a connected disc wind behaviour, they both have considerably different profiles shapes. Fig. 7.2 shows that the 14 systems which have been shortlisted for additional analysis show a wide variety of profile shape and, one aspect of the profile shape is the asymmetry. With the variety of profiles observed and without knowing the exact processes involved, it is not so easy to compare the profile shapes but, it is possible to quantitatively compare the profile asymmetries by taking equivalent width measurements either side of the absorption minimum. In Table 7.7, the velocity of absorption minimum, equivalent widths from

Name	P_{orb} (days)	v_{max} (km/s)	Blue EW (Å)	Red EW (Å)	$\frac{\text{Blue}}{\text{Red}}$
AH Men	0.127	-490	0.048	-0.065	-0.74
U Gem	0.177	-550	0.101	0.339	0.30
V795 Her	0.108	-640	0.744	1.597	0.47
Z Cam	0.290	-720	1.166	1.377	0.85
VW Hyi	0.074	-880	0.617	0.657	0.94
LS Peg	0.175	-1020	1.680	1.511	1.11
MV Lyr	0.132	-2980	2.032	1.492	1.36
BP Lyn	0.153	-770	1.391	0.960	1.45
EM Cyg	0.291	-1360	1.693	0.801	2.11
V592 Cas	0.115	-3310	0.933	0.246	3.79
RW Sex	0.245	-3520	1.526	0.276	5.53
V3885 Sgr	0.216	-2765	1.853	0.281	6.60
IX Vel	0.194	-1950	1.168	0.159	7.34
RX And	0.210	-3300	1.946	0.113	17.28

Table 7.6: A table showing the maximum blue-ward absorption velocity and equivalent width measurements from the C III 1176Å line to demonstrate blue or red-ward dominance of the absorption. The blue equivalent width measurements were taken between -1000 and 0 km/s and, the red equivalent width measurements were taken between 0 and 1000 km/s, both with respect to the rest wavelength. The final column is the ratio between the blue and the red equivalent width measurements, to provide a measure of whether the profile is blue-ward or red-ward dominance. A ratio greater than 1.0 indicates that the majority of the absorption is at blue velocities and a ratio less than 1.0 indicates that the majority of the absorption is at positive velocities.

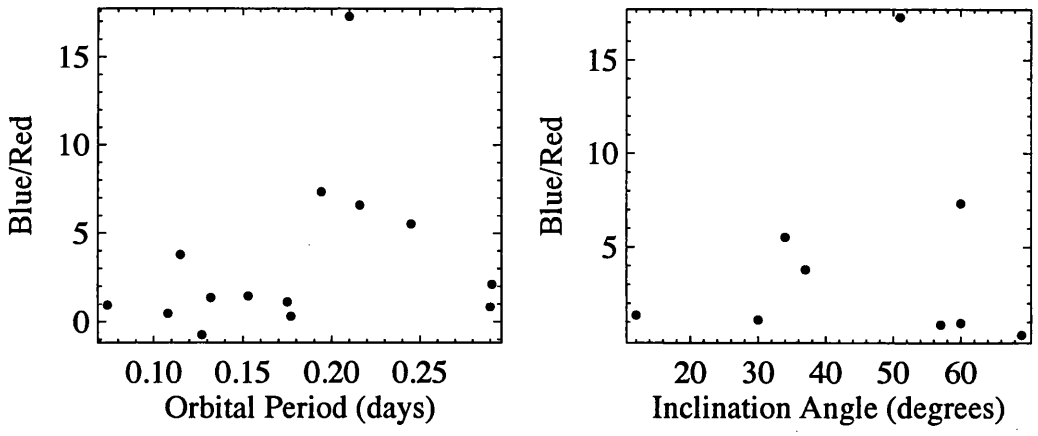

Figure 7.3: A comparison between orbital period and blue/red equivalent width measurements (left plot) and, inclination angle and blue/red equivalent width measurements (right plot) for the C III 1176Å profile.

either side of the absorption minimum and, the ratio between these measurements are listed for each system. The ratio between the equivalent width measurements provides a clear indication of how symmetric a profile is; if the ratio is equal to 1.0 for a particular CV then its C III profile is symmetric but, if it is above or below 1.0, then it indicates an asymmetry to the profile which is either stronger on the blue-side or red-side, respectively.

Firstly, the results of measuring the absorption minimum are discussed. The velocities of the absorption minima were measured by eye because in many cases if the lowest data point had been recorded the result would have been inaccurate. For the majority of the systems, the absorption minimum occurs between ±500 km/s of the line centre which means that for most systems, the column density of absorbers peaks very close to the base of the wind (assuming a linearly accelerating wind). In the case of V795 Her, who's absorption is predominantly at positive velocities, the wind actually peaks in absorption just negative of the line centre. There are only four systems where the peak in absorption is particularly distant from the line centre: RW Sex, V592 Cas, V3885 Sgr and RX And. In the cases of RW Sex and V592 Cas, the peak in absorption is related to their orbitally modulated behaviours, as discussed in the relevant case studies.

The ratio calculations presented in Table 7.7 indicate that although there are extreme cases of profile asymmetry such as for V795 Her and RX And, the majority of the profiles are very close to symmetric with just a slight enhancement towards either the blue or

Name	P_{orb} (days)	V (km/s)	Blue EW (Å)	Red EW (Å)	$\frac{\text{Blue}}{\text{Red}}$
AH Men	0.127	-60	-0.089	0.083	-1.08
V795 Her	0.108	-200	0.289	2.048	0.14
LS Peg	0.175	-100	1.516	1.769	0.86
MV Lyr	0.132	-130	1.754	1.882	0.93
VW Hyi	0.074	-100	0.531	0.541	0.98
RW Sex	0.245	-860	1.355	1.366	0.99
EM Cyg	0.291	-250	1.297	1.297	1.00
V592 Cas	0.115	-1060	0.999	0.916	1.09
U Gem	0.177	280	0.247	0.211	1.17
BP Lyn	0.153	-50	1.272	1.060	1.20
Z Cam	0.29	140	1.473	1.052	1.40
IX Vel	0.194	-360	0.855	0.606	1.41
V3885 Sgr	0.216	-360	1.495	0.954	1.57
RX And	0.21	-650	1.825	1.060	1.72

Table 7.7: A table showing the velocity of the absorption minimum and equivalent width measurements from the C III 1176Å line, to demonstrate the asymmetry of the profiles. The blue equivalent width measurements were taken between -1000 and 0 km/s and, the red equivalent width measurements were taken between 0 and 1000 km/s, both with respect to the velocity of the absorption minimum. The final column is the ratio between the blue and the red equivalent width measurements, to provide a measure of the profile asymmetry. A ratio close to 1.0 would indicate that the profile is symmetry, while a ratio greater or smaller than 1.0 would indicate an asymmetric profile which is either blue-ward or red-ward dominated, respectively.

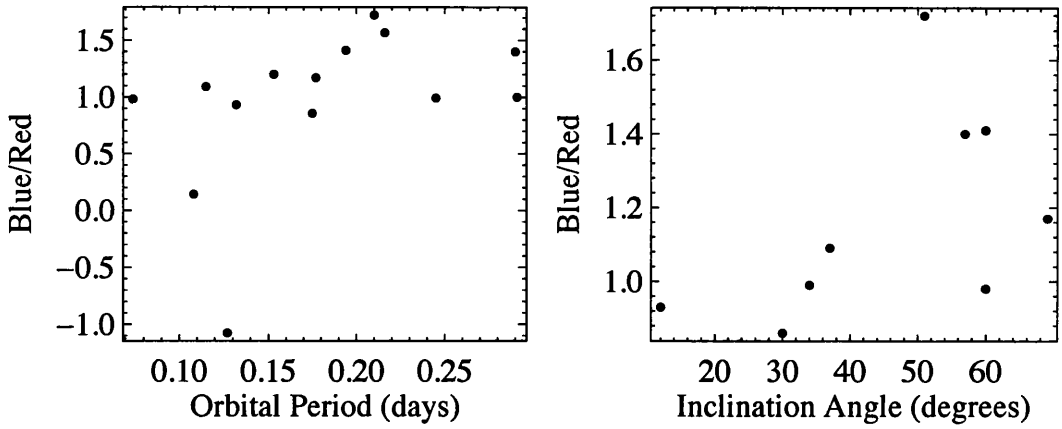

Figure 7.4: A comparison between orbital period and profile asymmetry (left plot) and, inclination angle and profile asymmetry (right plot) for the C III 1176Å profile.

the red. Comparing these profile calculations to the orbital period (see the left hand panel of Fig. 7.4) demonstrates this further, where a linear correlation of the two values could be confused with a general spread about a symmetric ratio. Note, however, that in the comparison of profile asymmetry to inclination angle, there is a hint of a possible correlation, favouring a more blue-ward asymmetric profile at greater inclination angles.

If an analysis into line profile geometry relied entirely on these asymmetry measurements, then the disc wind of a system such as LS Peg could end up being characterised with systems such as RW Sex and V592 Cas. However, Fig. 7.2 shows clear differences in profile shapes between these systems since the C III profiles of V592 Cas and RW Sex could be approximated by a Gaussian while the C III profile of LS Peg is more closely approximated in shape by the letter "U". A comparison between LS Peg and V592 Cas (or RW Sex) is an interesting one to make because LS Peg is believed to be a low inclination SW Sex system and therefore is believed to be undergoing stream overflow. In the case study for V592 Cas, the scenario was put that V592 Cas is an SW Sex system undergoing stream overflow, in an effort to explain the orbitally modulated disc wind. Clearly the profiles differ significantly inferring that this is not a realistic scenario, as it was also concluded in the case study.

7.6.2 A Comparison of Wind Line Strengths

So far in this survey, analysis has concentrated on the disc wind characteristics of the C III 1176Å line. It is unfortunate that such an analysis for the additional wind diagnostic lines of S IV 1073Å, P V 1118Å and O VI 1038Å is not so easy due to the differing contamination from interstellar lines of hydrogen and, narrow stellar absorption lines which are probably photospheric in origin. Nevertheless, in this section a simple, but nonetheless useful, comparison of line strengths is presented.

The equivalent widths of the C III 1176Å, S IV 1073Å, P V 1118Å and O VI 1038Å lines were measured across a velocity band of -2000 to 2000 km/s; this velocity band was chosen because it was believed to encompass the majority of a line profile, regardless of the location in velocity space of the absorption. These measurements were performed on the 14 systems chosen for further analysis in the previous section since the peculiarities observed for the C III profiles of the other ten CVs are additionally observed in the other lines. To provide evidence with respect to this issue, Figs. 7.5, 7.6 and 7.7 are plots of the S IV 1073Å, P V 1118Å and O VI 1038Å lines for all 24 target CVs in this survey. It is clear from these plots that in most cases, the potential problems observed for the C III line persist at other wavelengths (for example, the lack of absorption for V751 Cyg). The equivalent width measurements are listed in Table 7.8.

Fig. 7.8 is the first test of these measurements, where the strengths of the C III and P V lines are plotted against the orbital period. Although the C III line has already been heavily analysed, it has again been chosen for this analysis for its shear strength and lack of contamination from additional components. The P V line is likewise fairly strong and less contaminated by additional features than either the S IV or O VI lines. In the plot comparing the C III line strengths with the orbital periods, there is evidence of a trend towards a stronger absorption line for systems with longer orbital periods, although there is significant scatter of the data points about such a trend. However there is no evidence of such a trend in the comparison between the P V line strength and orbital period. There are several questions to take from these plots. Firstly, is there really a trend or correlation between the C III line strength and the orbital period? Secondly, why would there be a relationship between line strength and the orbital period and thirdly, why is no such relationship observed for P V? Given that all of these lines were observed to behave similarly in the V592 Cas and RW Sex case studies, this does not make any sense.

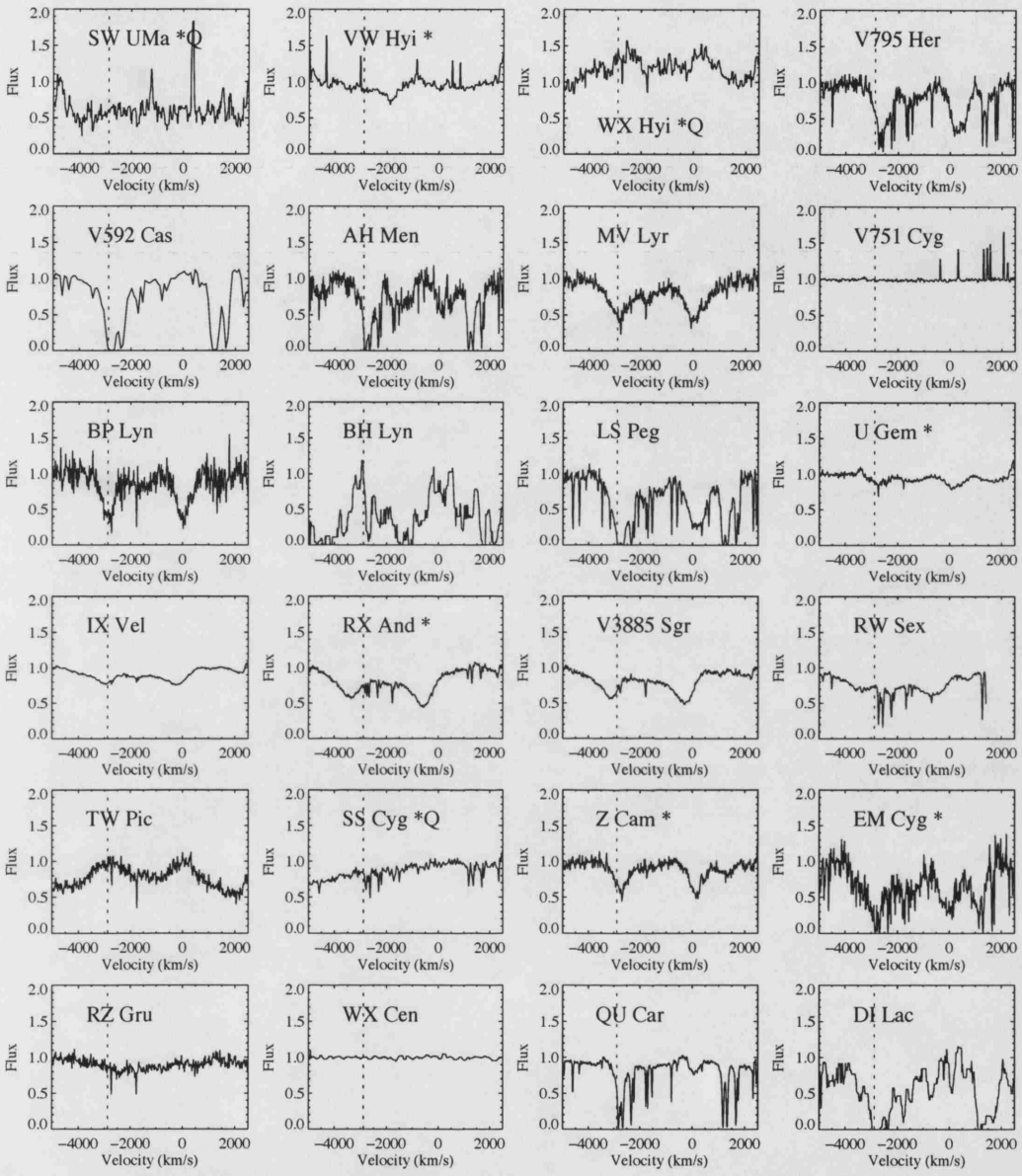

Figure 7.5: Normalised plots of the S IV 1073Å line in velocity space, for the 24 target nova-like and dwarf novae (indicated with an * - an additional "Q" indicates that the dwarf novae is in quiescence) CVs in this survey. The vertical dotted lines indicate the location of the rest wavelength of the S V 1063Å line. From left to right, top to bottom, the spectra are in order of increasing orbital period. Some of the spectra have been passed through a median filter to improve the clarity of the line profile.

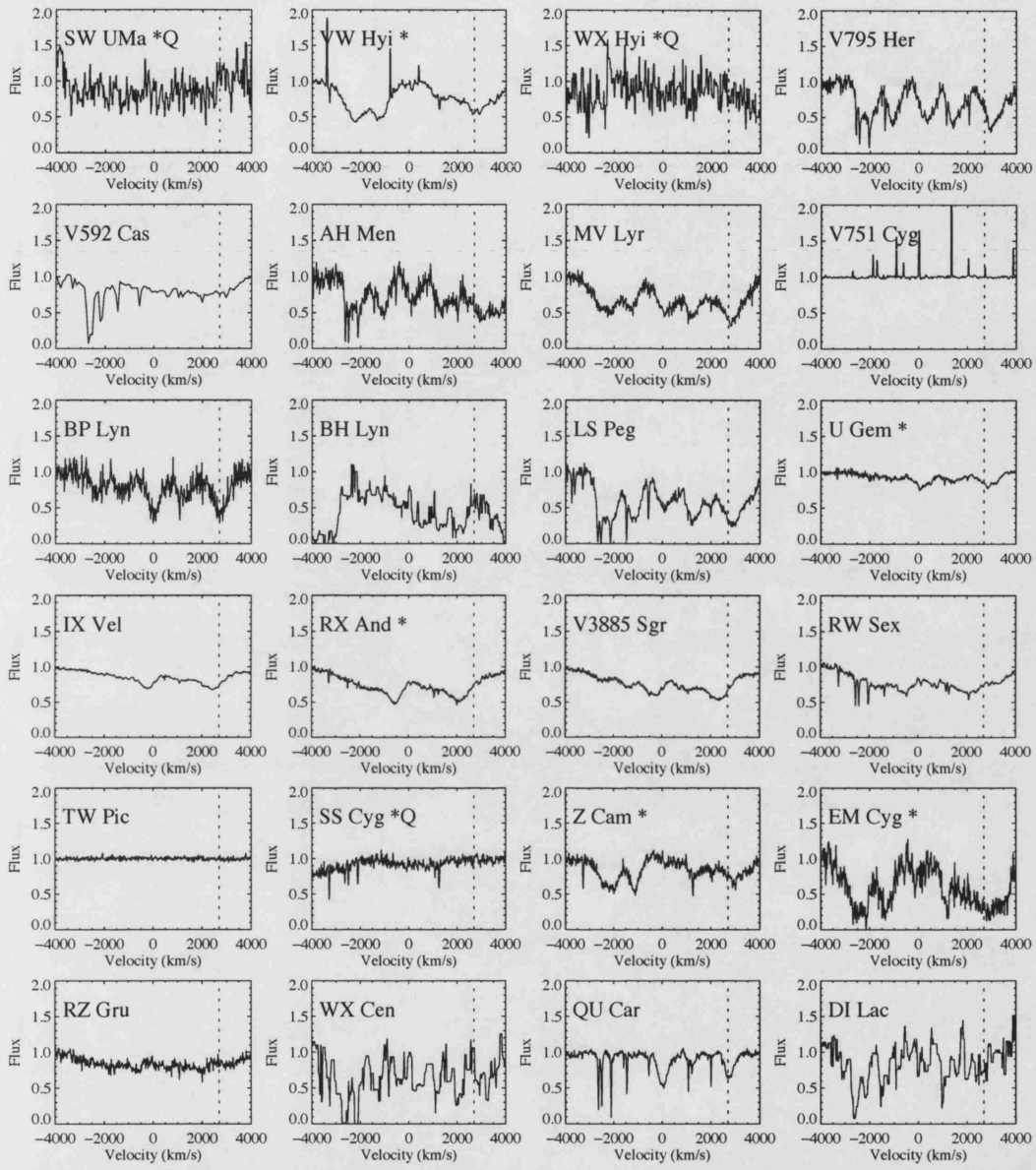

Figure 7.6: Normalised plots of the P v 1118Å line in velocity space, for the 24 target nova-like and dwarf novae (indicated with an * - an additional "Q" indicates that the dwarf novae is in quiescence) CVs in this survey. The vertical dotted lines indicate the location of the rest wavelength of the P v 1128Å line. From left to right, top to bottom, the spectra are in order of increasing orbital period. Some of the spectra have been passed through a median filter to improve the clarity of the line profile.

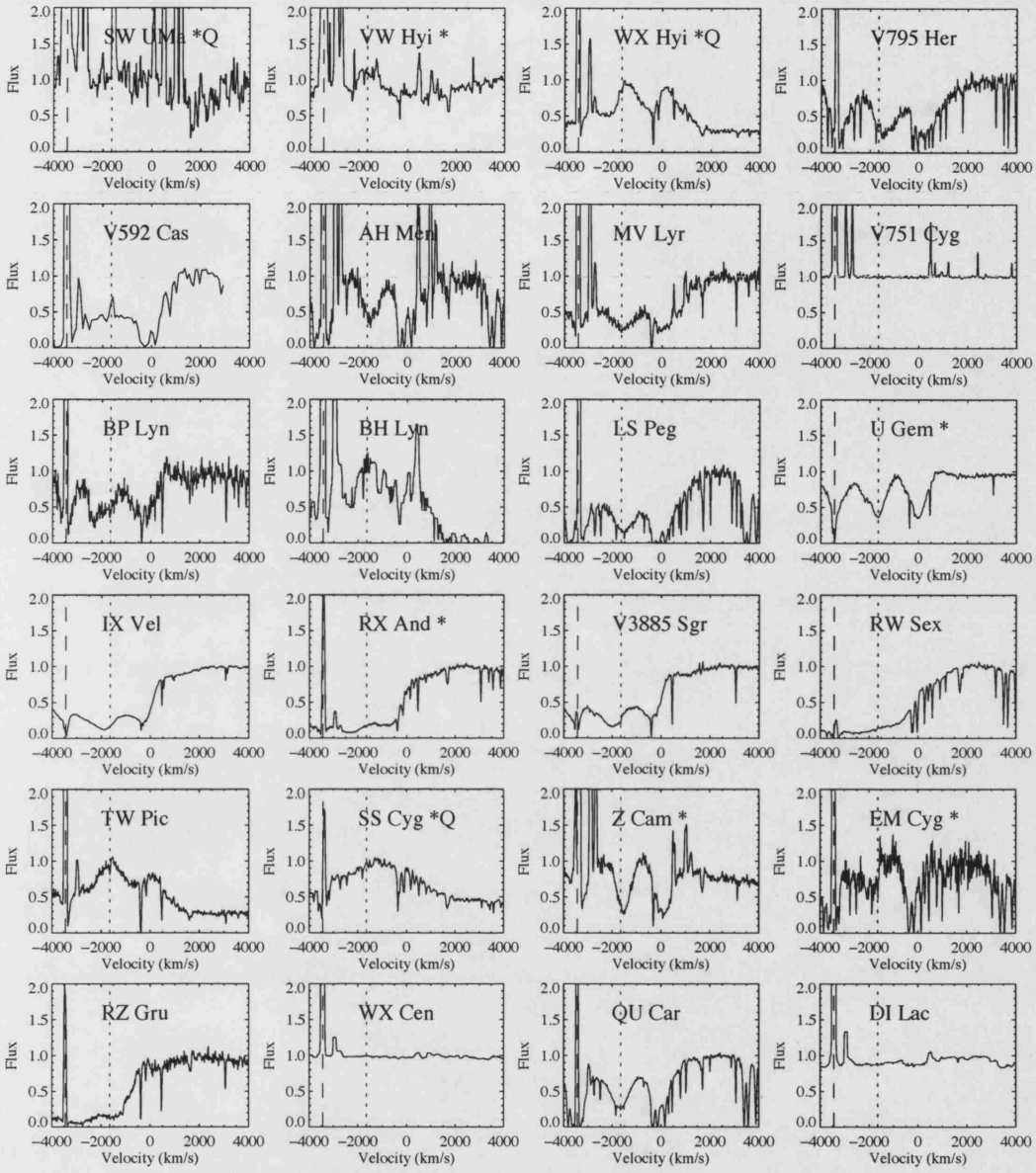

Figure 7.7: Normalised plots of the O VI 1038Å line in velocity space, for the 24 target nova-like and dwarf novae (indicated with an * - an additional "Q" indicates that the dwarf novae is in quiescence) CVs in this survey. The vertical dotted lines indicate the location of the rest wavelength of the O VI 1032Å line and the vertical dashed lines indicate the location of the rest wavelength of the Lyβ line. From left to right, top to bottom, the spectra are in order of increasing orbital period. Some of the spectra have been passed through a median filter to improve the clarity of the line profile.

Name	P_{orb} (days)	C III (Å)	S IV (Å)	P V (Å)	O VI (Å)
VW Hyi	0.074	1.347	0.881	3.384	1.540
MV Lyr	0.108	4.091	3.174	5.279	6.768
IX Vel	0.115	1.580	1.392	2.725	6.364
AH Men	0.127	-0.270	4.261	3.733	3.740
V592 Cas	0.132	2.159	3.026	2.896	6.101
U Gem	0.153	0.581	1.147	1.526	3.573
V795 Her	0.175	2.837	4.078	4.963	7.141
RW Sex	0.177	3.127	3.009	4.078	6.917
EM Cyg	0.194	3.661	5.605	5.057	3.031
RX And	0.21	3.171	3.121	5.099	6.371
BP Lyn	0.216	2.747	2.421	3.735	4.380
V3885 Sgr	0.245	2.820	2.839	4.320	5.485
Z Cam	0.29	2.871	1.850	2.201	3.867
LS Peg	0.291	3.903	6.295	6.645	8.440

Table 7.8: A table showing the equivalent width measurements in units of Å from the C III 1176Å, S IV 1073Å, P V 1118Å and O VI 1038Å lines, for the 14 CVs in this study selected for further analysis. The measurements were taken between -2000 and 2000 km/s from the rest wavelength. The table is in order of increasing orbital period.

There are no easy answers to these questions, except that one possible reason for why it is not observed for P V is the additional scatter of data points that these measurements have. Plots of the S IV and O VI line strengths against orbital period (see Fig. 7.9) show no trend either, although if the fears about the P V measurements are true, this does not necessarily mean anything.

Fig. 7.10 is the second comparison to be made directly from the line strength measurements, which is a comparison between the line strength and inclination angle; the C III and P V line have again been chosen for this analysis. There are obviously far less data points than in the comparison of line strength and orbital periods but, what can be seen is clear evidence of a negative trend, where a more highly inclined system has a weaker line. This loss of absorption strength for increasing inclination angle is a well observed

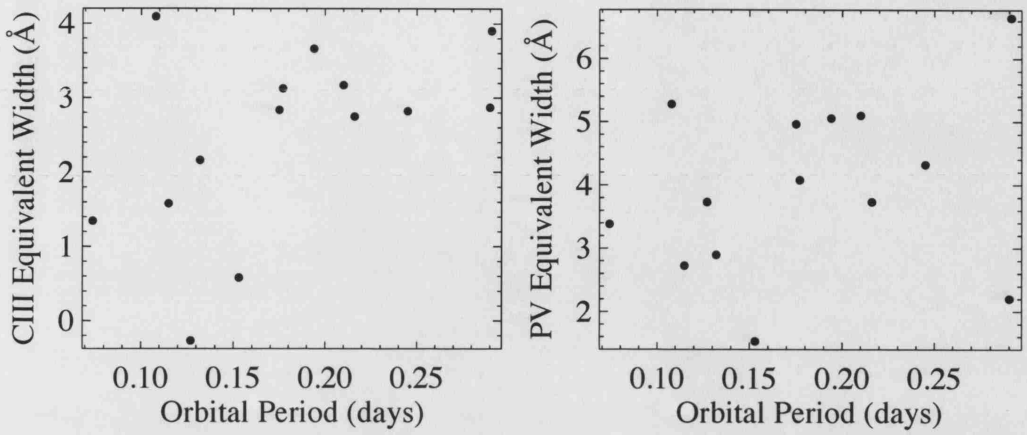

Figure 7.8: A comparison between the measured line strengths and orbital periods for the C III 1176Å and P V 1118Å lines.

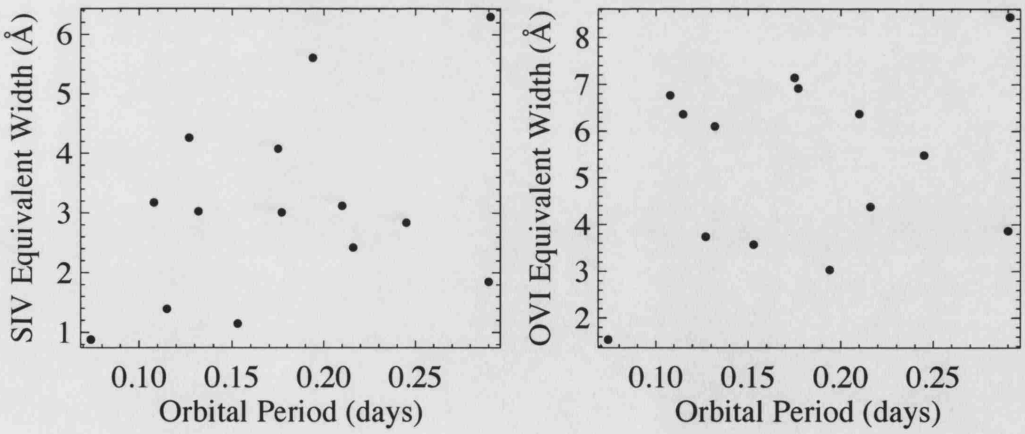

Figure 7.9: A comparison between the measured line strengths and orbital periods for the S IV 1073Å and O VI 1038Å lines.

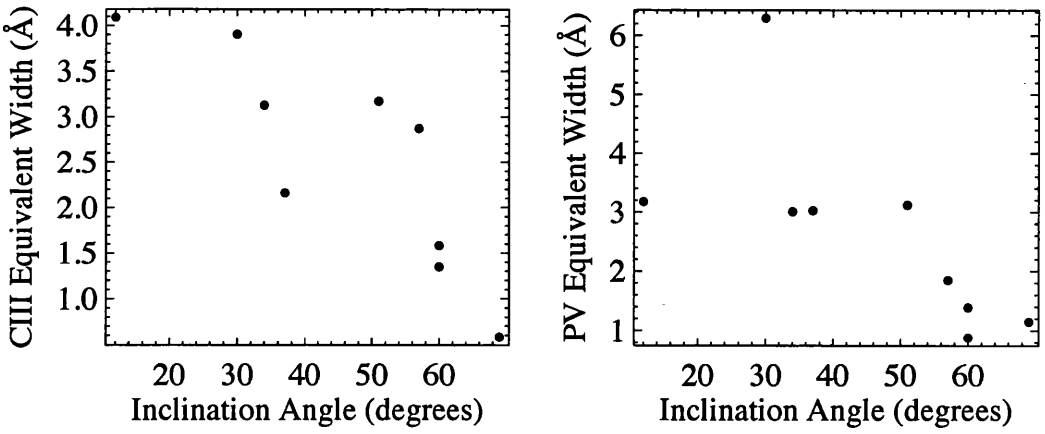

Figure 7.10: A comparison between the measured line strengths and inclination angles for the C III 1176Å and P V 1118Å lines.

effect and is thought to be due to the reduction of the perpendicular component to the wind (along the line of sight) as i increases.

With four sets of line strength measurements from these 14 targets, the logical step is to compare the ratios of the line strengths for each system to see if a pattern or fixed ratios are observed. Since no information with respect to the location in the wind is being used, a comparison of line ratios is more likely to offer information with respect to the ionisation conditions and relative elemental abundance; Table 7.9 lists all line ratios calculable, in order of increasing $\frac{\text{C III}}{\text{S IV}}$. Each column of this table shows a considerable range of values but, there is no obvious pattern between columns or even within columns. Figs. 7.11 and 7.12 compares $\frac{\text{C III}}{\text{S IV}}$ and $\frac{\text{P V}}{\text{O VI}}$ with the orbital periods and inclination angles and in none of the plots are there any indication of a correlation between parameters either. One interesting result which can be retrieved from the data is the average line strengths relative to the C III line; this is calculated to be 0.99, 0.68 and 0.55 for S IV, P V, and O VI respectively which means that although the S IV line is typically of the same strength as C III, the P V and O VI lines are normally much stronger. These ratios are likely to be predominantly a factor of true line strength and therefore do reveal some generic line conditions but, there will also be additional factors of photospheric lines and typical interstellar lines that correspond to these lines and contaminate them.

These line strength measurements and resulting line ratios may not have always revealed clear patterns to the disc winds but, what they do provide is an important archival

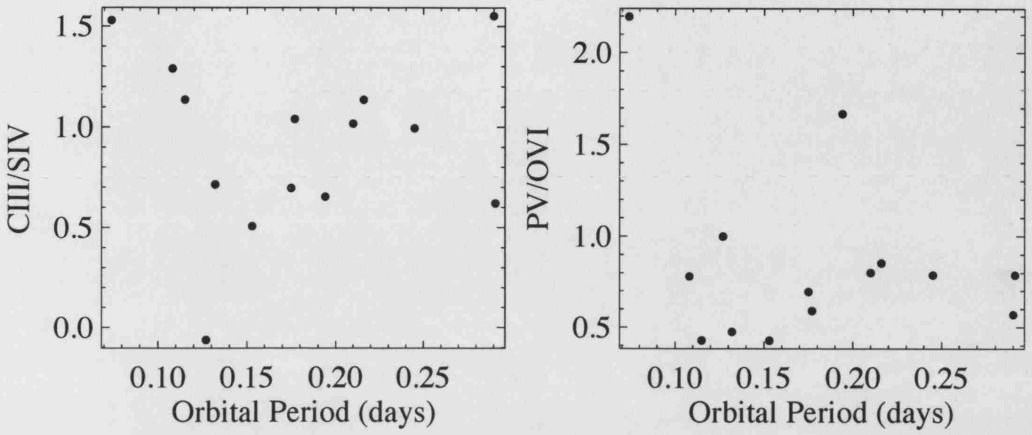

Figure 7.11: A comparison between orbital periods and line strength ratios for $\frac{\mathrm{C\,III}}{\mathrm{S\,IV}}$ and $\frac{\mathrm{P\,V}}{\mathrm{O\,VI}}$.

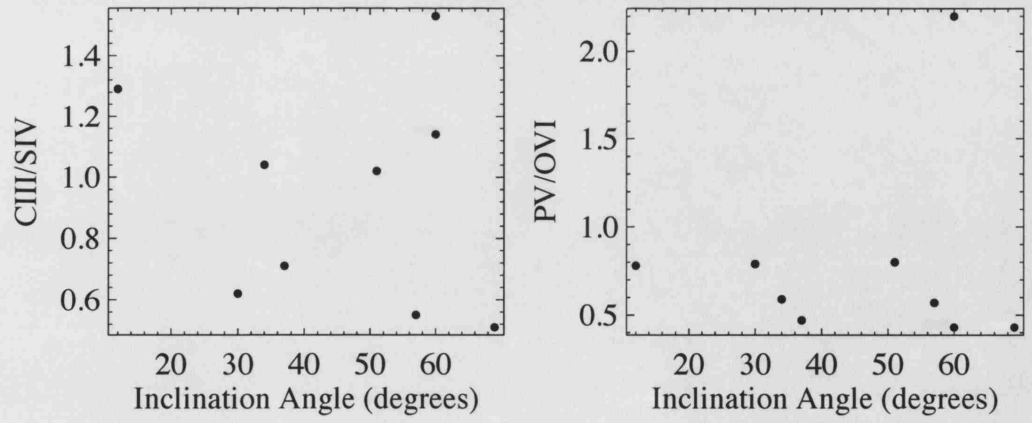

Figure 7.12: A comparison between inclination angles and line strength ratios for $\frac{\mathrm{C\,III}}{\mathrm{S\,IV}}$ and $\frac{\mathrm{P\,V}}{\mathrm{O\,VI}}$.

Name	P_{orb} (days)	$\frac{C\,III}{S\,IV}$	$\frac{C\,III}{P\,V}$	$\frac{C\,III}{O\,VI}$	$\frac{S\,IV}{P\,V}$	$\frac{S\,IV}{O\,VI}$	$\frac{P\,V}{O\,VI}$
AH Men	0.127	-0.06	-0.07	-0.07	1.14	1.14	1.00
U Gem	0.153	0.51	0.38	0.16	0.75	0.32	0.43
LS Peg	0.291	0.62	0.59	0.46	0.95	0.75	0.79
EM Cyg	0.194	0.65	0.72	1.21	1.11	1.85	1.67
V795 Her	0.175	0.70	0.57	0.40	0.82	0.57	0.69
V592 Cas	0.132	0.71	0.75	0.35	1.04	0.50	0.47
V3885 Sgr	0.245	0.99	0.65	0.51	0.66	0.52	0.79
RX And	0.21	1.02	0.62	0.50	0.61	0.49	0.80
RW Sex	0.177	1.04	0.77	0.45	0.74	0.44	0.59
BP Lyn	0.216	1.14	0.74	0.63	0.65	0.55	0.85
IX Vel	0.115	1.14	0.58	0.25	0.51	0.22	0.43
MV Lyr	0.108	1.29	0.77	0.60	0.60	0.47	0.78
VW Hyi	0.074	1.53	0.40	0.87	0.26	0.57	2.20
Z Cam	0.29	1.55	1.30	0.74	0.84	0.48	0.57

Table 7.9: A table comparing the measured lines strengths from C III 1176Å, S IV 1073Å, P V 1118Å and O VI 1038Å lines, for the 14 CVs in this study which were selected for further analysis. The table has been placed in order of increasing $\frac{C\,III}{S\,IV}$.

resource. It is clear that the measurements are functions of multiple parameters and the comparisons in this chapter are probably oversimplified but, the data will be useful for testing future disc wind theories and models and, once these systems are more accurately parameterised, patterns in the data presented here may yet still be revealed.

7.6.3 A Comparison Between Line Strengths at High and Low Velocities

The purpose of the line strength measurements taken in § 7.6.2 was to compare the overall strength of the four ions for each systems. Since the velocity range of these equivalent width measurements (from -2000 to 2000 km/s) were set to encompass each entire line, they do not provide any information with respect to the absorption strength at different velocities within the wind. The line profiles presented in Figs. 7.2, 7.5, 7.6 and 7.7 show

that for each ion of each system, the absorption is not uniformly spread between v_{max} and the line centre but, a question to arise from this is, is the ratio between the strength of the absorption at high velocities and low velocities consistent for different ions of the same system. The reasons for comparing the ratio between high velocity and low velocity absorption between different ions of the same system is because it could reveal some information about an ion stratification in the outflow, especially if a similar set of ratios is observed for multiple systems.

To make this comparison between the absorption strength at high and low velocities, two equivalent width measurements were taken from each ion of each system; the high velocity measurements (referred to as v_{high}) were taken between -2000 and -1500 km/s and, the low velocity measurements (referred to as v_{low}) were taken between -1000 and -500 km/s; the systems from which the measurements were taken was the same fourteen systems which were sub-selected earlier for further analysis. There are some caveats to these measurements which should be mentioned before the results are presented. Firstly, equivalent width measurements from these lines have already struggled to produce a clear pattern which in some part is due to how much or how little the spectral line has been contaminated by other features such as interstellar hydrogen. Secondly, not all of the systems have shown strong evidence of a wind at velocities as high as -2000 km/s so some may have equivalent measurements from v_{high} which are very small or even slightly negative (indicating the presence of emission). However an accurate comparison cannot be made if the velocity bands are changed between the systems. Nevertheless, the comparisons are still made because some pattern may yet be revealed in the data; Table 7.10 is a list of these measurements.

To compare the strength of the absorption at high and low velocities, a simple ratio between the measured equivalent widths at both velocities is calculated i.e. $\frac{\text{EW at } v_{high}}{\text{EW at } v_{low}}$; these resulting ratios are shown in Table 7.11 in order of increasing C III ratio. The lack of contamination from interstellar and additional stellar features means that the C III lines comfortably support this analysis as it can be seen from these measurements that for the majority of the systems, the absorption is much stronger at low velocities than it is at high velocities. This is however no correlation between the orbital period and the size of this C III ratio.

In the FUSE study of V592 Cas (see § 5), the idea was put forward from the observations of the orbital modulation, that an ion stratification may exist in the wind where by

Name	P_{orb} (days)	C III EW (Å)		S IV EW (Å)		P V EW (Å)		O VI EW (Å)	
		v_{high}	v_{low}	v_{high}	v_{low}	v_{high}	v_{low}	v_{high}	v_{low}
VW Hyi	0.074	-0.035	0.123	0.379	-0.090	0.784	0.399	-0.151	0.278
V795 Her	0.108	0.252	-0.085	0.513	0.222	0.653	0.456	0.930	0.805
MV Lyr	0.108	0.896	0.655	0.500	0.259	0.615	0.295	1.146	0.853
IX Vel	0.115	0.027	0.468	0.243	0.267	0.209	0.320	1.386	1.177
AH Men	0.127	-0.297	-0.504	0.649	0.120	0.431	0.338	0.684	0.308
V592 Cas	0.132	0.336	0.573	0.403	0.225	0.243	0.367	0.599	0.929
U Gem	0.177	0.011	-0.008	0.137	0.058	0.116	0.151	0.913	0.227
RW Sex	0.177	0.495	0.909	0.505	0.642	0.484	0.542	1.489	1.230
EM Cyg	0.194	0.386	0.542	0.870	0.342	0.717	0.313	0.480	0.204
RX And	0.210	0.291	1.252	0.471	0.805	0.561	0.790	1.379	1.366
BP Lyn	0.216	0.062	0.202	0.338	0.044	0.258	0.253	0.892	0.775
V3885 Sgr	0.245	0.158	0.836	0.371	0.567	0.364	0.542	1.275	1.015
Z Cam	0.290	0.095	0.142	0.177	0.014	0.481	0.179	0.749	0.012
LS Peg	0.291	0.294	0.423	0.797	0.378	0.778	0.599	1.287	1.067

Table 7.10: A table showing the equivalent width measurements from the high velocity wind regions (or v_{high}) between -2000 and -1500 km/s and, low velocity wind regions (or v_{low}) between -1000 and -500 km/s, of the C III, S IV, P V and O VI lines.

the ions of C III and S IV would be present at all velocities throughout the wind but the higher ionisation species such as P V and O VI would only be present at the lower velocities; this would mean that the ratio of high velocity to low velocity absorption would be higher for C III and S IV, than it would for P V and O VI. Even for V592 Cas where this is believed to occur, this is not seen in Table 7.11. In fact for 11 out of the 14 systems, the ions of P V and O VI show much higher ratios than is observed for C III. This could mean that this interpretation of an ion stratification for V592 Cas (and probably other systems) is incorrect. This is entirely possible but, a more likely scenario is that yet again the observed data for lines other than C III do not support these measurements because of the degree of contamination from features such as the interstellar medium. Thus unfortunately although the concept of these measurements is potentially useful, the data

Name	$P_{\rm orb}$ (days)	Ratio of v_{high} EW to v_{low} EW			
		C III	S IV	P V	O VI
V795 Her	0.108	-2.959	2.311	1.432	1.156
U Gem	0.177	-1.326	2.359	0.771	4.030
VW Hyi	0.074	-0.288	-4.208	1.962	-0.542
IX Vel	0.115	0.058	0.910	0.652	1.177
V3885 Sgr	0.245	0.189	0.655	0.672	1.257
RX And	0.210	0.233	0.585	0.710	1.009
BP Lyn	0.216	0.304	7.744	1.018	1.151
RW Sex	0.177	0.544	0.787	0.894	1.210
V592 Cas	0.132	0.586	1.794	0.660	0.645
AH Men	0.127	0.589	5.431	1.274	2.224
Z Cam	0.290	0.667	12.304	2.685	60.942
LS Peg	0.291	0.696	2.109	1.297	1.207
EM Cyg	0.194	0.712	2.545	2.288	2.350
MV Lyr	0.108	1.367	1.929	2.083	1.343

Table 7.11: A table showing the strength ratio of the high velocity wind regions (or v_{high}) between -2000 and -1500 km/s and, the low velocity wind regions (or v_{low}) between -1000 and -500 km/s, of the C III, S IV, P V and O VI lines.

being used does not support them.

7.7 A Comparison Between CVs with Similar and Different Line Profiles

From the plots of the individual line profiles to the measurements of profile asymmetry, it is clear from the results that have been presented so far that there is no single generic line profile for wind driving CVs. However, there are similarities in the profiles between some systems which provides a reason for them to be grouped together. In this section, two pairs of CVs with similar line profiles are discussed with the aim of discovering why they might have similar profiles. The two pairs of CVs are then compared against each other with the hope of discovering why the systems might have different profiles.

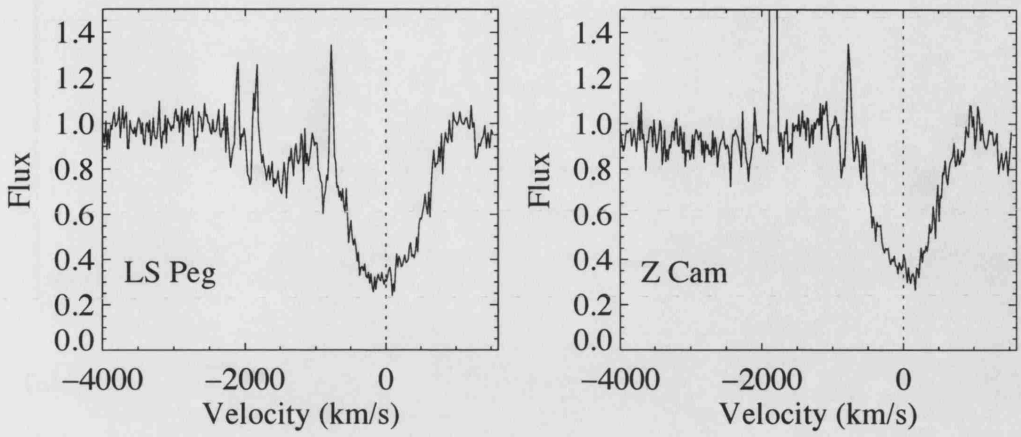

Figure 7.13: The C III 1176Å profiles for LS Peg and Z Cam.

The first pair of CVs to be compared are LS Peg and Z Cam (these two will later be referred to as pair *a*). From first appearances, the C III 1176Å profiles are extremely similar (they both have a characteristic "U" shaped profile, see Fig. 7.13) and it could almost be forgiven for thinking that they originate from the same system. However, measurements taken from the C III profiles in § 7.6.1 reveal that there are subtle differences between them; the LS Peg profile is inherently more blue-ward and slightly more symmetric than the Z Cam profile for example. Subtle differences aside, the question is why would these two systems produce similarly shaped wind driven profiles? Table 7.12 is a list of the basic properties of LS Peg and Z Cam to investigate these reasons; other than both systems being above the 2-3 hour period gap, this table actually reveals that these systems are not so similar. For example, LS Peg is an SW Sex type nova-like system and therefore likely to be undergoing stream overflow while Z Cam is a dwarf novae system. Although both systems are considered as low inclination, Table 7.12 also reveals Z Cam to be close to the upper extreme of low inclination while LS Peg is somewhat in the middle of the low inclination range. Other than the necessity that both systems are low inclination and in a high state or in a state of outburst as is probably for Z Cam, there does not appear to be any logical connection between these two systems which would result in them having extremely similar line driven profiles.

LS Peg is not the only SW Sex system in this survey, BH Lyn is also a confirmed SW Sex system and both V795 Her and BP Lyn have been flagged as candidates but, it is the only SW Sex system in this survey demonstrating line profiles with these characteristics.

Property	LS Peg	Z Cam	RX And	V3885 Sgr
Type	SW Sex	Z Cam	Z Cam	UX UMa
$P_{\rm orb}$ (days)	0.175	0.290	0.210	0.216
i	30°	57°	51°	$< 50°$
C III 1176Å v_{max} (km/s)	-1020	-720	-3300	-2800
C III 1176Å $v_{\rm abs.\ min.}$ (km/s)	-1020	-720	-3300	-2800

Table 7.12: A table listing the basic properties of the four CVs under comparison. These properties are: system type, orbital period, inclination angle, the maximum velocity of the C III 1176Å absorption (or v_{max}) and the velocity of the minimum absorption of the C III 1176Å line.

The similarity between LS Peg's wind driven profiles and Z Cam's wind driven profiles raises four possible scenarios with respect to stream overflow: this profile shape is not exclusive to stream overflow, Z Cam undergoes stream overflow during outburst, LS Peg is not undergoing stream overflow (this is unlikely) or this profile shape is unrelated to stream overflow. It is difficult but not impossible to comprehend that two unrelated processes could generate such similar profiles. It is also not impossible that Z Cam is undergoing stream overflow but to discover whether this is the case would require a separate study and no indication could be found in literature as to whether this study had already been performed. As for the concept that these line profiles are not the result of stream overflow, this would likely require modelling of far-UV lines in relation to this phenomenon and no published study related to this subject could be found. Clearly the reasons for this similarity cannot be resolved in the scope of this thesis.

The second pair of CVs (to be referred to as pair *b*) under comparison in this section are RX And and V3885 Sgr. Fig. 7.14 is a plot of their respective C III 1176Å lines and it is clear to see that the shapes of the profiles are very similar. The analysis of the blue or red dominance and, the asymmetry of the C III 1176Å lines in § 7.6.1 reveals that these systems are also quantitatively similar since for both CVs the C III line is very heavily shifted to the blue and is reasonably asymmetric. Hypothetically, two CVs which show such strong similarities between their wind driven profile should have relatively similar properties. Table 7.12 lists basic properties of both systems and it is evident that although they are not as different as pair *a*, neither are they identical; for example, RX And is a

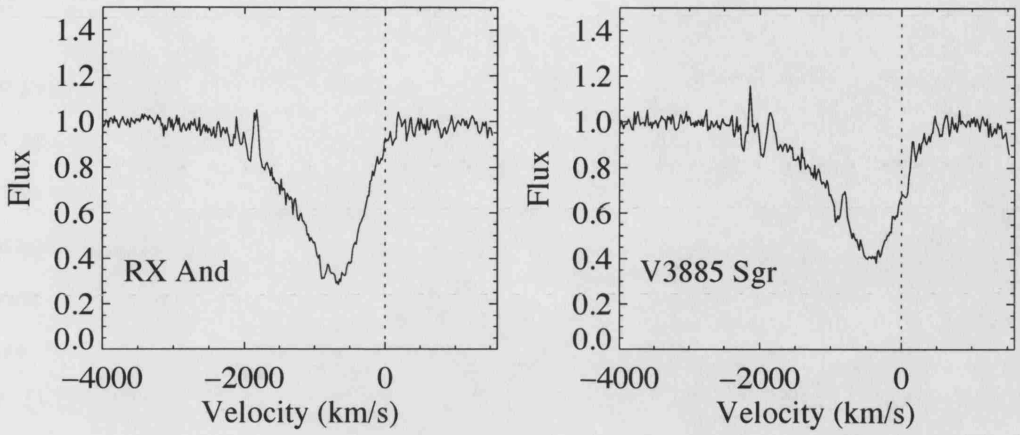

Figure 7.14: The C III 1176Å profiles for RX And and V3885 Sgr.

dwarf nova of the subgroup Z Cam and V3885 Sgr is a nova-like system of the sub-group UX UMa. The one property which is strongly similar between these two systems is the orbital period. In § 7.6.2 a possible link between the strength of the C III 1176Å line and orbital period was discovered but this could not be confirmed with other ions and in the case of RX And and V3885 Sgr, there is clearly a difference in strength between the profiles. No evidence has been published so far to link the shape of the line profile and orbital period so this one common property between the two systems is an unlikely indication of why they have similar profile shapes.

The two CVs in pair *a* (i.e. LS Peg and Z Cam) and the two systems in pair *b* (i.e. RX And and V3885 Sgr) have very similar C III 1176Å profiles despite having different basic properties. The purpose of finding out what links these two pairs of CVs was that it may reveal why the profiles were of a particular shape which inherently provides more information about the disc winds themselves. It is interesting to discover that if these four systems were to be grouped in terms of basic properties then it would be more logical to group LS Peg with V3885 Sgr since these are both nova-like systems and, Z Cam with RX And since these are both dwarf nova systems but this would ignore the evidence provided by the line profiles. Although these comparisons do not help decipher the nature of the disc winds from CVs, what they do indicate is that the type or sub-type by which a CV has been classified may be inherently be irrelevant to understanding the resulting outflow.

7.8 Summary

The purpose of this FUSE survey has been to record the far-UV disc wind characteristics of a number of known wind driving CVs, with a focus on searching for patterns relating to the orbital period and the inclination angle. The initial analysis focussed on the characteristics of the C III 1176Å profile and in the majority of cases, the absorption was shown to be blue-shifted, approximately symmetric or peaking in strength within 500 km/s of the line centre. Line strength measurements were additionally made of the S IV, P V, O VI lines and the ratios between these lines were calculated but, revealed no clear pattern.

The analysis presented in this chapter has focussed on comparing measured wind line characteristics with orbital periods and inclination angles. There was evidence of a possible connection between the strength of the lines and the orbital period but, this was only discovered for the C III line and it could not be confirmed for the other three ions. In the comparison between the strength of the lines and the inclination angle, a much stronger correlation was discovered whereby the higher the inclination the weaker the line strength but, this is a well known observation and it does not reveal any new information. A comparison between the line strengths at high and low velocities also revealed no new previously undiscovered relationships.

This survey has not been without its flaws; ideally the interstellar lines should have been modelled and removed before analysis took place, for example. There is also the lack of study of time-dependence of the disc winds but, that really requires an individual case study for each system, culminating in an overall comparison at the end. It would have been useful to compare the disc wind characteristics with the mass accretion rate but, this requires accurate knowledge of distances and for many of the systems in this survey this is a point of much contention. However, it was revealed that two systems with apparently different basic properties can produce very similar wind line profiles. Inevitably, there is a problem with the lack of accurate parameters for CVs and understanding of disc winds since it is not entirely clear which parameters have an affect on a disc wind profile but, this survey provides some initial results to model and is a good starting point for a much larger survey once more FUSE data is collected or further systems are observed to be wind driving.

CHAPTER 8

Conclusions and Future Work

In this thesis, cases studies describing the disc wind characteristics of several high state, nova-like cataclysmic variable stars have been presented. The key spectral line diagnostics of RW Sextansis, V592 Cassiopeiae and BZ Camelopardalis were derived using far-UV, UV and optical data; the far-UV and UV data were sourced from FUSE, HST and IUE. In this section these disc wind characteristics will be briefly described again and comparisons will be made between all three systems.

8.1 Summary and Conclusions

The far-UV diagnostic of the disc wind from RW Sex was found to be characterised by a strong blue-shifted absorption confined to between -1000 and 0 km/s for all ionisation states. This absorption is strongly modulated on the orbital period, undergoing cyclic changes in optical depth and velocity shift. The UV diagnostics of the disc wind from the HST time-series also showed the wind to be variable on time-scales of seconds to minutes. The far-UV diagnostic of V592 Cas was also found to be characterised by a blue-shifted absorption component which was modulated in strength and velocity shift on the orbital period.

The study into the optical wind diagnostics of V592 Cas was dominated by the Balmer line, Hβ. This single line was found to be composed of three components; a broad shallow absorption trough, a narrow central emission and a blue-shifted absorption. This last component, the blue-shifted absorption, was believed to originate from the disc wind and as was discovered with the far-UV observations, had an orbitally modulated velocity shift.

Unlike the far-UV observations however, this modulation was sinusoidal. Finally, there is the optical wind component of BZ Cam. This last system also showed evidence of a highly variable, blue-shifted absorption component to the Balmer and helium lines but, this absorption was found to be episodic and in the latest observations, was barely visible.

There is of course a strong similarity between the far-UV wind characteristics of V592 Cas and RW Sex so these two systems are discussed first. It would be interesting to investigate whether the optical characteristics of RW Sex's wind were similar to that of V592 Cas but this would require observations which have not yet been made. Clearly there must be a strong similarity in the way in which their winds are driven and how they are modulated on the orbital period. Both of these CVs are low inclination, high state systems of UX UMa type so their similarity in basic characteristics could explain why they might exhibit similar wind characteristics. A warped or tilted disc was one possible reason put forward for the modulation but ignoring whether the wind is modulated on the negative superhump period or not, RW Sex is not a superhumping system. Another possible reason for the observed modulation was that either star could be an SW Sex system undergoing stream overflow but this has been ruled out both in discussion (see § 4.6) and comparison with other known SW Sex systems (see § 7).

One of the characteristics of SW Sex systems is the presence of absorption when the absolute orbital phase of the CV is $\phi = 0.5$. Therefore, if the absolute orbital phase of V592 Cas and RW Sex were known then it may have been possible to rule out stream overflow from the outset. Where a wind is orbitally modulated, knowing the absolute phase of a system is a valuable source of information because it indicates what the orientation of the system was when the observed wind profile was generated. Deriving the absolute phase is not so easy for the low inclination systems because there is no eclipse from the secondary star to indicate the current phase. One potential method for determining the absolute phase for low inclination systems is skew mapping (discussed in § 3.2) which requires near-IR spectra containing spectral features from the secondary star. Determination of absolute phase is perhaps one area of CV disc wind studies which must be taken into consideration for future observations.

Another possible source of orbital modulation for RW Sex and V592 Cas would be if the outflow were confined by a magnetic field, for example, and were undergoing some kind of "light-house" effect such as what is observed for pulsars. Other than the orbital modulation, there is no evidence to support this as a possibility but, if magnetism is also

involved in driving material from the disc then these processes sound very similar to jets from accretion disc systems (Soker & Lasota 2004). CVs have remained the only accreting system for which a jet has not yet been observed but perhaps these orbitally modulated winds are in fact weakly confined jets. Although this is pure speculation, it could explain why no jets are observed for CVs.

So far, the discoveries of BZ Cam's wind have not been discussed in relation to V592 Cas and RW Sex. If the theories of VY Scl systems having no inner disc are true (see § 6.6), then BZ Cam could turn out to be a very different CV to both V592 Cas and RW Sex, as its wind characteristics suggest. The question is whether the wind (or at least the optical component to it) observed for BZ Cam is even remotely related to the optical wind of V592 Cas, which does at least show some similarity with its far-UV counterpart. Different driving mechanisms have been discussed in this thesis for the two systems; magneto-centrifugal ejection for BZ Cam for example and, line driving and magneto-hydrodynamics for V592 Cas. Clearly the need exists for additional time-series observations of all three systems involved in this thesis.

8.2 Future Work

The case studies of CV disc winds presented in this thesis reveal a genuine need for time-series observations of the wind diagnostic lines from many more high state systems. The UV domain has shown itself to be perfect for studying these disc outflows but unfortunately it may no longer be possible to obtain these important UV time-series. On the 3rd August 2004, the Space Telescope Imaging Spectrograph on the Hubble Space Telescope failed and although there is a strong possibility that a servicing mission will now go ahead for HST, there is no guarantee that the instrument will be repaired. The failure of STIS means that the only UV spectrograph left capable of performing time-series observations of the UV wind diagnostic lines is FUSE; FUSE has already out performed its original 3 year lifetime and although proposals have been put forward to NASA to extends its life for at least several more years, its future is by no means certain. At the time that this thesis was written, no plans had been put forward for a replacement to FUSE and the designs for the replacement to HST, the Next Generation Space Telescope (now referred to as the James Webb Space Telescope), have shown a focus towards images and spectra in the near-IR domain. The future of UV disc winds studies is indeed looking bleak.

The potential loss of future UV observations means that for these disc winds to be continually studied in the long term, there is a need to establish other, non-UV wind diagnostics. Wind diagnostics in the optical domain have already proved successful in the case studies of V592 Cas and BZ Cam (see § 4 and § 6) and at least in the case of BZ Cam, very short time-scale activity by the disc wind was observed. One way to improve the optical studies would be to perform very fast, high signal to noise spectroscopy on systems with known optical components to the disc wind to potentially resolve the formation of wind events such as that observed for BZ Cam and, to improve the understanding of other disc winds by studying the short time-scale stochastic variations that occurs in these winds (e.g. RW Sex); to perform these observations would require one of the larger class of telescopes such as Gemini. There is however no guarantee that the disc wind from a particular CV will have an optical component; during the observing run that the optical observations of V592 Cas were secured, additional observations of another high state, low inclination, nova-like CV called HL Aquarius were taken but despite IUE observations indicating the presence of a strong wind, no optical component to the wind was discovered. Optical telescopes will always be available so there will never be a problem (pending a suitable proposal of course) of obtaining optical time-series of CV disc winds. However, they do not provide ideal disc wind diagnostics and it would of course be ideal if advantage could be taken of the James Webb Space Telescope when it is eventually launched.

Perhaps a more suitable non-UV wind diagnostic line would be He I 10830Å. He I 10830Å is in fact a triplet line with components at 10832.1, 10833.2 and 10833.3Å. Helium lines in general have a high excitation potential meaning that line formation would be restricted to regions of high temperature or regions close to the source of the ionising radiation. He I 10830Å emission can occur immediately following a He I 5876Å emission, during a recombination cascade. However, one extremely important feature of He I 10830Å is that its lower level is metastable meaning that it has ideal conditions for resonance scattering. The high excitation potential and resonance scattering would theoretically result in the production of blue-shifted absorption, originating from the inner regions of the accretion disc wind (see Beristain *et al.* 2001). The opportunity to study the inner wind and understand its properties could perhaps provide the greatest evolutions in disc wind theory because it would be possible to discover exactly where on the accretion the mass is being lauched and perhaps even the driving mechanism for the wind, whether it be line-driving, magnetohydrodynamics or some process which has not yet been considered.

The other advantage of studying this line is that it not only takes advantage of current ground based telescopes such as the UK Infra-red Telescope (He I 10830Å is in fact the more suitable indicator of wind dynamics than any other line from the ground) but, it would also be possible to take advantage of the James Webb Telescope when it is launched. So far there have been no published attempts to study the accretion disc winds from CVs using the He I 10830Å but Takami *et al.* (2002) presented a study of the T Tauri star DG Tau and discovered a broad emission with a blue-shifted absorption feature. Edwards *et al.* (2003) have also extended the use of the He I 10830Å to studying the winds from accreting young stars and have found it to be somewhat successful.

There is of course the general need in the study of CV disc winds, to produce case studies similar to what has been presented in this thesis, for many more and a far greater range of systems. Time-independent studies simple cannot be relied upon to provide the information needed to understand the phenomena and each system must be studied using dedicated time-series data. There is the importance in understanding what is happening in the very inner regions of the winds and has it as been shown for BZ Cam and V592 Cas, this is not necessarily the same for every CV so it is important to study a wide range of systems. One aspect that has arisen throughout these case studies is the role that superhumping plays in "modifying" the outflow, for example in the case of having a warped or eccentric accretion disc. This obviously requires the study of many more systems with warped disc, perhaps not just CVs but any accreting system where warped accretion discs can occur. With respect to the inner disc region, where these winds are believed to originate from, what happens when there is no inner disc such as in the case of intermediate polar systems and how does this relate to the VY Scl systems (such as BZ Cam) which are believed by some (see Hameury & Lasota 2002) to have magnetic fields strong enough to disrupt the inner disc, just like intermediate polar systems do? Clearly, there is enormous scope for extending these case studies to many more CVs and other accretion disc scenarios.

The final word on accretion disc winds from CVs is given to computer modelling. Line synthesis models have come very far since the early codes such as Drew (1987). The code presented by Long & Knigge (2002) represents the latest advances in these line synthesis techniques with the ability to model multiple lines using a combined Monte Carlo/Sobolev technique. However, if these codes are to be developed further they must be compared with large quantities of real observations, which again leads to the need for disc winds case

studies of accurately parameterised CVs. It should also be noted that comparisons are still made with time-independent data and as it has been made clear, this does not always give the full picture of a disc wind. One possible direction to take this computer modelling would be to make a more analytical approach to the disc wind such as using the Sobolev with Exact Integration (or SEI) method to model these wind driven profiles. The SEI method assumes the Sobolev approximation to the outflow but the transfer equation is solved exactly; it may be possible to modify an already existing code to simulate the wind profiles from all accretion disc systems. Whatever the direction these codes inevitably take, there is a strong need for a better understanding of disc winds and this will only come from more observational case studies such as those presented here.

BIBLIOGRAPHY

Abell, G. O. & Margon, B., 1979, *Nature*, **279**, 701

Africano, J. & Quigley, R., 1978, *PASP*, **90**, 191

Beristain, G., Edwards, S. & Kwan, J., 2001, *ApJ*, **551**, 1037

Beuermann, K., Stasiewski, U. & Schwope, A. D., 1992, *A&A*, **256**, 433

Blandford, R. D. & Payne, D. G., 1982, *MNRAS*, **199**, 883

Bohlin, R. C., Savage, B. D. & Drake, J. F., 1978, *ApJ*, **224**, 132

Bolick, U., Beuermann, K., Bruch, A. & Lenzen, R., 1987, *ApSS*, **130**, 175

Borczyk, W., Schwarzenberg-Czerny, A. & Szkody, P., 2003, *A&A*, **405**, 663

Casares, J., Martinez-Pais, I. G., Marsh, T. R., Charles, P. A. & Lazaro, C., 1996, *MNRAS*, **278**, 219

Castor, J. I., Abbott, D. C. & Klein, R. I., 1975, *ApJ*, **195**, 157

Ciardi, D. R., Howell, S. B., Dhillon, V. S., Wagner, R. M., Hauschildt, P. H. & Allard, F., 1998, *PASP*, **110**, 1007

Cordova, F. A., Hjellming, R. M. & Mason, K. O., 1983, *PASP*, **95**, 69

Cordova, F. A. & Mason, K. O., 1982, *ApJ*, **260**, 716

Cowley, A. P., Crampton, D. & Hesser, J. E., 1977, *PASP*, **89**, 716

Cowley, A. P. & MacConnell, D. J., 1972, *ApJL*, **176**, L27

Diaz, M. P. & Steiner, J. E., 1995, *AJ*, **110**, 1816

Dixon, W. V. & Sahnow, D. J., 2003, in *ASP Conf. Ser. 295: Astronomical Data Analysis Software and Systems XII*, p. 241

Downes, R. A., Mateo, M., Szkody, P., Jenner, D. C. & Margon, B., 1986, *ApJ*, **301**, 240

Downes, R. A., Webbink, R. F., Shara, M. M., Ritter, H., Kolb, U. & Duerbeck, H. W., 2001, *PASP*, **113**, 764

Drew, J. & Verbunt, F., 1985, *MNRAS*, **213**, 191

Drew, J. E., 1986, *MNRAS*, **218**, 41P

Drew, J. E., 1987, *MNRAS*, **224**, 595

Drew, J. E., 1993, in *Cataclysmic Variables and Related Physics*, p. 128

Drew, J. E., Hartley, L. E., Long, K. S. & van der Walt, J., 2003, *MNRAS*, **338**, 401

Drew, J. E., Hoare, M. G. & Woods, J. A., 1991, *MNRAS*, **250**, 144

Drew, J. E. & Verbunt, F., 1988, *MNRAS*, **234**, 341

Edwards, S., Fischer, W., Kwan, J., Hillenbrand, L. & Dupree, A. K., 2003, *ApJL*, **599**, L41

Ellis, G. L., Grayson, E. T. & Bond, H. E., 1984, *PASP*, **96**, 283

Eracleous, M., Patterson, J. & Halpern, J., 1991, *ApJ*, **370**, 330

Feldmeier, A. & Shlosman, I., 1999, *ApJ*, **526**, 344

Fullerton, A. W., Gies, D. R. & Bolton, C. T., 1996, *ApJSS*, **103**, 475

Gänsicke, B. T. & Koester, D., 1999, *A&A*, **346**, 151

Garnavich, P. & Szkody, P., 1988, *PASP*, **100**, 1522

Gayley, K. G., 1995, *ApJ*, **454**, 410

Godon, P., Livio, M. & Lubow, S., 1998, *MNRAS*, **295**, L11

Greenstein, J. L. & Oke, J. B., 1982, *ApJ*, **258**, 209

Greenstein, J. L., Sargent, A. I. & Haug, U., 1970, *AAp*, **7**, 1

Greiner, J., Tovmassian, G., Orio, M., Lehmann, H., Chavushyan, V., Rau, A., Schwarz, R., Casalegno, R. & Scholz, R.-D., 2001, *A&A*, **376**, 1031

Griffith, D., Fabian, D. & Sion, E. M., 1995, *PASP*, **107**, 856

Guinan, E. F. & Sion, E. M., 1982, in *Advances in Ultraviolet Astronomy*, pp. 465–469

Högbom, J. A., 1974, *AApS*, **15**, 417

Hameury, J.-M. & Lasota, J.-P., 2002, *A&A*, **394**, 231

Harvey, D., Skillman, D. R., Patterson, J. & Ringwald, F. A., 1995, *PASP*, **107**, 551

Hellier, C. & Robinson, E. L., 1994, *ApJL*, **431**, L107

Hesser, J. E., Lasker, B. M. & Osmer, P. S., 1972, *ApJL*, **176**, L31

Hillwig, T., Livio, M. & Honeycutt, R. K., 2004, *PASP*, **116**, 397

Hoard, D. W. & Szkody, P., 1996, *ApJ*, **470**, 1052

Hoard, D. W. & Szkody, P., 1997, *ApJ*, **481**, 433

Hoard, D. W., Thorstensen, J. R. & Szkody, P., 2000, *ApJ*, **537**, 936

Hoare, M. G., 1994, *MNRAS*, **267**, 153

Hoare, M. G. & Drew, J. E., 1993, *MNRAS*, **260**, 647

Hollander, A. & van Paradijs, J., 1992, *A&A*, **265**, 77

Horne, K., 1999, in *Astronomical Society of the Pacific Conference Series*, pp. 349–+

Horne, K. & Marsh, T. R., 1986, *MNRAS*, **218**, 761

Howell, S. B., Nelson, L. A. & Rappaport, S., 2001, *ApJ*, **550**, 897

Huber, M. E., Howell, S. B., Ciardi, D. R. & Fried, R., 1998, *PASP*, **110**, 784

Jameson, R. F., Sherrington, M. R., King, A. R. & Frank, J., 1982, *Nature*, **300**, 152

Kato, T., 2001, *Informational Bulletin on Variable Stars*, **5122**

Kato, T., 2002, *A&A*, **384**, 206

Kato, T. & Starkey, D. R., 2002, *Informational Bulletin on Variable Stars*, **5358**

Kato, T. & Uemura, M., 2001, *Informational Bulletin on Variable Stars*, **5077**

Kholopov, P. N., Samus', N. N., Kukarkina, N. P., Medvedeva, G. I. & Perova, N. B., 1981, *Informational Bulletin on Variable Stars*, **2042**

King, A. R., 1988, *QJRAS*, **29**, 1

Knigge, C., Drew, J. E., Hoare, M. G. & La Dous, C., 1994, *MNRAS*, **269**, 891

Knigge, C., Woods, J. A. & Drew, E., 1995, *MNRAS*, **273**, 225

Krautter, J., Radons, G. & Klaas, U., 1987, *A&A*, **181**, 373

Kurucz, R. L., 1993, *VizieR Online Data Catalog*, **6039**

Lai, D., 1999, *ApJ*, **524**, 1030

Lamers, H. J. G. L. M. & Cassinelli, J. P., 1999, *Introduction to stellar winds* (Introduction to stellar winds / Henny J.G.L.M. Lamers and Joseph P. Cassinelli. Cambridge ; New York : Cambridge University Press, 1999. ISBN 0521593980)

Long, K. S. & Knigge, C., 2002, in *ASP Conf. Ser. 261: The Physics of Cataclysmic Variables and Related Objects*, p. 327

Lubow, S. H., 1989, *ApJ*, **340**, 1064

Marsh, T. R., Horne, K., Schlegel, E. M., Honeycutt, R. K. & Kaitchuck, R. H., 1990, *ApJ*, **364**, 637

Mauche, C. W., 1991, *ApJ*, **373**, 624

Mauche, C. W. & Raymond, J. C., 1987, *ApJ*, **323**, 690

Mauche, C. W., Raymond, J. C. & Cordova, F. A., 1988, *ApJ*, **335**, 829

McCandliss, S. R., 2003, *PASP*, **115**, 651

Moos, H. W., 2000, *Bulletin of the American Astronomical Society*, **32**, 1513

Mouchet, M., Siess, L., Drew, J., Lasota, J. P., Buckley, D. A. H. & Bonnet-Bidaud, J. M., 1996, *A&A*, **306**, 212

Moyer, E., Sion, E. M., Szkody, P., Gänsicke, B., Howell, S. & Starrfield, S., 2003, *AJ*, **125**, 288

Murray, J. R. & Armitage, P. J., 1998, *MNRAS*, **300**, 561

Murray, J. R., Chakrabarty, D., Wynn, G. A. & Kramer, L., 2002, *MNRAS*, **335**, 247

Nelson, R. F. & Spencer, R. E., 1988, *MNRAS*, **234**, 1105

Neustroev, V. V., Chavushyan, V. & Valdés, J. R., 2004, in *Revista Mexicana de Astronomia y Astrofisica Conference Series*, pp. 162–163

Norton, A. J., Beardmore, A. P., Retter, A. & Buckley, D. A. H., 2000, *MNRAS*, **312**, 362

Ogilvie, G. I. & Dubus, G., 2001, *MNRAS*, **320**, 485

Paczyński, B., 1971, *ARA&A*, **9**, 183

Paczynski, B. & Sienkiewicz, R., 1981, *ApJL*, **248**, L27

Parker, E. N., 1960, *ApJ*, **132**, 821

Patterson, J., 1979, *AJ*, **84**, 804

Patterson, J., 1984, *ApJSS*, **54**, 443

Patterson, J., 1995, *PASP*, **107**, 657

Patterson, J., Fenton, W. H., Thorstensen, J. R., Harvey, D. A., Skillman, D. R., Fried, R. E., Monard, B., O'Donoghue, D., Beshore, E., Martin, B., Niarchos, P., Vanmunster, T., Foote, J., Bolt, G., Rea, R., Cook, L. M., Butterworth, N. & Wood, M., 2002, *PASP*, **114**, 1364

Patterson, J., Kemp, J., Saad, J., Skillman, D. R., Harvey, D., Fried, R., Thorstensen, J. R. & Ashley, R., 1997, *PASP*, **109**, 468

Patterson, J., Patino, R., Thorstensen, J. R., Harvey, D., Skillman, D. R. & Ringwald, F. A., 1996, *AJ*, **111**, 2422

Patterson, J. & Skillman, D. R., 1994, *PASP*, **106**, 1141

Patterson, J., Thomas, G., Skillman, D. R. & Diaz, M., 1993, *ApJSS*, **86**, 235

Pereyra, N. A., Kallman, T. R. & Blondin, J. M., 1997, *ApJ*, **477**, 368

Plavec, M. & Kratochvil, P., 1964, *Bulletin of the Astronomical Institutes of Czechoslovakia*, **15**, 165

Polidan, R. S., Mauche, C. W. & Wade, R. A., 1990, *ApJ*, **356**, 211

Pringle, J. E., 1996, *MNRAS*, **281**, 357

Prinja, R. K., Drew, J. E. & Rosen, S. R., 1992, *MNRAS*, **256**, 219

Prinja, R. K., Knigge, C., Ringwald, F. A. & Wade, R. A., 2000*a*, *MNRAS*, **318**, 368

Prinja, R. K., Knigge, C., Witherick, D. K., Long, K. S. & Brammer, G., 2004, *MNRAS*, 425

Prinja, R. K., Long, K. S., Froning, C. S., Knigge, C., Witherick, D. K., Clark, J. S. & Ringwald, F. A., 2003, *MNRAS*, **340**, 551

Prinja, R. K., Ringwald, F. A., Wade, R. A. & Knigge, C., 2000*b*, *MNRAS*, **312**, 316

Prinja, R. K. & Rosen, R., 1995, *MNRAS*, **273**, 461

Prinja, R. K. & Rosen, S. R., 1993, *MNRAS*, **262**, L37

Proga, D., 2000, *ApJ*, **538**, 684

Proga, D., Kallman, T. R., Drew, J. E. & Hartley, L. E., 2002, *ApJ*, **572**, 382

Proga, D., Stone, J. M. & Drew, J. E., 1998, *MNRAS*, **295**, 595

Proga, D., Stone, J. M. & Drew, J. E., 1999, *MNRAS*, **310**, 476

Rappaport, S., Joss, P. C. & Webbink, R. F., 1982, *ApJL*, **254**, 616

Ringwald, F. A. & Naylor, T., 1998, *AJ*, **115**, 286

Ritter, H. & Kolb, U., 2004, *VizieR Online Data Catalog*, **5113**

Roberts, D. H., Lehar, J. & Dreher, J. W., 1987, *AJ*, **93**, 968

Rodríguez-Gil, P., Casares, J., Martínez-Pais, I. G., Hakala, P. & Steeghs, D., 2001, *ApJL*, **548**, L49

Rosen, S. R., Prinja, R. K., Drew, J. E., Mason, K. O. & Howell, S. B., 1998, *MNRAS*, **299**, 305

Sahnow, D. J., Moos, H. W., Ake, T. B., Andersen, J., Andersson, B.-G., Andre, M., Artis, D., Berman, A. F., Blair, W. P., Brownsberger, K. R., Calvani, H. M., Chayer, P., Conard, S. J., Feldman, P. D., Friedman, S. D., Fullerton, A. W., Gaines, G. A., Gawne, W. C., Green, J. C., Gummin, M. A., Jennings, T. B., Joyce, J. B., Kaiser, M. E., Kruk, J. W., Lindler, D. J., Massa, D., Murphy, E. M., Oegerle, W. R., Ohl, R. G., Roberts, B. A., Romelfanger, M. L., Roth, K. C., Sankrit, R., Sembach, K. R., Shelton, R. L., Siegmund, O. H. W., Silva, C. J., Sonneborn, G., Vaclavik, S. R., Weaver, H. A. & Wilkinson, E., 2000, *ApJ*, **538**, L7

Shafter, A. W., 1983, *ApJ*, **267**, 222

Shakura, N. I. & Sunyaev, R. A., 1973, *A&A*, **24**, 337

Shlosman, I. & Vitello, P., 1993, *ApJ*, **409**, 372

Sion, E. M., Huang, M., Szkody, P. & Cheng, F., 1995, *ApJL*, **445**, L31

Sion, E. M., Long, K. S., Szkody, P. & Huang, M., 1994, *ApJL*, **430**, L53

Skillman, D. R., Harvey, D. A., Patterson, J., Kemp, J., Jensen, L., Fried, R. E., Garradd, G., Gunn, J., van Zyl, L., Kiyota, S., Retter, A., Vanmunster, T. & Warhurst, P., 1998, *ApJL*, **503**, L67

Soker, N. & Lasota, J.-P., 2004, *A&A*, **422**, 1039

Spruit, H. C., 1989*a*, in *ASSL Vol. 156: Accretion Disks and Magnetic Fields in Astrophysics*, pp. 59–69

Spruit, H. C., 1989*b*, in *NATO ASIC Proc. 290: Theory of Accretion Disks*, pp. 325–340

Stringfellow, G. S., Robinson, C. R., Cordova, F. A. & Musgrove, M., 1993, *Bulletin of the American Astronomical Society*, **25**, 1379

Szkody, P. & Mateo, M., 1986, *ApJ*, **301**, 286

Takami, M., Chrysostomou, A., Bailey, J., Gledhill, T. M., Tamura, M. & Terada, H., 2002, *ApJL*, **568**, L53

Taylor, C. J., Thorstensen, J. R. & Patterson, J., 1999, *PASP*, **111**, 184

Taylor, C. J., Thorstensen, J. R., Patterson, J., Fried, R. E., Vanmunster, T., Harvey, D. A., Skillman, D. R., Jensen, L. & Shugarov, S., 1998, *PASP*, **110**, 1148

Thorstensen, J. R. & Freed, I. W., 1985, *AJ*, **90**, 2082

Thorstensen, J. R., Ringwald, F. A., Wade, R. A., Schmidt, G. D. & Norsworthy, J. E., 1991, *AJ*, **102**, 272

Vande Putte, D., Smith, R. C., Hawkins, N. A. & Martin, J. S., 2003, *MNRAS*, **342**, 151

Verbunt, F., Bunk, W. H., Ritter, H. & Pfeffermann, E., 1997, *A&A*, **327**, 602

Vogt, N., 1983, *A&A*, **118**, 95

Wade, R. A. & Hubeny, I., 1998, *ApJ*, **509**, 350

Walker, W. S. G., Marino, B. F. & Freeth, G., 1976, *Informational Bulletin on Variable Stars*, **1185**

Warner, B., 1973, *MNRAS*, **162**, 189

Warner, B., 1976, *The Observatory*, **96**, 49

Warner, B., 1987, *MNRAS*, **227**, 23

Warner, B., 1995, *Cataclysmic variable stars* (Cambridge Astrophysics Series, Cambridge, New York: Cambridge University Press, —c1995)

Witherick, D. K., Prinja, R. K., Howell, S. B. & Wagner, R. M., 2003, *MNRAS*, **346**, 861

Woods, A. J., Drew, J. E. & Verbunt, F., 1990, *MNRAS*, **245**, 323

Woods, J. A., Verbunt, F., Collier Cameron, A., Drew, J. E. & Piters, A., 1992, *MNRAS*, **255**, 237

Young, P. & Schneider, D. P., 1981, *ApJ*, **247**, 960